School of Physics and Astronomy

Accurate identification of the nature of signals in ground-based gravitational-wave interferometer data

Philip J. Relton

Submitted for the degree of Doctor of Philosophy
School of Physics and Astronomy
Cardiff University

March 31$^{\text{st}}$ 2023

Summary of thesis

The data from ground-based gravitational-wave interferometers has been used for direct astrophysical observations of transient signals for almost a decade. With this data, over 90 compact binary systems have been observed and studied via their gravitational-wave emission. These observations have, and continue to, provide new solutions to astrophysical questions. Gravitational waves can provide information about astrophysical systems that has previously been inaccessible through electromagnetic observations.

The aim of this thesis is to outline some of the dangers of making incorrect assumptions about observed signals in gravitational-wave interferometer data. In Chapter 1 I provide a summary of gravitational-wave interferometer data; from the basic design of the interferometers, through the form of the data, and some methods can be used to manipulate the data for analysis. I then describe the types of signals that can be observed in this data, how these signals are studied, and what further analysis can be performed on the results of these studies.

In Chapter 2 I calculate the probability that transient gravitational-wave signals will overlap with each other in the data. In the chapters that follow I outline the potential problems that time-overlapping transients will cause for the signal detection and analysis methods currently implemented by the LIGO-Virgo-KAGRA collaboration.

Chapter 3 shows how the presence of a second, time-overlapping, binary black hole signal can cause inaccuracies in the estimation of the parameters of the other binary black hole system. I show how this problem manifests in the estimated parameter distributions for different relative parameters between two compact binary signals.

In Chapters 4 and 5 I consider whether it is possible to detect these cases of time-overlapping transients with current methods, determining what cases will be missed without modifications to current algorithms. I also discuss possible modifications to these algorithms, and a separate bespoke method, designed to identify which detected signals contain time-overlapping transient signals.

Chapter 6, presents an analysis of the data of a gravitational-wave interferometer for the purposes of a search for scalar dark matter signals. In this work, we produced extremely precise estimations of the noise floor of the interferometer. We used this to identify and reject possible candidate signals from scalar dark matter.

Finally, in Chapter 7, I provide a summary of the key findings in each of the chapters of this thesis. This chapter includes recommendations of extensions and adaptations to the described investigations to expand and improve upon this work.

Contents

List of Figures

List of Tables

My children, let us not do that again. I, for one, am too old for [things] even vaguely related to that.
- Adrian Tchaikovsky

List of Publications

[1] **Philip Relton** and Vivien Raymond. *Parameter estimation bias from overlapping binary black hole events in second generation interferometers.* arXiv:2103.16225. Physical Review D, 104, 084039, Chapters 2 and 3 in this thesis.

[2] **Philip Relton**, Andrea Virtuoso, Sophie Bini, Vivien Raymond, Ian Harry, Marco Drago, Claudia Lazzaro, Andrea Miani, and Shubhanshu Tiwari. *Addressing the challenges of detecting time-overlapping compact binary coalescences.* arXiv:2208.00261. Physical Review D, 106, 104045, Chapters 4 and 5 in this thesis.

[3] Sander M Vermeulen, **Philip Relton**, Hartmut Grote, Vivien Raymond, Christoph Affeldt, Fabio Bergamin, Aparna Bisht, Marc Brinkmann, Karsten Danzmann, Suresh Doravari, and others. *Direct limits for scalar field dark matter from a gravitational-wave detector.* arXiv:2103.03783. Nature, 600, 424–428, Chapter 6 in this thesis.

I am also an author on several LIGO-Virgo-KAGRA collaboration papers, not listed here, for which my contributions vary.

Collaborative work

Portions of this thesis are the result of collaborative work. This work is outlined below:

– Chapters 2 and 3 are constructed from work performed with Vivien Raymond. This work was published in **Physical Review D**, titled: *Parameter estimation bias from overlapping binary black hole events in second generation interferometers* [1]. I was the lead author on this paper and performed the majority of the analysis.

– Chapter 4 and the first section of Chapter 5 contain work published in **Physical Review D**, titled: *Addressing the challenges of detecting time-overlapping compact binary coalescences* [2] I was the lead author of this paper and performed the majority of the analysis, with the exception of the cWB analyses.

– The analysis using neural networks in the second section of Chapter 5 is collaborative work between myself and Michael Norman. In this work I generated the data and performed the analysis on the output from the network.

– Chapter 6 is published in **Nature** under the title: *Direct limits for scalar field dark matter from a gravitational-wave detector* [3]. I was the second author on this paper. My responsibilities in this work were focused on the data acquisition, processing and testing. I also performed approximately half of the signal analysis, and lead the validation of our results with the blind injection.

I am the sole author of all other work presented in this thesis.

Scientific Acknowledgements

Acknowledgements

I would like to start by thanking my supervisor Vivien Raymond. My three and a half years here have been pretty manic and full of small problems, such as global pandemics. Despite this you have always provided sound advice for any problem I found myself stuck on, and extreme patience with my confused ramblings. It has been a pleasure working with you.

I would also like to thank my second supervisor, Mark Hannam, for his ability to explain many complicated things in an entertaining way. At this point I should definitely thank my two unofficial supervisors; Charlie Hoy and Jonathan Thompson. The two of you both went beyond what could rightfully be asked of you. Thank you for teaching me how to turn on my computer, what these "gravitational wave" things are, and for making me laugh in the process.

There are too many people to name everyone who has helped me through this PhD, but to name a few in quick succession. Thank you to Duncan for endless computing solutions; to Ian, Andrea and the cWB group for taking one of my ideas and helping make it a reality; to Eleanor, Lorenzo, Penny, Rhys, Sebastian, Shrobana, Tessa, Vassilis and Virginia for assorted guidance; and to the rest of the Cardiff GEI for everything over the last three and a bit years.

Thanks to Michael and Sander for entertaining evenings in the Flute, and more civilised establishments when the poor acoustics and overabundance of astronomers got to us.

I need to acknowledge the efforts of my former maths teacher Darren Stillman. Without him pushing me academically I would never have had the confidence in my ability that I needed to make it this far.

To my incredibly supportive friends: Tom, Ariane, David, Will, and the Leicester Physics gang (and partners therein). Thanks to you all for providing times, away from the horrors of science, where the world is always a little better.

I have been supported through this by my fantastic family. Mum, Dad, Steph and Ian, I couldn't have done this without your encouragement, care, and patience with my many protracted lamentations, both during the PhD and the years before. I am incredibly lucky to have you all. Thanks also to Alice's family for many of the same reasons.

To Granny, I will always be grateful for your encouragement. It has always amazed me how you pushed against the odds to win yourself an education. I know how fortunate I am to have had the chances from which you were excluded.

Lastly, and certainly most-mostly, to my best friend and partner Alice. Absolutely nothing in this thesis could have been achieved without your help, and none of it would have been worth it without you.

Chapter 1

Introduction to gravitational-wave interferometer data, signals and analysis methods

1.1 What are Gravitational Waves?

Gravity is an attractive force which governs the interaction of particles with mass. The first true gravitational theory was devised by Sir Issac Newton and published as the *Philosophiæ Naturalis Principia Mathematica* (The Mathematical Principles of Natural Mechanics), in 1687 [24]. This theory allowed classical mechanics to describe almost the entire world of the era. However, by the turn of the twentieth century, it had become clear that Newton's theory could not fully describe all of the behaviour of massive objects [25]. In 1915 Albert Einstein formulated a new theory of gravity, General Relativity (GR) [25, 26]. GR is a mathematical framework that considers gravity as the curvature of spacetime within which particles move along the shortest routes possible. The mass of the particles themselves can cause spacetime to curve. In the following year, Einstein noted the possibility that massive particles moving in a non-symmetric manner could produce waves that would propagate away from the source [25, 27]. These waves, called gravitational-waves (GWs), would be analogous to electromagnetic radiation from electrically charged particles, but orders of magnitude weaker. GWs have two polarisations, commonly referred to as the plus and cross polarisations. These two polarisations stretch and compress spacetime at a separation angle of $\pi/4$ radians.

The weakness of GW strain means that only the most dense, or highly accelerating, of sources produce signals detectable by current ground-based detectors. Examples of these detectable sources include the inspirals and mergers of compact

binary systems, stellar deaths via supernova, and non-spherically symmetrical spinning objects such as mountains on neutron stars. Other, more exotic, theories of GW sources may exist, such as the cusping of cosmic strings [28, 29].

The first indirect detection of GWs was made through observations of the Hulse-Taylor binary pulsar in 1974 [30], for which a Nobel prize was later won in 1993. The observation was made by measuring the change in orbital period of a binary pulsar system. The decay in the orbital period of the neutron stars (NSs) proved that energy in the system must have been radiated away in a manner matching General Relativity.

1.2 GW detectors

With the existence of GWs confirmed indirectly, work began on designing and building detectors capable of direct observation. Early attempts at direct GW detection had been made using bar detectors, proposed and built by Joseph Weber in the 1960s [31]. Bar detectors are static cylinders continuously measured to ascertain their precise dimensions. Bars are tuned to precise frequencies such that GWs of that frequency will cause the bar to resonate. These resonances, should they occur, would allow for direct observations of GWs. Weber claimed confident detection in 1969 [32]. However, no other bar detectors searches have produced confident detections [33–37].

In the 1970s Rainer Weiss suggested a method of GW detection via the change in the arm length of a Michelson interferometer [38]. These detectors could be tuned to different GW frequencies by setting fixed arm lengths. As such, the first GW interferometers were designed to observe the inspirals of known GW sources, binary neutron stars (BNSs). The signals, visible from a few Hz to several kHz would require interferometer arm lengths of several kilometres, with extension via Fabry-Pérot cavities, to produce discernible strain.

GW Michelson interferometers are formed of two, typically orthogonal, arms [39]. Laser light is generated and directed towards a beamsplitter at an angle of $\pi/4$ to the beam. The beamsplitter, situated at the junction of the interferometer arms, reflects half the light down one arm. The rest of the light is refracted through the beamsplitter and down the other arm. The photons in the light travel the length of the arm to be reflected off mirrors suspended at the end. These mirrors, often called test masses, are suspended to simulate free fall. The lengths of the arms are set such that, under the presence of zero strain, the light from both arms will interfere destructively producing a null signal in most cases[1]. If, for any reason the length of the detector arm changes, such as under the presence of a transient GW, then the light from the two arms will not correctly interfere and the light will be collected by

---

[1]In practice, the interferometers are constructed so as to produce a slight offset signal. This allows for testing of the signal in the detector.

a photodiode, producing a measurable signal.

The construction of these instruments is of course far more complex than the summary given above. There are a great many sources of potential noise, as shown in Section 1.3.4, that require mitigation. For more detailed explanations of some of the methods used in current generation interferometers see their design papers [39–41].

1.2.1 First generation interferometers

In the late twentieth century, several collaborations of scientists formed to undertake the task of constructing and operating GW interferometers [42]. The Laser Interferometer Gravitational-Wave Observatory (LIGO) collaboration, initially built three detectors. One four kilometre arm interferometer in Livingston, Louisiana state, and two co-located interferometers were constructed in Hanford, Washington state, with arm lengths of four kilometres and two kilometres. The two Hanford detectors shared arm cavities, the shorter interferometer was much less sensitive, particularly at low frequencies [43]. The LIGO interferometers began their first science runs in 2002[2] [44].

The two LIGO detectors were placed at opposing sides of the continental United States, approximately three thousand kilometres apart. The distance allows for measurement of the sky location of any transient event detected by both interferometers. This can be done via triangulation [45, 46], using two or more detectors, assuming that GWs travel at the speed of light. This was later proved using the transient GW observations [47–49].

Alongside LIGO, three other collaborations built first generation interferometers. The European Virgo collaboration constructed a three kilometre armed detector in Pisa, Italy [50]. A British-German collaboration built the 600 metre GEO 600 detector in Hannover, Germany [51], and a Japanese collaboration built a 300 metre interferometer called TAMA300 in Tokyo, Japan [52].

These detectors operated in several science runs across the first decade of the millennium. Despite a decade of development and improvements in data analysis techniques, no detections were made of GWs [53]. Model sensitivity curves for these detectors can be seen in Figure 1.1, shown by the dashed lines. At the end of the decade they were switched off in order to perform large upgrades [40, 54]. The replacement detectors have since been referred to as second-generation GW interferometers[3].

---

[2]The term "science run" refers to a period of data collection aimed at making a GW detection, without result. The current term for runs, with claimed detections, is "observing run"

[3]It should be clarified that TAMA300 was not upgraded, however another Japanese detector, KAGRA, was later constructed.
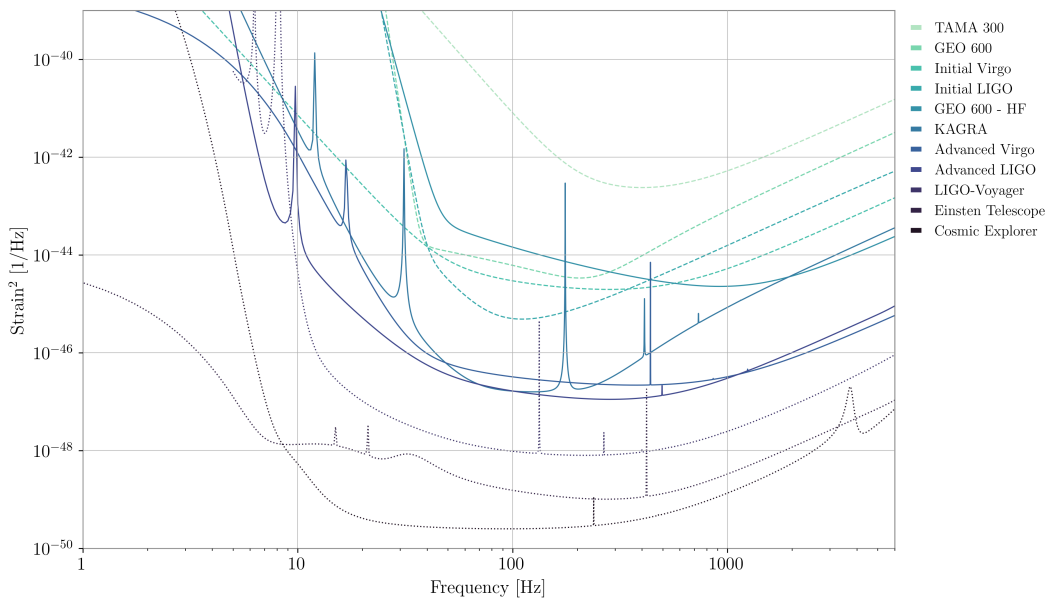
Figure 1.1: Power Spectral Density (PSD) estimations for the noise curves of first generation detectors (dashed lines), predicted final state second-generation detectors (solid lines), and third generation ground-based GW interferometers (dotted lines). The PSD used for this plot are taken from the standard predicted noise representations of each detector listed in the `PyCBC` PSD package. The LIGO-Voyager PSD here is an exception as it is not present in this package. This PSD was generated using the `pygwinc Python` package [10, 11].

1.2.2 Second-generation interferometers

Upgrades to the LIGO interferometers, now called Advanced LIGO, were significant in the period between 2010 and their first observing runs in 2015. The two kilometre detector on the Hanford site was dismantled. Almost all instruments on the two sites were replaced with improved technologies, the original mirrors were replaced by larger test masses with new mirror coatings applied to reduce thermal noise. Laser power was increased, reducing shot noise contributions. Finally, seismic noise was reduced through improvements in the isolation systems. The result were detectors with much better sensitivities, an order of magnitude across the 100 Hz sensitive region. The reduction in seismic and thermal noise led to a much better low frequency threshold of 10 Hz[4], down from 40 Hz in Initial LIGO [39].

At this time an upgrade to the GEO 600 interferometer was also made. The upgrades were limited to improved the sensitivity at high frequency, with the detector now called GEO 600-HF[5] [56, 57]. However, the lack of sensitivity in the compact binary coalescence (CBC) sensitive region limits the science usage of this interfer-

---

[4]This was the aim of the collaboration at the time. However, for most, if not all, analyses the low frequency limit has been set as 20 Hz [55], due to a lack of sensitivity between 10 Hz and 20 Hz.

[5]For the remainder of this thesis we will continue to refer to the detector as GEO 600, except where necessary to make the distinction between the two generations.

ometer. The site is now mainly used as a testing ground for new interferometer technology [58].

The observing runs of the new aLIGO detectors began in September 2015. The first direct observation of a GW was made on September the 14th 2015, just a few days after these detectors were first switched on. This detection was of a 36^{+5}_{-4} + $29^{+4}_{-4}M_\odot$ binary black hole merger [59, 60]. This detection led to the awarding of the 2017 awarding Nobel prize in Physics to Rainer Weiss, Barry Barish and Kip Thorne.

The LIGO and Virgo collaborations have an agreement to share interferometer data in exchange for shared authorship on results. This data sharing between the detectors increased the chance of making a coincident signal detection and improved source localisation for GW signals. Between 2011 and 2017, the Virgo interferometer underwent significant upgrades. The new Advanced Virgo (adVirgo) interferometer was fitted with heavier test masses, higher power lasers, and baffles to reduce stray light [40]. Once these upgrades have been fully implemented, there should be an order of magnitude increase in sensitivity in the 100 Hz region. The adVirgo detector began it's first observing run in 2017 and, alongside the aLIGO detectors second observing run, made the first three-detector observation of a binary black hole (BBH) signal [61], and the first observation of GWs from a BNS inspiral [62].

In 2020, a fourth second-generation interferometer began its first operating run [63]. The KAGRA (Kamioka Gravitational-Wave Detector) detector in the Kamioka Observatory, Japan [64]. KAGRA is an indirect replacement of the TAMA300 interferometer, and is now part of the LIGO-Virgo-KAGRA Collaboration (LVK). Unfortunately, no direct observations were made by KAGRA, due to the relatively low sensitivity of the detector. However, lower limits were placed upon the distances of several gamma ray bursts observations [63].

The second-generation aLIGO detectors have now had three observing runs, two with adVirgo and one with KAGRA. In this time they have made approximately 90 confident[6] observations of different forms of CBCs [55, 65–67] with several other groups claiming the detection of other binaries [68–71] via publicly released data [72–75]. However, none of the interferometers have yet to reach their full second-generation design sensitivity. The observing runs are therefore split by long periods of sensitivity upgrades.

The fourth observing run, fourth observing run (O4), is due to begin some time in mid-2023. The detectors will then shut down for another round of upgrades, before reaching the proposed design sensitivity of LIGO A+ towards the end of 2026 [76–80]. They will then begin a much longer, high sensitivity observing run. These detectors will be joined by another aLIGO detector LIGO-India [81, 82], in

---

[6]These events are those published by the LVK in catalogues or significant event papers. However, the threshold values of $p_{astro} > 0.5$ [55], see Section 1.5.2, will allow a significant number of non-astrophysical sources to be classified as GW events. Despite this, we refer to all these events as "confident" as the collaboration has chosen to present them in this manner.

the late 2020s, which will further improve source localisation [82, 83]. LIGO-India is to be constructed partially from the remaining components of the two kilometre detector originally situated at the Hanford site.

There are several plans to improve these detectors beyond their current design sensitivity. These improvements should lead to significant increases in the observing range of the detectors. They should also increase the low frequency end of the sensitive region. The suggested modifications include heavier test masses, new mirror coatings and higher laser power. The main proposed versions of this are LIGO-Voyager and LIGO A# [78, 80, 84], however, this design it yet to recieve approved funding. There is also a plan for Advanced Virgo+ [85]. Sensitivity curves for the second-generation detectors are shown by the solid lines in Figure 1.1.

1.2.3 Third generation interferometers

By the mid 2030s, a new generation of detectors are expected to begin their observations. These will have order of magnitude better sensitivities and be able to make observations at lower frequencies, potentially down to 1 Hz. There are currently two main designs of ground-based third generation detectors; Cosmic Explorer (CE) and The Einstein Telescope (ET). CE is a similar design to the current aLIGO detectors, but with right angled arms of 40 kilometres rather than 4 kilometres [86–88].

ET is a much more radical design [89–94]. This interferometer design involves three arms at 60 degrees to each other. These arms will be 10 km long, leading to the equivalent sensitivity of a 7.5 km right angled detector. The corners of each arm of the triangle will contain two interferometers, one sensitive to high frequency, one for low frequency. The proposed low frequency of this observatory will allow for source localisation regardless of the active status of other detectors [93]. This detector is also to be built underground to reduce seismic noise.

Alongside these detectors, there are several detectors planned for different frequency ranges of the gravitational spectrum. The Laser Interferometer Space Antenna (LISA) will be a space based, triangular interferometer, with sensitivities between 0.1 mHz and 0.1 Hz [95–97]. Other proposed space based interferometers include Taiji [98–101], a Chinese detector with similar sensitivity and DECIGO (DECi-hertz Interferometer Gravitational-Wave Observatory) [102, 103], a Japanese detector designed to be sensitive in the 0.1 to 10 Hz band, bridging the gap between LIGO and LISA. These detectors will view much lower frequency signals, such as super massive black hole binaries, extreme mass ratio inspirals and the early inspirals of aLIGO-detectable compact binaries [95]. They are also expected to suffer from continuous confusion noise produced by the large number of galactic white dwarf binaries [104–107].

Even lower frequency GW signals, down to frequencies of approximately 10^{-9} Hz can be observed using modulations in the arrival time of known pulsars observed

with radio telescopes. Several collaborations have been collecting data since 2005, these include; the Parkes Pulsar Timing Array (PPTA) [108, 109], the European Pulsar Timing Array (EPTA) [110] and the North American Nanohertz Observatory for Gravitational Waves (NANOGrav) [111]. These collaborations now combine their efforts under the name International Pulsar Timing Array (IPTA) [112]. These ultra-low frequency GW measurements are expected to detect GWs from the the early universe and the inspirals of supermassive black hole binaries. For the remainder of this thesis we will only consider ground-based interferometers of a second-generation design, unless otherwise stated. Comparisons of the strain sensitivity for past, current and planned ground-based interferometers are shown in Figure 1.1.

1.3   Interferometer data

Interferometers return multiple time-sampled data channels concerning the condition of the detector. The main channel for each interferometer records information about the strain in the arms of the detector. The other channels are used mainly as cross references in terms of checking data quality and to understand the state of the hardware [113]. Data segments, taken from these channel, are often referred to as time-series. Typically ground-based GW interferometers, such as aLIGO and adVirgo, use 16 kHz sampling rates for data acquisition[7], however some channels are sampled at different rates. Secondary channels are often sampled at higher rates to provide clearer time-stamps for transient noise artifacts.

1.3.1   Fourier transforms

While the interferometers take time-sampled data, the majority of transient astrophysical astronomy is performed in the frequency domain. Frequency domain data can be estimated from time domain data by taking a Discrete Fourier Transform (DFT). The estimation of DFTs is shown in Equation 1.1:

$$A_k(f) = \sum_{n=0}^{N-1} A_n(t) \cdot e^{-\frac{2\pi i}{N}kn} \tag{1.1}$$

where A is the amplitude in terms of either the frequency, f, or time, t, N is the number of time samples. k and n are the frequency and time bins identifiers respectively. A pure, monochromatic sinusoidal wave in the time domain would, under a DFT, show as a delta function peak in the frequency domain. In practice, no stretch of data is long enough to provide such a distinct peak. Noise in the data would also provide peaks in other frequency bins.

Generally, Fourier transforms are calculated using the Fast Fourier Transform (FFT) algorithm [114]. The FFT algorithm is one of the most efficient and widely

---

[7]The actual sampling rate is 16384 Hz.
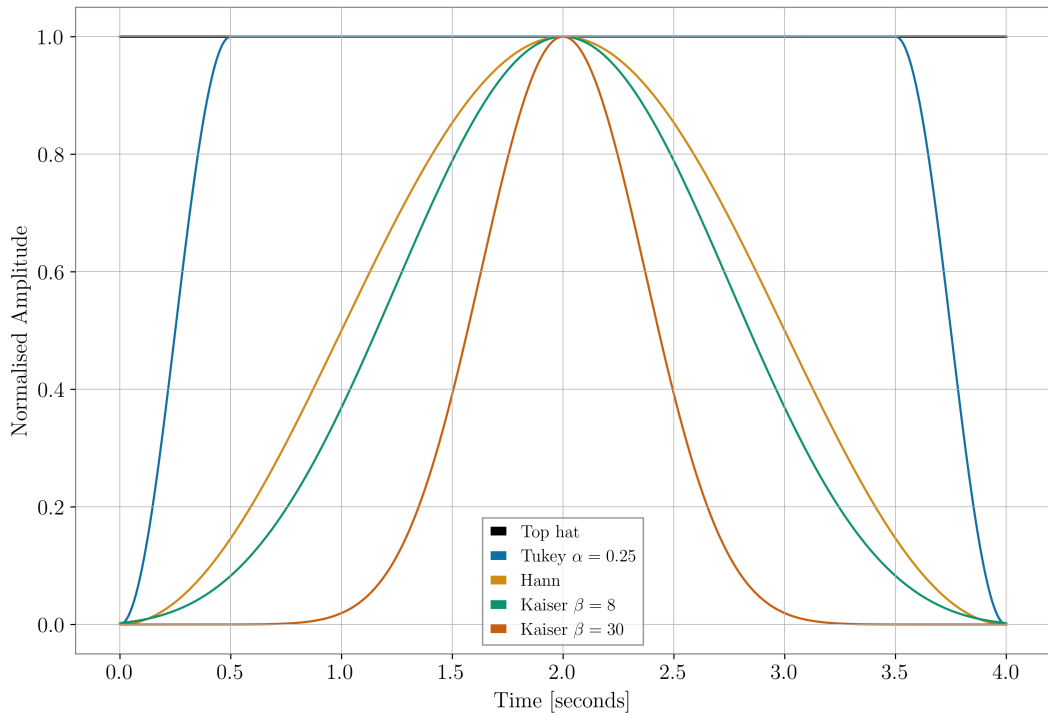
Figure 1.2: Comparisons of four different window functions, generated using the `SciPy Python` package [21], across a four second data segment.

utilised algorithms in computer science. The standard `Python` implementation in `SciPy/NumPy` [14, 21] relies upon the `FFTW` package in `C` [9]. More GW-specific data analysis code used throughout this thesis, such as `GWpy` [12] and `PyCBC` [16–20] rely upon the `NumPy` version.

1.3.1.1 Window Functions

Due to the finite nature of collected data, there can be issues with spectral leakage between different frequencies in the time domain data. To avoid this data is often windowed, or filtered, prior to transformation. An example of how spectral leakage between frequencies can occur in Fourier transforms of aLIGO data, are shown in Figure 1.3.

Window functions are functions, applied in the time domain, to help account for discontinuities at the edges of data segments. This is done by suppressing the amplitude of the data at the start and end of the segment. Examples of some typical windows are shown in Figure 1.2.

Some windows, such as the Hann window [115], are generated purely by the number of time domain samples of the segment. Windows typically used by the LVK collaboration are tunable. Transient astrophysical analysis using aLIGO interferometer data often uses Tukey windows with half second transition regions [116], this is shown by the blue line in Figure 1.2. In the Fourier analysis of GEO 600

data, presented in Chapter 6, we use a Kaiser window with the tunable parameter $\beta = 30$.

1.3.2 Power Spectral Density

For the purposes of transient GW astrophysics, it is often useful to have an estimation of the noise floor of the detector[8]. This is done by calculating a power spectral density (PSD)[9]. PSDs are typically calculated by taking several DFTs of equal length and calculating an average for each frequency bin. The result is an estimate of the mean, or median, of each frequency bin, but with a reduced variance compared to a typical single DFT. The most common method of PSD averaging used in GW observational science is known as Welch's method or Welch averaging. Welch's method calculates DFTs of overlapping time segments to decrease the variance further by averaging over more data [17, 117]. Figure 1.3 shows an example of the difference between a single PSD estimation and a Welch averaged PSD of data from the LIGO: Livingston interferometer. This figure shows that an incorrectly windowed segment of interferometer data can collapse to a $1/f^2$ function [116].

1.3.3 Filtering and Whitening

It is often necessary to filter data to remove unnecessary noise in frequency regions separate from the signal frequency. Figure 1.4 demonstrates how windowing and filtering aid in understanding interferometer data for signal analysis. The top plot shows the raw strain recorded in LIGO: Livingston at the time of GW150914

The middle plot shows the same data, but whitened using a PSD estimation of the same data. The PSD was estimated over 32 seconds of data surrounding the signal, excluding the half second containing the signal itself. Whitening is a process used to normalise the noise in detectors. PSD estimations of the average noise floor are made; this average is then used to suppress the data in the frequency domain to provide equal amplitude across all frequencies. The expression for the estimation of the nth detector's PSD, $S_n(f)$, at frequency f, is given in Equation 1.2.

$$S_n(f) = 2 \int_{-\infty}^{\infty} R_n(t)e^{-2\pi ift}dt \tag{1.2}$$

where $R_n(t) = \langle n(\tau)n(\tau + t)\rangle$ is the auto-correlation function for stationary data.

The process for whitening, for time-domain data $d(t)$, is given by Equation 1.3:

$$d(t) \xrightarrow{FFT} \tilde{d}(f) \xrightarrow{Whiten} \tilde{d}_w(f) = \frac{\tilde{d}(f)}{S_n^{1/2}(f)} \xrightarrow{iFFT} d_w(t) \tag{1.3}$$

---

[8]See Sections 1.3.3 and 1.5.1 for examples.

[9]For clarification the Power Spectral Density is the equivalent of the Power Spectrum (PS), but normalised by the frequency at each point. There are also equivalents of Amplitude Spectrum (AS) and Amplitude Spectral Density (ASD) which is the square root of the PSD.
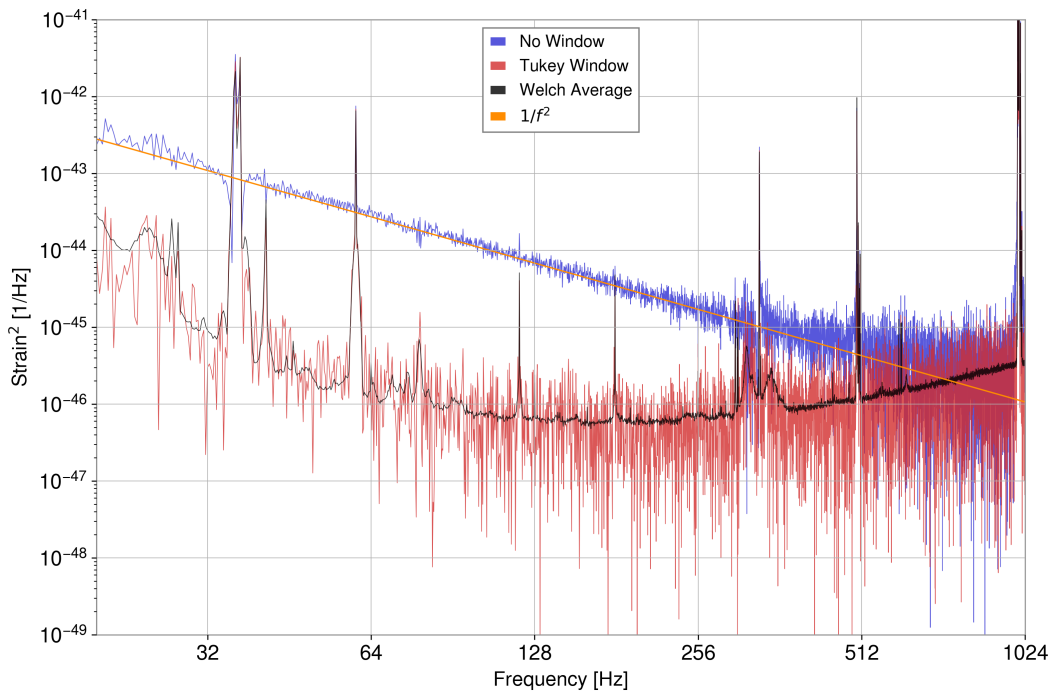
Figure 1.3: A PSD estimation of data from LIGO: Livingston around the time of the detection of GW150914, the first GW detection. The red line shows the strain of the detector calculated across a 32 second segment of data, with a Tukey window function. The black line is an estimation of the same data using Welch averaging. The blue line shows the estimation without proper windowing of the data and the orange line showing the trend of the unwindowed data. It should be noted that this plot is an adaptation of Figure 4 in Abbott et al. 2020 [116] generated with public LIGO data.

The bottom plot shows the whitened strain with a low pass filter removing frequencies above 200 Hz and a high pass filter removing frequencies below 35 Hz. There are also separate filters removing the excess power at specific frequencies due to power lines[10]. These filters are applied prior to the inverse Fourier transform in Equation 1.3.

1.3.4 Interferometer noise

Any non-astrophysical strain produced in the data can be categorised as noise[11]. Noise can be further divided into transient and non-transient noise.

---

[10] The AC power in the United States is transmitted at a frequency of 60 Hz. Due to this there are peaks in the noise at 60 Hz, and subsequent harmonics at 120 Hz and 180 Hz.

[11] In sufficiently sensitive detectors, such as LISA, it is likely that large numbers of astrophysical noise sources could form stochastic noise in the detector. However, these have not been detected in either past or current ground-based interferometers as such signals occupy a frequency range outside the sensitive bands of ground-based interferometers.
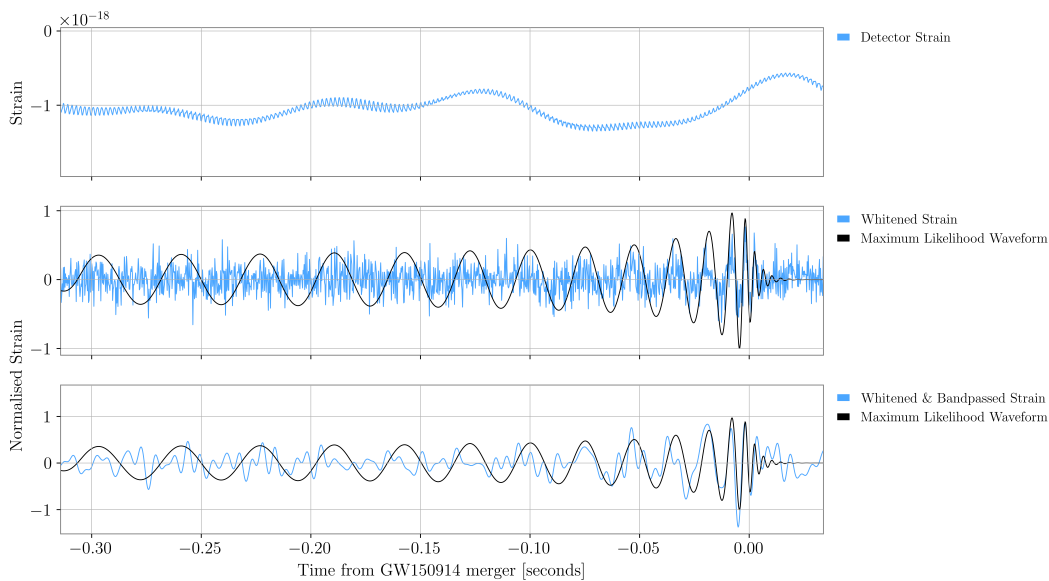
Figure 1.4: A demonstration of the effects of windowing and filtering of data. The data in this figure is the public strain, sampled at 4kHz, of GW150914 released by the LVK, the strain for the waveform of GW150914 is calculated using the `PESum-mary` plotting library [15] and the maximum likelihood from the public samples of GW150914 [74], the approximant used is `SEOBNRv4PHM` [118].

1.3.4.1   Non-transient noise

Non-transient noise in GW interferometers comes from numerous sources, each contributing to the noise floor at different frequencies. These contributions can be seen in Figure 1.5. For example, at low frequencies, typically below 20 Hz, the dominant noise comes from environmental noise, sometimes called "seismic noise" such as the movement of vehicles in the surrounding area. A significant peak can be seen at about 10 Hz from resonant oscillations in the test mass suspensions, other modes of these suspensions can be seen at higher frequencies, 500 and 1000 Hz respectively. These oscillations are sometimes called the "violin modes".

Above 200 Hz, the sensitivity is dominated by quantum vacuum fluctuations. This noise is a combination of shot noise, variations in photon arrival time at the photodiode, at high frequencies and radiation pressure noise at low frequencies. This can be reduced via quantum squeezing [76, 79]. Quantum squeezing of the phase of the laser increases the measurement precision of the amplitude and reduces precision of phase measurement, while in turn squeezing the amplitude increases the measurement precision of the phase. In GW interferometers phase squeezing is implemented to reduce shot noise and increase high frequency sensitivity [119].

For the majority of current astrophysical analyses noise from these sources are assumed to be normally distributed about the mean noise floor and to not change over the length of observed transient signals. These assumptions of Gaussianity and stationarity are crucial in order to perform accurate analyses.
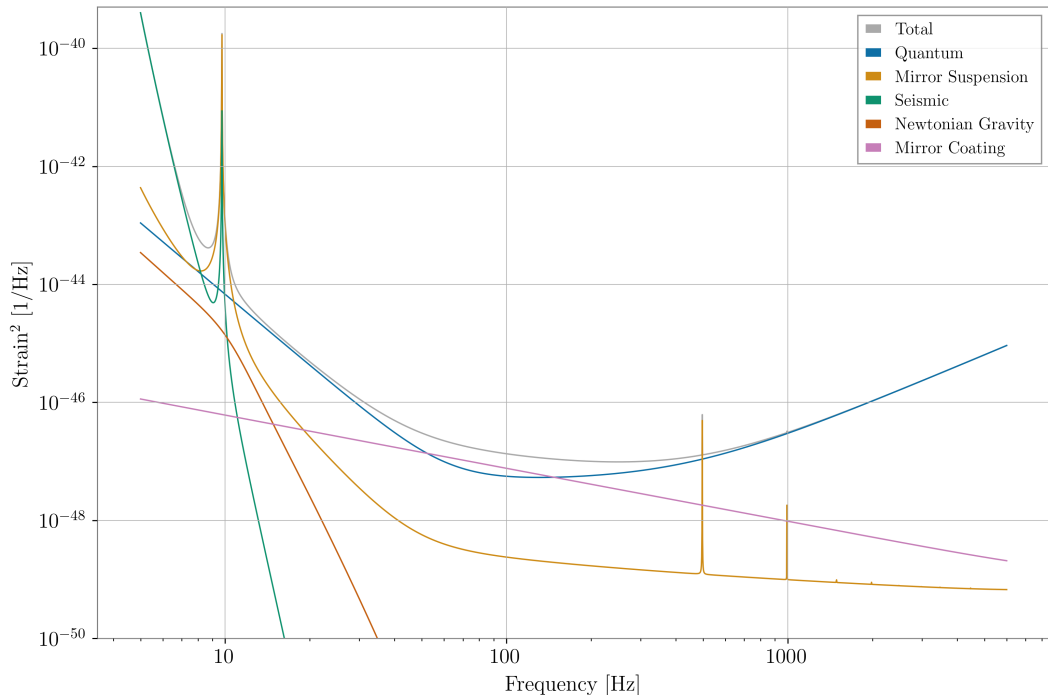
Figure 1.5: Example PSDs of the contributions of different noise sources to the design sensitivity of an Advanced LIGO interferometer. The data in plot was produced using the `pygwinc` package [10, 11]. Environmental noise consists of contributions from seismological shifting in the Earth's crust, the Newtonian Gravity component is due to the affect of gravity on the test masses and the Mirror Coating noise is due to thermal oscillations in the components.

1.3.4.2 Transient non-Gaussian noise

Transient non-Gaussian noise, or "glitches", appear as significant differences from the noise floor of the detector. These occurrences can be up to several seconds in length, typically shorter, and significant glitches can be as frequent as several per minute [55]. Only a limited number of these glitches have known sources, such as scattered light on the test masses, weather, or interactions with electromagnetic communications [113, 120, 121]. These sources can often be removed or reduced. There are hundreds of auxiliary channels which check the status of known noise sources, such as changes in the environmental conditions or detector measurement systems, that can be used to test data quality [113]. Other glitches, such as blip glitches, are less well understood [121]. Blip glitches cause significant problems for searches as they are frequent, can cover portions of real signals, and can also cause transient signal triggers. These glitches have to be modelled and subtracted from the data after recording [62, 122, 123]. Where this is not possible, data segments can be vetoed and removed from analyses. They can cause false signals to occur in transient signal searches [121], and later cause problems for astrophysical analysis if improperly subtracted [122, 124]. Examples of glitches in interferometer data can be

seen in Figure 4 of [113]. The presence of these glitches cause the assumptions of stationarity and Gaussianity to fail, however, work is being done to better understand these sources, and to account for these assumptions [125–128].

Non-stationarity in the data can also occur as slow drifts in the noise floor over hours and days. To avoid this, transient signal analysis typically generates PSD estimations just prior to the signal. This ensures the most accurate possible representation of the noise at that time [55]. For transient GW analyses a PSD will be calculated for each interferometer, this is then assumed to accurately represent the interferometers noise floor for the duration of that potential signal. This assumption may fail for long duration signals, such as low mass CBCs inspirals, and could cause significant problems in future generations of detectorsi [126].

1.4 Compact Binary Coalescences

The ground-based GW interferometers were designed to detect the signals of inspiralling BNSs, as they were considered to be the most likely candidate for observation in the accessible frequency-strain domain [129]. Despite this, the first confident detection of any transient GW was from the merger of a BBH. On the 14th of September 2015 the two aLIGO detectors observed the the merger of a $36^{+5}_{-4}M_\odot$ black hole (BH) with a $29^{+4}_{-4}M_\odot$ BH [59, 60] with a network signal-to-noise ratio (SNR) of 24. Since then, over 90 confident detections of CBC GW signals have been observed [55, 65–71].

CBCs are the observable collisions of two dense objects, typically BHs or NSs. Such objects are extremely massive, of the order of a few to a few tens of stellar masses. The extreme densities allows the objects to orbit each other at very small radii before merger, therefore allowing for extreme GW strains to be produced. The observable length and signal strain are related to the masses of the compact objects. Low mass binaries produce less strain in a detector at fixed distances, but merge at higher frequencies, compared to high mass binaries.

The observable lifespan of such signals can be split into three distinct regions:

– *Inspiral*: In which the signals orbital radii decays. This is typically the longest observable portion of a detectable CBC signal, particularly at lower masses. Customarily, the observational start of this portion of the signal is when the GW frequency reaches 20 Hz. This is the low frequency cut off of current GW interferometers due to the lack of sensitivity at lower frequencies. However the region theoretically extends back to the formation of the binary.

– *Merger*: The point at which the two objects inspiral ends and the objects collide to form a single object. This is almost always the point of maximal strain in the interferometer. For high mass CBCs this will dominate the observable signal, due to the inspiral mostly occurring below the low frequency

cut off of current interferometers. BNS systems, and potentially neutron star-black hole (NSBH) systems with low BH masses, could produce observable electromagnetic counterparts [130] at, or just prior, to this point.

– *Ringdown*: This is the coalescing of the final object from merger to its final state. At this point the two complex objects have formed a single black hole, this black hole will be distorted away from its equilibrium state and will "ring" as it relaxes back into this final state.

1.4.1   Modelling CBC systems

The strain produced by a CBC can be modelled. In current LVK analyses, which assume that these systems will have circular orbits [59, 131], a BBH signal is described by a total of fifteen parameters for a BBH signal, with seventeen for BNS. The parameterisation can be divided into two parameter sets:

– *Intrinsic*: Parameters relating to the internal dynamics of the system. These will include the masses and spins of the signal. For very simple analyses the intrinsic parameters are considered to be two mass parameters and the two aligned spin parameters. However most modern analyses will include in-plane spin, totalling eight parameters [132]. In the cases of systems including NSs there may also be a parameter describing the tidal deformability of each NS. Extra parameters can also be included, for example to describe a systems eccentricity [133]. For all analysis in this thesis we have considered only BBH systems with in-plane spin giving a total of eight parameters, two describing the masses and six for the spins.

– *Extrinsic*: Parameters describing the relation of the signal source to the location of its detection. These typically include right ascension and declination, the parameters giving where this signal is on the sphere of the sky. The distance to the source, typically referred to as the luminosity distance. The inclination of the binary plane to the line of sight of the signal, the time of arrival, and the angles of the signal's phase and polarisation angle upon detection [132]. The these parameters are typically presented by their estimated values when the signal meets the centre of the Earth, rather than from any single detector.

A list of typical parameterisations and values can be found in Tables A.1 and A.2 in Appendix A.

Some of these parameters are best represented in terms of combinations of multiple parameters. For example, one possible representation of a system's mass would be the masses of the primary and secondary components, m_1 and m_2 respectively. However, it is often more convenient for analyses to use the parameters of *chirp mass*, $\mathcal{M}$, and *mass ratio* q[12], these are shown in Equations 1.4 and 1.5.

---

[12]By convention the secondary component mass is always smaller than the primary. As such,

$$\mathcal{M} = \frac{(m_1 m_2)^{3/5}}{(m_1 + m_2)^{1/5}} \tag{1.4}$$

$$q = \frac{m_1}{m_2} \tag{1.5}$$

Mass parameters are typically given in units of solar mass, $M_\odot = 1.9885 \times 10^{30}$ kg. The chirp mass of a standard $1.4 + 1.4\, M_\odot$ BNS is approximately $\mathcal{M} = 1.22\, M_\odot$, and that of a $30 + 30\, M_\odot$ BBH is $\mathcal{M} = 26.1\, M_\odot$.

The spins of the components can be represented in a number of ways, two common representations encode the aligned and misaligned components of each objects spin into two parameters χ_{eff} and χ_{p} [134]. These parameterisations are shown in Equations 1.6 and 1.7.

$$\chi_{eff} = \frac{1}{M} \left(\frac{\boldsymbol{S_1}}{m_1} + \frac{\boldsymbol{S_2}}{m_2} \right) \cdot \hat{\boldsymbol{L}} \tag{1.6}$$

where M is the total mass of the binary, $\boldsymbol{S_N}$ is the spin of component N, and $\hat{\boldsymbol{L}}$ is the orbital angular momentum of the system.

$$\chi_p = \max \left(\chi_1 sin\theta_1, q\frac{4q+3}{4+3q}\chi_2 sin\theta_2 \right) \tag{1.7}$$

where χ_1 and χ_2 are the dimensionless spin magnitudes of the two binary components, normalised to the range $[-1, 1]$.

The most common CBC signals found by the LVK are identified as aligned spin systems, with little evidence of in-plane spin inferred [135]. A system with high in-plane spin, up to $\chi_p = 1$, is known as a precessing system. In these cases the unaligned spin angular momentum is large enough to cause the orbital angular momentum of the system to rotate around the total angular momentum of the system. This causes a beating-like pattern in the waveform [136, 137].

The modelling of the inspiral and mergers of CBCs is a complex process. There are currently no analytical solutions for CBC systems found through Einstein's equations [25]. It is possible to simulate such systems using numerical simulations [138, 139]. However, the simulations required to do this are incredibly slow and complex. As such, the waveforms used in analysis are approximations constructed from catalogues of numerical relativity simulations.

There are four main families of CBC waveform approximants which take different approaches to the physical representation of the systems. Inside each of these families there are several variations of the underlying principles including different physical aspects, such as incorporating spin, tidal effects and eccentricity.

– *Taylor*: These approximants are constructed from Taylor expansions of the

---

Equation 1.5 will always have value $q \leq 1$. However, some analyses will use the inverse of Equation 1.5. This is not done in any analysis in this thesis.

Post-Newtonian approximation [140]. There is a significant limitation to these approximants as they only approximate the inspiral of the system and cannot simulate the merger and ringdown. As such, they are most commonly used for long inspiral systems such as sub-solar mass binary black holes and BNSs, where the inspiral is the dominant portion of the SNR. In these systems more advanced approximants can be very slow, however, as these expansions are just numerical functions, they are very quick to evaluate for different parameter sets. They can be generated in either the frequency domain, *TaylorF*, or the time domain *TaylorT* [141].

– *Phenomenological*: These approximants are constructed from functions that approximate to catalogues Numerical Relativity simulations. Unlike Taylor waveforms they can approximate the inspiral, merger and ringdown of the signal. The two most commonly used approximants in this family are versions of either `IMRPhenomT` [142–144], in the time domain, or `IMRPhenomX` [145–147] in the frequency domain. Other than the Taylor approximants these are typically the fastest available approximants. Adaptions for each of the time and frequency domain versions are available to account for in-plane spin and higher multipoles. Example representations of a highly spinning BBH system under three `IMRPhenomX` approximants can be seen in Figure 1.6[13].

– *Effective One Body (EOB)*: This family of approximants is broadly similar to the `Phenom` family, in the manner of being approximated to Numerical Relativity simulations. However, they then fit the system by combining the mass of the system into a single "body" with orbiting point masses. These approximants can often be very slow to estimate and are only available in the time domain[14]. The most common approximant currently used in this family is `SEOBNRv4` [118, 148, 149]. Like `IMRPhenom` this waveform has more detailed models accounting for in-plane spin and higher multipoles. Example representations of a highly spinning BBH system under three `SEOBNRv4` approximants can be seen in Figure 1.7[15].

– *Surrogates*: Surrogate approximants are constructed directly from catalogues of numerical relativity simulations [150]. These will be gridded, typically in terms of mass ratio, from equal mass up to around $q = 0.25$. Between points in this grid the surrogate will return an interpolated waveform between the two closest simulations.

Versions of several of these waveforms are available including extra parameters,

---

[13]It should be noted here that the lack of in-plane spin in this waveform means that the parameters given to the aligned spin model were slightly different to those in the other two models.

[14]Although frequency domain analysis is possible via Fourier transforms

[15]It should be noted here that the lack of in-plane spin in this waveform means that the parameters given to the aligned spin model were slightly different to those in the other two models.
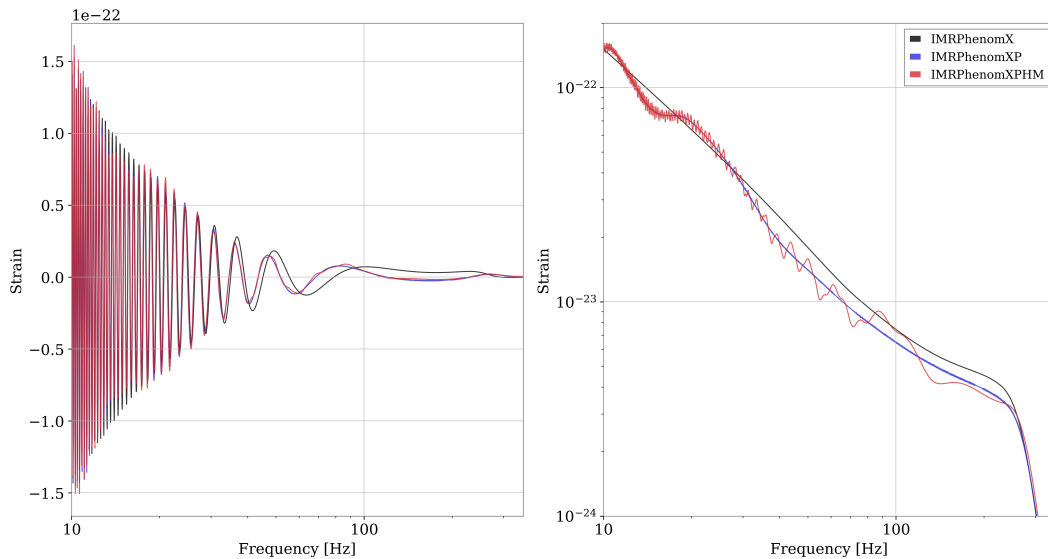
Figure 1.6: Frequency domain representations of a BBH signal, using three versions of the `IMRPhenomX` waveform approximant. The left plot shows the strain as a function of frequency, right the power in the waveform at each frequency across the waveform. The three approximants shown here each include different physics, aligned spin only (`IMRPhenomX`), in-plane spin (`IMRPhenomXP`), higher multipoles and in-plane spin (`IMRPhenomXPHM`). These signals have the following parameters $\mathcal{M} = 24.3 \, \mathrm{M_\odot}$, $q = 0.5$, $\chi_{\mathrm{eff}} = -0.3$, and $\chi_{\mathrm{p}} = 0.4$ (`IMRPhenomX` has $\chi_{\mathrm{p}} = 0$). These signals were generated at a distance of 400 Mpc.

for example with tidal deformability for BNS approximants. Current BBH waveforms, in general use by the LVK, include modelling for in-plane spins and higher multipoles. They do not, in standard CBC analyses, typically include eccentricity. Generation times typically increase as physics is included and as the total mass decreases. This leads to longer analysis times for later studies.

These approximations will not be perfect representations of the true systems. However, due to the weakness of currently observed signals, compared to detector noise, the systematic errors of these approximants has very rarely caused problems with analysis [151].

Systematic errors from inaccuracies in waveform approximants are more likely to occur for signals with a significant SNR [152, 153]. In these cases the likelihood in the data will be a sharper, more defined peak. There has been one case in which this has occurred in GW astronomy. GW200129 was analysed and categorised by the LVK as a standard BBH merger [55]. However, there were significant differences between the two analyses performed by the LVK using the `SEOBNRv4PHM` and the `IMRPhenomXPHM` approximants [55]. Hannam et al, 2023, noted that the `SEOBNRv4PHM` waveform suffers from systematics in this region of the parameter space and that the surrogate waveform and the Phenomenological waveform would be better approximants in this case [154]. This is the case in large part due to the
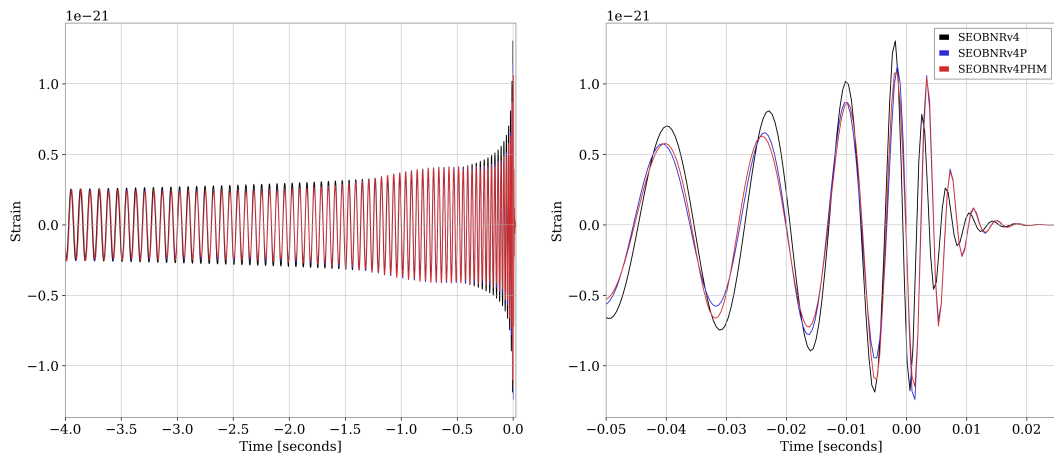
Figure 1.7: Time domain representations of a BBH signal's strain, using three versions of the `SEOBNRv4` waveform approximant. Left shows the strain from 20 Hz to the merger and ringdown, right shows a close in representation of the merger and ringdown. The three approximants each include different physics, aligned spin only (`SEOBNRv4`), in-plane spin (`SEOBNRv4P`), higher multipoles and in-plane spin (`SEOBNRv4PHM`). The parameters of these signals are the same as those given in Figure 1.6.

signal being one of the highest SNR signal yet recorded[16].

1.4.2 CBC categories

1.4.2.1 Binary Black Holes

Binary Black Holes are currently the most commonly observed transient GW signals. To date there have been over 80 confident detections. The most famous of these is GW150914, the first detection. This signal fits into the category often called "vanilla BBHs". These are BBH mergers, typically with near equal component masses between 10 and 50 $M_\odot$, most commonly showing little evidence of misaligned spin or higher multipoles. This category fits the vast majority of detected GW signals. The reasonably high mass of these objects allows for large viewing ranges, out to z 1. As such they are the most common signals observed in ground-based GW interferometers.

Other cases of more interesting BBH systems include the first detection of an asymmetric mass ratio [155], GW190412, in which the masses of the two components were $30\,M_\odot$ and $8\,M_\odot$, this event also showed evidence of high order multipoles and in-plane spin. There is also the high SNR, strongly precessing signal GW200129 [55, 154], see Section 1.4.1.

---

[16]The detection was shown to have significant, measurable in-plane spin. The first of its kind. It should be noted that this has been disputed due to the overlap with a glitch [124], however, it is unlikely that the glitch would provide enough SNR to account for the physical effects, even under imperfect subtraction.

1.4.2.2 Binary Neutron Stars

Binary Neutron Stars are much lower mass signals and as such are visible in the detector band for longer durations. They are however visible to much lower distances due to their lower masses, compared to BBH mergers. The component objects, Neutron Stars, are the high-mass dense remains of large stars. Neutron star observations are particularly valuable for astrophysical study due to their extreme conditions. It is not currently known what the distribution of NS masses in binaries is [135, 156–160], the radii of these NSs [161], or the condition of the matter within the star itself [162–164]. As such GW observations are particularly valuable for constraining the NS equation of state [62, 123, 165–168]. These uncertainties in the population of observable NSs leads to broad, potentially non-astrophysical, parameter ranges in analyses [169, 170]. The `PyCBC` search presented in Chapter 4 considers NSs with masses from 1 $M_\odot$ to 2.5 $M_\odot$ in its template bank.

Observable BNS mergers are assumed to have relatively low spins [171], compared to BBH systems. The maximal NS spin is likely below $|\chi| < 0.7$ [172]. Typically, analyses of signals of this nature are considered under two possible spin priors high spin, $|\chi| < 0.89$, and low spin $|\chi| < 0.05$[123, 173].

As the components are not BHs they are subject to tidal deformation [174, 175]. This means that modelling of the systems requires careful consideration of the matter effects, although the contribution to the waveform from tidal deformation is quite weak [176–178]. The two main waveform approximant families, `IMRPhenom` and `SEOBNR`, construct specific approximants for analysis of these systems, these are typically suffixed with *NRTidal* [179, 180]. The tidal deformation can lead to tidal shredding of one or both objects, prior to or during the merger. This can cause concurrent observations of the event in electromagnetic bands [62, 123].

To date there have been two confident observations of BNS GW emissions. The first, GW170817, is one of the most significant astrophysical events ever recorded [62, 123]. It was the merger of two neutron stars, with masses $1.46^{+0.12}_{-0.10}M_\odot$ and $1.27^{+0.09}_{-0.09}$ $M_\odot$. The signal was found in three interferometers, both aLIGO detectors and ad-Virgo, this allowed for extremely accurate source localisation. For the first time a coincident Gamma Ray Burst observation GRB170817A [181–183]. The GW observations measured the sky location to a region of 16 square degrees [62, 123] at the 90% credible region, subsequent electromagnetic observations allowed the source to be located to its host galaxy. The resulting kilonova was observed in all electromagnetic bands from Radio through to Gamma Rays [184].

The second BNS observation was that of GW190425 [173]. This observation was not coincident with any confident electromagnetic observations [173]. However, there have since been low-confidence claims of link to a coincident Fast Radio Burst [185, 186]. The lack of confident electromagnetic observations is likely due to the lack of sky location sensitivity from operating interferometers. GW190425 had measured

masses of $2.0^{+0.6}_{-0.3} M_\odot$ and $1.4^{+0.3}_{-0.3} M_\odot$, higher than that of GW170817.

1.4.2.3 Neutron Star - Black Hole Binaries

During the second half of the third observing run, two observations of the merger of a NS with a BH were observed [187]. These events, GW200105 and GW200115, did not coincide with any electromagnetic observations, this could be because the systems were too distant for a detectable electromagnetic counterpart, the lack of accuracy in inferred sky location, or because no such counterparts were produced. In high mass ratio scenarios it is likely that the merger occurs before the NS is tidally disrupted [188, 189]. There are also two other possible NSBH events, GW190426_-152155 [66] and GW190917_114630 [67], although these signals were deemed less significant by the LVK [187].

Another significant GW detection that could fit into this category is the merger of a $23.2^{+1.1}_{-1.0} M_\odot$ black hole and a $2.59^{+0.08}_{-0.09} M_\odot$ neutron star, GW190814 [190]. This signal, again with no electromagnetic counterpart, is possibly the heaviest NS ever detected, or the lightest BH ever observed. It falls within the mass gap between the heaviest estimates of NSs and the lowest formation scenarios for BHs [191–194]. For the purposes of many LVK analyses this mass gap is defined to component masses between $2.5 M_\odot$ and $5 M_\odot$.

1.4.2.4 Intermediate Mass Black Hole Binaries

BHs with masses less than $100 M_\odot$ are known as stellar mass BHs, while those above masses of $10^5 M_\odot$ are Supermassive Black Holes, between these two ranges objects are known as Intermediate Mass Black Holes (IMBH) [195–198]. Mergers of binaries in these mass ranges are likely to be some of the loudest detectable signals in ground-based GW interferometers. However, to date no observations of these mergers have been made [199, 200].

Despite this, observations of high mass mergers have proved the existence of IMBHs, the most significant of these being GW190521 [201], in which the final remnant BH had a mass of $156.3^{+36.8}_{-22.4} M_\odot$. Several other mergers with similar masses have since been observed [55]. The high masses involved in these signals leads them to be observable at large distances. They are also only observable in the detector band for a few cycles, due to the relatively low frequency of their mergers.

1.5 Transient signal observations

For confident signal detection we need to test if a signal, $h(t)$, is present in our strain data, $d(t)$ at time, t. To do this we draw a null hypothesis, H_0, that the data contains solely noise $n(t)$, and an alternative hypothesis that it contains both noise and signal.

$$H_0 : d(t) = n(t) \tag{1.8}$$

$$H_1 : d(t) = n(t) + h(t) \tag{1.9}$$

So far, the only GWs confidently observed by ground-based detectors have been transient signals from the inspirals and mergers of compact binaries. Despite the relative intensity of these signals, compared to other transient GW sources, the detector data containing the signal is generally dominated by noise.

1.5.1 Matched filtering

Due to the dominance of the noise in the interferometer data, observations and analysis often utilise a method known as *matched filtering* [202]. Matched filtering works best for complex, but modelable signals. In matched filtering, a template is created for a signal. By convolving this template with the noise and data of the detector a quantity known as the matched filter SNR. An SNR greater than one indicates that a signal, matching this template, could be present in the data. The difference between the classic definition of SNR and matched filter SNR are subtle, but important. Throughout this thesis SNR will refer to the matched filter SNR unless otherwise stated.

The first step in estimating the SNR is to calculate the noise weighted inner product of template $h(f)$ with data $d(f)$. These quantities are generally estimated in the frequency domain, either by direct generation or Fourier transform from the time domain, as shown in Equation 1.10 [202].

$$\langle h | d \rangle = 4Re \int_0^\infty \frac{h^*(f)d(f)}{S_n(f)} df \tag{1.10}$$

Here, $S_n(f)$ is a frequency domain estimation of the noise in the data. This is typically calculated using PSD estimation on detector data just prior to the region of interest[17]

The matched filter SNR, ρ, can then be estimated from this inner product, and the inner product of the template with itself, using Equation 1.11 [202].

$$\rho = \frac{\langle h | d \rangle}{\sqrt{\langle h | h \rangle}} \tag{1.11}$$

For detected GW signals the SNR is one of the most commonly quoted values, often alongside the False Alarm Rate[18] and relevant signal specific parameters such

---

[17]Single estimations of detector PSDs are not typically used across long periods of time. This reduces errors arising from the non-stationary nature of the noise.

[18]See Section 1.5.2 for a definition
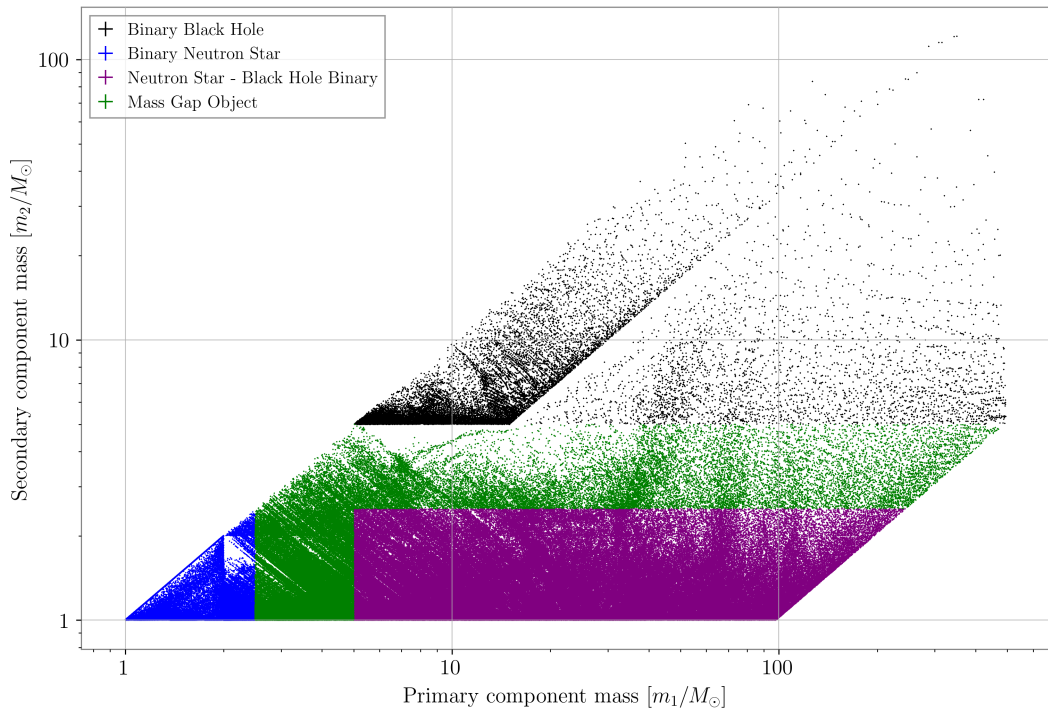
Figure 1.8: A plot of the component masses of templates in the template bank used for the `PyCBC`-broad search in the third aLIGO observing run (O3).

as the chirp mass[19].

1.5.2   Searches for transient signals

The most common, and successful, transient GW searches utilise matched filtering through template banks. In a template bank search, the parameter space of the possible subject signals is divided up into a grid of possible signal templates. For example, in the third observing run, the `PyCBC` template bank was a grid across the parameter space of component mass and dimensionless aligned-spin of each of the compact objects [203]. The templates in these banks are spaced in order to provide minimal loss in SNR, 0.5% for the bank shown in Figure 1.8, between a signal and its closest template [203–205]. An example of a template bank is given in Figure 1.8

The search pipeline will iteratively generate a waveform template, constructed from the parameters of each template in the bank. It will match each template to the data at each time stamp in the data in order to return an SNR time-series. Peaks, above a certain significance, are considered as single detector triggers. Generally, detections are not claimed on single detector triggers [206], therefore further steps are taken in which two or more detectors are checked for coincident triggers within the light travel-time separation between active interferometers.

Often, as in O3, some parameters are left out in order to reduce the size of the

---

[19]See Equation 1.4

template bank, mostly for reasons of computational expense. In the template bank shown in Figure 1.8 the parameters governing template placement are primary and secondary component mass and the aligned spin of each component. This could lead to searches missing significant signals; for example, if a bank does not account for in-plane spin, then highly precessing signals may be missed entirely by such searches [207].

These searches for transient signals can produce a very large number of triggers. These can be reduced under the condition of multiple detector coincidence. However, even with this constraint it is likely that the vast majority of returned signals would occur from random fluctuations in the detector noise. To avoid this several constraints are applied; False Alarm Rate (FAR), SNR, and search specific detection statistics.

Signals are not claimed as confident detections by the LVK unless they have a network SNR of 12 or higher [77]. The network SNR is a calculated by adding the individual detector SNRs in quadrature. For a three detector, Hanford (H1), Livingston (L1), Virgo (V1), detection this calculation would be:

$$\rho_{\text{network}} = \sqrt{\rho_{\text{H1}}^2 + \rho_{\text{L1}}^2 + \rho_{\text{V1}}^2} \tag{1.12}$$

All searches use FAR as a measurement of trigger significance. A FAR estimation is made by taking the data from one detector and offsetting the other by an amount greater than the maximum light travel time between the two detectors. This means that there can be no real coincident signals between the two data sets. The template is then matched with each data set to estimate the number of coincident events with a matched filter SNR equal or higher than that of the true trigger. If the number of these "false events" is high then the trigger is more likely to have been produced by similar noise in the detectors and the event is less likely to be astrophysical. LVK events are typically only considered significant if they meet the threshold of FAR < 2 per year [66].

Each search uses its own specific detection statistic. For example, `PyCBC` uses a reweighting of the SNR with a χ^2 statistic, sometimes called "new SNR" [19, 53]. Recently confident triggers are required to meet a probability of astrophysical origin threshold of greater than 50% [55]. This threshold uses the value p_{astro} which makes assumptions about trigger distribution and knowledge of merger rates [208].

There are several matched filter based searches, two of the most commonly used of these are `PyCBC` [16–20] and `GstLAL` [209, 210]. There are also other, non-matched filter based searches performed for transient signals. These unmodelled[20] searches are less optimal CBCs than modelled matched filter searches and therefore can miss significant signals found by other searches. They are, however, a more ag-

---

[20]Some searches, including `cWB` are sometimes referred to as "weakly-modelled", as they often include constraints for chirp-like behaviour. Commonly this is done by searching for signals that increase in frequency with time.

nostic tool and therefore are capable of finding unexpected and unmodelled sources.

The one commonly used unmodelled/weakly-modelled search is the coherent Wave Burst, `cWB`, pipeline [6, 7, 211]. `cWB` finds regions of excess power in the noise. It compares these regions with data in other active detectors in order to find coincident power. By using light travel times between detectors it compares the profile of these power regions in order to find coherent sky locations for these events. If there is a reasonably coherent sky location it is then able to reconstruct the waveform of the signal in the noise via excess power subtraction.

1.5.3 Parameter Inference

If a confident detection is made of a transient GW signal then it is often considered in further detail in order to establish features of the signal's source. This processes is called parameter estimation (PE). There are several PE algorithms currently in use by different groups. However, the most common method is Bayesian Inference via stochastic sampling.

1.5.3.1 Bayes Theorem

Bayes theorem allows for the estimation of the probability that the data, d, contains some signal $h(\theta)$, comprised of parameters θ. This relates the conditional probabilities between the two as shown in Equation 1.13.

$$P(h(\theta)|d, M) = \frac{P(d|h(\theta), M)P(h(\theta)|M)}{P(d|M)} \tag{1.13}$$

Here the posterior probability, $P(h(\theta)|d, M)$, of a signal $h(\theta)$ being in data d, given model M, is given by the estimation of the likelihood, $P(h(\theta)|M)$, the prior probability of the signals having the set of parameters (θ) and given evidence $P(d|M)$.

Bayes theorem therefore allows us, given some model, to estimate the probability of a signal with set parameters being present in the data. To do so we need to estimate the values of the prior, likelihood and evidence.

Customarily, the prior distributions of these parameters are chosen to be uniform across their particular parameter space. This allows for increased agnosticity in parameters. It should be noted that this does not necessarily mean that all prior distributions are straight, uniform distributions. For example, the most agnostic distribution for the inclination of a binary is uniform in the cosine of the inclination angle. Another example is the use of a cubic power law distribution for luminosity distance, as this is flat in volume. Some analysis may be done with more astrophysically informed priors, such as predicted mass distributions from published signal catalogues [135], however, this is not done for any PE in this thesis.

By far the most complex and expensive step in PE is the likelihood estimation.

This involves generating waveform approximants for the set of parameters and then performing inner product calculations. The quantity calculated is generally the log-likelihood and is given in Equation 1.14.

$$\ln\left(P(d|\theta)\right) = (d|h(\theta)) - \frac{1}{2}(h(\theta)|h(\theta)) \tag{1.14}$$

As, for each set of parameters, we must estimate a waveform approximant and then calculate the match; this step can take several seconds, leading to analysis times on the order of days. This is particularly the case for low mass systems, analysis at low frequencies, and approximants with complicated physics and many parameters. The evidence is the integral of the likelihood across all possible parameters in the model and is essentially used as a normalisation constant.

1.5.3.2   Stochastic Sampling

With these values estimated for a set of parameters, it is possible to estimate posterior probabilities. As shown in Section 1.4.1, CBC signals require many different parameters to describe the observed signal. To accurately infer the parameters of the system we must estimate the true value all of these parameters. The standard approach for this is to explore the parameter space via stochastic sampling, of which there are two main approaches; *Markov Chain Monte Carlo* (MCMC) and *Nested Sampling*.

Markov Chain Monte Carlo involves performing one or more, randomised walks around the parameter space [5, 212–215]. The posterior probability is estimated at each step and is used to decide if the sample should be accepted or rejected and another drawn. Once a new sample is accepted then it is used as a base for the step to the next sample. The next step depends only on the previous step. This allows the walk to tend towards local maxima, but also escape to catch other modes.

While MCMC techniques have several methods to avoid being stuck in local maxima [216], they can often miss other modes in the data. Nested sampling, if distributed sufficiently densely in its initial samples, can avoid this [217, 218]. Here a large number of points are placed randomly across the parameter space. These are then ordered by likelihood. Depending on the method the sample are then rejected or accepted by trying to find a new sample with a better likelihood than that of the least "likely" sample.

Stochastic sampling methods like this are generally very slow, mostly due to the likelihood estimation and waveform generation. Alternative methods are now in use [219–223]. While these methods draw samples, they do so in different, less agnostic, ways.

There are multiple ways to speed up parameter estimation. A common method is to reduce the number of sampling parameters through marginalisation [132, 224], in which certain parameters are removed from sampling. These parameters can

later be constructed using analytical approaches. This can be only be done over certain parameters such as time [225], phase [226] and distance [227]. This is because these parameters are less astrophysically interesting and simple to remove during sampling. Other possible methods, typically designed around speeding up the likelihood evaluation and waveform approximant estimation, are commonly used. These include, but are not limited to; efficiently binning waveform generation in frequency space [228], and constructing waveforms from linear combination of basis vectors [229].

1.5.4   Posterior distributions

Parameter estimation runs are performed over many dimensions. This is impossible to accurately visualise, so the distribution of samples are shown on a parameter by parameter basis, either as a one dimensional histogram, or as a comparison between two or more parameters. Figure 1.9 (left) shows a plot of the distribution of component masses in public samples of GW150914[59, 60, 230], while Figure 1.9 (right) shows the same samples but parameterised over chirp mass and mass ratio. Both plots show from analysis with two different waveform approximants[21]. These figures also contain one dimensional posterior distributions, shown by the Kernel Density Estimations (KDEs) on the horizontal and vertical axis. KDEs are smoothed estimates of distributions [231]. The width of the posterior shows how well constrained the analysis is of that parameter, for example, the mass ratio of the signal is not well constrained in either analysis.

1.6   Population analyses

With a selection of GW signals detected analysis can be made to examine the makeup of the universe of GW producing binaries. Such studies provide insight into how the universe forms such systems. For example, if the distribution of binaries indicates that binaries often have in-plane spin then more binary systems may form dynamically than in isolated binaries [232].

These studies have been used to interpret the mass distribution of both BBH and BNS systems [135]. They have also interpreted how the mass distribution of BBHs varies with redshift and how the spins of such systems behave. These studies have large error margins due to the low numbers of events, particularly for BNS systems, and also due to the selection effects of ground-based interferometers biasing towards higher mass binaries. For an example of this see the difference between the

---

[21]It should be noted that, while the posterior distribution from the two sets of analyses are given equal significance in these plots, direct comparisons between the two should be made with caution. There are almost 90 times more samples in the `IMRPhenomXPHM` analysis than in the `SEOBNRv4PHM` analysis. This is due to the relative speeds of waveform approximant generation allowing for faster analyses with the `IMRPhenomXPHM` approximant.
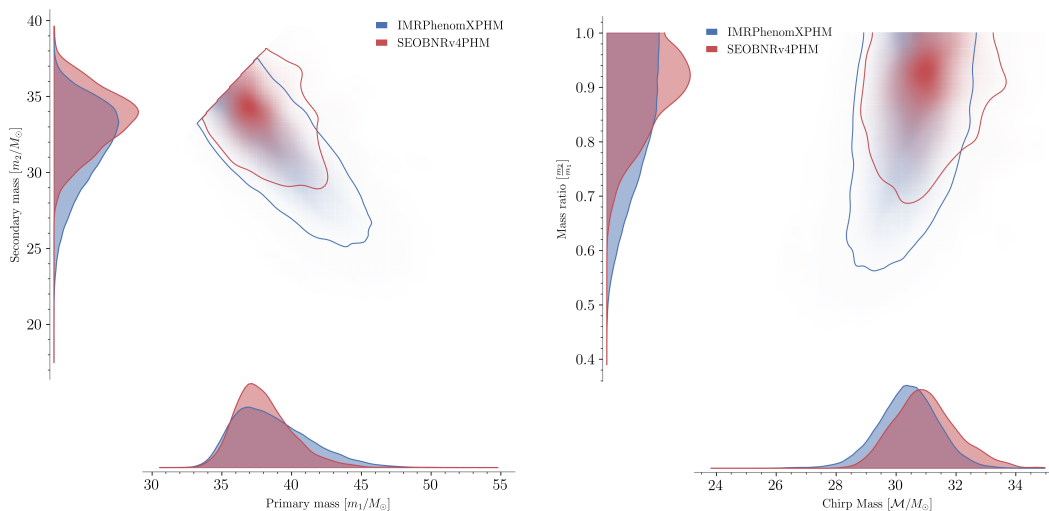
Figure 1.9: Posterior distributions for component masses (left) and chirp mass-mass ratio (right) of the first transient GW detection, GW150914. The KDEs on the horizontal and vertical axis represent one dimensional marginalisations the individual parameters. The central plot shows a two dimensional representation of the parameters.

distribution of the detected, Figure 2, and inferred, Figure 10, merger rates of BBH mergers by mass in the most recent LVK rates and populations estimates [187].

Throughout this thesis, where parameters are drawn from distributions we have used distributions from [233] for BBH systems, unless stated otherwise. However, we use a variety of different BNS mass distributions, both due to a lack of available model data at the time of some work, and due to the specific needs of different studies. The specific choices of BNS distribution is explained where relevant.

1.7 Other observable signals in interferometer data

While all GW studies in this thesis are based upon CBCs, there are a number of other signals that ground-based interferometers could detect. As yet there have been no confident observations of any non-CBC GWs.

1.7.1 Bursts and other transients

The most commonly searched for transient signals, other than CBCs, are sources such as supernovae [234]. These are the violent explosions of large stars, which often then form a NS or a BH. These systems are very difficult to model and as such there has been little success in generating waveforms for their GW signals. Because of this they are, currently, best characterised as burst-like, or "unmodelled" signals. Supernovae are likely to be much weaker signals than those from CBC mergers. The LVK was only able to rule out detections of supernovae within 20 Mpc in the first two observing runs [235]. At this time the viewing range of a typical BNS signal

was up to five times greater [65]. Despite this small range, it is possible that such an event could be observed within the current generation of detectors.

Another burst candidate is that of cosmic strings [28]. Cosmic strings are theoretical one dimensional boundaries left over from the formation of the universe. These strings could potentially tangle with themselves and "cusp" creating loud GW transients. There are little to no theoretical constraints on the length or mass of such strings and as such there can be no efficient template based searches. There is also no knowledge as to the frequency ranges of such possible signals. Therefore, they could quite likely emit detectable GWs outside the frequency range of ground-based interferometers [28].

There are also several, modellable, GW emitting binary systems that have not been observed, and will likely emit waves outside the range of current detectors. These systems are predicted to emit at lower frequency, typically in the range of the planned space-based detector LISA or the Pulsar Timing Array. These include: Supermassive Black Hole binaries [236], Intermediate Mass Black Hole binaries [237], White Dwarf binaries [238] and Extreme mass Ratio Inspirals [239].

1.7.2 Continuous waves

Non-transient, or long duration signals, are typically predicted from non-spherically symmetrical spinning NSs [240, 241]. "Mountains", predicted to be on the order of a few centimetres high, on the surface of NSs, will cause broadly monochromatic long durations signals. These should be detectable by ground-based detectors. Searches for such signals are typically performed by searching for signals in the sky location of known pulsars, or as all-sky searches for unknown systems. These searches, while currently unable to observe such signals, have been able to place limits on the spherical nature of known neutron stars [242–245]. There are other potential sources of continuous waves, such as matter accreting pulsars [246] and dark matter boson cloud-black hole orbits [247].

There is also the possibility of other, non-GW signals interacting directly with the interferometer in a similar manner to continuous waves. One such possibility is the coupling of scalar field dark matter signals with the beamsplitter. In Chapter 6 we describe this possibility in more detail.

1.7.3 Stochastic background

Stochastic GWs have two theoretical sources, astrophysical and cosmological. Astrophysical sources are caused by the confusion noise from large numbers of similar sources [104–107]. For example, between approximately 2×10^{-4} and 2×10^{-3} Hz, the LISA detector will likely have a noise floor set by the number and frequency of galactic white dwarf binaries [96] and not by the technological noise of the instrument. The sheer number of such signals will cause a near-Gaussian signal. Long

duration studies of these signals, matched with electromagnetic observations of signals should allow for studies of the loudest/nearest signals. However, the majority of these signals will contribute to the noise [248].

Cosmological stochastic GWs come from the big bang and the early universe [249, 250]. This signal, analogous to the cosmic microwave background, would be at very low frequencies and therefore only detectable by the pulsar timing array. Such a signal would allow for measurements of the early universe, earlier than any current, electromagnetic observation has made. There are upper limits set on the GW background with ground-based GW interferometers [251, 252].

1.8   Thesis overview

The purpose of this thesis is to outline how signals in GW interferometer data can be misidentified and the effect this has on analysis of those signals. The thesis is structured in the following way:

Chapter 2 presents an estimation of how and when transient compact binary GW signals will overlap in the visible band of ground-based GW interferometers. Chapter 3 covers how typical parameter estimation techniques will behave in the presence of time-overlapping binary black hole mergers. Chapter 4 discusses how two typical transient GW search algorithms behave when transient signals overlap in time. Chapter 5 considers possible methods for ensuring that detected GW transients are correctly identified to be either single signals or time-overlapping transients. Chapter 6 gives an example of a method of estimating the power spectral estimate of GW interferometer data and how this can be used to search for scalar dark matter. Finally, Chapter 7 concludes this thesis, giving a summary of the work and its importance for the field of GW data analysis.

Chapter 2

Estimation of the probability of observing two time-overlapping Compact Binary Coalescences

2.1   Introduction

To date the only GWs observed by ground-based interferometers have been transient signals. Specifically, these signals have been CBCs. This is due to these signals typically being the loudest and most common signals predicted in the frequency range of these interferometers. For the majority of detectable CBCs, the observable portion of the signal is typically only the last few seconds, or fewer, of the binary's life. This means that these signals are only present in the detector band as transient signals.

Since the second-generation of GW interferometers began observations in 2015 [59], they have confidently detected over ninety distinct CBC signals, across three different observing runs [55, 65–71]. While the detectors have yet to reach their design sensitivity, the periods between observing runs allow for increased viewing range and therefore increases in the number of observed signals [55, 77]. For example, between the first and second observing runs, O1 and O2 respectively, the range at which LIGO: Livingston could observe a typical BNS signal increased from 60 to 80 Mpc. This was in large part due to the replacement of a faulty temperature sensor, but also improved mass dampers and the mitigation of scattered light in the detector [65, 253]

Figure 2.1 gives an example of how the sensitivity of the LIGO: Livingston detector increased across the three observing runs[1]. In each run, this sensitivity lead to an increase in the mean rate of detected transients as shown in Table 2.1.

---

[1]See Section II.A of B. P. Abbott et al, 2019 [65], for the changes between O1 and O2, Section II of R. Abbott et al, 2021 for changes between O2 and O3 [66], and Section II of R. Abbott et al, 2022 for changes between O3a and O3b [55]
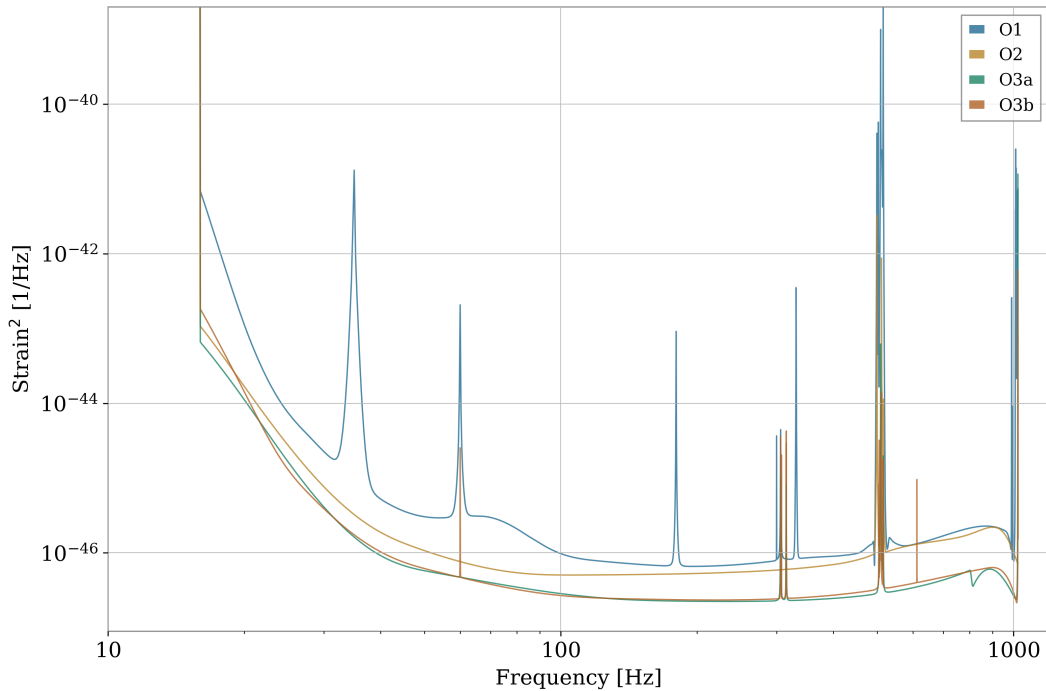
Figure 2.1: Example PSD estimations of the LIGO: Livingston detector across the three observing runs of LIGO. The data for these PSDs are taken from publicly released estimates at the time of signals in those observing runs. O1: GW150914 [230], O2: GW170814 [254], O3a: GW190828_063405 [255], O3b: GW200306_093714 [256]. The third observing run was split into two halves, O3a and O3b. There were only minor upgrades, such as through the adjustment of the vacuum squeezers, to the sensitivity during the break [55]. In this figure we have applied a low frequency cut off of 15 Hz.

The current generation of detector are due to reach design sensitivity in 2025 [77], with the next generation of detectors expected to start observations by the middle of the next decade [87, 89]. In this time, the rate of signal detection is expected to increase to the point at which multiple transient signals could be observable by detector at any one time.

Current methods of CBC data analysis rely upon the assumption that the data contains either solely noise, or noise with a single signal. As the presence of one or more secondary signals would break this assumption, it is necessary to estimate when we are likely to start observing such cases, and then if and how much it affects current signal analysis techniques. This will allow for the preparation of future detection and analysis techniques for such an occurrence. In this chapter we outline how such time-overlapping signal rate estimates can be made and give estimates of when, and how often, such signal overlaps could occur.

Observing Run	Length (days)	Detected Events	Mean Event Rate (per week)
O1	130	3	0.16
O2	269	8	0.21
O3a	183	47	1.80
O3b	148	35	1.66

Table 2.1: The mean rate of event detection for LVK reported events for O1 [65], O2 [65], O3a [66, 67] and O3b [55]. Length of time, in days, are rough estimates and do not account for short losses in lock. Other candidate events have been suggested by other groups, but are not included here [68–71].

2.2 Calculating the probability of observing time-overlapping CBCs

The number of CBC signals observed by a detector depends on the merger rate of such systems, the length of the observing period, and the volume of space in which that merger is visible by the detector. As CBC signals are random and independent, their merger times can be modelled by a Poisson distribution [257]. This means that the probability of a merging system being observed within a specific time period is then given by:

$$P(\text{k signals in time } T_{\text{obs}}) = \frac{(R\,T_{\text{obs}})^k \exp^{-RT_{\text{obs}}}}{k!} \tag{2.1}$$

where R is the rate of mergers, T_{obs} is the period of observation, k is the number of mergers in that period. For two mergers to overlap in time, there must be two signals that are detectable within the visible duration of a single signal, T_{signal}. With this duration we can use Poisson statistics to calculate the inter-arrival time for two signals. For example, if the first signal occurs at time t_0, with the second signal occurring at time $t_1 = t_0 + \Delta T$, then we can find the probability that ΔT is less than the observable period of the signal:

$$P(\Delta T < T_{\text{signal}}) = 1 - \exp^{-RT_{\text{signal}}} \tag{2.2}$$

This is the probability that a detected signal is overlapping another signal. Further, by estimating the number of detectable signals in an observing period of a detector, the number of time-overlapping signals can also be predicted. A rough estimate of this is given by the number of detectable signals multiplied by the probability of signals overlapping in time.

Current estimates on the merger rate of compact binaries are confined to redshifts of $z \lesssim 1$ due to the nature of observed signals. It is known that this rate will increase with increasing redshift [135]. An increase in the rate of detections would lead to an increase in the rate of time-overlapping signals. However, for the purposes of

our study we have assumed a constant merger rate, regardless of redshift. This assumption should hold well for all detectors discussed here, with the exception of Einstein Telescope, as their viewing ranges are largely constrained within the volume $z \lesssim 1$. Calculated values for ET should be treated with caution due to this uncertainty. The true values are likely to be much larger, potentially over an order of magnitude higher. This will lead to a significant increase in the number of overlapping binary signals.

To estimate the distance at which a particular detector configuration can observe different merging systems we use the BNS range. By convention, the BNS range of a detector is the horizon distance at which the detector can observe a binary neutron star coalescence with masses $1.4M_\odot + 1.4M_\odot$ with an SNR of 8, from an optimal sky location. This horizon distance assumes that the signal is in an optimal sky location for the detector, all calculations in this study have included this assumption. The equivalent for binary black hole mergers is for two $30M_\odot$ black holes at an SNR of 8. The mean BNS range for the second part of the third observing run, O3, were 115 Mpc and 133 Mpc for LIGO: Hanford and LIGO: Livingston respectively [55]. The LVK does not release BBH range estimates from observing runs, however estimates of that BBH range for the two detectors at this time would be 1080 Mpc and 1250 Mpc respectively[2].

2.2.1 Probability of time-overlapping BBH mergers

The rates and populations companion paper for the third GW transient catalogue produced by the LVK collaboration estimated the rate of BBH mergers from the signals it observed at: $\mathcal{R}_{\mathrm{BBH}} = 28.3^{+13.9}_{-9.1} \, \mathrm{Gpc}^{-3}\mathrm{yr}^{-1}$ [135].

The relatively large sample of observed BBH mergers allows for the rate of merger to be calculated as a function of the systems component masses [135]. We used publicly available data [233], for the *PowerLaw+Peak* mass distribution shown in [135]. This distribution gives a rate estimate for a variety of different merging black hole systems with primary masses between $[5, 100]M_\odot$ and mass ratios in the range $[0.1, 1]$. For each system in this grid we used the `inspiral-range` Python package [11, 258], alongside estimates of the PSD for different detector configurations [92, 259–262][34] to estimate the distance at which the detector could observe a merging BBH system of that mass pairing to an SNR of 8. Estimates of the visible duration of the signal were then made by generating waveforms for each mass pairing and calculating the duration of the signal between a low frequency cutoff and the merger. These were 20 Hz for the aLIGO configurations [77], 10 Hz for

---

[2]This agrees with the estimates by the collaboration prior to the observing run [77]. It also agrees with an estimate using the PSD for O3b shown in Figure 2.1.

[3]The PSD used for aLIGO: O3 is taken from the first three months of the Livingston detector during O3.

[4]The LIGO-Voyager PSD is a noise estimate calculated via the `pygwinc` Python package as described in Chapter 3.3.4

LIGO-Voyager [78] and 1 Hz for Einstein Telescope [90].

Estimates for the probability that an observed signal contains an overlap can then be calculated in the following way:

$$
\begin{aligned}
P(\text{Overlap}) &= 1 - \exp^{-\langle RT \rangle} \\
&= 1 - \exp^{-\langle \mathcal{R} V(m) T(m) \rangle} \\
&= 1 - \exp^{-\mathcal{R} \int V(m) T(m) p(m) dm}
\end{aligned}
\tag{2.3}
$$

where $\langle RT \rangle$ is the average of the merger rate and visible signal duration over all mass pairings, $V(m)$ is the visible volume, calculated as a sphere in comoving volume[5] at inspiral range for mass pairing m, $T(m)$ is the visible duration for the mass pairing, and $p(m)$ is the probability of observing such a mass pairing.

From this we found the probability that an observed binary, in the next aLIGO operating run, O4, overlaps another signal at approximately $1.0^{+0.5}_{-0.3} \times 10^{-5}$. Estimating the number of signals, by multiplying the rate of BBH mergers with VT, the visible volume and observing duration, leads to an expected $100.0^{+56.0}_{-29.0}$ signals in O4. From these values there is very little chance of observing any time-overlapping signals in this observing run. The same is true for the final aLIGO configuration at design specifications.

However, when aLIGO is replaced by the proposed LIGO-Voyager detector [84, 264] the sensitivity, and therefore viewing range, will increase. LIGO-Voyager is expected to have a significant increase in low frequency sensitivity. We therefore set a low frequency cutoff of 10 Hz. This increases the observable period for BBH signals, further increasing the probability of overlap.

With this detector configuration, the number of mergers in a year's observing run is $2700.0^{+1300.0}_{-880.0}$. The probability that an observable signal in LIGO-Voyager is overlapping another detectable signal is approximately $2.3^{+1.2}_{-0.8} \times 10^{-3}$. This could occur in as many as $6.3^{+7.7}_{-3.4}$ of observable BBH detections in LIGO-Voyager per year. LIGO-Voyager is therefore the most likely detector to first observe such signals. While this will only occur for a small fraction of signals, it could cause significant problems if the signals are incorrectly identified. This will be the case, particularly if the bias from the overlap causes drastic changes to the recovered signal parameters.

By the mid 2030s, 3G detectors, such as ET and CE[6], will start their observation runs. These detectors will have almost an order of magnitude better sensitivity and much lower frequency cutoffs. Observing time-overlapping signals here is near certain and should account for the majority, if not all, BBH signals. Values for these calculations are given in Table 2.2.

---

[5]The conversion to comoving volume was estimated using the `Python` package `Astropy` [4] with the Hubble constant set to the value found by the Planck mission in 2018 [263]

[6]We have not included estimates for Cosmic Explorer, however we do not expect that the signals in this interferometer to face similar rates of time-overlapping signals as Einstein Telescope.
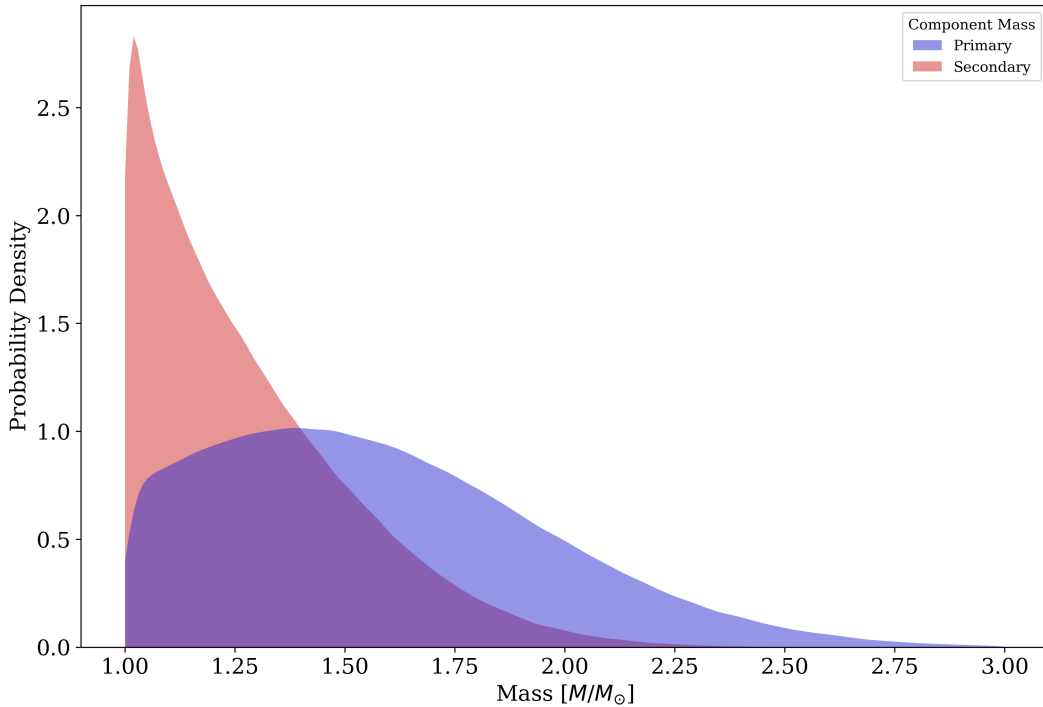
Figure 2.2: Distribution of primary mass (blue), secondary mass (red) for BNS mergers

2.2.2 Probability of time-overlapping BNS mergers

The BNS merger rate is not well constrained due to the small number of observed BNS mergers. To date the LVK collaboration has only observed two BNS mergers [62, 155]. To calculate the average visible duration of such signals, we have defined a probability distribution function for the mass of the primary neutron star and drew a sample grid. The grid covered the range $[1, 3]\mathrm{M}_\odot$ for primary mass and $[0.3, 1]$ for mass ratio. For each mass pair the probability of the primary mass was drawn from a truncated normal distribution between $1\mathrm{M}_\odot$ and $3\mathrm{M}_\odot$, with a mean of $1.4\mathrm{M}_\odot$ and variance 0.5. The probability of the secondary mass was drawn from the same distribution, but with truncated limits between $1\mathrm{M}_\odot$ and the primary mass. The probability of that mass pair is then the product of these two probabilities. These two distributions can be seen in Figure 2.2.[7]

We followed the same method described in Section 2.2.1 to calculate the probability of two or more time-overlapping signals occurring in O4. The rate of BNS mergers is $\mathcal{R}_{\mathrm{BNS}} = 105.5^{+190.2}_{-83.9}\,\mathrm{Gpc}^{-3}\mathrm{yr}^{-1}$ [135], the predicted BNS range is $190\,\mathrm{Mpc}$ [77]. BNS signals have much lower masses than BBH systems, as such they merge

---

[7]This work was performed before an estimate of the BNS mass distribution was made in the most recent release of the LVK rates and populations paper. Due to this, the distribution was set as shown here. We have since rerun these calculations with updated rate estimates from this data release, however we did not update the BNS mass distribution. Similar results for this analysis with distributions taken from the second LVK rates and populations estimates [265] can be found in the original published work [1]

at much higher frequencies and can have a visible duration on the order of minutes in a second-generation detector.

We predict that the number of observed BNS mergers in O4 will be $3.2^{+5.7}_{-2.5}$ mergers per year. Over the full year of O4 the probability of detecting two signals from BNS signals that overlap is $1.4^{+2.5}_{-1.1} \times 10^{-5}$. Therefore it is not expected that time-overlapping BNS signals will be observed in the next aLIGO observing run.

The increase in visible volume allowed by LIGO-Voyager, coupled with the increase in visible duration via a lower low frequency cutoff, leads to a drastic increase in the number of observed time-overlapping BNS mergers. However, initial studies of time-overlapping binaries, imply that only signals that overlap with mergers close in the time domain, less than fractions of a second apart, will cause significant problems, see Chapter 3 for more details. This calculation only sets the requirement that the signals overlap in the time domain. Despite the large number of time-overlapping BNS signals in LIGO-Voyager, it is unlikely that any will overlap across a significant portion of the inspiral. Several studies have looked at parameter estimation upon such overlaps [266, 267].

As with BBH mergers, during third generation detector observing runs, it is likely that most, if not all, BNS mergers will overlap. This is mostly due to the increased number of observable cycles. Values for these calculations are given in Table 2.3.

2.2.3   Probability of BBH mergers overlapping with BNS mergers

BBH mergers are visible in ground-based interferometers for much shorter periods than BNS. The visible period for a typical $30 + 30 M_\odot$ BBH merger in aLIGO is approximately 0.894 seconds, from a starting frequency of 20 Hz. For a typical $1.4 + 1.4 M_\odot$ BNS merger, this is 161 seconds. However, at the sensitivities of aLIGO and LIGO-Voyager, BBH signals are observed at a much higher rate. It is therefore possible, and likely, that time-overlapping signals will be observed with a BBH merger occurring within the visible period of a BNS inspiral.

Detector Configuration	Mean BBH Range (Mpc)	Low Frequency Cut Off (Hz)	Mean Visible Duration (s)	$P(Overlap)$ (BBH)	N_{events} (BBH)	$N_{Overlap}$ (BBH)
aLIGO: O3	611.0	20	6.735	$3.9^{+1.9}_{-1.3} \times 10^{-6}$	$42.0^{+21.0}_{-13.0}$	$0.0^{+0.0}_{-0.0}$
aLIGO: O4	842.5	20	6.735	$1.0^{+0.5}_{-0.3} \times 10^{-5}$	$100.0^{+56.0}_{-29.0}$	$0.0^{+0.0}_{-0.0}$
aLIGO: Design	882.9	20	6.735	$1.2^{+0.6}_{-0.4} \times 10^{-5}$	$120.0^{+60.0}_{-38.0}$	$0.0^{+0.0}_{-0.0}$
LIGO-Voyager	2684.0	10	43.11	$2.3^{+1.2}_{-0.8} \times 10^{-3}$	$2700.0^{+1300.0}_{-880.0}$	$6.3^{+7.7}_{-3.4}$
Einstein Telescope	4961.0	1	19830.0	$1.0^{+0.0}_{-0.0}$	$15000.0^{+7100.0}_{-5000.0}$	$15000.0^{+7100.0}_{-5000.0}$

Table 2.2: The probabilities of detecting overlapping BBH signals, and estimates on the number of such detections, in different GW detector configurations, across a years observations. All quoted error margins are 90% credible intervals. We note here that the number of observed signals in O3, according to R. Abbott et al 2022 [55], is slightly higher than this value. This is likely due to the specific PSD estimation used for this analysis. However, these numbers are meant to be only broadly demonstrative of typical observing run values.

Detector Configuration	Mean BNS Range (Mpc)	Low Frequency Cut Off (Hz)	Mean Visible Duration (s)	$P(Overlap)$ (BNS)	N_{events} (BNS)	$N_{Overlap}$ (BNS)
aLIGO: O3	133.8	20	151.3	$4.8^{+8.7}_{-3.8} \times 10^{-6}$	$1.1^{+2.0}_{-0.87}$	$0.0^{+0.0}_{-0.0}$
aLIGO: O4	189.8	20	151.3	$1.4^{+2.5}_{-1.1} \times 10^{-5}$	$3.2^{+5.7}_{-2.5}$	$0.0^{+0.0}_{-0.0}$
aLIGO: Design	197.7	20	151.3	$1.6^{+2.8}_{-1.2} \times 10^{-5}$	$3.6^{+6.5}_{-2.9}$	$0.0^{+0.0}_{-0.0}$
LIGO-Voyager	771.6	10	957.0	$5.8^{+10.4}_{-4.6} \times 10^{-3}$	$210.0^{+390.0}_{-170.0}$	$1.2^{+8.5}_{-1.1}$
Einstein Telescope	2185.0	1	440000.0	$1.0^{+0.0}_{-0.0}$	$4800.0^{+8500.0}_{-3800.0}$	$4800.0^{+8500.0}_{-3800.0}$

Table 2.3: The probabilities of detecting overlapping BNS signals, and estimates on the number of such detections, in different GW detector configurations, across a years observations. All quoted error margins are 90% credible intervals.

Detector Configuration	Mean BBH Range (Mpc)	Low Frequency Cut Off (Hz)	Mean Visible Duration (s)	$P(Overlap)$ (BNS+BBH)	N_{events} (BBH)	$N_{Overlap}$ (BNS+BBH)
aLIGO: O3	611.0	20	151.3	$6.9^{+3.2}_{-2.2} \times 10^{-2}$	$42.0^{+21.0}_{-13.0}$	$2.9^{+3.4}_{-1.6}$
aLIGO: O4	842.5	20	151.3	$6.9^{+3.2}_{-2.2} \times 10^{-2}$	$100.0^{+56.0}_{-29.0}$	$7.2^{+8.5}_{-3.9}$
aLIGO: Design	882.9	20	151.3	$6.9^{+3.2}_{-2.2} \times 10^{-2}$	$120.0^{+60.0}_{-38.0}$	$8.3^{+9.8}_{-4.4}$
LIGO-Voyager	2684.0	10	957.0	$0.4^{+0.1}_{-0.1}$	$2700.0^{+1300.0}_{-880.0}$	$970.0^{+990.0}_{-490.0}$
Einstein Telescope	4961.0	1	440000.0	$1.0^{+0.0}_{-0.0}$	$15000.0^{+7100.0}_{-5000.0}$	$15000.0^{+7100.0}_{-5000.0}$

Table 2.4: The probabilities of detecting a BBH signal while a BNS signal is present in the detector, and estimates on the number of such detections, in different GW detector configurations, across a years observations. Here the range, and number of individual events, is given for BBH mergers. The duration is for BNS events. All quoted error margins are 90% credible intervals.

To calculate the probability of such an signal, we use the observing range for BBH mergers to estimated the number of BBH mergers observed in the given observing run. We then treat the signal as having the duration of a BNS merger to account for the overlap with such a BNS. As the visible volumes and visible durations now do not depend on the same mass parameter, we must modify Equation 2.3 to account for the difference:

$$
\begin{aligned}
P(\text{Overlap}) &= 1 - \exp^{-\langle R_{BBH} \rangle \langle T_{BNS} \rangle} \\
&= 1 - \exp^{-\mathcal{R}_{BBH} \langle V(m_{BBH}) \rangle \langle T(m_{BNS}) \rangle} \\
&= 1 - \exp^{-\mathcal{R}_{BBH} \int V(m_{BBH}) p(m_{BBH}) dm_{BBH} \int T(m_{BNS}) p(m_{BNS}) dm_{BNS}}
\end{aligned}
$$

(2.4)

It is possible that such signals would be observed before the end of the current aLIGO detectors. They are likely to account for around 36% of all BBH mergers in LIGO-Voyager, as many as $970.0^{+990.0}_{-490.0}$ BBH signals overlapping BNS signals in a years observation. Values for these calculations are given in Table 2.4. However, as stated in Section 2.2.2, due to BNS signals being particularly long, the vast majority of these signals will overlap at significantly different frequencies, with merger times particularly far apart.

2.3 Overlaps of other signals

The Advanced LIGO and Advanced Virgo detectors are sensitive to GW sources other than CBCs. Since the writing of this work, the mergers of two neutron star-black hole binaries have been observed by the LVK [187]. To the same extent very high mass collisions, such as intermediate mass black hole mergers (IMBH) [201], are rare enough to make their merger rates difficult to predict. These signals are also much shorter, further reducing the chances of signal overlaps. For these reasons we do not consider these signals any further in this study.

At the time of writing, there have been no observed GW signals from supernovae, or any other proposed GW burst source, announced by the LVK collaboration. It is of course possible that these signals could overlap. However, we do not consider these due to the lack of observations limiting signal rate estimates.

It is likely that non-transient, or very long signals, would overlap with any transient signal. These signals, such as continuous waves from neutron star mountains, would produce monochromatic, or narrow band excess power at specific frequencies. These would likely not vary across the duration of the transient [268, 269]. This overlap is unlikely to cause problems for transient analysis. Such a signal would not be too dissimilar from noise lines already present in the detector, such as that of power lines at the detector sites. These lines can either be notched out in the

frequency domain, or included as part of the PSD estimation, which should cause no problems in the matched filter process.

There are plans to launch The Laser Interferometer Space Antenna (LISA), a space-based GW detector, in the mid 2030s [95]. However, the detector is designed to observe a different frequency range than ground-based detectors. Sensitive between the 10^{-5} Hz and 10^{-1} Hz band, it should observe the mergers of much more massive objects than LIGO. These more massive signals, such as supermassive black hole mergers, will be much longer than LIGO BBH mergers. It will not be possible to study these signals without accounting for the interference from signal overlap.

2.4 Calculating the probability of observing more than two time-overlapping CBCs

Considering the large number of signals we expect to see in Einstein Telescope, we now examine the probability of observing more than two signals at the same time. This is possible by extending Equation 2.2 to the case of N time-overlapping signals:

$$P(k > N) = 1 - \sum_{k=0}^{k=N} P(k) = 1 - \sum_{k=0}^{k=N} \frac{(RT_{obs})^k \exp^{-RT_{obs}}}{k!} \qquad (2.5)$$

We calculated the probability for every value of N up to $1,000$ for three cases of time-overlapping signals; BBH, BNS and BNS+BBH, using the rate and viewing range estimates given in Tables 2.2, 2.3, 2.4 respectively. Assuming the median merger rates given above, each BBH merger in Einstein Telescope will overlap 9^{+5}_{-3} other BBH signals. For BNS mergers this is 66^{+120}_{-53}. These results are shown in Figure 2.3.

It follows from Figure 2.3 that it is unlikely Einstein Telescope will be able to observe any signal that does not overlap with multiple other signals. However, the probability of observing $P(k > 2)$ in second-generation detectors such as aLIGO or LIGO-Voyager is negligible. Therefore, it is reasonable to consider the two signal situation for these detectors as a first attempt at mitigating the potential problems.

2.5 Validation of analytical probability calculation

Previous studies of the probability of observing time-overlapping signals have considered a similar analytic approach to this calculation [266]. Others have considered a more numerical approach. For completeness, we here check our result numerically in a similar method to that described in Section 2 of [267].

From the distributions described in Sections 2.2.1 and 2.2.2 we drew random samples of component masses as estimates of possible observing runs. For each signal we calculate the observable period and assigned a merger time drawn from a
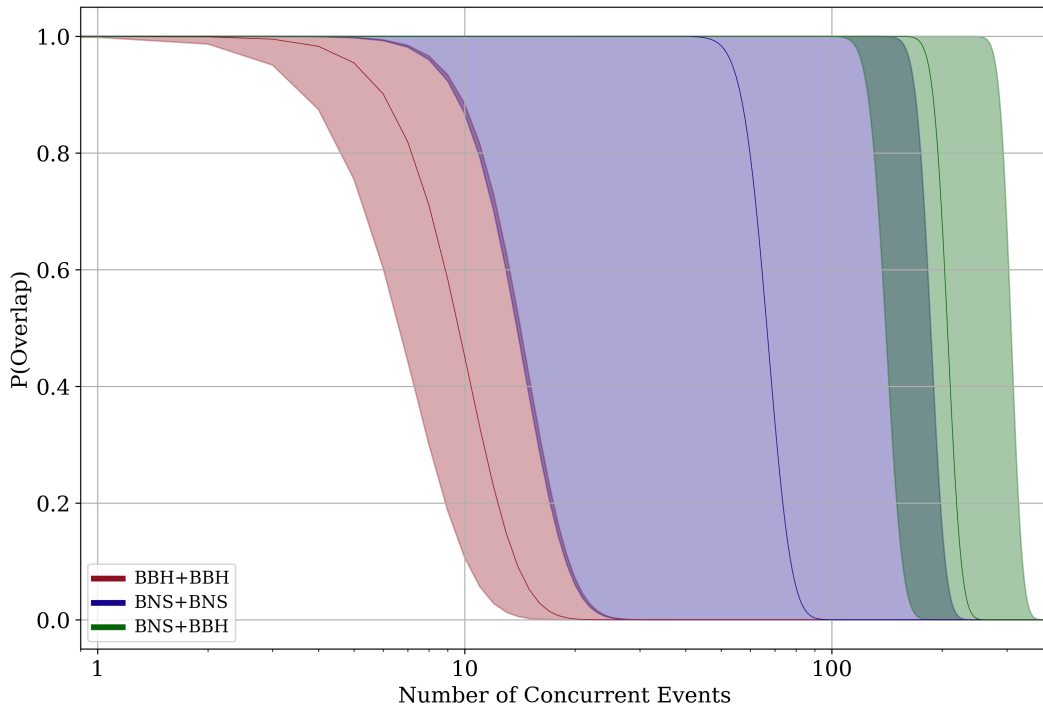
Figure 2.3: Probability distribution for the likely number of BNS (blue), and BBH (red) mergers, that overlap that each signal of that type in Einstein Telescope. The likely number of BBH signals overlapping each BNS signal is also presented in the green curve.

uniform distribution across a years observing period. We then counted how many signals in that observing period overlap in time. This process was repeated 10^6 times to obtain a reasonable average for each run. The resulting number of overlaps and P(overlap) agree qualitatively with our analytical predictions. We can therefore conclude that our analytical estimates are reasonably accurate, given the current merger rate estimates and our assumptions.

2.6 Discussion

This chapter contains an outline of how estimates can be made for the number of transient compact binaries that overlap in-band in a ground-based GW interferometer. It shows that, while such signals are unlikely to visibly overlap within the life span of the current, second-generation of detectors, they are almost certain to be observed in an end of generation detector configuration. Data analysis methods for detections in a LIGO-Voyager network must therefore be developed to spot such cases and disentangle the two signals.

We also show that most, if not all, transient signals in the proposed third generation will overlap with another transient in-band. Further, it is likely that most of these transients will overlap with multiple other transients. Signal subtraction

in these cases will likely be much more complex than the two signal overlaps that would occur in LIGO-Voyager. It is therefore even more necessary to establish how to spot and separate signals with advanced LIGO-Voyager-like detectors before such a third generation detector is built.

Findings from the parameter estimation study in Chapter 3 led to a re-estimation of the probability of observing problem time-overlaps. This can be found in Section 3.4

Chapter 3

Parameter estimation bias from time-overlapping binary black hole signals in second-generation interferometers

3.1 Introduction

If time-overlapping signals begin to make up a significant fraction of detected signals, as shown in Chapter 2, their effects could bias wider reaching studies such as population modelling and tests of general relativity. Even a single time-overlapping signal could negatively affect scientific results, if the bias from the second signal causes significant deviation from a true signal.

In this chapter, we investigate the effects time-overlapping signals can have on stochastic sampling, the main PE technique currently in use within the LVK Collaboration. Previous studies of time-overlapping transients have investigated the bias caused when attempting to recover either of the two signals in the data [266, 267]. For our analysis, we treat time-overlapping signals as a single signal and apply parameter estimation in an agnostic manner, making only the assumption that the signal is a merging BBH. We attempt to constrain the regions in which such time-overlapping signals would show significant bias. We also show what forms this bias can take when analysis with parameter estimation includes sampling over black hole spin parameters and uses waveforms that include spin-induced precession.

In Section 3.2 we outline our method of signal overlap and recovery. The results of this study are described in Section 3.3, with updates on our probability calculation from our results in Section 3.4. Section 3.5 provides a summary of our findings and proposals of avenues for further study.

3.2   Method

3.2.1   Parameter estimation of gravitational waves

There are many different methods of parameter estimation used to establish the probable dynamics of detected CBCs. However, the conventional method is to use stochastic sampling via Bayes' Theorem. Explanations of Bayes' Theorem and stochastic sampling are given in Sections 1.5.3.1 and 1.5.3 respectively.

For this analysis we used the `BILBY` parameter estimation code [5, 270], with its default nested sampler `DYNESTY`. This is now the typical approach to CBC used by the LVK collaboration [55, 67].

For this analysis we used the precessing waveform approximant `IMRPhenomPv2` [271–274] to estimate the parameters of the merging binary. While the `IMRPhenomPv2` approximant is not the most advanced waveform, notably missing higher multipoles, it does allow for the analysis to contain the majority of signal physics without drastically increasing the computational cost.

To speed up the sampling time of the large number of sampling runs performed in this analysis we allowed the sampler to marginalise over time, phase and distance. Phase marginalisation is not always possible with precessing waveforms, creating likelihoods that can differ from the true likelihood. However, `IMRPhenomPv2` contains both $(2,\pm 2)$ multipoles in the co-precessing frame [271]. This allows for precession to be measured reliably with marginalisation over phase.

3.2.2   Studying time-overlapping signals

In the case of a detected signal, current data analysis techniques assume only the presence of a single signal in the noise. We perform our analysis on a similar basis, in which the data segments containing one or more signals are treated as single signals. This is a realistic situation as, if such a signal were discovered in current search pipelines it would likely produce a single trigger time stamp. This trigger would likely then be treated as a single signal.

However, if two or more GWs are present in the detector at the same time their signals will interfere and produce a non-physical, composite waveform. The sampling software will then select sets of parameters that match this composite waveform, rather than those of the component signals.

For this study we have restricted transient overlaps to two signals only. The observed waveform is therefore comprised of two component signals, Signal A and Signal B, where Signal A is the primary waveform that remains constant throughout the analysis. We perform parameter estimation on a variety of combinations of the two signals and observe the situations in which the sampler recovers signals that differ significantly from the true posterior of either signal. Throughout our analysis we keep Signal A to be a GW150914-like merger with chirp mass of $28.1\,\mathrm{M_\odot}$ and

mass ratio 0.806.

Estimates of the probability of observing transient overlaps showed that BNS+BBH overlaps are the most likely to be observed first. However, our preliminary analysis showed that there should not be significant problems in distinguishing these signals in the case of an overlap, as there are large differences between the time-frequency evolution of these kinds of CBC mergers. These differences, particularly as most of these BBH signals will merge long before the BNS signal merges, should cause the two signals to be distinguishable. In these cases, PE could be performed on only the portion of the signal containing the clean BNS signal. The merging BBH portion would be gated out, as has been done for glitches present in BNS signals [62, 123]. It is also possible to perform multi-signal "global-fit" parameter estimation, see Chapter 5. The process of gating allows for less reliable data to be removed from the analysis. Due to this, we do not present any analysis into these types of overlap here.

There are four main differences that can describe the relationship between the two signals. The first being the relative merger time, the time separation between the mergers of Signal A and Signal B. In our analysis, we control this separation by manually setting a displacement of Signal B's merger time upon signal creation. For the majority of our analysis, we keep this separation constant between detectors by giving both signals the same sky location. This is of course an unlikely situation, but should have little effect on the outcome of the PE for studies of signals in a single detector. For detector networks it does increase the coherence between observed signals in the network, see Sections 3.3.2.1 and 3.3.2.2. For our primary analysis we allow the merger time of Signal B to vary according to $|\Delta t_c| : [-0.1, 0.1]$seconds, relative to the merger time of Signal A.

The second relative parameter compares the SNRs of the two signals, how loud Signal B is in comparison to Signal A. In order to vary this, we keep Signal A at a constant SNR of 30 throughout the whole analysis. The SNR of 30 was set for the LIGO: Hanford detector. The SNR in LIGO: Livingston was 24.3. We then vary the luminosity distance of Signal B such that it would independently appear at several, frequently lower, SNRs in the detector. For our primary analysis we allowed $SNR_B : [5, 30]$, for the LIGO: Hanford detector, in order to vary from very low relative SNRs to almost equal.

The third relative parameter is the difference in the two signals true waveforms. The frequency evolution of each waveform is described uniquely by its own set of parameters. To this extent we describe the frequency evolution of each signal by controlling its chirp mass, $\mathcal{M}$. The chirp mass dominates the frequency evolution of the waveform [202]. To observe how this changes overlaps we vary Signal B's chirp mass according to $\mathcal{M} : [24.1, 32.1]\,M_\odot$ giving a wide range around that of Signal A. The mass ratio of Signal B was kept constant at 0.9, as a typical "vanilla" BBH mass ratio.

The composite frequency evolution of the two signals is also dominated by each signals initial phase. For our analysis, we keep Signal A's phase constant and perform several sets of analysis for each configuration of Signal B at different random phases.

We have restricted all analysis to time-overlapping BBH signals. This was done as we expect these types of overlap to cause the most significant bias in parameter estimation within the next decade of ground-based observations, see Section 2.2.1 for further information. From preliminary, exploratory studies we also found that time-overlapping BBH signals could show precession-like effects. This is due to the constructive and destructive interference of the two signals causing a beating pattern in their combined waveform. This is the case even when the component signals contained little to no precessing spin.

Other studies [266, 267] have considered time-overlapping BNS signals and BBH signals that merge during a visible BNS signal. For the sake of reducing computational time we have left these studies for future analysis. However, we expect that BNS+BBH mergers are less likely to cause significant bias due to their vastly different frequency evolutions. Unless the SNR of the BBH signal is very high relative to the BNS, sampling will likely recover the BNS correctly when given priors for the BNS, due to the much larger number of cycles. The signal will remain clean for much of its observable period. If recovery of the BBH is desired then, unless the relative SNR is very large, it is likely that no reliable PE can be performed in this situation without prior subtraction of the BNS system. This may not be possible for low mass BBH signals which will have long inspirals.

For the recovery a constant set of priors were used throughout the study. These priors were kept as close as possible to those outlined in Appendix C of [65], in order to best match initial analysis that would be performed in the signal of a detection trigger. To fully encompass the parameters of both systems, some of these priors were widened slightly. The luminosity distance prior was set with an upper limit of 6000 Mpc in order to cover the large luminosity distance of the lowest mass Signal B at SNR 5.

It is possible that the interference of the waveforms could cause merger like effects earlier in the period of the signal. Therefore, the merger time prior was also widened from 0.2 seconds to 1 second. This was done in order to encompass the full chirp of both signals. This would allow for any signals that might interfere in such a way to cause chirp-like characteristics far from the true merger.

The runs were all performed with signals injected in the commonly used "zero-noise" approximation where the noise is assumed to be identically zero across all frequencies. The resultant obtained posteriors are then expected average posterior under a large number of noise realisations. In addition, we performed runs with Gaussian noise added to the signal to ensure consistency in our zero-noise results. None of these runs differed qualitatively from the posteriors found in the zero noise case and all conclusions held.

3.3 Results

3.3.1 Single detector runs

Our primary analysis considered time-overlapping signals as seen in a single detector. Events are rarely published if only found in a single detector, however, this can occur in the case of an interesting signal. This is possible for a signal which has been significantly biased by a second signal.

For each run; two signals were generated as described in Section 3.2, Signal B was then injected into the same data frame as Signal A using the `Python` package `GWpy` [12]. The created data frames were then given to the parameter estimation software, `BILBY`, [5, 270] using the nested sampler `DYNESTY` [8]. The data segments were treated as potential observed BBH signals with no further assumptions. Each data segment was 8s long, with 6s prior to the merger time of Signal A. This was done in order to best match the detection process of a true GW signal. The PSD used for these runs is the aLIGO Design PSD, from the "Design" column of the table of publicly released PSDs [261].

We find that in the case of a signal pairing with an unequal ratio of the SNRs of the two signals, the sampler will recover parameters much closer to those of the louder signal. The sampler can almost always correctly recover Signal A in the situation where its SNR is more than three times the SNR of Signal B. The results are more reliable when Signal A shares less of the parameter space with Signal B. If Signal B is allowed to exist at SNRs greater than that of Signal A then the posterior settles on the values of Signal B. The effect of the SNR ratio is shown in Figure 3.1, where the SNR of Signal B is increased with other signal parameters kept constant.

All plots presented here will be posterior distributions of parameters, in the form of violin plots[1]. The first two posteriors will show the posterior distributions for separate, single signal runs of Signal A and Signal B. The posteriors that follow these are for two time-overlapping signals of near identical parameters, but with stated differences. Horizontal grey lines show the 90% credible intervals for the posteriors. The two horizontal lines in blue and red show the injected values for the parameter for Signal A and Signal B respectively. All posterior plots were made using the parameter estimation plotting software, `PESummary` [15].

When the two signals have a time separation greater than the visible duration of the signal, the time between the low frequency cut off and the merger, in the detector then the sampler will favour the louder signal. In this situation the signals would have been recorded as separate detections and would not be studied with wide enough time priors to cover both signals.

---

[1]Violin plots can be read most conveniently by considering the right side of each violin to be a histogram of the posterior distribution. Often the left side of the violin will represent the prior, however, due to our priors being quite wide and flat, this is uninformative in this case. The violins are therefore mirror images of the posterior only.
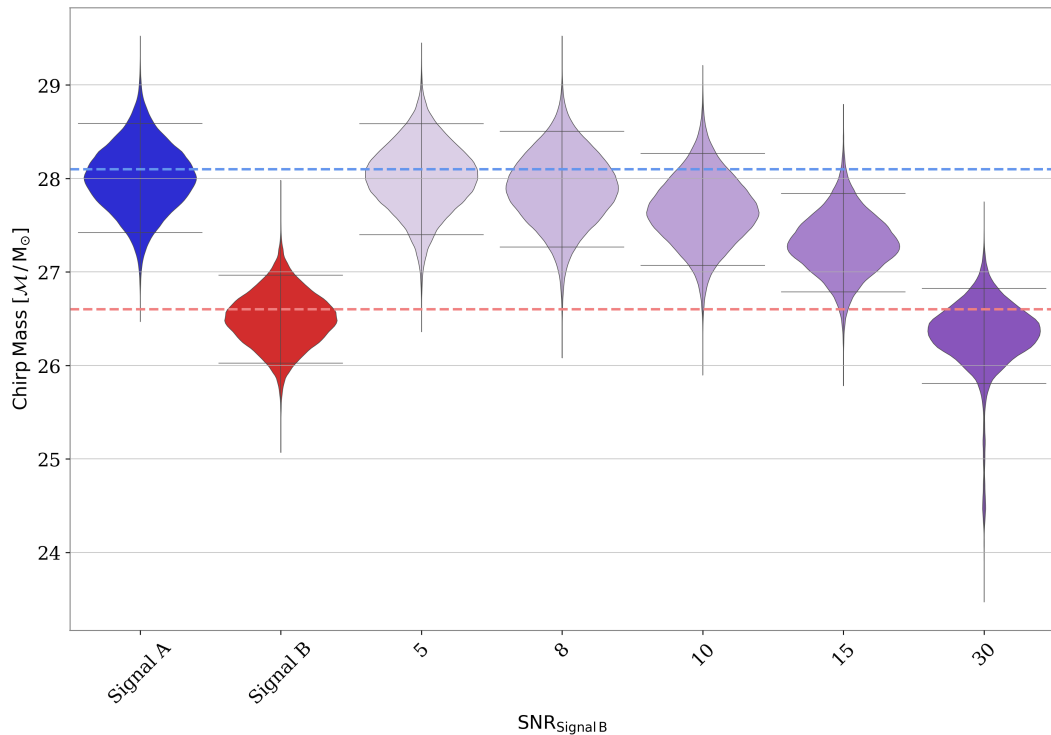
Figure 3.1: Recovered chirp mass posterior distributions. Posteriors labelled Signal A and Signal B are for data with a single signal injected at SNR 30. Signal B is injected with a relative merger time of $|\Delta t_c| = +0.025$ seconds and a chirp mass of $26.6 \, \mathrm{M_\odot}$. The next five posteriors have the two signals injected with the same properties but with the SNR of Signal B varying from 5 to 30. Signal A is kept with an SNR of 30 in all runs. The two horizontal lines in blue and red show the injected values of the chirp mass for Signal A and Signal B respectively.

In the situation where Signal A is both louder than Signal B and merges at a later time, the recovered posterior is much closer to that of Signal A. This is because most of the power is within the period of Signal A. However, if Signal B merges after Signal A, the posterior is more likely to recover significant bias, even at lower SNR ratios. The reverse is true if the relative SNRs of the two signals are swapped.

When signals do overlap in the time domain there will always be some bias in the parameter estimation. The bias from time overlap increases as the merger times of the two signals are brought closer together. Figure 3.2 shows the recovered posteriors for the chirp mass of near identical runs where the SNR of Signal B is constant, but the time separation of the mergers varies between runs. We also find that the bias in the samples is much more significant if the quieter signal merges after the louder signal. This is likely due to there being significant non-noise power remaining in the data after what would typically be the merger of the signal. This is outlined in Figure 3.3. Here it is clear that the top plot, where the quieter signal merges before the louder signal, shows the beating pattern of a precessing CBC signal, however it is not drastically different from common CBC waveforms. However, the bottom plot,
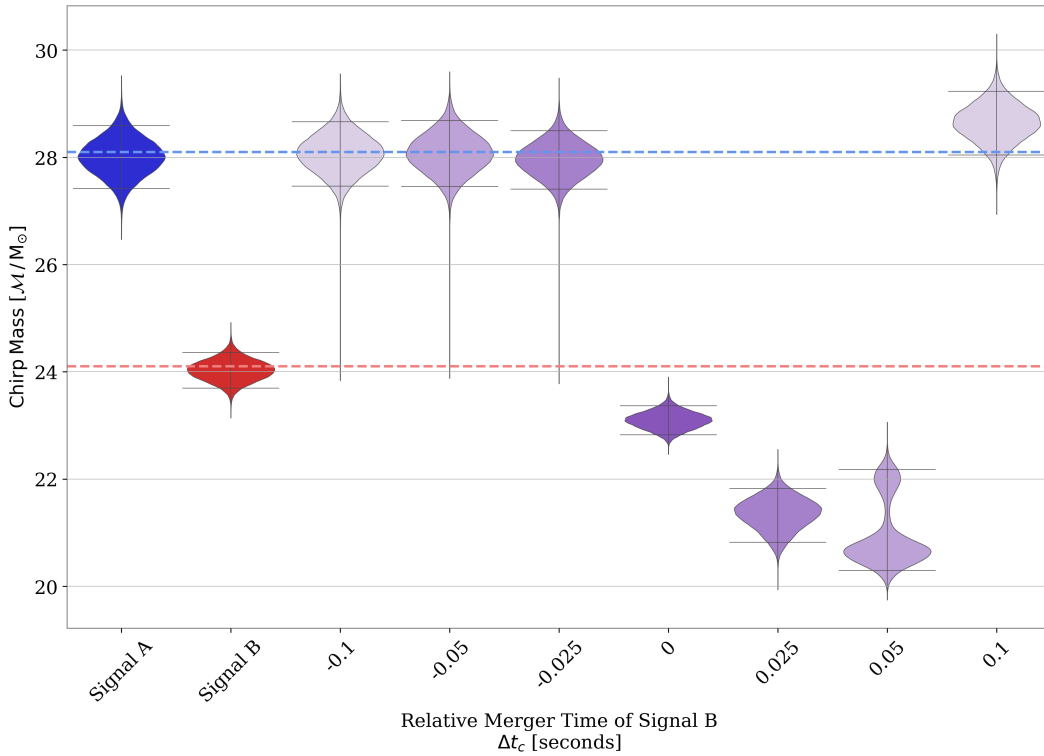
Figure 3.2: Recovered chirp mass posteriors. Posteriors labelled Signal A and Signal B are for data with a single signal injected at SNR 30. Signal B is injected with SNR 30 and a chirp mass of $24.1\,\mathrm{M_\odot}$. The next seven posteriors have the two signals injected with the same properties but with the relative merger time of the secondary varying. The two horizontal lines in blue and red show the injected values of the chirp mass for Signal A and Signal B respectively.

where the quieter signal merges later, there is significant power left in the waveform after the significant merger of Signal A. This leads to more extreme parameter sets being selected.

For strongly overlapping signals, the significance of the bias is dominated by the frequency evolution of the signals. The bias is amplified if the signals are close in the frequency domain. If the parameters of the two systems are such that they have a very different frequency profiles, for instance if they have very different chirp masses, then the sampler struggles to build waveform templates that match the wide variations in frequency. The sampler is therefore more likely to match to the louder signal. On the other hand, if the signals have similar frequency evolution then the power in the signals are combined and the sampler has any easy job matching the composite, interfering signal.

The strongly overlapping case, in which the two signals have similar SNRs, frequency profiles and merger times, is shown in Figure 3.4. Here there are ten, near identical runs of the same signal configuration. The differences between the recovered posteriors is due to the initial phase of Signal B alone, which was drawn randomly for each run. We performed this analysis for several combinations of Signal
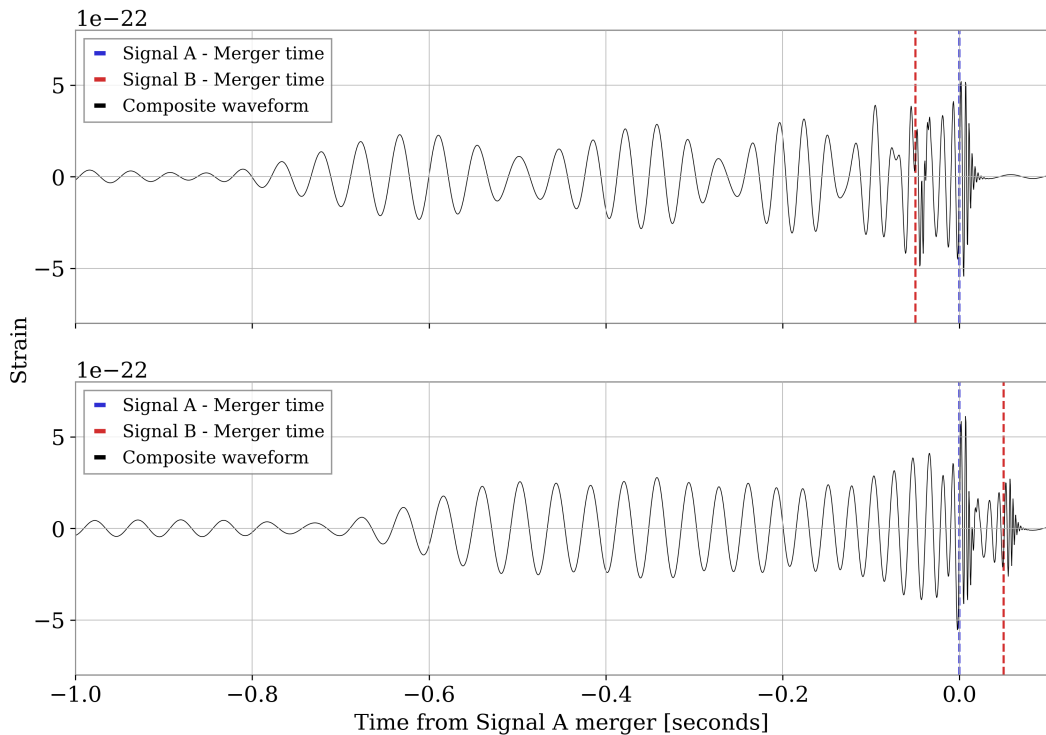
Figure 3.3: Time domain composite waveforms of two time-overlapping waveforms creating a composite waveform. The top plot shows this when Signal B merges 0.05 seconds before Signal A, the bottom shows the case where Signal B merges 0.05 seconds after Signal A. These waveforms are identical to those injected in two of the time-overlapping runs shown in Figure 3.2, however we have here shown the case where Signal B is half the SNR of Signal A.

B SNR and relative merger time. For each combination we performed the same ten phase realisations. Figure 3.4 shows how much effect the phase has in the strongly overlapping case. In all cases in these phase-varied runs, the recovered chirp mass is lower than either injected values. It is likely that the sampler is selecting lower mass signals in order to match the longer duration of excess power caused by the longer composite signal.

In the case of signals that are very similar in merger time, SNR and frequency evolution, the sampler has to fit to a waveform that is varying significantly in frequency space. It therefore, often picks waveforms that are precessing. This leads to samples that have very unequal, and often well constrained, mass ratios. This is shown in Figures 3.5 and 3.6, where the recovered values of mass ratio and χ_p are shown as the SNR of Signal B is increased. The apparent precession caused by time-overlapping signals is a similar process to one described in Fairhurst et al [275]. In this paper they model precession with the beating of two non-precessing signals. Here we have shown that this can occur from two time-overlapping signals that are visible in the detector.

Residuals were taken for all runs performed with non-zero noise. This was done
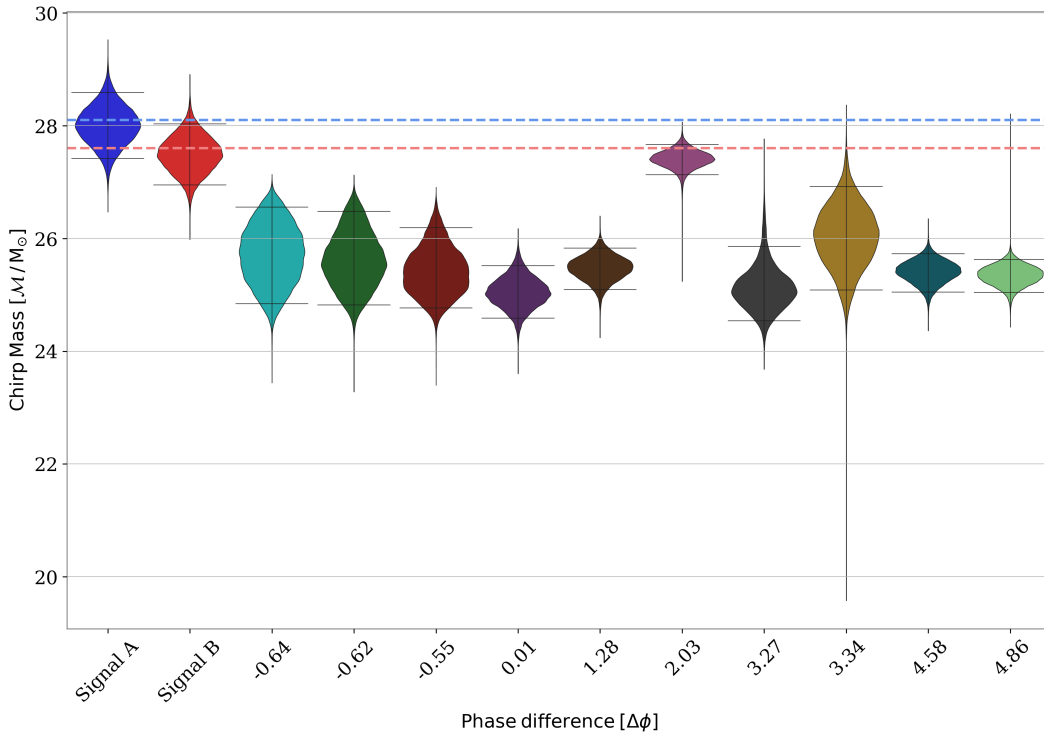
Figure 3.4: Recovered chirp mass posteriors. All runs are identical with Signal B of chirp mass $27.6\,\mathrm{M_\odot}$, relative merger time of $|\Delta t_c| = -0.025$ seconds and SNR 30. As in all runs, Signal A has a chirp mass of $28.1\,\mathrm{M_\odot}$. The time-overlapping signal posteriors differ due to the initial phase of Signal B, which was selected at random from a uniform distribution. The two horizontal lines in blue and red show the injected values of the chirp mass for Signal A and Signal B respectively.

by calculating the maximum likelihood sample set, generating an approximant from this and subtracting the signal from the data. For each residual, we performed Anderson-Darling tests [276] to check how consistent the remaining data was with Gaussian noise. Very few of the cases failed to pass this test at the stringent 1% level. Those that did were entirely high in SNR and close in merger time.

3.3.2 aLIGO-adVirgo network runs

Single detector signals are rarely accepted as real signals and should always be treated carefully. To examine the more likely case where two time-overlapping signals are observed in a network of detectors, we performed a similar set of injections into three detectors. Two of these detectors were located at the two aLIGO sites in Hanford, Washington and Livingston, Louisiana. These detectors were given an aLIGO design PSD from the penultimate column of the table of publicly released PSDs [261]. The third detector was located in Pisa, Italy and given a PSD of the Advanced Virgo detector at design sensitivity. This PSD was taken from the penultimate column of the table of publicly released PSDs [277].

In these runs, Signal A's parameters were identical to those in the single detector
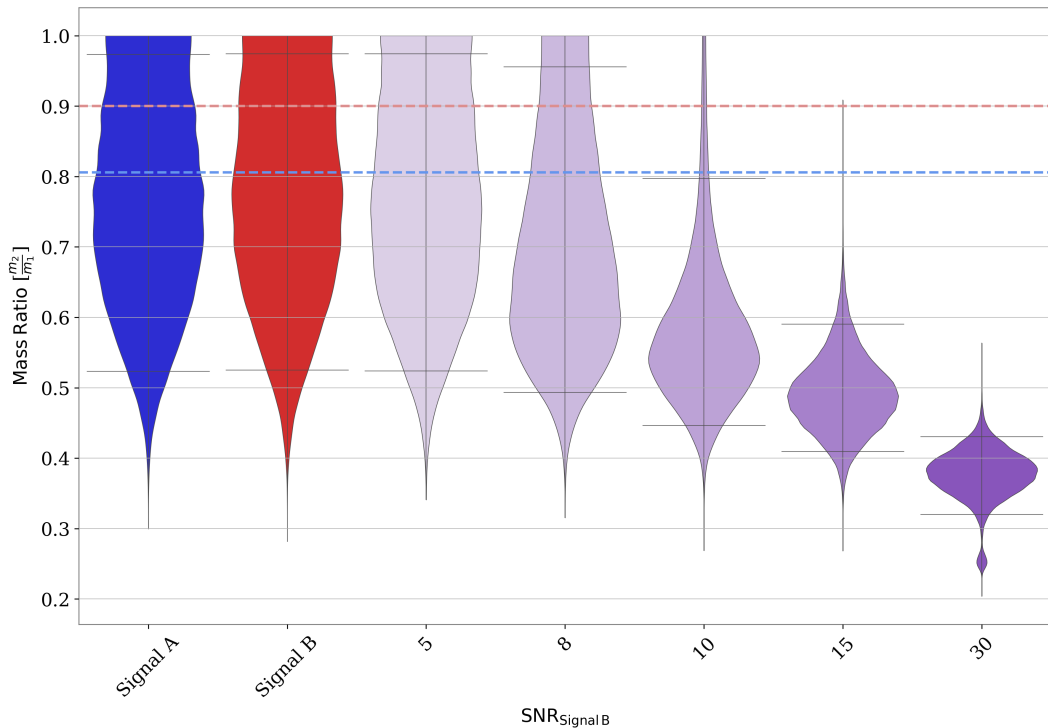
Figure 3.5: A plot of posteriors for recovered mass ratio. Here Signal B has chirp mass $26.6 \, \mathrm{M_\odot}$ relative merger time of $|\Delta t_c| = +0.025$ seconds compared to Signal A. The numerically labelled posteriors are at different injected SNRs of Signal B. Signal A has SNR 30 throughout. The two horizontal lines in blue and red show the injected values of the mass ratio for Signal A and Signal B respectively.

runs, as outlined in Section 3.2. Signal B was allowed to vary in luminosity distance such that it went from one thirtieth to twice the SNR of Signal A, in LIGO: Hanford. These runs were performed at a variety of different time separations and phases, but with a single chirp mass for Signal B of $24.1 \, \mathrm{M_\odot}$.

In multi-detector networks the position of the true signal in the sky controls the time of arrival at each detector. The difference in arrival time between detectors is that of the light travel time between the detectors at a given sky location and arrival time. The maximum difference is between the LIGO: Hanford site and the Virgo site in Pisa, this is approximately 27.3 ms. This time separation-sky location dependency means that signals that overlap in the detector interfere differently in different detectors and have different merger time separations in each detector.

Due to this sky location dependency we present two scenarios. The best case, in which the two signals arrive at the detectors from two positions at opposite sides of the line connecting LIGO: Hanford and Virgo. This maximises the difference in arrival time between detectors to 54.6 ms, twice the travel time between them. This situation should lead to the smallest, bias causing, overlap region and are the most likely time-overlapping signals to be recognised and separated.

We also examine the case in which the two signals arrive from sky locations
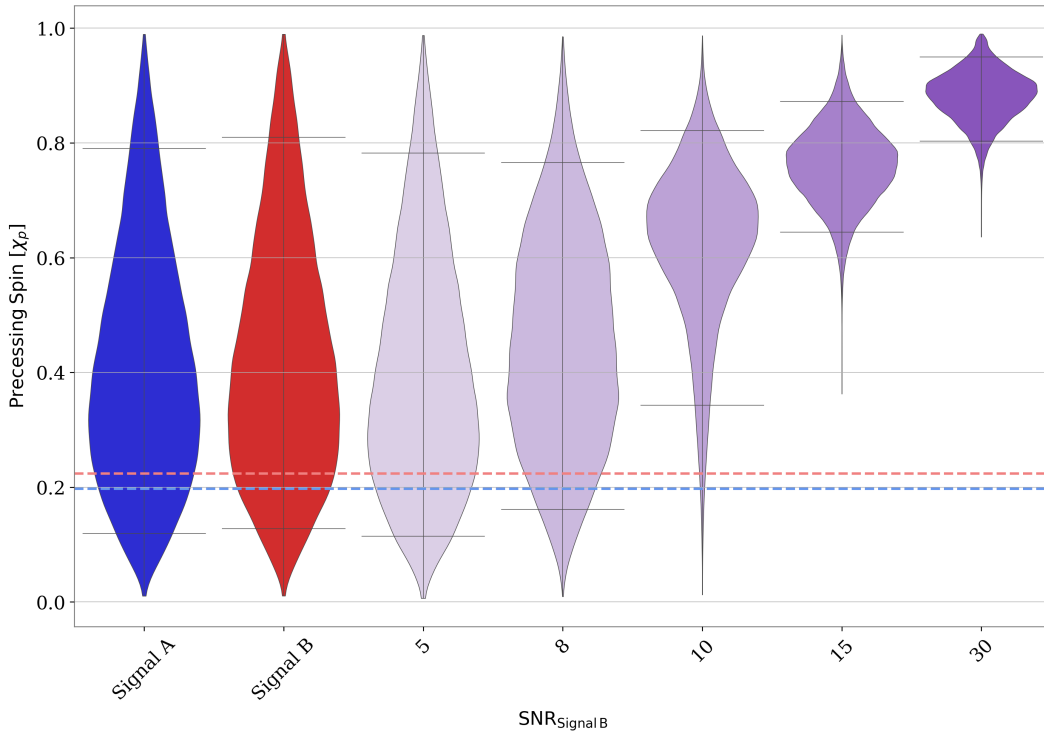
Figure 3.6: A plot of posteriors for recovered χ_p. Here Signal B has chirp mass $26.6\,\mathrm{M_\odot}$ relative merger time of $|\Delta t_c| = +0.025$ seconds compared to Signal A. The numerically labelled posteriors are at different injected SNRs of Signal B. Signal A has SNR 30 throughout. The two horizontal lines in blue and red show the injected values of χ_p for Signal A and Signal B respectively.

inducing time delays consistent across the detector network. It is likely that these signals will be more challenging to distinguish from real signals due to the inter-detector consistency. It should be noted that these "worst case scenario" signals are more likely than the best case signals. This is because for the merger times to be consistent across the network the signals can either arrive from the same sky location or come from a location perpendicular to the line of sight between detectors. These two scenarios show the extremes of the overlap for detectors based in their current locations, in reality most overlap cases will fall somewhere in between the two.

3.3.2.1 Best case scenario

We simulate signals at two sky locations at opposite sides of the line of sight between LIGO: Hanford and Virgo. Each signal was created at several time separations, $\Delta t = [-0.1, 0.1]$, as set in the LIGO: Hanford detector. The resulting Virgo time separations are $\Delta t = [-0.155, 0.045]$. The time separations in LIGO: Livingston also differ slightly from the LIGO: Hanford values.

For each of these cases, four randomly selected values for the phases were given to Signal B. The chirp mass of Signal B was kept to $24.1\,\mathrm{M_\odot}$. The same agnostic, wide prior set and marginalisations were used as in the single detector runs.

In these runs, the sampler tends to recover a GW150914-like signal for almost all the cases in which Signal B merges before the merger of Signal A. In these situations the recovered signal is closer to the parameters of whichever signal is louder in the detector network. This is most likely due to the majority of the power of Signal B being disguised by the more significant Signal A. This is increased by the time separation skewing to before Signal A for the majority of the runs due to the sky location and separation in Virgo.

The recovered posteriors show most evidence of bias in time-overlapping situations where Signal B merges after Signal A. This can be seen in Figures 3.7 and 3.8. These show the recovered mass ratio and luminosity distance posterior distributions for the case where Signal B has an SNR of 25 and merges at time separations of ± 0.025 seconds, relative to Signal A. It can be seen that, in the case where Signal B merges 0.025 seconds after Signal A, in the LIGO: Hanford detector, the bias is much larger than for the equivalent case of earlier merger[2]. At wider time separations the recovery skews toward a GW150914-like signal, although significant bias still occurs in some signals.

For the case of $\text{SNR}_A > \text{SNR}_B$; if Signal B merges before Signal A then the majority of the power of Signal B is contained within the inspiral of Signal A. The composite waveform does not differ significantly from that of Signal A. However, if Signal B merges after Signal A, the composite waveform appears Signal A-like, but with a second chirp or elongated chirp. Therefore the sampler tries to match to this composite waveform, selecting more exotic sets of parameters.

However, we find that in all of these runs there is still significant bias in runs that merge with a small time separation. As with the single detector analysis, the bias is reduced at wider time separations and at less even SNR ratios. Effects such as recovered precession and well constrained values of mass ratio, as found in single detector runs, are also present in these strongly overlapping network signals.

As in the single detector runs, the recovered signal appears highly precessing. With mass ratio and χ_p constrained away from 1 and 0 respectively. To account for this the sampler selects waveforms that look like an edge-on system, as edge-on systems are more likely to show clearly detectable precession. The sampler therefore predicts that all the power of the signal is in the plus polarisation and leaves little in the cross polarisation. The luminosity distance is therefore recovered to be much smaller than the real value, in order to account for the high SNR. This is shown in Figure 3.8.

This behaviour of the polarisations can be represented by examining the inclination of the binary. The gravitational-wave polarisations are related to the inclination

---

[2]Here Signal B merges 0.020 seconds after Signal A in the LIGO: Livingston detector, and 0.030 seconds before Signal A in Virgo.
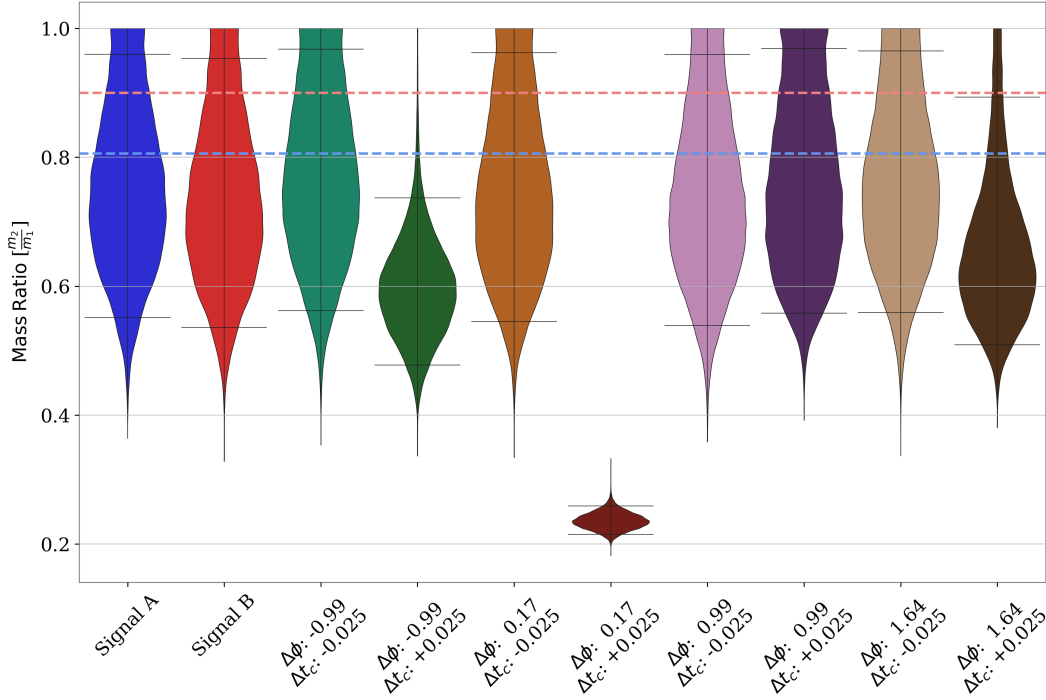
Figure 3.7: Recovered mass ratio posteriors for Signal B overlapping either 0.025 seconds before or after Signal A at a variety of initial phases, injected into an aLIGO-adVirgo network. Signal B was injected with an SNR of 25. The sky locations of the two systems of Signal A and Signal B were selected to maximise the travel time between the LIGO: Hanford and Virgo sites. Stated relative merger times apply to the LIGO: Hanford detector, the equivalent merger time separations in LIGO: Livingson are -0.03s and 0.02s, and -0.080s and -0.030s in Virgo. The two horizontal lines in blue and red show the injected values of the mass ratio for Signal A and Signal B respectively.

as shown in Equations 3.1 [278].

$$h_+(t) \propto 1 + cos^2(\iota)$$
$$h_\times(t) \propto 2cos(\iota)$$

(3.1)

where ι is the inclination of the binary. Due to this when a system is edge-on, $\iota \simeq \pi/2$, $h_\times$ tends to zero, with all remaining power in the plus polarisation. For a signal to be selected at edge-on inclinations with large SNRs it must then be significantly closer to Earth. This is shown Figure 3.9 where the significantly overlapping system has a small inferred luminosity distance and a highly constrained inclination, close to edge-on. In the weaker time-overlapping case the sampler returns parameter distributions similar to those of the, unbiased, single signal case.
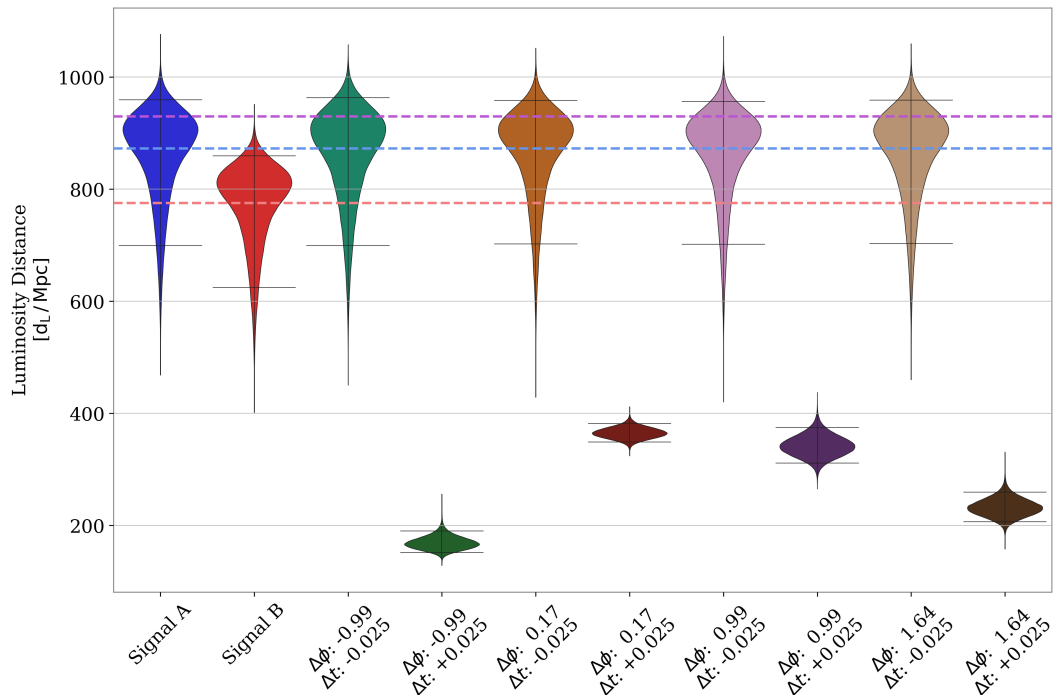
Figure 3.8: Recovered luminosity distance posteriors for Signal B overlapping either 0.025 seconds before or after Signal A at a variety of initial phases, injected into an aLIGO-adVirgo network. Signal B was injected with an SNR of 25. The sky locations of the two systems of Signal A and Signal B were selected to maximise the travel time between the LIGO: Hanford and Virgo sites. Stated relative merger times apply to the LIGO: Hanford detector, the equivalent merger time separations in LIGO: Livingson are -0.03s and 0.02s, and -0.08s and -0.03s in Virgo. The two horizontal lines in blue and red show the injected values of the luminosity distance for Signal A and Signal B respectively. The final horizontal line shows the injected luminosity distance for Signal B in the combined runs at the lower SNR.

3.3.2.2 Worst case scenario

We performed runs in which the two signals merge at the same location in the sky, relative to the detectors. This situation is the most likely to cause a signal that is not recognised as time-overlapping due to the relative merger time remaining constant regardless of detector. The relative merger times of these signals are constant.

Here we find similar results to those in the Section 3.3.2.1, however, we find that the observed bias is much larger and skews away from the recovery of a GW150914-like signal, particularly in the situation where Signal B merges after Signal A, relative to the detectors. The higher significance of the bias is due to the coherence of the composite waveforms across the network. The two signals interfere in the same manner in all detectors due to their identical sky location. These results are shown in Figures 3.10 and 3.11.

Similar runs were performed with only the two aLIGO detectors at design sensitivity. The posterior distributions of these runs had the same qualitative results but
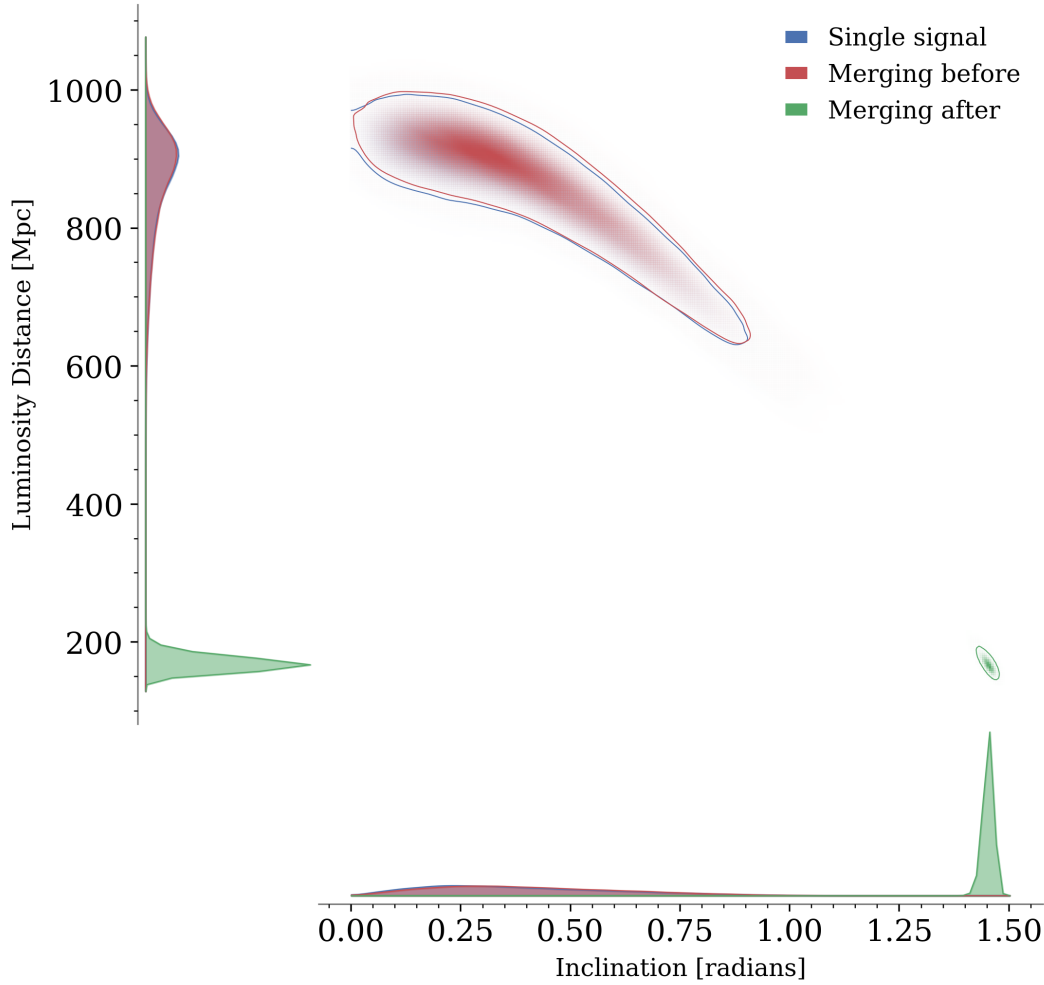
Figure 3.9: Two dimensional posterior distributions showing the relationship between the recovered binary inclination and the luminosity distance of the source. One dimensional posteriors for each parameter are shown on their respective axis. Shown here are the posteriors of the single signal injection, Signal A (blue), a weakly biased time-overlapping case where the quieter signal merges before the louder signal (red), and a strongly biased time-overlapping case where the loud signal merges first. The two time-overlapping cases are the first two phase cases from Figures 3.7 and 3.8.

with less precise constraints on certain parameters, as expected with fewer detectors.

3.3.3 Events below the detection threshold

It is possible that signals can be biased by the presence of a second signal, even if that signal were not detectable itself. To test this we performed PE on systems where the Signal A was identical to the GW150914-like signal described previously, but with an SNR of 8 in the LIGO: Hanford detector. This is often regarded as the threshold SNR for signal detection in an individual detector [77].

In this analysis Signal B merged 0.025 seconds after Signal A in order to provide
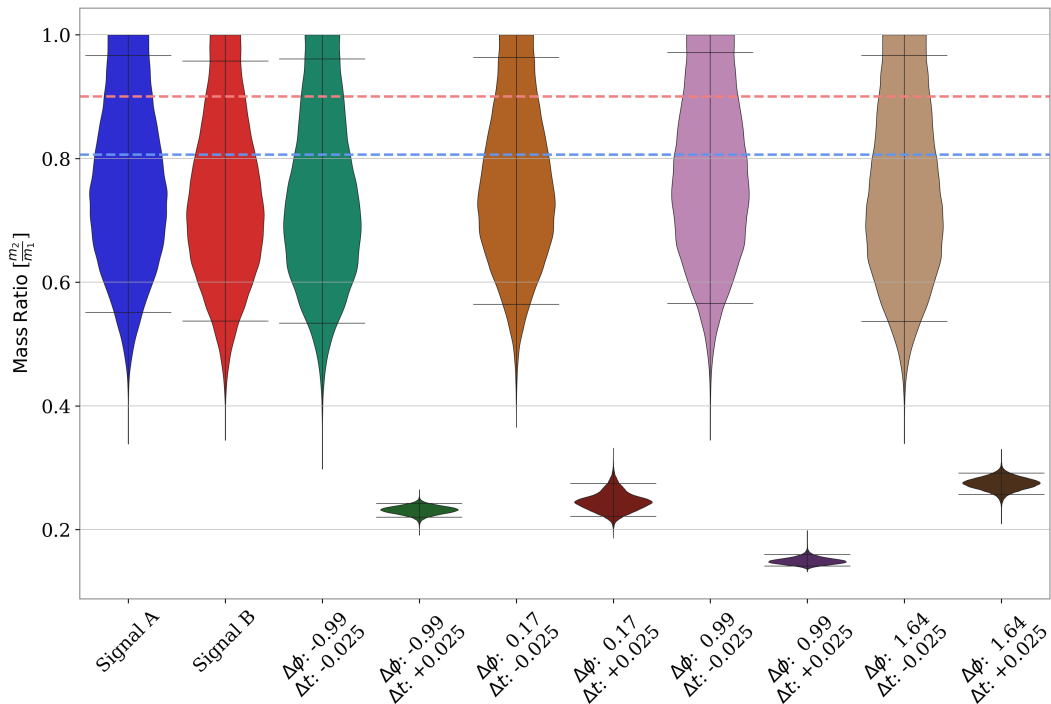
Figure 3.10: Recovered mass ratio posteriors for Signal B overlapping either 0.025 seconds before or after Signal A at a variety of initial phases, injected into an aLIGO-adVirgo network. Signal B was injected with an SNR of 25. The sky locations of the two signals are identical creating identical arrival times at all three detectors. The two horizontal lines in blue and red show the injected values of the mass ratio for Signal A and Signal B respectively.

significant bias. Runs were performed with increasing SNR for Signal B from 1 to 8. These runs were performed for the full, three detector aLIGO-adVirgo network at design sensitivity. The network SNR of Signal A was 13.3, slightly higher than the network SNR detection threshold of 12 [77]. Sky locations were defined such as to give the two signals a consistent relative merger time across the network of detectors.

The posterior distributions for the chirp mass of these runs are given in Figure 3.12. These posteriors show that, while these signals are not detectable, they can still cause significant bias in the recovery of Signal A when approaching equal SNR. Such signals would also cause bias in the recovery of a louder Signal A, however, this would not be as significant an issue due to the largely unequal ratio of SNRs.

3.3.4 LIGO-Voyager network runs

Identical runs to the three detector aLIGO network, worst case scenario, were performed with a LIGO-Voyager detector sensitivity. The network kept the same locations as the two aLIGO detectors in Hanford and Livingston, with identical signal
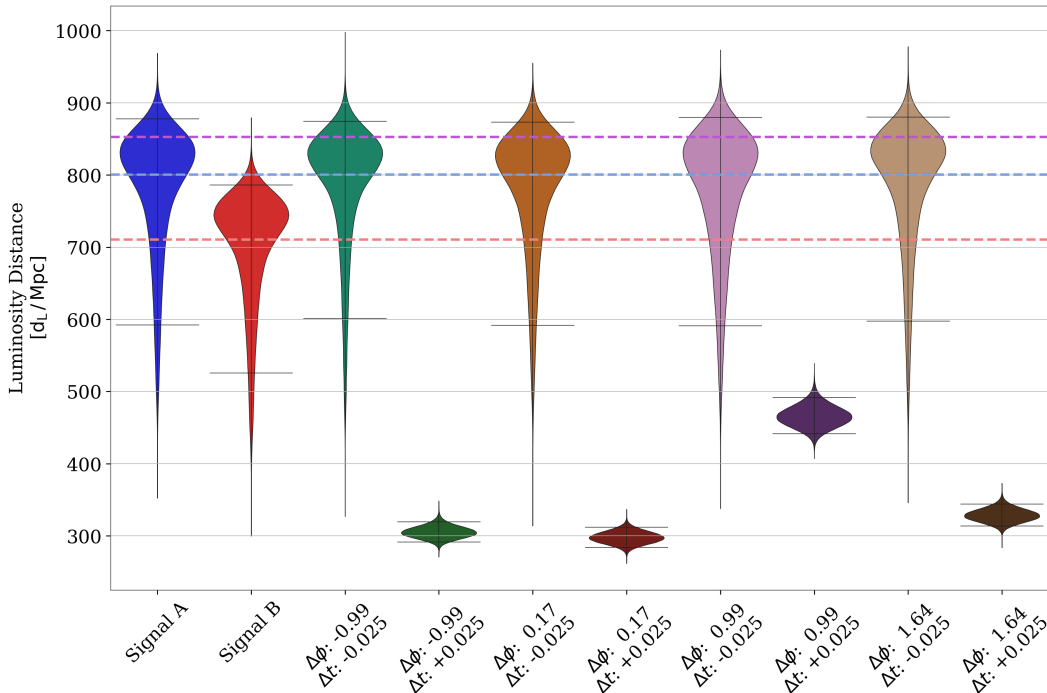
Figure 3.11: Recovered luminosity distance posteriors for Signal B overlapping either 0.025 seconds before or after Signal A at a variety of initial phases, injected into an aLIGO-adVirgo network. Signal B was injected with an SNR of 25. The sky locations of the two signals are identical creating identical arrival times at all three detectors. The two horizontal lines in blue and red show the injected values of the luminosity distance for Signal A and Signal B respectively. The final horizontal line, purple, shows the injected luminosity distance for Signal B in the combined runs at the lower SNR.

parameters. No detector was included in the location of the Virgo detector as no current plans for such a future detector were available.

Two sets of runs, identical to those described in 3.3.2, were performed. These runs were performed with two differences. The aLIGO design PSD was replaced with a predicted LIGO-Voyager PSD. The PSD used was created from an estimate of the noise budget calculated through the `Python` package `pygwinc` [10, 11].

One set of runs kept the low frequency cutoff equal to that of the aLIGO network runs, 20 Hz, the other reduced this to 10 Hz, as expected for LIGO-Voyager. The increase in detector sensitivity, combined with identical parameters to the aLIGO network runs, produces signals with much greater significance in the LIGO-Voyager detector. However, it is the relative SNR that is relevant in these situations. This remains constant.

The results of these runs did not differ greatly from those of the aLIGO network. The recovered posteriors were much more precise than from the aLIGO runs, particularly for the mass ratio, Figure 3.13. Better constraints of the posteriors were found in the 10 Hz runs than the 20 Hz runs. This is due to the increased number
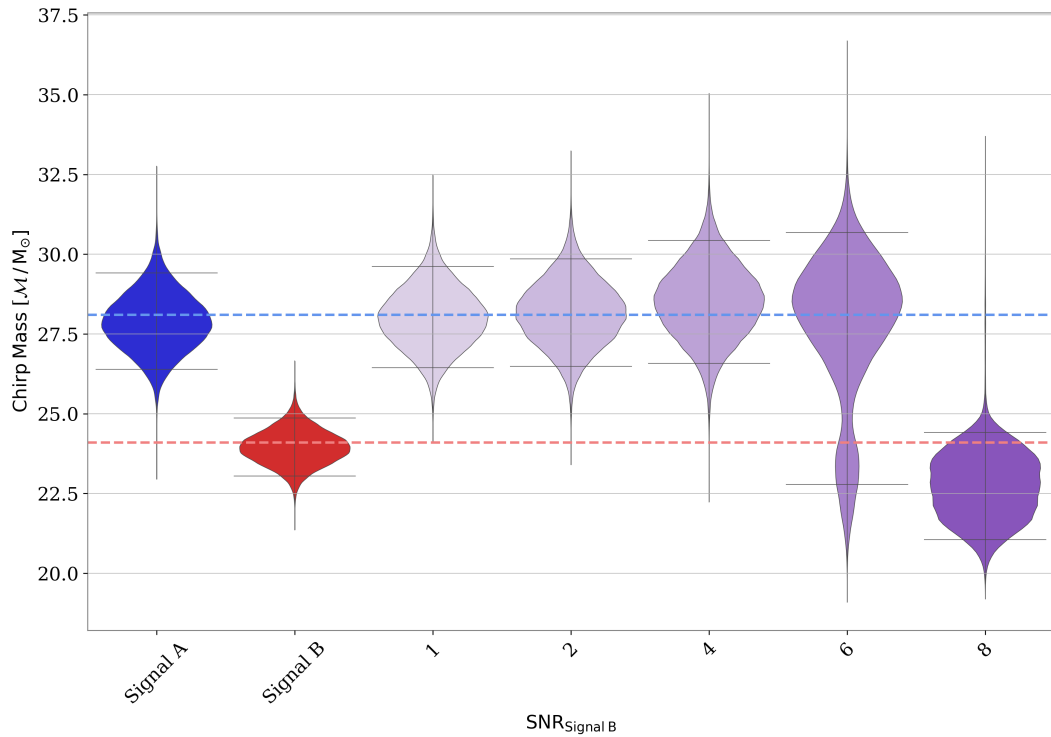
Figure 3.12: Recovered chirp mass posteriors for Signal B overlapping either 0.025 seconds after Signal A at a variety of different SNRs, injected into an aLIGO-adVirgo network. The values given for each posterior are the SNR of Signal B in the LIGO: Hanford detector. Signal A was injected with an SNR of 8. The two horizontal lines in blue and red show the injected values of the chirp mass for Signal A and Signal B respectively.

of cycles visible in the detector. This increased number of cycles also shows more interference between time-overlapping signals. As such the 10 Hz runs show more bias from time-overlapping signals than the 20 Hz runs in all scenarios.

One notable difference between these runs and those in Section 3.3.2.2 can be seen by comparing Figures 3.11 and 3.14. The distance posteriors shown in Figure 3.14 are much broader than those in Figure 3.11 and biased towards smaller distances. This is an effect of the position of the detectors. The Voyager network is a two detector network and therefore cannot provide as accurate a location of the source as the three detector network, despite the higher sensitivity of the LIGO-Voyager detectors. The wider sky localisation leads to poorer constraints on distance and a favouring of nearer sources.

Example posteriors of the 10 Hz runs are shown in Figures 3.13 and 3.14. These show identical runs from the 10 Hz LIGO-Voyager runs as are show in Figures 3.10 and 3.11 for the aLIGO network, worst case scenario.
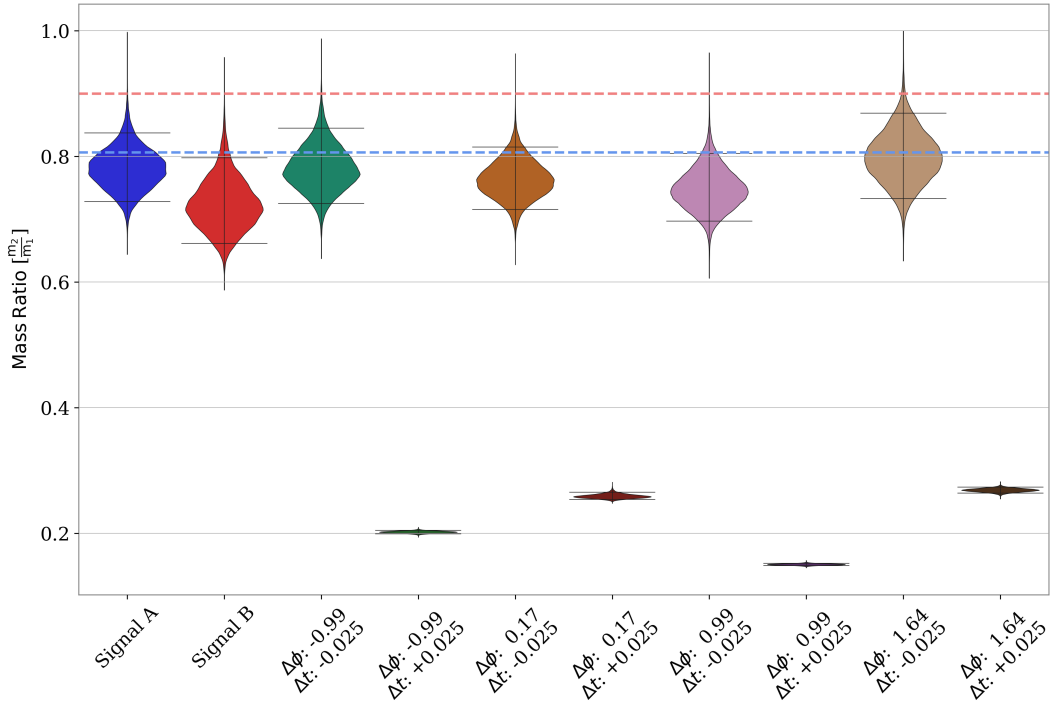
Figure 3.13: Recovered mass ratio posteriors for Signal B overlapping either 0.025 seconds before or after Signal A at a variety of initial phases, injected into a LIGO-Voyager network. The plot for the equivalent aLIGO run is given in Figure 3.10. The two horizontal lines in blue and red show the injected values of the mass ratio for Signal A and Signal B respectively. Due to the shift in detector sensitivity, here Signal A has an SNR of 120, and Signal B has an SNR of 100. Signal A's chirp mass was kept constant at $28.1M_\odot$, and Signal B has a chirp mass of $24.1M_\odot$. Signal B is here recovered with the 90% credible interval not covering the injected value for the chirp mass. This difference is not significant enough to change the conclusions from the time-overlapping analyses. The cause of this is unclear, we expect this is due to the sampler getting stuck in a local maxima.

3.4 Probability Re-estimation

The probability estimations in Chapter 2 shows that these time-overlapping transients are unlikely to occur until the end of the second-generation of GW interferometers. We found that, in a year's observations with LIGO-Voyager, there should be approximately $6.3^{+7.7}_{-3.4}$ and $1.2^{+8.5}_{-1.1}$ overlapping BBH and BNS signals respectively, per year of observation. There will also be around $970.0^{+990.0}_{-490.0}$ BBH signals that merge during the observable duration of a BNS merger. However, our study into parameter estimation of such signals indicates that the signals need to be within approximately ± 0.1 seconds in merger times in order to cause significant bias. Here we consider what effect this has on the probability of observing time-overlapping signal bias.

Here, we follow a similar analytical process to that outlined in 2.2. However, to enforce the bias-time difference constraint we shorten the durations of the signals
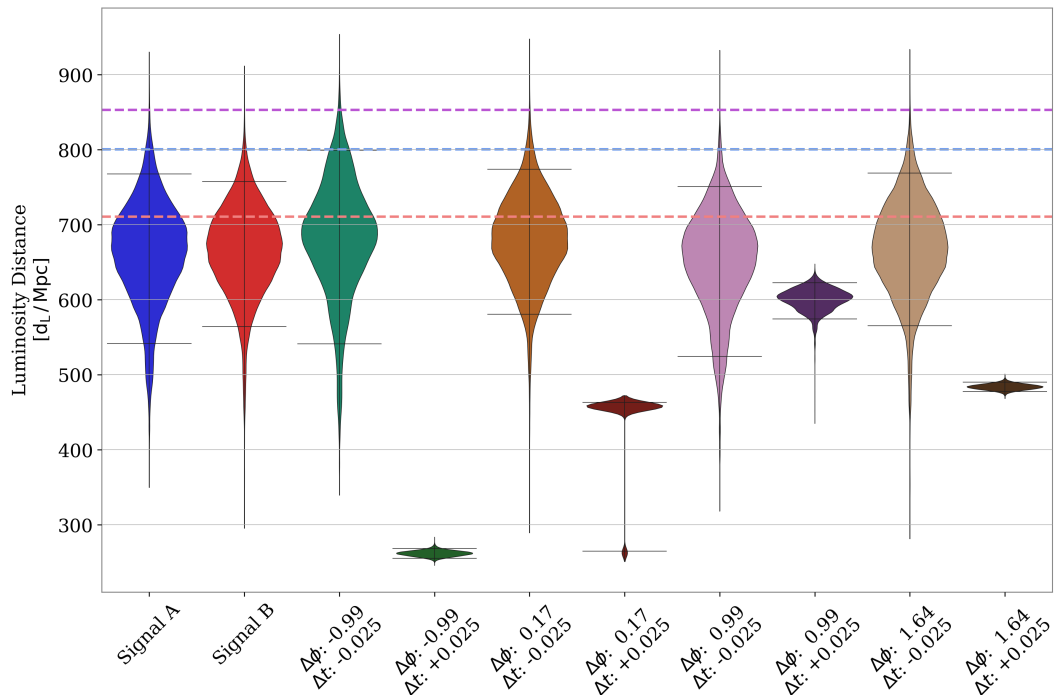
Figure 3.14: Recovered luminosity distance posteriors for Signal B overlapping either 0.025 seconds before or after Signal A at a variety of initial phases, injected into a LIGO-Voyager network. The plot for the equivalent aLIGO run is given in Figure 3.11. The two horizontal lines in blue and red show the injected values of the luminosity distance for Signal A and Signal B respectively. The final horizontal line, purple, shows the injected luminosity distance for Signal B in the combined runs at the lower SNR. The parameters of these signals are the same as those listed in the caption of Figure 3.13.

to 0.2 seconds in length. When applying this constraint LIGO-Voyager will only see significant bias causing events once in every four years of observations. When applied to Einstein Telescope there are still some signals that will show significant bias, purely from proximity of merger times. This will occur in approximately $1.39^{+1.70}_{-0.75}$ BBH events and $0.143^{+0.982}_{-0.137}$ BNS events each year.

Despite this, we have shown that bias can still occur from time-overlapping signals with relative merger times $|\Delta t_c| > \pm 0.1$ seconds. This wont be as severe as shown in some of the strongly overlapping results, but it could still be quite different from the true astrophysical source.

These values are only valid for the time-overlap of two signals. We find negligible probability of three or more signals overlapping within ~ 0.2 seconds, even in third generation detectors. However, our analysis of the significant bias region only applies to two signal overlaps. It is likely that multiple signals polluting the data will cause significant deviations from the true waveforms and that current parameter estimation techniques will struggle to account for this.

3.5 Discussion

While a few, weakly overlapping, detections may not be a significant problem, their presence is likely to cause trouble for studies of binary black hole populations, and tests of general relativity [279]. In the case of detecting a strongly overlapping signal; the system could appear highly precessing leading to a further detailed analysis and publication. These signals may affect any further astrophysical studies. We have only considered this for single signal cases and leave the effects on population studies for future works.

Overall, we find that time-overlapping BBH mergers do not show significant bias unless their waveforms overlap significantly in time and frequency. Bias is often small unless the separation of the two signals time of coalescence is less than ~ 0.1 seconds. However, the bias is often stronger if the quieter signal merges later than the louder signal, even beyond the ~ 0.1 second window. The ratio of the SNRs of the two signals must also be fairly equal, less than three, for the sampler to recover signals that differ significantly from the true posterior of the louder signal. Outside these narrow cases the bias is often negligible enough that stochastic sampling methods will select parameter sets similar to that of the louder signal. The vast majority of signals will be recoverable to a reasonable approximation.

Due to these narrow bias limits, it is reasonable to assume that most early detections of time-overlapping BBH mergers will not show significant bias. They should, however, only recover the louder signal. To recover the quieter signal new analysis techniques must be found to sample over the parameter space of two signals. Recently, some methods have been proposed that may solve this problem [280, 281].

In a network of detectors the relative sky locations of the two signals, and their relation to the line of sight between the detectors, has an effect upon the significance of the bias. We find that signals in sky locations along the line of sight between two detectors have a smaller region of significant bias. However, if the signals are in locations perpendicular to the line of sight, or at similar sky locations, the bias is more significant.

In the situation of two strongly overlapping waveforms the position and distribution of the posterior varies wildly with respect to the initial phase of the two waveforms. In these scenarios the sampler often selects waveforms that match highly precessing signals. This is due to the modulation of the frequencies present in the combined waveform. The result is often posteriors with mass ratios well constrained and away from the equal case. The sampler will then put the majority of the power into the plus polarisation and compensate by constraining a low luminosity distance.

We find that biases from time-overlapping signals can occur even if the quieter signal causing the bias is itself undetectable. Detections of signals with low SNRs should be treated with caution due to the possibility of bias from an undetectable signal.

The results for LIGO-Voyager show that, while higher-sensitivity detectors are more likely to detect bias, they are also more likely to present significant biases in detections. If these can be properly characterised it should be possible to establish which detections contain a potential overlap. It may be necessary to look closely at any signals that show significant evidence of precession or unequal mass ratios.

Our analysis of the effects of time-overlapping transients has been confined to the case of time-overlapping BBH mergers. We don't expect to observe the overlap of BNS systems until significant improvements are made in low-frequency detector sensitivity. This limits the observation of such overlaps until third generation detectors.

We did not examine the case of a BBH signal overlapping the merger of a BNS signal. However, we expect that the mergers of BBH signals that occur within the inspiral of BNS signals should not be recoverable unless they are much louder than the BNS signal. In this case a process similar to the gating of glitches can be used to remove the BBH for analysis of the BNS signal. When the BNS is louder than the BBH then we would expect only the BNS to be recoverable.

For the less likely case that a BNS merger is close to a BBH merger we expect the signals to not be easily recoverable without bias. It may be possible to correctly recover the BNS from its inspiral. Further, it may then be possible to use the inspiral to predict the merger cycles of the BNS. In this case, it can be removed from the data to reveal the BBH merger for further analysis. This could be a viable method of distinguishing such signals and we leave this for future analysis. However, we have not performed any analysis on time-overlapping BNS systems.

Chapter 4

Can modelled and unmodelled gravitational-wave searches detect time-overlapping transients?

4.1 Introduction

In Chapter 3 we investigated how parameter estimation techniques are affected by time-overlapping CBCs transients. Several other studies have been performed considering such events [266, 267, 281, 282]. The findings of these studies indicate that the parameters of modelled signals should be recoverable, unless the two signals overlap strongly with a small relative merger time. The bias is stronger if the signals have similar SNRs, as stated in Chapter 3, or chirp masses, mostly due to similar frequencies in the signals [282]. In the case where time-overlapping astrophysical signals are misidentified as a single signal, the data will be passed on to these parameter estimation methods. As these methods aim to minimise their residuals, it is possible that the overlap would not be noticed. Any resulting non-Gaussianity would likely be attributed to other causes such as glitches, precession or eccentricity [62, 123, 124, 283].

Current methods of gravitational wave detection rely upon the assumption that only a single signal is present in the detector and, in most algorithms, that this signal can be matched to modelled signal waveforms. As this assumption will break for time-overlapping transients, we have investigated how current search pipelines will behave in their presence. A previous study on simulated data of the third generation interferometer, Einstein Telescope, found that time-overlaps were not a problem for the detection of BNS signals [284]. However, this analysis was only performed with a modelled search and did not consider other categories of CBC time-overlaps.

Our investigation was performed by injecting pairs of time-overlapping CBCs into the coloured-Gaussian noise of a three detector, LIGO-Virgo, network [40, 54]. We then performed an offline search of these data sets using a modelled search, `PyCBC` [16–20, 285], and an unmodelled search, `cWB` [6, 7]. We investigated how the parameters of the signal pairings affected whether the signals were detected and how accurate the recovered parameters of those signals were.

Section 4.2 outlines how the data were generated, and how each search works. Section 4.3 covers the findings of how signal pairings were detected and the effect of the overlap on recovered parameters. Section 4.4 contains a summary of our findings.

4.2 Method

4.2.1 Overview

For this study we consider two types of CBCs, BBH and BNS. Our main interest in including these two forms of signal was to see how current search methods behave under the presence of time-overlapping CBCs of different visible durations and frequency profiles. We did not include neutron star-black hole signals, which should have similar observable durations [187] to low mass BBH signals, as these events are rare and less relevant to this study. Their presence in overlaps should be considered in future studies. We also did not include tidal deformability in the BNS signals, as it should have little effect on the length and frequency of the signal [180]. Three separate investigations were performed for this study, each examining one of three combinations of CBC overlap: BBH+BBH, BNS+BNS and BNS+BBH.

4.2.2 Data generation

Each investigation in this study included generating ten days of coloured-Gaussian noise for a three detector network. This length of time was chosen to give a reasonable estimate of false alarm rate of significant signals and to allow a reasonable number of events to be studied. The detectors were added as two advanced LIGO detectors at design specification in the locations of LIGO: Hanford and LIGO: Livingston [54, 286] and a third detector with an Advanced Virgo sensitivity in the position of Virgo [40].

For each of the three studies mentioned in Section 4.2.1 we made three injection sets. The first two only included individual, non-overlapping signals from the pairings, labelled as SINGLES$_A$ and SINGLES$_B$. This provides comparison data to see whether each signal is detectable alone. The final injection set, labelled as PAIRS, contained both Signal A and Signal B as time-overlapping pairs.

Signals were injected into the data internally in each search pipeline. BBH signals were generated using the `SEOBNRv4PHM` approximant [118] to allow for the

inclusion of spin precession and higher modes. BNS signals were generated with the `SEOBNRv4` [148] approximant; this only allows for aligned spin and, does not include neutron star tidal deformability.

With the exception of merger time, the extrinsic parameters of both Signal A and B were drawn from uniform distributions in sky locations, phase, polarisation and binary inclination. Each signal was generated from 9 Hz, just below the noise cutoff of 10 Hz, to avoid discontinuities in the data. Further details of intrinsic parameters, merger times and luminosity distances are given in the subsections below.

This distribution is designed to be as close to a true astrophysical distribution, but to also allow reasonable study of possible time-overlapping CBC cases. As such our study is aimed at the methodology of the pipelines and not at providing an astrophysical study of such events.

4.2.2.1 Masses and spins

The masses of the two objects in a binary were drawn in pairs. BBH mass pairing were drawn from the most recent binary mass distribution estimation by the LIGO-Virgo collaboration. The chosen mass distribution was the *PowerLaw+Peak* distribution covering primary masses in the range $[5, 100]\,M_\odot$ and mass ratios in the range $[0.1, 1]$ [135]. As the detectors have some bias as to the events they will detect, we included a biasing factor on the mass distribution. Using the PSD of the advanced LIGO detectors [286], and the `inspiral-range` Python package [11, 258], we estimated viewing ranges for each binary pairing in the mass distribution grid. These distance estimates were used to generate volume estimates and were then multiplied by the per volume merger rate to estimate a true merger rate of each signal. This was then normalised to produce a weighted distribution to bias the astrophysical merger rates, by mass, to the observable merger rate. This produces binaries with more even mass ratios and higher masses, as is expected in these detectors.

The neutron star (NS) binary mass range is still an area of active research [135, 160], with observed and predicted maximum NS masses differing [156, 158]. As such, for BNS mergers we defined a mass range of $[1.14, 3]\,M_\odot$ and drew uniformly across this. This is broadly consistent with both gravitational wave and electromagnetic observations. No mass distribution biasing was performed due to the smaller luminosity distances drawn for these binaries.

BBH spins were drawn from the spin distributions estimated by the *PowerLaw+Peak* mass model from the most recent estimates by the LIGO-Virgo collaboration [135]. This includes both aligned and in-plane spins with azimuthal orientations between $[\frac{-\pi}{2}, \frac{\pi}{2}]$, polar angles between $[0, 2\pi]$ and magnitudes ranging between $[0, 0.99]$ in dimensionless magnitude. Parameter estimation on time-overlapping signals has shown that highly time-overlapping pairs can mimic precession effects in the waveform, see Section 3.3.1, so it is interesting to consider how well searches

will observe such events. Spins were drawn independently of binary masses. BNS signals were given aligned only spins with magnitude range $[-0.05, 0.05]$, based on observations of BNS systems [62, 123, 173, 287].

4.2.2.2   Distances and times

The distance of events was drawn from a third-order power law between $[200, 1300]$ Mpc for BBH systems and $[5, 200]$ Mpc for BNS systems. These values were set to ensure a reasonable number of visible events in the injection sets, without too many events being too quiet to observe, SNR < 5, or overwhelmingly loud, SNR > 50. These ranges are broadly consistent with observations in current detectors [55]. While redshift does have an effect at these distances it will not change any conclusions drawn from this study, and therefore was not included in these injections. For consistency, all detector frame masses are identical to the source frame masses.

The merger times of Signal A events were drawn uniformly across the ten days of simulated data. To avoid overlaps of $N_{\text{signals}} > 2$, these times were spaced out within this data set such that no mergers were within 60 seconds of the start of when the next pairing reached 10 Hz. The merger times of Signal B events were then selected by generating a waveform for each Signal A, calculating the time of first visibility at 10 Hz and that of the merger, and drawing a time uniformly between these values. To ensure observations of close relative merger times, some pairings in the BNS+BNS and BNS+BBH runs were drawn to ensure mergers within two seconds of each other. The BNS studies with narrower merger time separations were performed as a separate ten day segment, which does not affect the estimated false alarm rates in those runs.

As lower mass signals, such as BNS inspirals, are in-band in the detector for much longer than lower mass, BBH signals, this leads to many fewer signals in the BNS study. However, we did not increase the length of the BNS studies beyond ten days as this would have drastically increased the computational expense.

4.2.3   Searches

4.2.3.1   `PyCBC` search

`PyCBC` is a matched-filter search pipeline for the detection of CBC signals in a wide parameter space [16–20, 70, 285]. The triggers are generated in coincidence with the network of detectors by correlating the data with templates. The *bank* of templates used in this study is exactly the same as the one used for `PyCBC-broad` in GWTC-3 [55]. In this work we have employed a slightly modified version of `PyCBC-broad` which was used for the GWTC-3 catalogue [55]. These modifications were made in order to accommodate the complexity induced in the signal space due to time overlap. In particular, for this work the "clustering window" of the `PyCBC` search is modified. This is discussed in more detail in Section 4.2.4.

Background estimates are generated by time shifting the data of the three detectors by more than the time of flight between the detectors, producing a background trigger list. This process is repeated until enough events are acquired to measure a false alarm rate (FAR) of 1 per year ($1\,\mathrm{yr}^{-1}$). The injections are then processed and ranked according to the background. This process is same for both the pipelines used in this study, however the detection statistics between the two pipelines are very different.

`PyCBC` uses detection statistics based on the matched-filter SNR , with information about the event rate and the background rate incorporated as described in [70, 170].

4.2.3.2 `cWB` search

`cWB` is an unmodelled analysis pipeline which detects and reconstructs GW signals without assuming any waveform model [6, 7, 211]. `cWB` decomposes each interferometer data into a time-frequency (TF) representation using Wilson-Daubechies-Meyer wavelets [288]. Each wavelet amplitude is normalised by the corresponding detector amplitude spectral density, `cWB` then selects those wavelets having energy above a fixed threshold. Finally, clusters from different detectors are combined coherently into a likelihood function, which is maximised with respect to the sky location.

From the likelihood we define the statistical quantities to distinguish between a possible GW signal and glitches coming from the noise. The first being the coherent energy E_c, which represents the coherent contribution of the likelihood by cross-correlating data from different detectors. Another key statistic is the null, or residual, noise energy E_n, which is given by subtracting the likelihood from the whitened data energy.

From coherent and null energy we can define two further quantities. The first is the penalty, χ^2, defined as the null energy divided by the number of independent wavelet amplitudes used for describing the detected event. The second is the correlation coefficient c_c:

$$c_c = \frac{|E_c|}{|E_c| + E_n} \tag{4.1}$$

This estimates the coherence of the data among different detectors: when $c_c \simeq 1$ ($|E_c| \gg E_n$) there is a high coherence and it is likely that there is an astrophysical signal, while when $c_c \simeq 0$ ($E_n \gg |E_c|$) the data is incoherent and so is less likely to contain an astrophysical signal.

The correlation coefficient and the penalty are used in post-production analysis for recognising non-Gaussian noise transients, commonly referred to as "glitches", which could trigger the pipeline, even if they are not GW events. In this work we applied the same thresholds used for O3 analysis, these are $c_c > 0.7$ and $\log_{10}(\chi^2) < 0.2$ [55].

4.2.4 Finding signals

Once the searches were performed, trigger sets were recovered for each of the three injection sets in each run. Injections were marked as found if there was a trigger found in the trigger sets within a defined time separation at merger. These separations differed between the two pipelines.

As a matched filter search, `PyCBC` returns a time for each trigger that corresponds to the visible end of the signal in the data. This was directly matched to the injected signals merger time. If the injected signal had a `PyCBC` trigger with an end time in the range ± 0.1 seconds then the injection was counted as found by the pipeline.

A slight problem arises for signal pairings in which the mergers are within ± 0.1 seconds. `PyCBC` often finds that several templates match the same signal, particularly for significant triggers. To avoid this, a clustering window is specified for the run. This window, set to ± 1 second for our study, will reject all but the most significant trigger within the window. If signals overlap in this region, then only one trigger will be returned for the pairing. This situation is covered in more detail in Section 4.3.2.

`cWB`'s approach of searching for regions of excess power requires a different approach. The standard returned time is the mean time, weighted with energy, but for this study it is more suitable to use the end time of the reconstructed waveform as estimated by `cWB`. This allows for the reconstructed waveforms to be counted correctly. Initial applications of the `PyCBC` time constraints led to a large number of triggered injections being rejected. A window for signal finding of injected/reconstructed signal end time was set to ± 2.5 seconds. This time allows for the best recovery rate of `cWB` triggers, without missing separate signal pairings.

4.3 Results

4.3.1 Bias regions for time-overlapping signals

Previous studies of time-overlapping CBCs, including the study presented in Chapter 3, have focused on their effect on the parameter estimation of the underlying signals [1, 266, 267, 281, 282]. By considering the findings of these studies, we define three regions in which the presence of a second signal affects the recovered parameters of the primary signal:

Strong bias: This is the region in which the two signals most strongly affect each other. In this region, recovered parameters will be significantly biased away from their true values. Largely this is bound by the separation of merger times between the signals. As this boundary is not consistent between all studies, to be conservative we define this as a merger time separation of $|\Delta t_c| \leq 0.5\,\mathrm{s}$ for BBH+BBH overlaps. However, some studies [266, 282], indicate that the similar region for BNS+BNS

overlaps is closer at $|\Delta t_c| \leq 0.01\,\text{s}$. The literature has not defined any such value for BNS+BBH overlaps, so for this study we have applied boundaries to be the same as BNS+BNS overlaps. This region is smaller, likely due to the number of clean cycles in the later merging BNS, due to their high merger frequency, unlike BBH mergers which merge at lower frequency.

Weak bias: In this region signals are often recovered with slightly biased, but broadly correct, parameters. Considering the literature we define this region as $0.5 < |\Delta t_c| \leq 2\,\text{s}$, with the lower limit varying for overlaps containing a BNS merger.

Negligible bias: In this region the signals are dissimilar enough to not cause any noticeable bias in the recovered parameters. Pairings in this region should both be recovered. The bias in one signal, caused by the presence of the other, should be small enough to not negatively impact the results. We define this region to be for merger time separations of $|\Delta t_c| > 2\,\text{s}$.

Parameter estimation studies also indicate that the bias will be negligible if the ratio of the SNRs of the signals is particularly unequal, one signal being at least greater than three times louder than the other, see Section 3.3.1. Pairings in this category are likely to fall into the negligible bias region, regardless of merger time proximity. Some indication of relative chirp mass, and therefore waveform frequency range, is likely to also have an effect [282]. If signals differ significantly in chirp mass, $\mathcal{M}$, then the bias may be smaller as the signals are dissimilar in frequency at merger. While we include signal overlaps of differing chirp mass in the study, we do not examine how this effect is present in trigger selection.

	$N_{Overlaps}$ by region		
Overlap configuration	Strong	Weak	Negligible
BBH+BBH	$6.94^{+8.49}_{-3.74}$	$20.8^{+25.4}_{-11.2}$	$15000.0^{+7100.0}_{-5000.0}$
BNS+BNS	$0.014^{+0.098}_{-0.014}$	$2.85^{+19.5}_{-2.73}$	$4800.0^{+8500.0}_{-3800.0}$
BNS+BBH	$0.138^{+0.170}_{-0.075}$	$27.6^{+33.7}_{-14.9}$	$15000.0^{+7100.0}_{-5000.0}$

Table 4.1: Estimated number of signals occurring for different CBC overlap configurations in a year's observations of the Einstein Telescope. For the BNS+BBH row this is the expected number of BBHs, rather than the number of BNSs. The other columns represent the predicted number of overlaps of this kind in each bias region.

Table 4.1 shows estimated numbers of events falling within each of the bias regions, defined above, over a year's observation of ET [89]. These numbers were estimated by calculating the visible volume for a variety of different mass CBCs as described in Chapter 2, using the `inspiral-range Python` package [11, 258], and a PSD for ET [262]. The viewing time for each signal, in the negligible bias region, was estimated from $1\,\text{Hz}$ to the time of merger. Signals in the strong and weak bias regions were fixed to the durations described above, merger time separations of

0.1 s and 2 s, respectively, for BBH signals. For a more detailed explanation of this method see Section 2.2.1.

From the numbers in Table 4.1 it is clear that, despite the strong and weak regions being the most cause for concern, only a very small fraction of events will ever fall into these regions. By far the dominant case is the negligible bias region, covering almost all detectable transients in ET

4.3.2 Injection studies

4.3.2.1 BBH+BBH overlaps

BBH+BBH		Injected	PyCBC		cWB	
			SINGLES	PAIRS	SINGLES	PAIRS
Total	Counts	13172	10454	9818	6885	5634
	Percentage	-	79.37%	74.54%	52.27%	42.77%
$FAR < 1\,yr^{-1}$	Counts	13172	8436	7947	6883	5310
	Percentage	-	64.04%	60.33%	52.25%	40.31%

Table 4.2: Injected and recovered individual overlapping signals in different injection sets and search pipelines. Here the two signals in a pairing are both BBH mergers. The SINGLES column here is the union of the results from both SINGLES$_A$ and SINGLES$_B$ data sets. The FAR threshold of $< 1\,yr^{-1}$ means that, in a years observation, fewer than one event of this kind will occur due to statistical fluctuations in the noise. This is a fairly typical cut for assuring an event is astrophysical. The total column is for all events matching a trigger, with no FAR threshold.

Table 4.2 contains values of the number of injected and recovered signals in each injection set in both PyCBC and cWB. As can be seen, in PyCBC, the vast majority, close to 80%, of injected non-overlapping signals were recovered by any trigger. The other 20% were largely missed due to the signals having low network SNRs, $\lesssim 12$, due to their large distances or sky locations that are a challenge for the detectors. However, another 15% are removed once a FAR threshold of $< 1\,yr^{-1}$ is applied, these could be true astrophysical signals, but are rejected due to poor significance. This is an artefact of the injected distribution to provide a reasonable number of detectable events.

As expected [135], cWB is less sensitive, with respect to modelled searches, for this range of masses. The missed signals here are largely low mass CBCs, $\mathcal{M} \lesssim 15\,M_\odot$, in which the majority of the SNR comes from the inspiral, which is difficult for cWB to recover. As expected, if the injections are present in the template bank of the matched filter search, then the unmodelled method will always be less optimal than the matched filter searches. This is the case here since our injections have source parameters which are well described by the template bank.
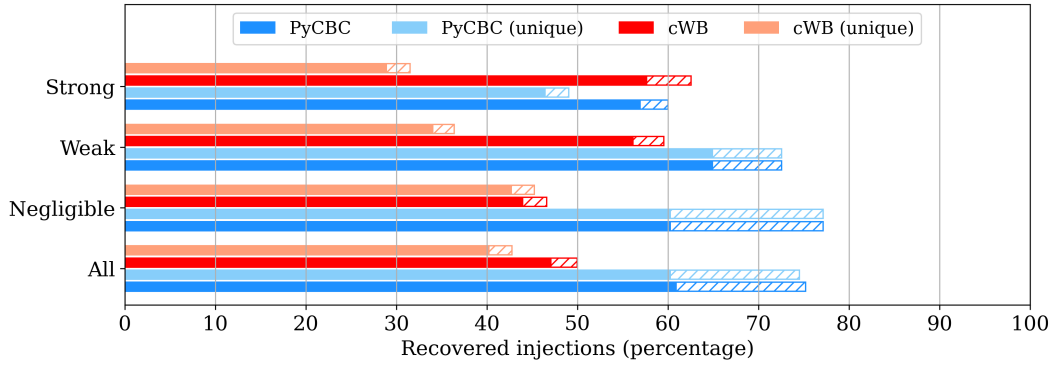
Figure 4.1: Bar charts for the found injections, in the BBH+BBH injection sets, in both pipelines in the different overlap bias regions. Each region has four bars, split into two for each pipeline. These show the percentage injections in which the pipeline found a trigger. The "unique" column shows the percentage of unique triggers, i.e. if both signals are found by the same trigger, then they are only counted once. The shaded segments show injections recovered at a FAR threshold of $< 1\,\mathrm{yr}^{-1}$.

Figure 4.1 shows bar charts for the percentage of injections that were found by a trigger in each pipeline in the PAIRS injection set. As expected the pipelines perform reasonably well in the negligible bias region, with the majority of signals found in PyCBC. For both pipelines, in this region, the number of injections found matches the findings in the SINGLES injections. There is some decrease in the fraction successfully caught when moving to the weak and strong bias regions.

Inside the strong bias region for PyCBC, and some of the weak region for cWB, some of the injections are both found in the same trigger. This means that they are counted twice. To show this we have added extra bars for each search in which we have removed duplicated triggers here. This is an effect of the criteria we have applied to decide if an injection is found. See Section 4.2.4 for more details.

At the threshold of FAR $< 1\,\mathrm{yr}^{-1}$ we see a 5% increase of found injections in the weak bias region compared to the negligible bias region. This comes largely from constructively interfering signals increasing the recovered SNR of the pairing and hence decreasing the false alarm rate of the trigger.

The strong bias region here shows a functional problem with the pipelines for signals in this region. These numbers are slightly lower than they theoretically should be, due to the clustering of triggers in the pipeline. In PyCBC, as templates are matched to the data, numerous triggers are recorded for each signal as multiple templates may match the signal to differing levels of significance. To avoid all of these triggers being returned for a single signal, a clustering window is set. This window, set to $\pm 1\,\mathrm{s}$ in our study, clusters these triggers and returns a single trigger of highest significance.

In the case of time-overlapping signals within this $\pm 1\,\mathrm{s}$ merger time separation window, only the most significant signal is returned. As such, in the strong bias
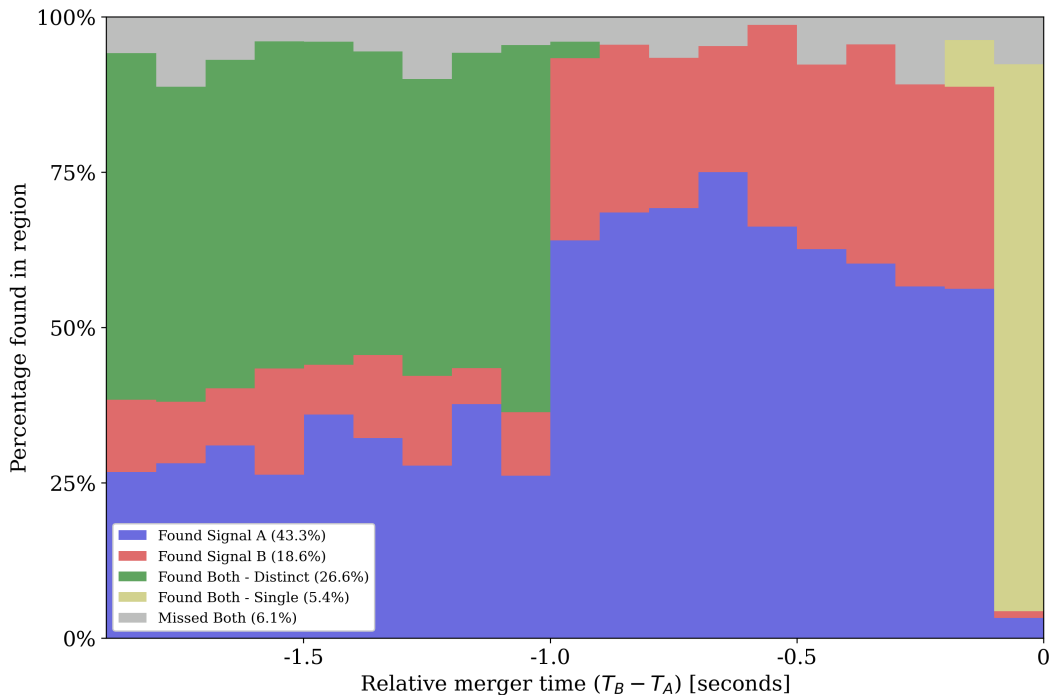
Figure 4.2: A stack plot showing the distribution of how injected signals were found by relative merger time in the `PyCBC` BBH+BBH PAIRS injection set. Blue and red show the pairings in which only one signal was found, Signal A or Signal B respectively. Green shows the the pairings in which both signals were found with separate triggers, while yellow shows signal pairings where both signals were found by a single trigger. Grey represents entirely missed pairs. This plot covers both the strong and weak bias regions. The time convention is $T_B - T_A$, this is always less than 0 due to the convention of drawing Signal B's merger within the observable duration of Signal A. The percentages in the caption refer to the fraction of pairings in this region, $|\Delta t_c| \leq 2\,\text{s}$, that fall in each category.

region and some of the weak bias region, many of the signals are missed due to only the most significant being returned. In our study the triggered signal is usually Signal A. Due to our method of drawing of the merger time, Signal B always merges before Signal A. Therefore, in a matched-filter search, Signal A is favoured as it is still providing power in the data at this time. This is not necessarily the case with unmodelled searches, such as `cWB`, see Section 5.2.2 for further details. An example of this can be seen in Figure 4.2.

Both found triggers are only in the region outside the clustering window of `PyCBC`, $|\Delta t_c| \leq 1\,\text{s}$[1]. In the region $|\Delta t_c| \leq 1\,\text{s}$, Signal A is clearly favoured, as it is the later merging signal. Pairings in this region that are found with Signal B are largely either very close in merger time or have $\text{SNR}_B > \text{SNR}_A$. This is shown in the top plot of Figure 4.3, where the distribution of SNR ratio between signals in found pairings is shown. In the region $< 1\,\text{s}$ here Signal A is louder, and

---

[1]Three pairings have both signals found inside the clustering window. These pairings have merger time separations of approximately $-0.999\,\text{s}$ and, in some detectors have separations $|\Delta t_c| > 1\,\text{s}$
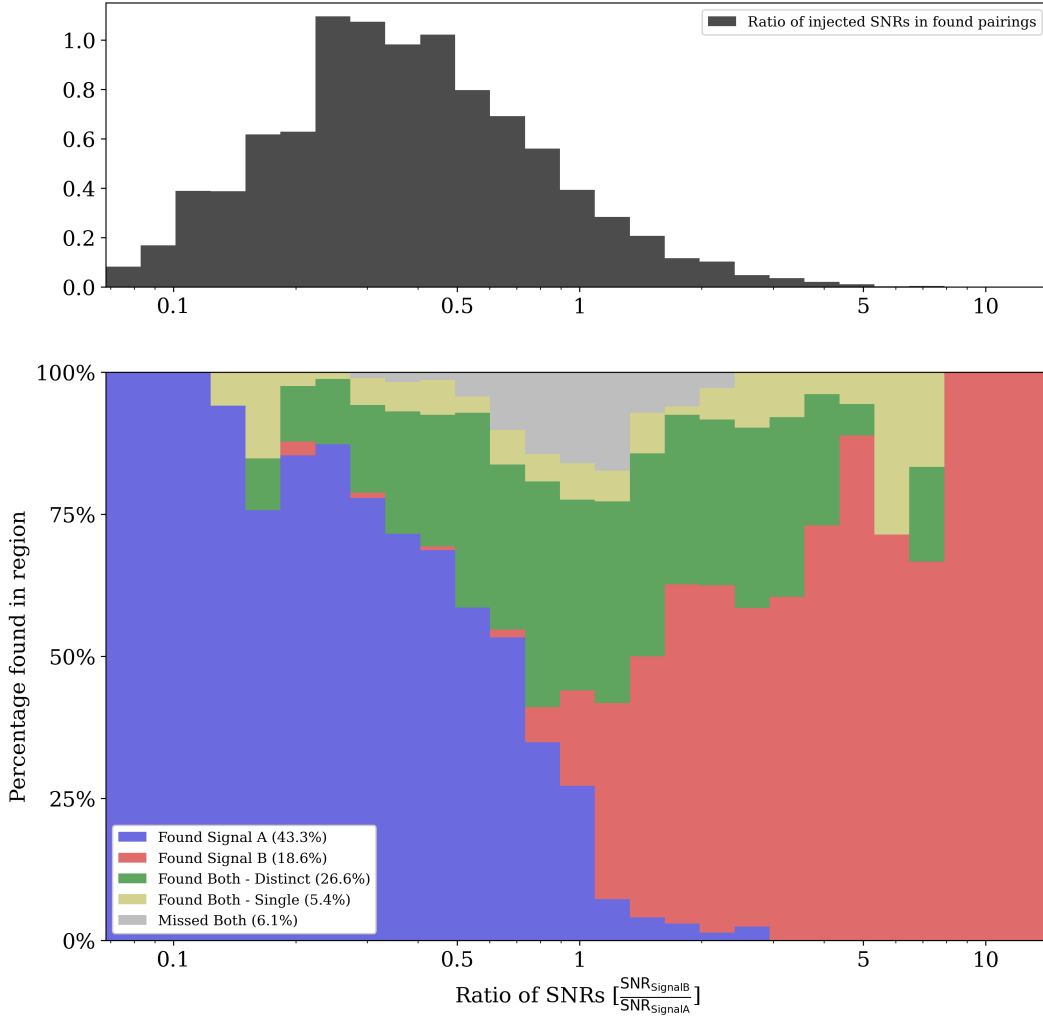
Figure 4.3: A stack plot showing the distribution of how pairings were found as a function of SNR ratio between the two signals. The ratio is defined to be $\mathrm{SNR_B}/\mathrm{SNR_A}$. Colours are consistent with those in Figure 4.2. Similarly, the data comes from pairings in the strong and weak bias regions of the `PyCBC` BBH+BBH PAIRS injection set. The percentages in the caption refer to the fraction of pairings in this region, $|\Delta t_c| \leq 2\,\mathrm{s}$, that fall in each category.

therefore favoured, and in the region $> 1\,\mathrm{s}$ Signal B is louder and more likely to be found. Missed pairings here have generally even SNR ratios due to them both having poor SNRs. These regions are artefacts of the pipeline settings and as such remain the same for the longer signals in the BNS+BNS and BNS+BBH runs outlined in Sections 4.3.2.2 and 4.3.2.3.

It should be noted that signals pairings in the region $|\Delta t_c| \leq 0.1\mathrm{s}$ are classed as "both found" as both signals meet our criteria for a found signal, they are less than 0.1 seconds from a trigger. However, they are found within the clustering window of the search and would only return a single trigger for the pairing. In such cases the a trigger would be returned but, most likely, the second signal would be missed.

For Figures 4.2 and 4.3, we have only included `PyCBC` results. This is due to the large time window criteria we applied to count found `cWB` injections. Most signals with such close mergers will only be found as a single trigger in `cWB`. `cWB` internally applies time windows on regions of excess power, under the assumption that it would only ever be a single signal. In wider regions, such as the negligible bias region, the search returns separate triggers for each component signal in the pairing. This is akin to the clustering window of `PyCBC`, however, when `PyCBC` finds both injections by a single trigger it will return a template for a single signal under the assumption that it is a single signal, `cWB` returns the coherent power of one, or potentially both signals, see Chapter 5.

There are some signals in the negligible bias region that are found in the single signal injection sets, but missed in the time-overlapping runs. Generally, these signals have relative merger times just beyond the two second negligible bias region and have fairly unequal SNR-ratios. This follows the findings of previous parameter estimation studies. In those studies, if one signal is much louder than the other then samples are recovered matching the parameters of the louder signal. In the case of match filter searches, the template bank search will recover templates closer to the louder signal, the remaining power from the weaker signal will be rejected as either noise, or excess power in the inspiral of the louder signal.

The drop in efficiency due to the presence of time-overlapping signals can be estimated by comparing the efficiency of the overlapping and non-overlapping signals. For `PyCBC` this drop off is approximately 4% across the entire run. In `cWB` this drop in efficiency is approximately 12%. The differences in pipeline efficiency means that a direct comparison is not a simple matter. We also report the relative efficiency drops as 6% and 23% for `PyCBC` and `cWB` respectively. The relative efficiencies were estimated as described in equation 4.2.

$$DIFFERENCE = 100 \times \frac{SINGLES - PAIRS}{SINGLES} \tag{4.2}$$

The errors on all efficiencies are less than 0.01% and as such were not included. All quoted efficiencies are for events found with a FAR threshold of < 1 per year.

Outside the clustering window of `PyCBC`, this fall in efficiency is approximately 1%, while inside the clustering window the fall in efficiency is 26% due to the majority of paired signals being found by a single trigger, or not at all. These regions are not directly comparable for `cWB`, in these cases it will find both signals and return them as one trigger, however, similar numbers would be 9% and 32% for outside and inside the $|\Delta t_c| = 1\,\text{s}$ boundary.

4.3.2.2 BNS+BNS overlaps

Table 4.3 shows the results for the BNS+BNS overlap injection set. There are fewer signals in these injection sets as a higher number of signals would have caused

BNS+BNS		Injected	PyCBC		cWB	
			SINGLES	PAIRS	SINGLES	PAIRS
Total	Counts	2212	2042	1677	554	467
	Percentage	-	92.31%	75.81%	25.05%	21.11%
FAR< $1\,\mathrm{yr}^{-1}$	Counts	2212	1854	1544	550	461
	Percentage	-	83.82%	69.80%	24.86%	20.84%

Table 4.3: Injected and recovered individual overlapping signals in different injection sets and search pipelines. The SINGLES column here is the union of the results from both SINGLES$_A$ and SINGLES$_B$ data sets. Here the two signals in a pairing are both BNSs. It should be noted that these values are not directly comparable to those in Table 4.2, as the luminosity distances were arbitrarily set for BBH and BNS injections such that most were visible in the detector. As such we have a slightly higher proportion of BNS signals recovered in PyCBC than we did for BBH signals.

$N_{signals} > 2$ overlaps, which we do not consider in this study. As expected, cWB finds a lower percentage of the injections, as it is not designed to find longer, inspiral dominated signals such as binary neutron stars. This can be seen in Figure 4.4 where cWB recovers only about 20% of injections with unique triggers. PyCBC has a slightly higher efficiency here than in the BBH+BBH run, however, this is most likely a consequence of the injected luminosity distances of the signals rather than the design of the search pipeline.

Due to these long durations and the uniform drawing of merger time separation, the signals were drawn such that approximately half fell into the negligible bias region with a further quarter falling in each of the weak and strong bias regions. Due to the narrow strong bias region for these overlaps, a very high percentage of injected pairs fall inside the PyCBC clustering window. These are then both found by the same trigger. This is apparent in the strong region of Figure 4.4 where the unique bar is half that of the non-unique found.

The efficiency drops between overlapping and non-overlapping BNS signals is 14% for PyCBC and 4% for cWB. The cWB values drop is small, compared to PyCBC, as the majority of BNS signals found by cWB are very significant regardless of overlap. The relative drop in these efficiencies are 17% and 16% respectively.

4.3.2.3 BNS+BBH overlaps

As described in Section 4.3.2.2 cWB is not tuned to low mass, inspiral dominated signals, like BNSs. As such it does not perform well for the BNS portion of the SINGLES injection sets. The efficiencies of the pipeline for these injection sets highlights this. For cWB, the SINGLES$_A$ run recovered 25% of injections, while the SINGLES$_B$ run recovered 52%, with 86% and 82% being the comparable numbers
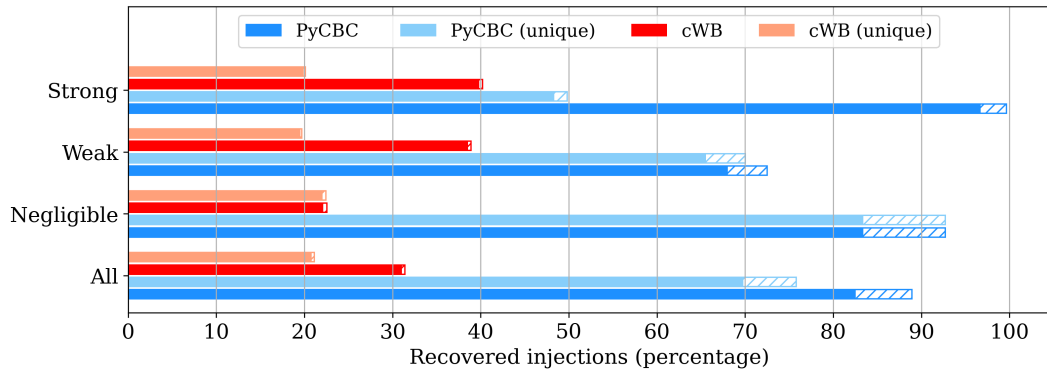
Figure 4.4: Bar charts for the found injections, in the BNS+BNS injection sets, in both pipelines in the different overlap bias regions. Each region has four bars, split into two for each pipeline. These show the percentage injections in which the pipeline found a trigger. The "unique" column shows the percentage of unique triggers, i.e. if both signals are found by the same trigger, then they are only counted once. The shaded segments show injections recovered at a FAR threshold of $< 1\,\mathrm{yr}^{-1}$.

BNS+BBH		Injected	PyCBC		cWB	
			SINGLES	PAIRS	SINGLES	PAIRS
Total	Counts	2400	2086	1713	928	706
	Percentage	-	86.92%	71.38%	38.67%	29.42%
FAR$< 1\,\mathrm{yr}^{-1}$	Counts	2400	1782	1519	922	673
	Percentage	-	74.25%	63.29%	38.42%	28.04%

Table 4.4: Injected and recovered individual overlapping signals in different injection sets and search pipelines. The SINGLES column here is the union of the results from both SINGLES$_A$ and SINGLES$_B$ data sets. Here the two signals in a pairing are a BNS and a BBH. It should be noted that the comparison between PYCBC and cWB for the SINGLES runs is challenging as cWB will perform significantly differently for the BNS SINGLES run. See Table 4.3 for a more precise comparison of single signal runs for these events.

for PyCBC.

Table 4.3.2.3 shows a significant falloff between the SINGLES and PAIRS injection sets, compared to the BBH+BBH run. This, as in Section 4.3.2.2, is in large part due to a large percentage of strong bias pairs falling inside the clustering windows and being found by the same trigger. This can be seen in Figure 4.5 where, as in Figure 4.4 the strong bias region sees a significant falloff from any to unique found injections.

Here PyCBC performs better for BNS+BBH overlaps than for BNS+BNS overlaps. The same cannot be said for cWB, which would appear to perform more consistently in the BNS+BNS run. The robustness of this conclusion should be considered due to the low efficiency of the run.
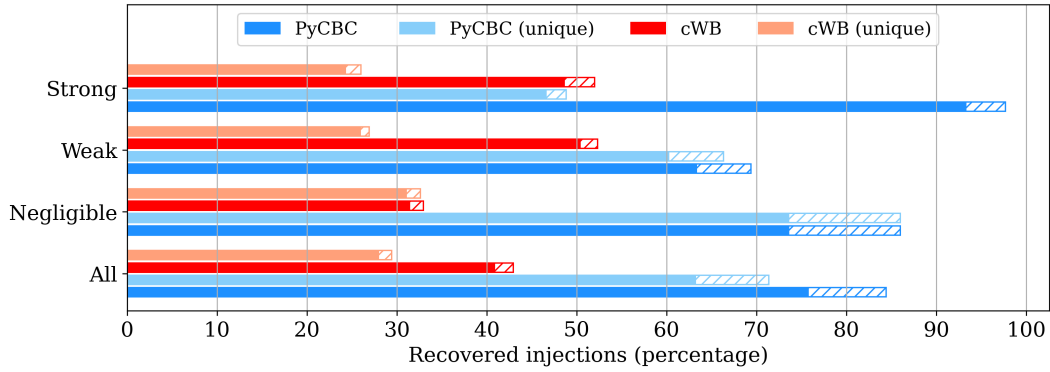
Figure 4.5: Bar charts for the found injections, in the BNS+BBH injection sets, in both pipelines in the different overlap bias regions. Each region has four bars, split into two for each pipeline. These show the percentage injections in which the pipeline found a trigger. The "unique" column shows the percentage of unique triggers, i.e. if both signals are found by the same trigger, then they are only counted once. The shaded segments show injections recovered at a FAR threshold of $< 1 \, \text{yr}^{-1}$.

The efficiency drop between overlapping and non-overlapping BNS signals is 11% for `PyCBC` and 10% for `cWB`. Care should be taken here in comparisons between the pipelines, as `PyCBC` has similar sensitivities to BBH and BNS signals, whereas `cWB` will favour higher mass signals and is therefore more sensitive to one half of the non-overlapping signals. The relative drops in efficiency are 15% and 26% respectively.

4.3.3 Accuracy of recovered triggers

Figure 4.6 contains histograms of the fractional chirp mass difference between the triggers recovered, by `PyCBC`, in the PAIRS injection set and the true injected values. It also includes a similar distribution for the SINGLES injection set, shown in grey.

In most cases the recovered trigger in the PAIRS injections match what is found in the single signal injections to a reasonable level, $|\Delta\mathcal{M}|/\mathcal{M} < 1$. This can be seen by comparing the distribution of negligible bias region injections to the SINGLES distribution. The weak and negligible regions match this distribution fairly well, with few outliers. However, the strong bias region skews towards a high fractional difference, up to ~ 6 times the value found in SINGLES. Therefore, we can say that signal pairings in the strong bias region are affected in a similar way in matched filter searches to matched filter based parameter estimation.

The skew of this distribution shows that incorrectly found signals tend to be found with higher chirp mass templates than the injected signal. As this is also true for the inaccurately found single signals, this is a feature of how we calculate the fractional difference. The recovered chirp mass can never be less than -1 as for a trigger to be recovered it must have a positive chirp mass. Triggers with much larger values of fractional chirp mass are likely extreme due to the lower density of templates at the high mass tail of the template bank.
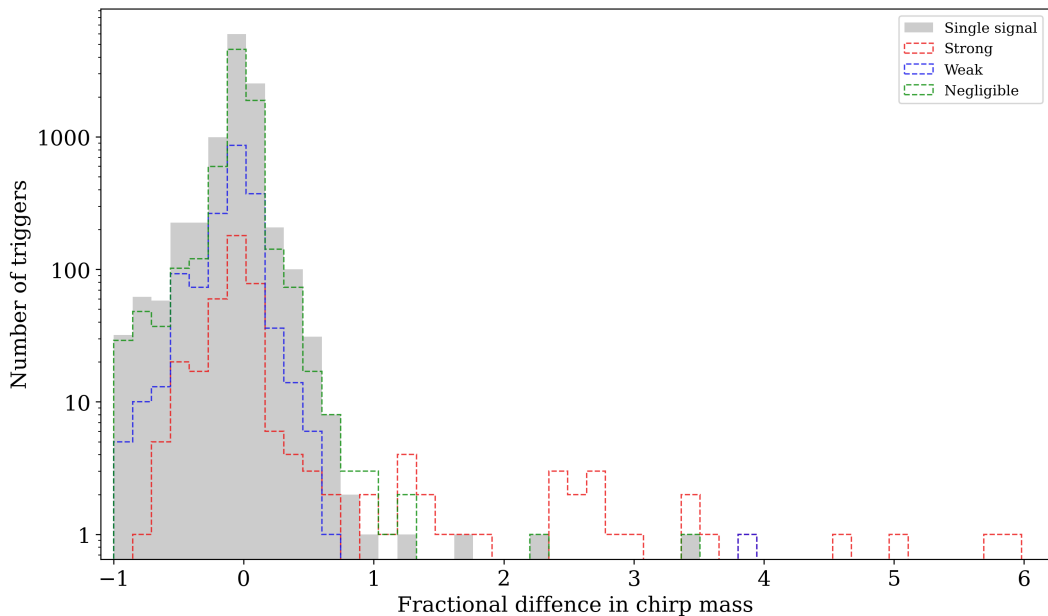
Figure 4.6: Distribution, across the overlap regions, of the fractional difference between the recovered and injected chirp masses for `PyCBC` triggers in the PAIRS injection set. Also shown, in grey, is the same distribution for recovered and injected in the SINGLES injection set. A perfect pipeline, with an infinitely finely gridded template bank, running on clean detector data would find injections close to a delta spike centred on zero on this plot. These distributions have been given in terms of the number of triggers. For a direct comparison between the overlap regions we have included normalised distributions in Figure B.1 in the Appendix B.

4.4 Discussion

We have shown that both modelled, and unmodelled searches can detect time-overlapping CBC signals in the negligible bias region of $|\Delta t_c| > 2\,\text{s}$. Within the weak bias region, so long as the signals are separated by more than the matched filter clustering window, here $|\Delta t_c| > 1\,\text{s}$, the matched filter search should recover both signals, provided one is not much louder than the other. These findings match those of Regimbau et al [284]. We also show that in the narrower weak and strong bias regions both pipelines can successfully recover one or both signals in the overlap most of the time.

Inside the clustering window, matched filter pipelines do struggle to successfully recover both signals due to internal methods designed to reduce the number of false triggers returned. However, it is possible that these searches could be modified to find templates that best match each signal in the pairing. This could provide reasonable best guesses for multi-signal parameter estimation. However, a proper method of time-overlapping transient identification is still required to prevent signal misidentification. The effect of adjusting the clustering window is discussed further in Section 5.2.1 of Chapter 5. It is possible that such modification methods could be

used to identify time overlapping signals without large adjustments to these search pipelines.

Chapter 5

Can we accurately identify which transient signal search triggers contain time-overlapping transient signals?

5.1 Introduction

In Chapter 4 we showed that two of the most successful modelled and unmodelled transient GW search algorithms are not likely to miss transient signals purely because there is a second, significant, signal concurrently in the detector. It has also been shown that the background noise from near constant transient CBC signals will not affect noise curve estimation in third generation detectors to the point where the majority of signals will be missed by searches [289]. However, unless the signals are separate enough in time, these search techniques will only return a single trigger with no information as to the number of signals present within that time.

In this chapter we discuss possible methods of identifying which triggers that contain more than a single signal. This includes methods based on matched filter searches, unmodelled searches and machine learning techniques. We then discuss potential methods of separating these signals.

5.2 Adapting current methods for transient overlap identification

Figure 5.1 shows a comparison of the whitened strain of an injected BBH single signal in simulated LIGO: Hanford detector strain. This signal, combined with coloured-
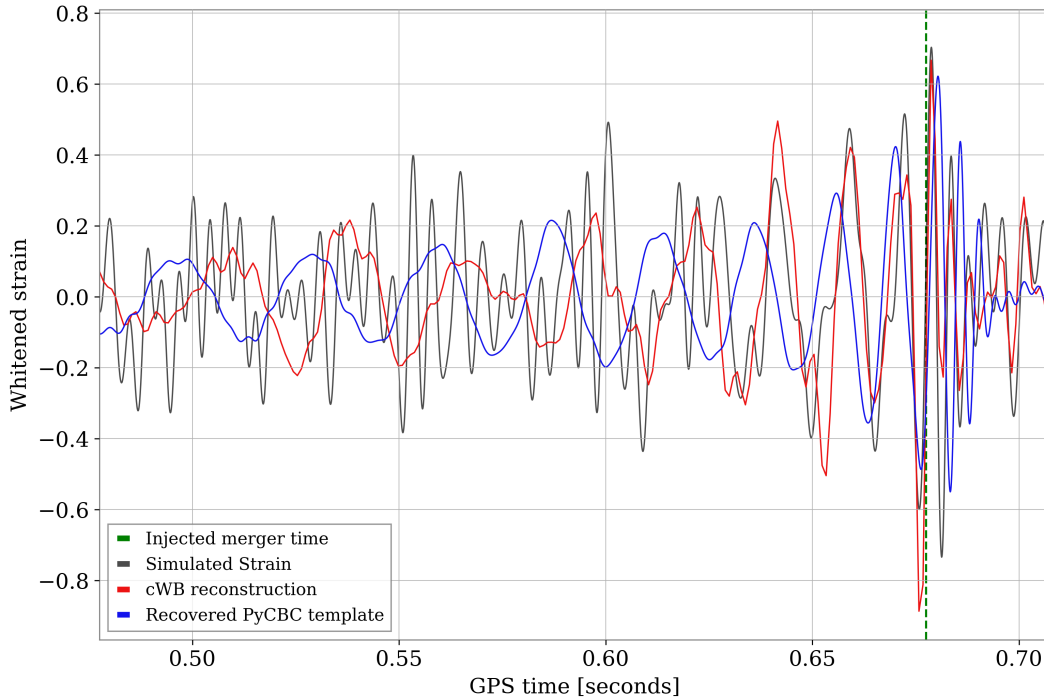
Figure 5.1: A plot of whitened strain, in the LIGO: Hanford detector, for a single BBH injection. The blue lines shows the matched template found by `PyCBC` in the SINGLES_A injection set from Chapter 4. The red line is the `cWB` reconstructed waveform from the same injection set. The green, dashed, vertical line indicates the injected merger time.

Gaussian noise was given to `PyCBC` and `cWB` as a part of the transient signal search study described in Chapter 4. The plot includes the maximum likelihood template found by the modelled search in blue[1], and the reconstructed waveform found by the unmodelled search in red.

Here, outside the merger, the template found by `PyCBC` does not match the signal as well as the `cWB` reconstruction. This is most noticeable at lower frequency, although the mergers are broadly similar. This is due to the coarseness of the gridding at higher masses in the `PyCBC` template bank selecting a template that is a poor match for this signal.

Figure 5.2 shows an equivalent plot involving the same signal, here Signal A, represented in Figure 5.1 overlapping with a second signal, Signal B[2]. It can be seen that Signal B, merging first, is found in `cWB` but not in `PyCBC`. Both signals are significant, with network SNRs of 26 and 27. Despite this, due to the close mergers of the signals and clustering, the template for Signal A is returned in the `PyCBC` PAIRS analysis due to its later merger time. The Signal B from this pairing was

---

[1] `PyCBC`, by default, does not return information about amplitude for templates. For the purposes of clarity in showing the template accuracy, we have here applied fitting methods to approximate the amplitude of the template to the signal.

[2] See Section 4.2.2 for details.
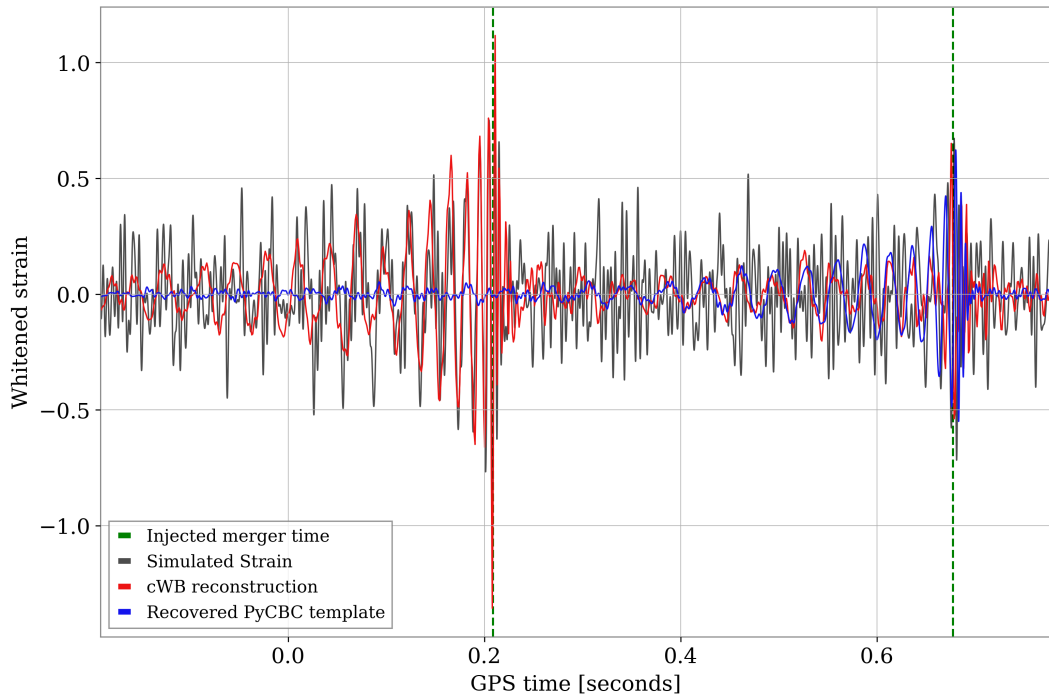
Figure 5.2: A plot of whitened strain, in the LIGO: Hanford detector, for a BBH+BBH injection. The blue line shows the matched templates found by `PyCBC` in the PAIRS injection set, see Chapter 4. The red line is the `cWB` reconstructed waveform from the PAIRS injection set. The green, dashed, vertical lines indicates the injected merger times of each signal.

found by both `PyCBC` and `cWB`, as an individual signal, in the SINGLES$_B$ injection set.

The phase of the `cWB` reconstruction for Signal A in Figure 5.2 is different compared to that showing in Figure 5.1 as the algorithm is trying to fit both signals to the same, coherent sky location. Indeed, as shown in Figures 5.5 and 5.6, in that case the likelihood maximisation is considerably affected by Signal B, and so Signal A's reconstruction is not optimal. This is discussed in detail in Section 5.2.2.

This case is typical of a situation in which current search techniques would only return a single trigger, resulting in difficulties for later signal analysis. The signals being less than 0.4 seconds apart would comfortably fall within the clustering windows of both the `PyCBC` and `cWB` searches. Due to this only a single trigger would be returned. This is indicated by the single blue `PyCBC` template[3].

5.2.1 Identification via matched filter template searches

When searching for signals in data, matched filter searches, such as `PyCBC`, will match a template waveform to the data at time intervals in order to create an SNR

---

[3]While the reconstructed waveform (red) shows both signals the algorithm would return this as a single trigger.
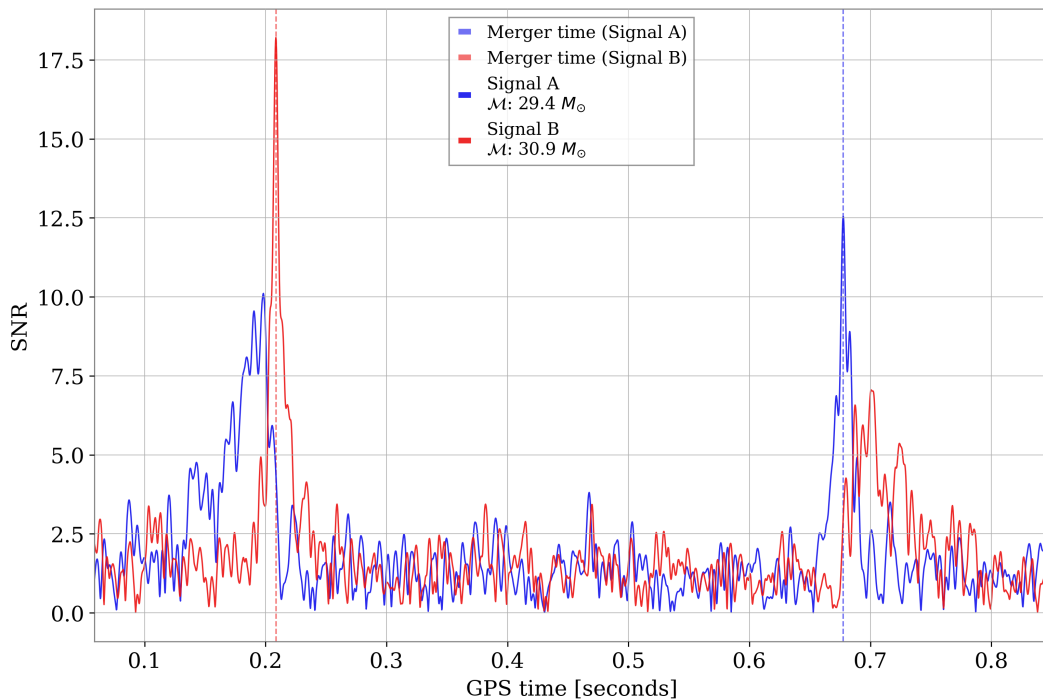
Figure 5.3: A plot of SNR time-series for two perfect templates against simulated data containing both signals in the LIGO: Hanford detector. The blue line shows the SNR of the Signal A template against the data, the red line shows the equivalent for the Signal B template. The blue and red, dashed, vertical lines show the injected merger times of Signal A and B respectively. The signals are the same as those shown in Figure 5.2. The peak SNRs here are smaller than those given in Section 5.2 as they are single detector SNRs, not network SNRs.

time-series of the data. This time-series is a map of the SNR of that template with the data. When one of these templates closely matches a signal, the time-series will peak.

In a situation in which there are two signals in the data, this time-series should peak twice, once for each signal in the data. Figure 5.3 shows this for two perfect templates against data with two signals injected. The blue line, for Signal A's template, shows a small peak around the merger of Signal B, where the match is not perfect. It then peaks again, cleanly and more significantly, around the merger of Signal A. The reverse is shown for a perfect Signal B template in red.

The signals and templates used in Figure 5.3 have very similar chirp masses, and as such match reasonably well with each other's templates. Conversely, if the signals have very different chirp masses, then this plot will only show a single peak for each signal, as can be seen in Figure 5.4. Although, there will likely be some non-Gaussianity in the region of the non-ideal signals merger time.

`PyCBC`'s clustering routines, as described in Section 4.2.4, will ignore these features and only return the maximum likelihood signal, in this case Signal A. However, it should be possible to modify the clustering routines to check for multiple peaks in
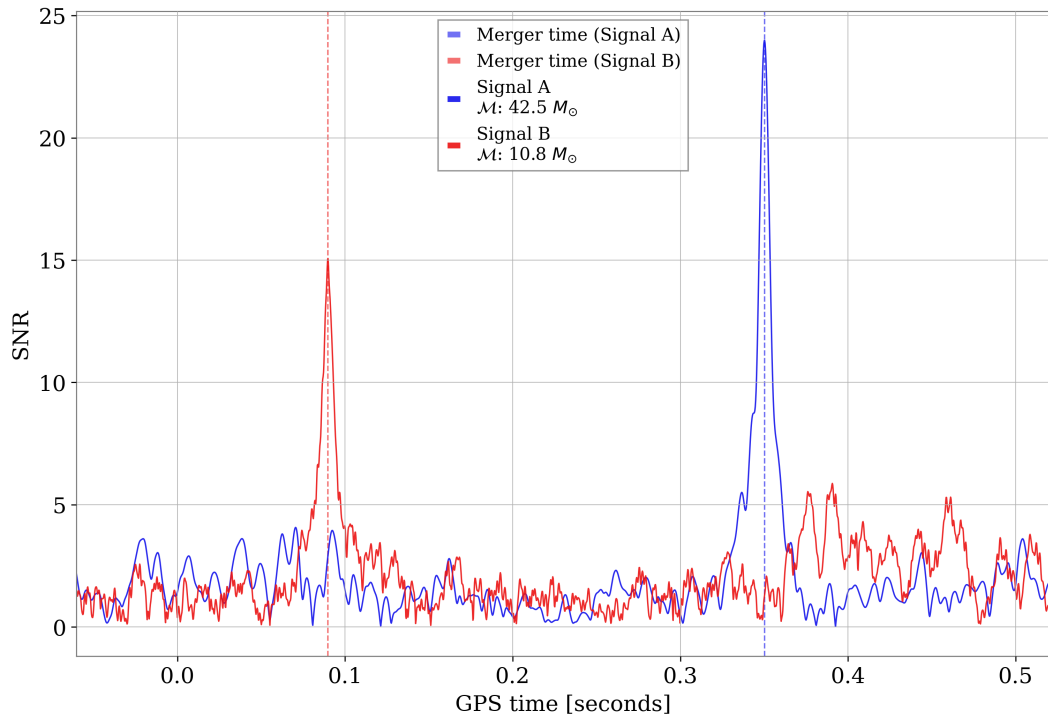
Figure 5.4: A plot of SNR time-series for two perfect templates against simulated data containing both signals in the LIGO: Hanford detector. The blue line shows the SNR of the Signal A template against the data, the red line shows the equivalent for the Signal B template. The blue and red, dashed, vertical lines show the injected merger times of Signal A and B respectively. This plot is an equivalent of that shown in Figure 5.3, but with less similar signals and templates.

a single template, or for single peaks in multiple templates. These results can then be used both as checks for the number of signals, and also to identify reasonable parameter ranges for each signal in the overlap. This would allow for a reliable starting point for multi-signal parameter estimation [281].

5.2.2 Identification via unmodelled searches

The `cWB` framework, as described in Section 4.2.3.2, is designed to analyse a single signal. The pipeline finds regions of excess power and then maximises the likelihood with respect to one source location, regardless of the number of present astrophysical signals. In the standard case of a single signal trigger, the pipeline maximises the likelihood with respect to that signal, and so almost all its energy is placed in the likelihood, while the null is almost entirely noise, as shown in Figure 5.5.

For the case of two time-overlapping signals, the likelihood is maximised considering both signals, generally with one favoured over the other, considering this signal as the "primary" and the other as the "secondary". In this case, the likelihood is largely maximised with respect to the primary signal, though often with some contamination from the secondary signal, depending on its energy. This means that
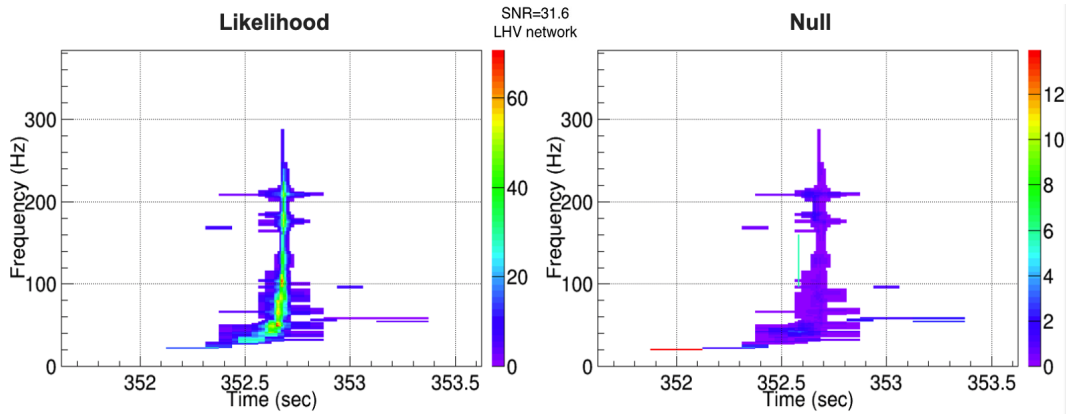
Figure 5.5: A spectrogram of likelihood and null energy for a single signal event. The likelihood contains almost entirely signal energy, while the null almost entirely noise. The data is the same as for the Single A signal in Figure 5.1

the primary signal energy is almost entirely found in the likelihood. The energy of the secondary signal is divided between likelihood and null depending on its source location. If this is considerably different with respect to that of the primary signal, then a considerable amount of the energy of the secondary signal will remain in the null. This is similar to the situation in Figures 5.1 and 5.2.

Figure 5.5 shows the time-frequency representation of the likelihood and null energies of Signal A, in which likelihood has been properly maximised. The signal is almost entirely caught in the likelihood. The remaining energy in the null is likely excess noise. Figure 5.6 represents the same signal in an overlapping pairing, as in Figure 5.2. In this case, the likelihood is maximised mainly with respect to Signal B, here the primary signal. The null contains the secondary, here Signal A, and is increased with respect to the single detection. The likelihood has been maximised with respect to a different sky location, and both the null and likelihood contain a non-negligible contribution from each signal.

This contribution of the signal to the residual noise energy increases the penalty, lowering the correlation coefficient. For this reason, triggers containing time-overlapping transients are penalised when applying post-production cuts, as it can be seen in detection efficiencies reported in Tables 4.2, 4.3 and 4.4 and in Figures 4.1, 4.4 and 4.5.

These results suggest that, to produce an optimal analysis of time-overlapping transient signals, a future development of cWB should allow for the estimation of multiple likelihoods. If a time-frequency (TF) map suggests the presence of two time-overlapping transient signals, then the information about the way to analyse it can be obtained firstly, by analysing the data with a likelihood following the primary signal. If the null then contains an indication for another signal, then it could be used to select the pixels related to this signal and try to maximise the likelihood with respect to them only. It is important to remark that the TF representation is able to
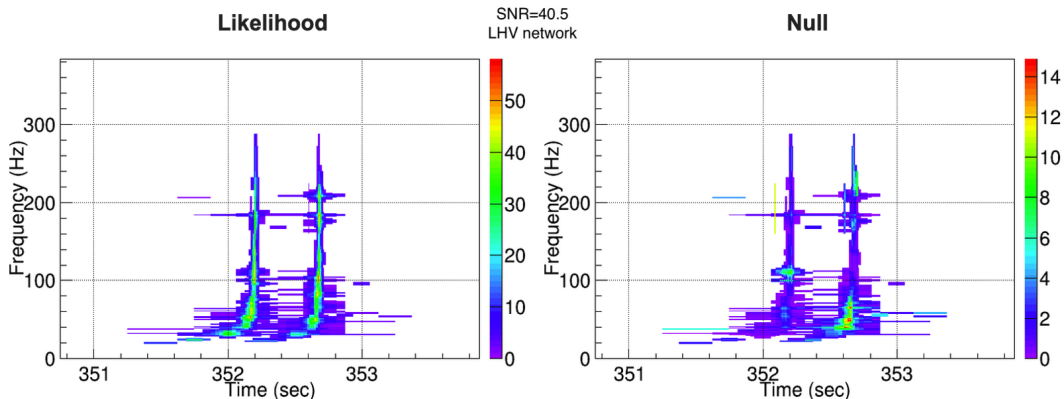
Figure 5.6: A spectrogram of likelihood and null energy for two time-overlapping transient signals. The likelihood has been maximised with respect to the primary signal, so a relevant fraction of the energy associated with the secondary one remains in the null. The data is the same as for the signals in Figure 5.2

.

disentangle, by itself, the two time-overlapping signals only if these cover different TF pixels. In this case, the separate maximisation of two different likelihoods, via two different sets of pixels, would give the signal reconstruction as optimally as it is currently for single signal triggers. It should be noted that in the unlikely case in which the two signals come from almost the same source location the two likelihoods would be almost the same.

If a pixel has contributions from both signals, then the TF separation is not possible. In that case there is still the possibility to exploit the likelihood-null energy distribution for the involved overlapping pixels, if the signals come from different sky locations. When the two signals cover the same pixel the likelihood-null disentangling would be non-optimal as some fraction of the secondary signal will fall into the likelihood of the primary, as shown in Figure 5.6. This implies that we may not be able to fully recover the secondary signal from the null. If the signals come from almost the same sky position, then there is no way to disentangle them through cWB's unmodelled processes. This is true in those TF pixels covered by both signals; here the likelihood-null approach fails as well because in that case the null is also almost the same for both signals.

A previous study performed as an unmodelled search for transients in the first two observing runs of the LIGO-Virgo Collaboration [290]. In this search they identified a case in which one signal, GW151012, showed a chirp-like feature 200ms after the identified signal merger. They matched this signal to a catalogue of sub-threshold triggers and found that it is a possible overlap with another CBC transient signal. However, due to the search sensitivity of the detectors at this time and the significance of that sub-threshold trigger, it is likely that this chirp-like situation is purely noise fluctuations.

5.3 Creating bespoke overlap identification methods

While Sections 5.2.1 and 5.2.2 have shown that it may be possible to adapt current searches to identify which triggers contain more than one signal, it is possible that the optimal method is to produce an independent check upon triggers to find the number of signals. For this we trained a Neural Network to identify triggers that contain multiple CBC signals.

5.3.1 Methods

5.3.1.1 Convolutional Neural Network

Convolutional Neural Networks (CNNs) are a machine learning technique that allow for the categorising of previously unseen data based on networks trained on large sets of training data. In this way the analysis performed by the network is very rapid as the computationally expensive portion is completed beforehand. CNNs are neural networks that can extract features from data using layers of filters [291]. Each layer in the network is comprised of multiple neurons. These neurons take inputs for each example in the training data, in this case each generated data segment. By comparing each training example to the label provided with it the network can obtain a weight for each example. The output of each neuron is given by Equation 5.1.

$$O = \sigma \left(\sum_{i=0}^{n} w_i x_i + b \right) \tag{5.1}$$

where x_i is the ith training example associated with the weight w_i. The neuron itself has a bias, b, applied to it. σ is an activation function that allows for the variation of the output. For the networks in this study we used a combination of "ReLU" [4] and the "softmax" functions. These are given by Equations 5.2 and 5.3 respectively.

$$\sigma_r(z) \equiv \max(0, z) \tag{5.2}$$

$$\sigma_s(z) \equiv \frac{\exp(z_i)}{\sum_{j=1} \exp(z_j)} \tag{5.3}$$

The ReLU function allows for quick output generation between layers, while the softmax function is normalised in order to produce a value between zero and one.

CNNs are constructed from several layers of multiple neurons. The outputs of each layer can be used as inputs for subsequent layers. During training, the input data is shuffled and given to the network. The network uses this to train the weights and biases of each neuron. Typically the data is shuffled multiple times and applied to the network repeatedly in order to tune the parameters to the data. Secondary,

---

[4]Or "rectifier"

	Layer								
Parameter (Option)	1	2	3	4	5	6	7	8	9
Type	C	C	C	C	C	C	H	H	H
No. Neurons	8	8	16	16	32	32	64	64	2
Filter size	64	32	32	16	16	16	-	-	-
Max pool size	-	8	-	6	-	4	-	-	-
Drop out	0	0	0	0	0	0	0.5	0.5	0
Activation function	R	R	R	R	R	R	R	R	S

Table 5.1: Table representing the network adapted from Gabbard et al, 2018 [295]. The network is constructed from six convolutional layers (C) and three hidden layers (H). The first eight layers use a ReLU activation function (R), and the final layer uses a Softmax function (S).

validation, training examples can then be used to test that the network is working correctly.

Other groups have shown that CNNs can be used to identify glitches in GW data [120, 292, 293], to find signals [294, 295] and to perform parameter estimation of CBC signals [222, 223]. We used the network described in Gabbard et al, 2018 [295]. This network was used to prove that CBC signals can be identified in GW strain data. The network was shown to correctly identify BBH signals, in the aligned spinning case only, to a similar sensitivity as the matched filter approach. We constructed our implementation of Gabbard et al's network using the `TensorFlow` [23] package in `Python`. The structure of the network is shown in Table 5.1.

The network structure is comprised of nine layers. The first six layers are convolutional layers, with the final three being hidden layers. The first nine layers use the ReLU activation function, producing values between $[-1, \infty]$. The final, hidden, layer uses the Softmax function to produce a single number output, between zero and one, with zero representing a confident classification of single signal and one being classified as confidently time-overlapping. The majority of signals will have values between the two, indicating how confident the network is that the data segment contains more than one signal.

Prior to layers two, five, and six we perform pooling in order to reduce the dimensions of the data. This process filters the results of multiple neurons, here two, to one neuron in the subsequent layer. In this network we use "Max pooling", in which the new neuron's input is the maximum of the previous neurons [291].

To reduce over-fitting the network utilises drop out after layers seven and eight. This process removes neurons from the result, at random, here with a 50% probability of the neuron being accepted or rejected. This means that not all nodes are trained on the entirety of the data and therefore reduces over fitting.

5.3.1.2 Training data generation

We generated data segments containing sections of simulated interferometer data. This was done for a two detector network of aLIGO design sensitivity detectors in the positions of LIGO: Hanford and LIGO: Livingston. Each data segment contained 16 seconds of Gaussian noise, coloured to the aLIGO design sensitivity, sampled at 1024 Hz. This is a high enough frequency information to account for most BBH signals, due to their relatively low merger frequencies.

Each data segment contained either one or two time-overlapping transient CBC signals. For simplicity we constrained all signals to be BBH inspirals. The parameters of such signals were set to be uniform for both intrinsic and extrinsic parameters. This is required to train the network on all possible signal cases. The only parameters which were drawn specifically were the merger times. These followed the convention set in previous studies in this thesis that Signal B merges before Signal A. Here the merger time separations were drawn from the distribution $U(0, 2)$ seconds[5].

The masses of the primary component in each signal was drawn in the range $U(10, 70)\text{M}_\odot$, with the mass ratio constrained to the range $U(0.1, 1)$[6]. This range kept both signals short enough that their visible duration, from 20 Hz to merger and ringdown, could easily be contained in the 16 second segments. The signals were generated using the waveform approximant `IMRPhenomTPHM` to provide time domain strain estimations of the waveform including the physics of precession, which is important for time-overlapping signal studies[7], and higher modes [144].

For this study it was assumed that the 16 second data segment is found from a trigger produced by another search pipeline. We therefore apply a null hypothesis that the data contains both noise and a single signal. The alternative hypothesis is then that there is also a second signal in the data. Equation 1.8 is therefore modified to:

$$H_0 : d(t) = n(t) + h_A(t) \tag{5.4}$$

$$H_1 : d(t) = n(t) + h_A(t) + h_B(t) \tag{5.5}$$

Each time-series data set, containing either individual signal or a pair of signals, was normalised such that the strain varied between values of ± 1, however the data was not whitened. For each data set we created separate strains for a two detector network, LIGO: Hanford and LIGO: Livingston, the injected signals were projected into the detector frames according to their drawn sky location, and the noise representations were generated for each detector based on the aLIGO design

---

[5]This ensures that we cover signals that might be missed due to the `PyCBC` clustering window, but we assume that most signals with $|\Delta t_c| > 2$ would be found by separate triggers

[6]This mass ratio distribution is varied slightly, depending on primary component mass, such that no signal has a component with mass less than 8 $\text{M}_\odot$

[7]See Section 3.3.1

PSD [261].

We produced 100,000 individual signal pairings. This meant we could produce 200,000 individual signal data cases, each with different coloured-Gaussian noise realisations. We produced two overlapping time-series for each signal pairing by adding the cases to two different noise realisations, this allows for equal cases of individual signal cases and time-overlapping cases. This totalled 400,000 training cases for the network, with a further 40,000 apiece for testing and validation. This data was used to train and test the CNN described above.

5.3.2   Results

Figure 5.7 shows the network's overlap classification as a function of each signals SNRs in the data segment[8]. Here the single signal sets are constrained to the horizontal and vertical axis at zero, as the second signal has an SNR of zero. It is clear that the majority of these points have a light green colour, indicating that the network is confident that these signals do not contain a secondary transient signal.

Data segments that contain two signals are located off the axis. These, largely show complete, or near complete, confidence as time-overlapping transients. However, there are a few, particularly at low SNR that are less confidently identified by the network. To examine which pairings are not identified by our network we must set a threshold below which we accept that a data segment is a single signal and above which the network would refer the segment for further investigation.

It is clear from the results of the time-overlapping signals in Figure 5.7 that the majority of signals at low SNR are not correctly identified by the network. In the majority of current transient GW analysis, signals with a network SNR below 12 are not considered due to the difficult in detecting them [77]. Therefore, for the remainder of this investigation, we added a cut in network SNR to remove signals that were not identified due to poor SNR. In applying this cut we rejected approximately 7400 of data segments. The equivalent of Figure 5.7 for this investigation is shown in Figure 5.8, but focused on the relevant region of $12 \leq \text{SNR} \leq 25$.

5.3.2.1   Setting a threshold for time-overlapping signal identification

We estimated the number of false identifications in the network as a function of the acceptance threshold. That is, the point in the network's binary output at which we claim identification of transient signal overlap. This can be seen in Figure 5.9.

The green line in Figure 5.9 shows the two σ confidence level, at which we claim confident time-overlap identification. At this level, an acceptance threshold of 0.288 in the network output, we correctly identify 84.9% of single signal segments and 95.4% of time-overlapping segments. At this point the number of misidentifications

---

[8]The SNRs are estimated as single signals in the data segment. These values are the SNR if they were non-time-overlapping transients.
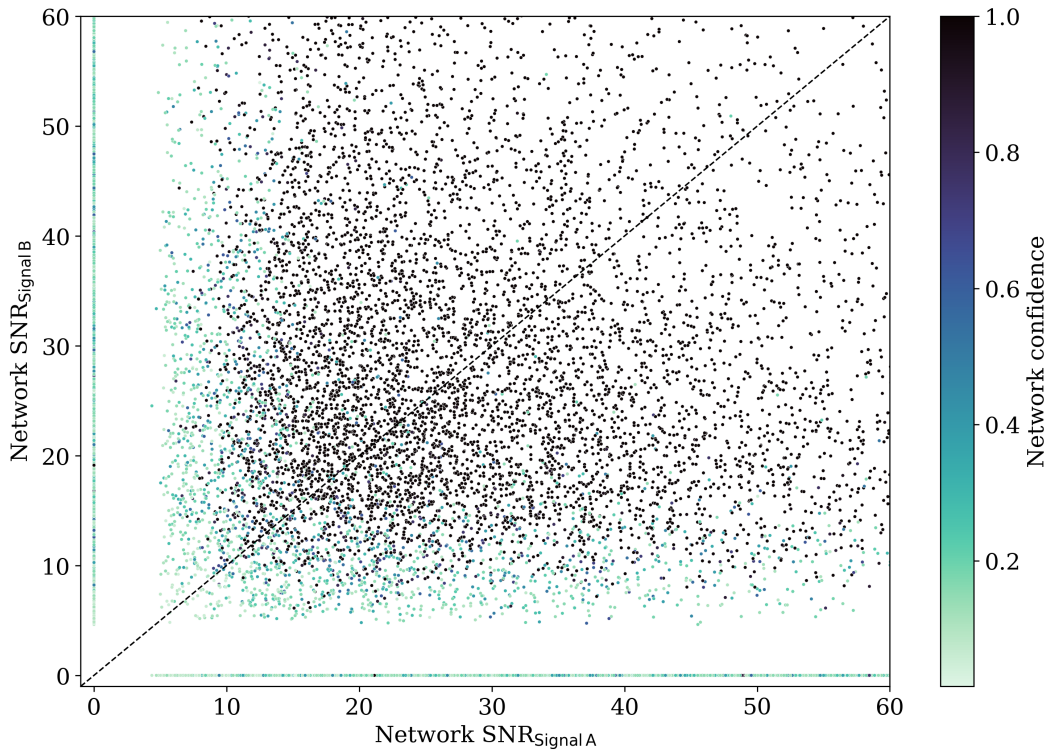
Figure 5.7: A scatter plot showing the SNR of each signal in a pairing given to the network. Where the data segments contained only a single signal the other signal has been given an SNR of zero. The colour of each point represents the classification of the pairing by the network, with zero being confidently single signal and one being confidently time-overlapping.

is not equal either way. However, it is advantageous to misidentify in such a way that you find more single signal segments as time-overlapping. Identified time-overlapping segments would most likely be subjected to further analysis, such as bespoke parameter estimation methods [281]. Misidentified single signal segments would then be filtered out at a later stage. However, misidentified time-overlapping segments would likely be only considered by standard parameter estimation techniques and then subject to the biases of such processes, see Chapter 3.

We set this threshold at the 2σ level as higher confidence levels, at lower acceptance thresholds, lead to a rapid increase in the number of misidentified single signal segments. With the rate of signals likely at the sensitivity at which time-overlapping signal are likely to occur, see Chapter 2, this would leave far too many signals to perform further analysis on.

Figure 5.10 shows the percentage of data segments incorrectly identified by the network as a function of the SNR of the injected signals. This is shown in the region $12 \leq \text{SNR} \leq 35$, beyond which the percentage of misidentified signals no longer varies as signals are then correctly identified in both cases. As expected, low SNR time-overlapping transients, and high SNR single signal transients, are the most
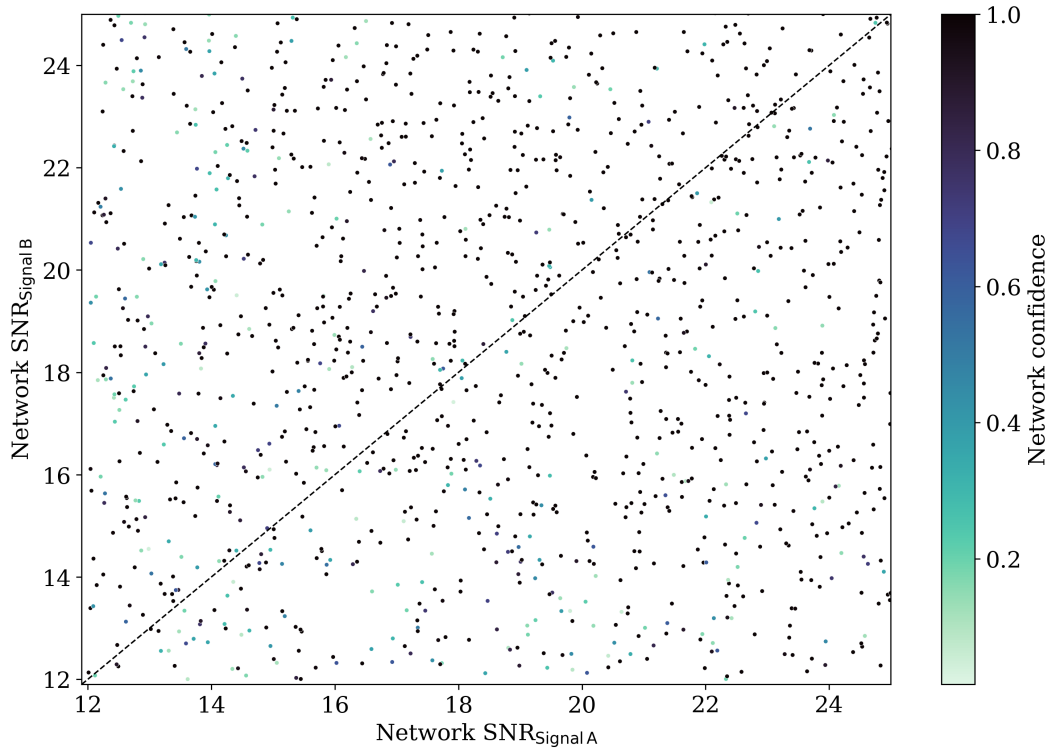
Figure 5.8: A scatter plot showing the SNR of each signal in a pairing given to the network. Where the data segments contained only a single signal the other signal has been given an SNR of zero. The colour of each point represents the classification of the pairing by the network, with zero being confidently single signal and one being confidently time-overlapping. This plot shows the same data as in Figure 5.7, but focused on the region $12 \leq \text{SNR} \leq 25$.

.

likely to be misidentified as the network is likely learning that data segments with higher power are more likely to contain multiple signals.

5.3.2.2 Misidentified single signal segments

As stated above, approximately 15.1% of single signal segments in this network were misidentified as time-overlapping. We performed some simple investigations into these signals to attempt to identify the features of these signals. The majority of the parameters of signals that were correctly identified as single signal and those that were incorrectly identified as time-overlapping, had near-indistinguishable distributions. However, there is an indication that cases of misidentified single signal cases occur more readily in higher SNR signals. This is most likely due to the network identifying the power in the time-series and weighting the high power cases in favour of time-overlaps. Time-overlapping data segments will most likely contain more power. This can be seen in Figure 5.11.

It is clear from both plots in Figure 5.11 that the network SNRs in these segments are not drawn from the same distribution. A Kolmogorov–Smirnov test[296], hence
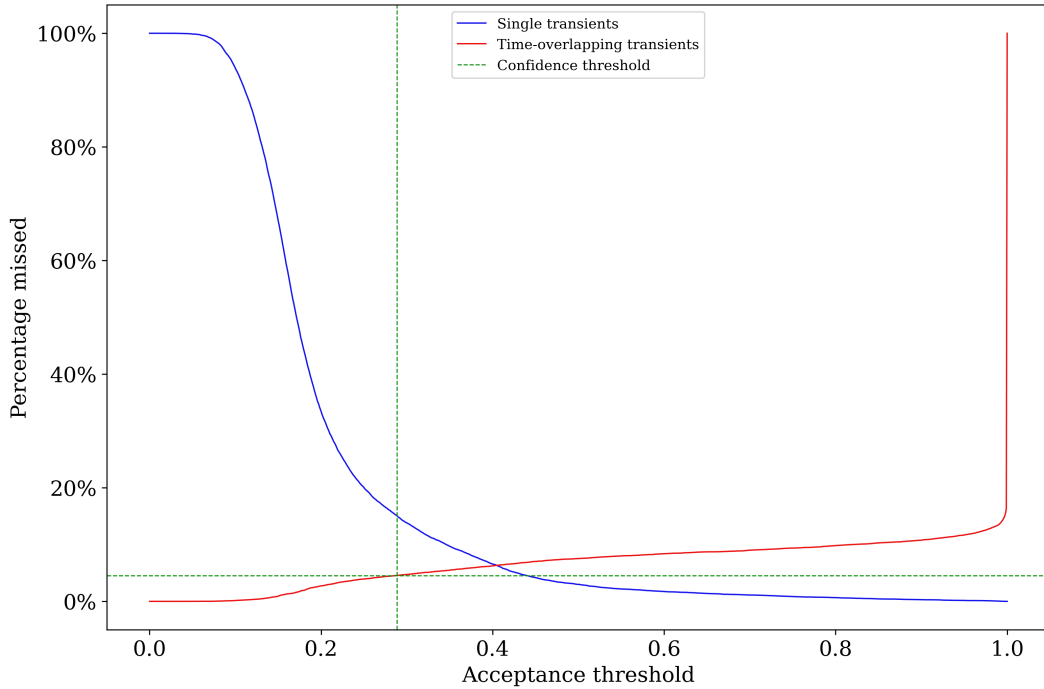
Figure 5.9: Percentage of segments misidentified as a function of acceptance threshold. The blue line shows time-overlapping signal segments misidentified as single signals, and the red line shows single signal segments identified as time-overlapping. The cross composed of the two green dashed lines shows the threshold at which we have a 2σ confidence that we are correctly identifying the segment as time-overlapping.

KS, proves that they are not to a confidence level of $p = 3.95 \times 10^{-9}$, with the correctly identified signals matching the distribution of the injections. We note here that the acceptance threshold was calculated and applied to the data to distinguish the identified/misidentified signals after the SNR threshold was applied. Due to this order of the applications the distributions in the two plots of Figure 5.11 are not identical with a cut at an SNR of 12 in the second plot.

There is some indication, with a KS test accepted above a threshold of 2σ, that the misidentified single signal segments tend towards shorter, higher mass signals. We expect that this is an artefact of the segments containing time-overlapping pairs having a higher total power, as the combination of the two signals. As such the network may identify higher SNR single signals as more likely to be time-overlapping.

5.3.2.3 Misidentified time-overlapping signal segments

Due to our acceptance threshold, we only misidentify approximately 4.55% of segments containing time-overlapping signals. The parameters of the signals in the segments misidentified as containing only one signal do not noticeably differ from those correctly identified as time-overlapping across chirp mass, relative merger time, or the separation of the signals in sky location. However, unlike our findings in Chap-
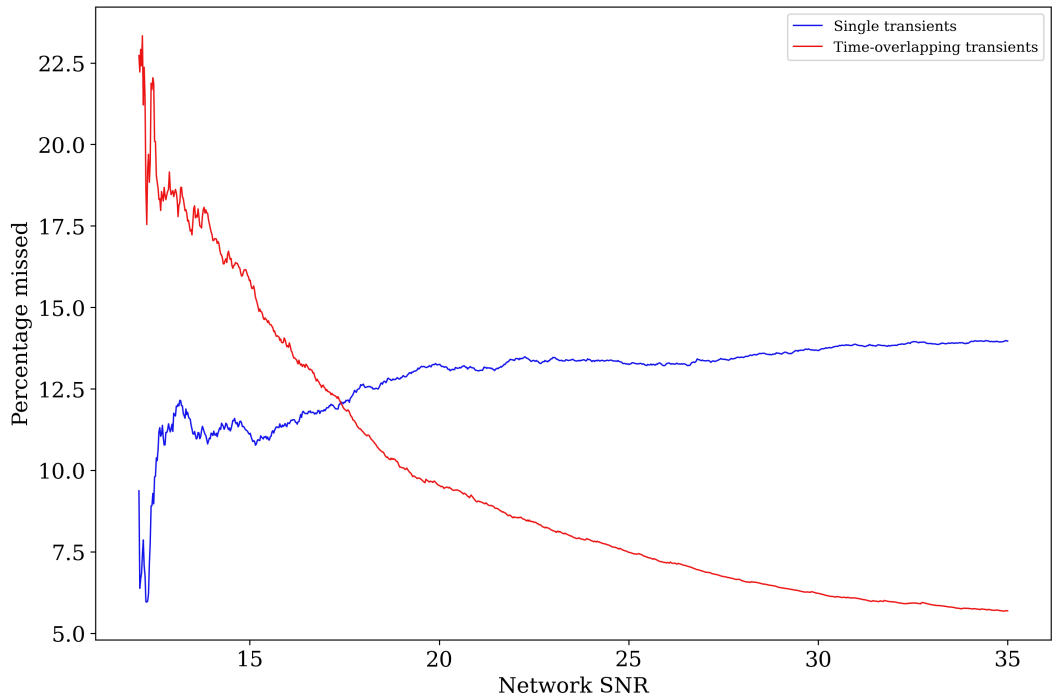
Figure 5.10: Percentage of segments misidentified at this acceptance threshold as a function of the SNR of the injected signal. For time-overlapping transients the shown SNR is that of Signal A, the later merging signal.
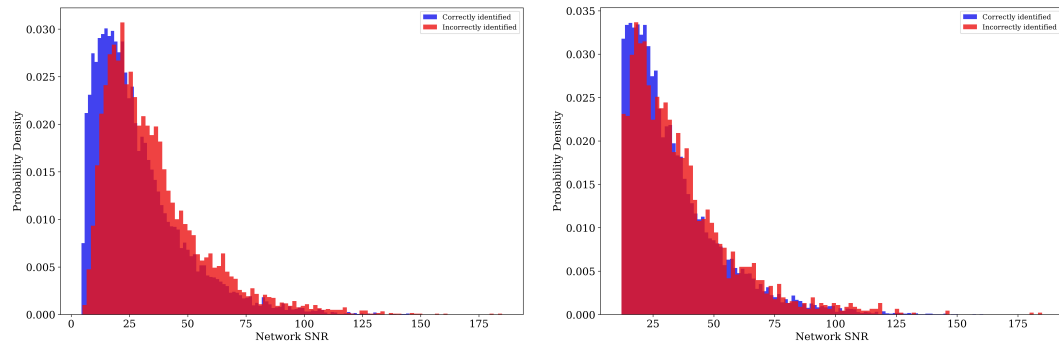
Figure 5.11: Plots of the distributions of network SNR in correctly identified (blue) and incorrectly identified (red) single signal data segments. The left plot shows the distributions of all signals, including those with network SNR less than 12, the right plot shows the distributions with the SNR cut.

ter 4, there is no significant indication that unequal ratios of SNRs in the signal pairings lead to misidentification of the signals. Though this may be obscured by the relatively small sample of such signals, and the high number of missed low SNR signals. Figure 5.12 shows the distribution of the SNRs in the pairings for both correctly and incorrectly identified segments.

Figure 5.13 shows the distribution, in network SNR, of correctly and incorrectly identified time-overlapping signal segments. Is is apparent from this that signal pairings containing signals of a low network SNR are those most likely to be misidentified,
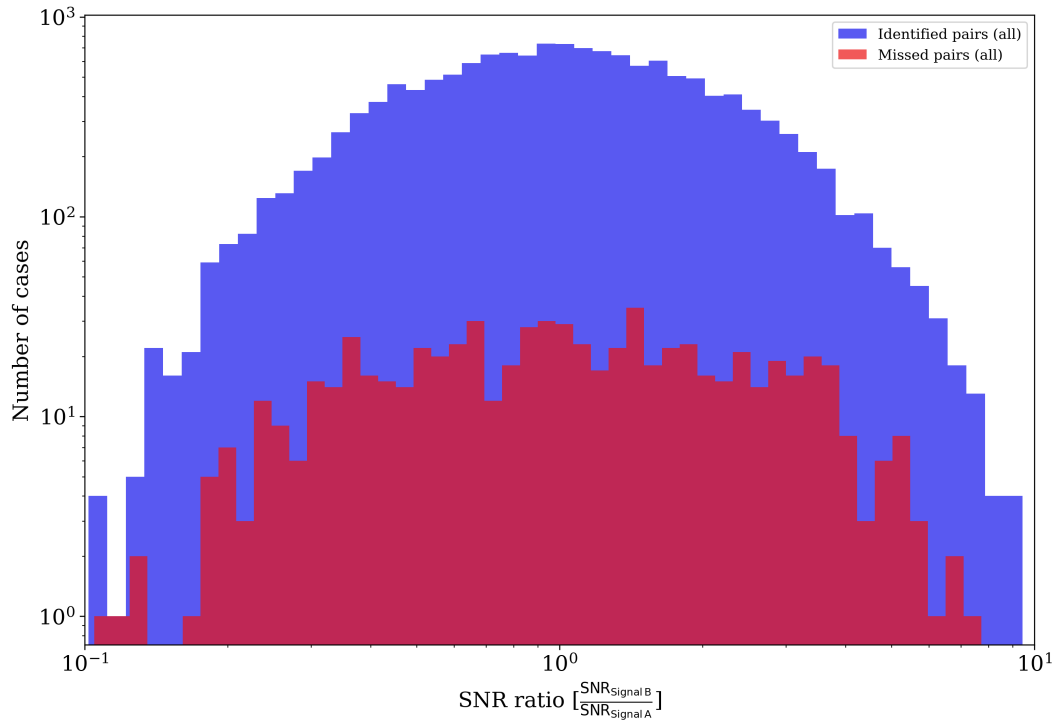
Figure 5.12: Histograms showing the distribution of the ratio of network SNRs in the signal pairings, correctly identified (blue) and misidentified (red).
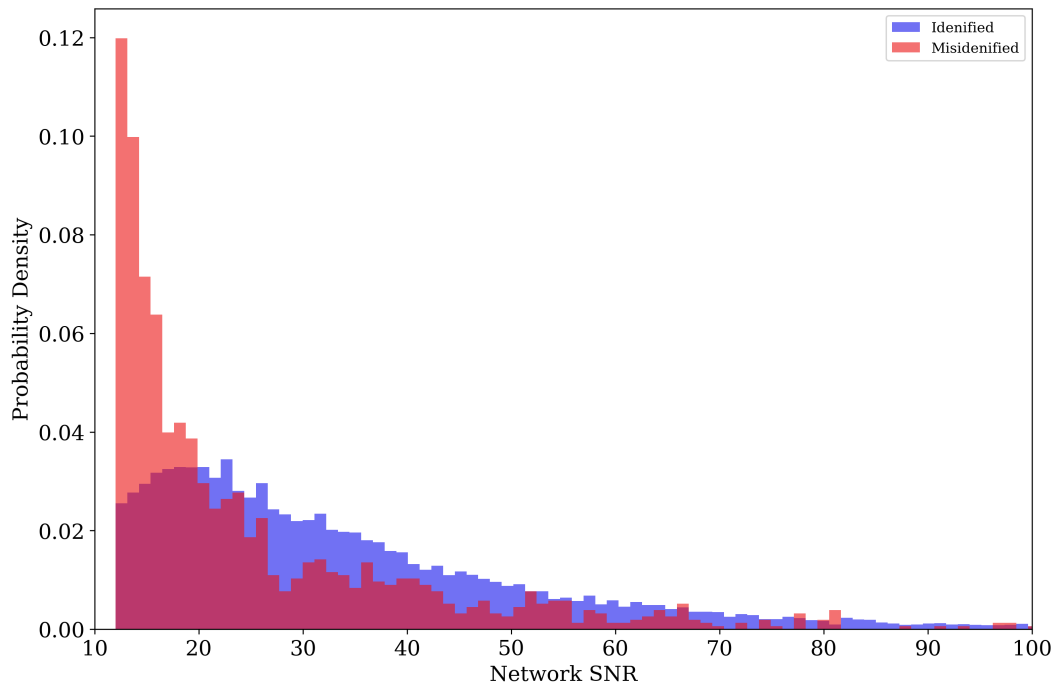
Figure 5.13: Histograms showing the distribution of network SNRs in the signal pairings, correctly identified (blue) and misidentified (red).

the reverse for the case of misidentification of single signals in Section 5.3.2.2.

   We did find a relation in the relative merger time between signals in the misiden-
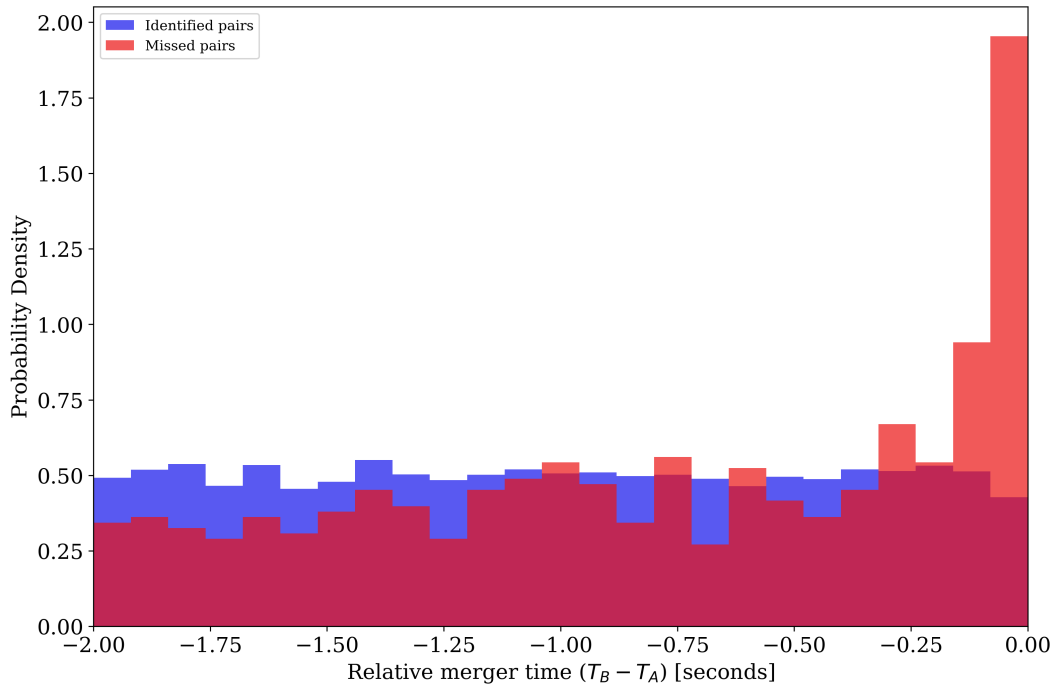
Figure 5.14: Histograms showing the distribution of merger time separation between the signals in time-overlapping data segments, correctly identified (blue) and misidentified (red).

tified time-overlapping cases. As with previous studies, signals that merge closer together in time are more likely to be misidentified. This is shown in Figure 5.14. The distributions differed by statistically significant amounts both in analysis of signals above a network SNR of 12 and including signals below that threshold.

Half of the time-overlapping segments are contained the same combination of signals with different noise realisations. Of the segments that differ only by noise realisation only 8.7% were found in one noise realisation but not the other. These signals have a fairly even ratio of SNRs across the pairing and are typically relatively low in SNR.

5.3.3 Discussion of the effectiveness of Neural Networks for identification

The resulting network from this training data is clearly able to distinguish the vast majority of segments containing single signals from those containing time-overlapping signals. The segments that cause problems for the network are those containing signals that are low in SNR and those that merge very closely in time. These signals are also those that would also cause a problem for the initial searches, see Chapter 4, and are those that would potentially go unnoticed in standard parameter estimation techniques, see Chapter 3.

In order to correctly train the network we relied upon signals with parameters

drawn from uniform distributions. It would be interesting to test this network upon data drawn from the astrophysical distributions used in Chapter 4. This would allow for a more direct comparison between the time-overlapping CBC signals that cause triggers in standard search pipelines, and those that would be identifiable as time-overlapping in the CNN.

We note that such a network is not intended as a method of separating such signals, although we will comment on using CNNs for this purpose in Section 5.3.3.1. The purpose of this network is purely to identify single signal data segments from those containing multiple signals, with no comments made on the parameters of those signals. It is likely that training the network on larger sets of data would allow for a more efficient identification of these signals and a reduction in the number of false positives.

5.3.3.1 Signal Separation

Several methods of separating time-overlapping CBCs have been proposed. These include:

- *Global-fit*[9]: This method proposes simultaneously fitting every parameter for all signals in the data [281, 297–300]. As a single BBH signal has at least 14 independent parameters to sample over, current parameter estimation techniques would struggle with doubling the parameters for a secondary signal. In the case where further signals are present the parameter spaces would be very large.

- *Local-fit*: Here an algorithm separately fits each signal in the data independently, correcting for biases using a Fisher-matrix formalism as presented in [281]. The original proposal suggests using the findings of such a method as a basis for a later *global-fit* approach.

- *Hierarchical Subtraction*: This method proposes initially analysing a single signal in the overlap. This signal would then be subtracted from the data. The residual would then be analysed to estimate the parameters of the second signal[300].

- *Machine Learning*: This is a machine learning approach to extracting the parameters of two time-overlapping CBC signals. The study outlined in Langendorff et al [301], trained a network on segments of data containing time-overlapping BBH signals and used the network to estimate the parameters of each signal.

Each of these methods performs better if more is known about the signals contained within the data. For example, a global-fit study of two time-overlapping BBH

---

[9]This method is sometimes called Joint Parameter Estimation.

signals requires sampling over 30 parameters.

To provide a reduction in the degrees of freedom that later studies need to sample over, we attempted to extract the merger times from each signal in our CNN study. This attempt, with a slightly modified network, showed some successes. However, it was only able to consistently identify the merger time of the louder signal, the returned time for the secondary signal was inaccurate for the vast majority of cases. However, with more work this method could provide more information about time-overlapping signals to improve the accuracy of parameter estimation.

5.4 Discussion

In this chapter we have shown that unmodelled searches can successfully recover both signals in the pairing, both as a single trigger when the mergers are close, and as separate triggers when far apart. cWB, when recovering signals via coherent sky location, is able to disentangle time-overlapping signals, so long as they cover different frequencies in the TF map. In the case in which the signals are in the same TF pixels, the secondary signal should be at least partially separable via the null energy map, if coming from a different sky location than the first. This should be another indicator of the presence of a secondary signal. It is possible that the second signal's sky location may be recoverable leading to further first guess parameters for multi-signal parameter estimation.

We have also shown that matched filter searches may be capable of identifying both signals, via careful examination of the SNR time-series of each templates match. Such an approach would potentially identify both signals, provided the two signals are not too close in merger time or too similar in closest template. Through such an approach it is possible to extract some simple guesses at the parameters of each signal for later, more detailed, multi-signal parameter estimation.

We have also shown that convolutional neural networks can be used to identify segments containing two signals from those containing only a single signal. While this method cannot currently identify the overlaps of low SNR signals, or for segments containing signals that merge close in time, it would be a useful tool for checking the results of any transient GW search in order to identify which signals would require further study.

Chapter 6

Direct limits for scalar field dark matter from a gravitational-wave interferometer

6.1 Introduction

Beyond their revolution in astrophysics, the detection of GWs has shed light on fundamental physics questions, and could lead to breakthroughs in the study of dark matter.

Beyond their applications to direct GW observations, ground-based interferometers can also be used in direct searches for dark matter [302]. Scalar field dark matter is a prominent theory that is being explored with precision instruments, such as atomic clocks and optical cavities [303–309].

Due to their excellent sensitivity at or beyond quantum limits, GW interferometers can be used directly for fundamental physics, without the mediation of GWs. Examples include a possible search for vacuum birefringence [310], and the search for signatures of quantum gravity [311–313]. Several ideas have been proposed as to how different candidates of dark matter can directly couple to GW detectors, ranging from scalar field dark matter [305, 314] to dark photon dark matter [315], and to clumpy dark matter coupling gravitationally or through an additional Yukawa force [316]. Upper limits for dark photon dark matter have already been set in a narrow mass-band using data from the first observational run (O1) of the Advanced LIGO GW detectors [317].

In this chapter, we present the first search for signals of scalar field dark matter in the data of a GW detector. Scalar field dark matter would cause oscillations of the fine structure constant and electron mass, which in turn drive oscillations of the

size and index of refraction of the beamsplitter in an interferometer, such as that of the GEO 600 detector. This would produce an oscillatory signal in a GW detector at a frequency set by the mass of the dark matter particle. With this we can set new upper limits on the parameters of scalar dark matter particles. Such a signal would not cause issues for the analysis of transient gravitational-wave signals as it would contribute purely to the noise in the detector.

6.2 Scalar dark matter theory

Models of weakly coupled low-mass ($\ll 1\,\mathrm{eV}$) scalar fields predict that such particles could be produced in the early Universe through a vacuum misalignment mechanism, and would manifest as a coherently oscillating field [303, 305],

$$\phi(t,\vec{r}) = \phi_0 \cos\left(\omega_\phi t - \vec{k}_\phi \cdot \vec{r}\right),\tag{6.1}$$

where $\omega_\phi = (m_\phi c^2)/\hbar$ is the angular Compton frequency, and $\vec{k}_\phi = (m_\phi \vec{v}_{\mathrm{obs}})/\hbar$ is the wave vector, with m_ϕ the mass of the field and $\vec{v}_{\mathrm{obs}}$ the velocity relative to the observer. The amplitude of the field can be set as $\phi_0 = (\hbar\sqrt{2\rho_{\mathrm{local}}})/(m_\phi c)$, under the assumption that this scalar field constitutes the local dark matter (DM) density ρ_{local} [318].

Moreover, these models predict such DM would be trapped and virialised in gravitational potentials, leading to a Maxwell-Boltzmann-like distribution of velocities $\vec{v}_{\mathrm{obs}}$ relative to an observer. As non-zero velocities produce a Doppler-shift of the observed DM field frequency, this virialisation results in the DM field having a finite coherence time or, equivalently, a spread in the observed frequency [315, 319]. The observed frequency, or linewidth, is determined by the virial velocity, which is given by the depth of the gravitational potential. For DM trapped in the galactic gravity potential, as in the standard galactic DM halo model, the expected linewidth is $\Delta\omega_{\mathrm{obs}}/\omega_{\mathrm{obs}} \sim 10^{-6}$. This would correspond to a coherence time for a signal of $\tau = 10^6/\omega$, a DM signal at 1000 Hz would have a coherence time of 1000 seconds. Certain kinds of scalar particles, such as Relaxion DM [320, 321], may also form gravitationally bound objects and be captured in the gravitational potential of the Earth or Sun, producing a local DM overdensity where the field has a much narrower linewidth [322]. The observed DM frequency is further modulated by the motion of the Earth with respect to the local DM's centre of mass, changing the frequency of the observed DM field.

$$\omega_{\mathrm{obs}} = \omega_\phi + \frac{m_\phi \vec{v}_{\mathrm{obs}}^2}{2\hbar}.\tag{6.2}$$

Scalar field DM could couple to the fields of the Standard Model (SM) in numerous ways. Such a coupling, sometimes called a "portal", is modelled by the addition of a parameterised interaction term to the SM Lagrangian [323, 324]. In

this study, we consider linear interaction terms with the electron rest mass m_e and the electromagnetic field tensor $F_{\mu\nu}$:

$$\mathcal{L}_{\text{int}} \supset \frac{\phi}{\Lambda_\gamma} \frac{F_{\mu\nu}F^{\mu\nu}}{4} - \frac{\phi}{\Lambda_e} m_e \bar{\psi}_e \psi_e, \tag{6.3}$$

where ψ_e, $\bar{\psi}_e$ are the SM electron field and its Dirac conjugate, and Λ_γ, Λ_e parameterise the coupling. Specific types of scalar DM, such as the hypothetical Moduli and Dilaton fields motivated by string theory, have couplings to the Quantum Chromodynamics (QCD) part of the SM as well [325–327].

The addition of the terms in Eq. 6.3 to the SM Lagrangian entails changes of the fine structure constant α and the electron rest mass m_e [303, 304].

$$\frac{\delta\alpha}{\alpha} = \frac{\phi}{\Lambda_\gamma}, \qquad \frac{\delta m_e}{m_e} = \frac{\phi}{\Lambda_e}, \tag{6.4}$$

to first order.

The apparent variation of these fundamental constants in turn changes the lattice spacing and electronic modes of a solid, driving changes of its size l and refractive index n:

$$\frac{\delta l}{l} = -\left(\frac{\delta\alpha}{\alpha} + \frac{\delta m_e}{m_e}\right), \tag{6.5}$$

$$\frac{\delta n}{n} = -5 \cdot 10^{-3} \left(2\frac{\delta\alpha}{\alpha} + \frac{\delta m_e}{m_e}\right), \tag{6.6}$$

where δx denotes a change of the parameter x: $x \to x + \delta x$. Equations 6.5, 6.6 hold in the adiabatic limit, which applies for a solid with a mechanical resonance frequency much higher than ω_ϕ (the driving frequency) [314, 326, 328].

GW interferometers, by design, have exquisite sensitivity to differential changes in the optical path length of their arms. The thin cylindrical beamsplitter in such an instrument interacts asymmetrically with light from the two arms, as the front surface has a 50% reflectivity and the back surface has an anti-reflective coating. Therefore, a change in the size (δl) and index of refraction (δn) of the beamsplitter affects the two arms differently, and produces an effective difference in the optical path lengths of the arms $L_{x,y}$[1]

$$\delta(L_x - L_y) \approx \sqrt{2}\left[\left(n - \frac{1}{2}\right)\delta l + l\delta n\right], \tag{6.7}$$

The mirrors in the arms of GW interferometers would also undergo changes in their size and index of refraction, but as the wavelength of the DM field is much greater than the distance between the arm mirrors ($\lambda_\phi/L \gtrsim 10^3$) for all frequencies

---

[1]This expression includes a correction to Eq. 17 in [314]. In addition, a geometrical correction ($\approx 6.4\%$) from Snell's law is applied to Equations 6.7 and 6.8 for calculating the results below.

of interest here, and because the mirrors have roughly the same thickness, the effect is almost equal in both arms and thus does not produce a dominant signal.

The interferometer most sensitive to potential DM signals is the GEO 600 detector, as it has the highest sensitivity to optical phase differences between the two arms. The squeezed vacuum states of light currently employed in this instrument allow for a world-record quantum noise reduction of 6 dB [329]. Although other GW detectors, such as aLIGO, are more sensitive to GWs through the use of Fabry-Pérot cavities in the arms, these do not boost their sensitivity to signals induced at the beamsplitter, so their relative sensitivity to scalar DM is lower [314].

From Equations 6.1–6.7 it follows that an oscillating scalar dark matter field is expected to produce a Doppler-shifted and -broadened signal in the GEO 600 interferometer of the form

$$\delta(L_x - L_y) \approx \left(\frac{1}{\Lambda_\gamma} + \frac{1}{\Lambda_e} \right) \left(\frac{n\, l\, \hbar\, \sqrt{2\, \rho_{\text{local}}}}{m_\phi\, c} \right) \cos\left(\omega_{\text{obs}} t \right), \qquad (6.8)$$

where we have neglected the contribution of the refractive index changes to the signal, as it is three orders of magnitude smaller than that of the size changes. Given this prediction, we can examine the data from the interferometer for the presence of such signals, and if none are found, place upper limits on the mass and coupling constants of scalar field DM.

6.3 Logarithmic power spectral density estimation

6.3.1 Standard PSD estimation methods

As mentioned in Section 1.3.2 most analysis of gravitational wave interferometer data relies upon estimations of the noise floor. This is done through PSD estimation. In order to correctly estimate a PSD of the GEO 600 detector we experimented with using standard PSD estimation techniques, with Welch averaging in the `GWpy` software package [12]. In doing so we found the correct parameter to reduce spectral leakage in the resulting spectrum. This is a Kaiser window with the tuneable parameter $\beta = 30$. The effect of incorrect windowing on GEO 600 data can be seen in Figure 6.1

6.3.2 Logarithmic power spectral density method

As shown in Section 6.2 the scalar DM signal has a linewidth of approximately 10^{-6} of its frequency. Unfortunately, linear PSD estimations would only provide a single frequency bin at which the width would be optimal for the search, $\Delta f = 1/T_{\text{segment}}$. An optimal analysis could be performed by taking standard PSD estimations with different data segment lengths for each required frequency bin. Unfortunately, this is not available in most standard Fourier transform software packages such as `GWpy`
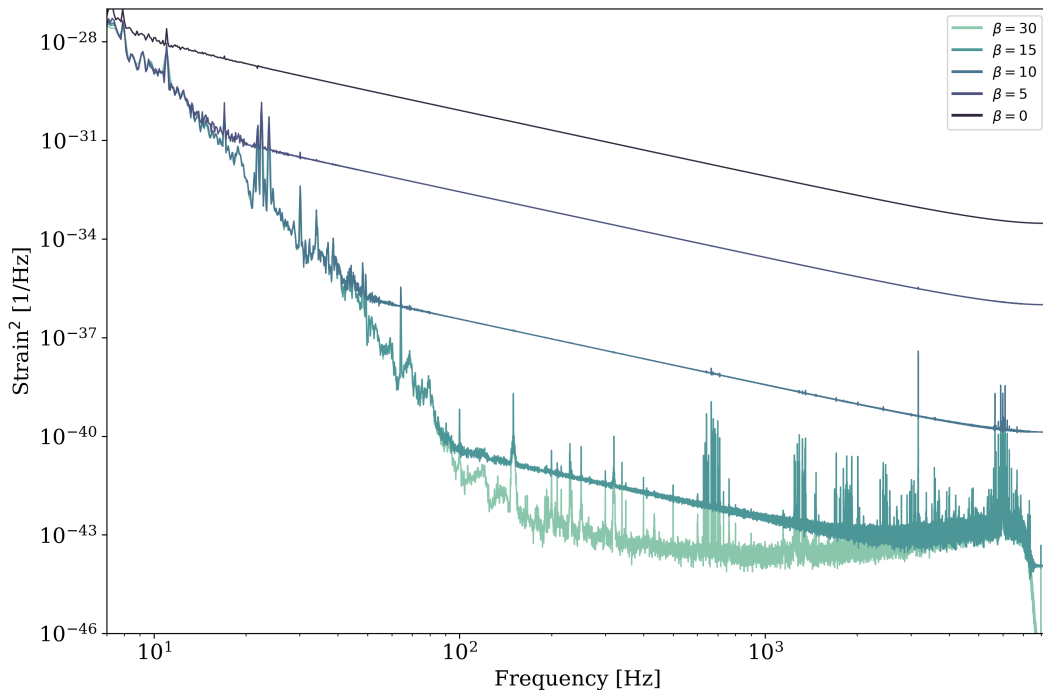
Figure 6.1: Power spectral density estimations, made with `GWpy`, on 100 seconds of GEO 600 data using Kaiser windows with different β parameter values.

and `NumPy`. Adaptions could be made, but such a process would result in excess frequency estimations being made and discarded, drastically increasing computational wastage.

Instead of standard FFT estimations, we utilised and adapted the Logarithmic frequency axis Power Spectral Density (LPSD) method [330, 331]. This method calculates bin placements across a desired frequency range, to provide logarithmically spaced frequency bins. This method is optimal as each bin can be specified to have a width of $\Delta\omega/\omega \approx 10^{-6}$. As such the maximal loss in a potential scalar dark matter signal would occur if the peak of the signal straddles the boundary of two bins.

The LPSD technique divides the full time-series of data into N_{seg} overlapping subsegments as described in Equation 6.9.

$$N_{\text{seg}} = \left\lceil \frac{T - \tau_{\text{coh}}(f)}{\tau_{\text{coh}}(f)(1 - \xi)} + 1 \right\rceil \tag{6.9}$$

The subsegments, $S_f^k(t)$, have a length equal to the expected coherence time $\tau_{\text{coh}}(f)$ of the DM signal at a frequency f, where $\xi \in [0, 1]$ is the fractional overlap of the subsegments, and $k \in [1, N_{\text{seg}}]$. As the expected coherence time and linewidth are frequency dependent, this subdivision is unique for every frequency of interest. After subdivision, the subsegments were multiplied with a Kaiser window function $W_f(t)$ and subjected to a DFT at a single frequency:

$$a^k(f) = \sum_{t=0}^{T_{\mathrm{DFT}}} W_f(t)\, S_f^k(t)\, \mathrm{e}^{2\pi i f t}, \tag{6.10}$$

with $T_{\mathrm{DFT}} = \tau_{\mathrm{coh}}(f)$, where $a^k(f)$ is the complex spectral estimate at frequency f for the kth subsegment. The frequency bin placements are estimated between a provided minimum and maximum frequency. For this study we chose the sensitive region of the GEO 600 detector, 50 Hz to the Nyquist frequency, 8192 Hz. The number of frequency bins in the returned spectra is set by the desired linewidth, shown in Equation 6.11

$$N_f = \mathrm{int}\left[1 + \frac{\ln\left(\frac{f_{max}}{f_{min}}\right)}{\ln\left(1 + \frac{\Delta\omega}{\omega}\right)}\right] \tag{6.11}$$

The power spectrum is then obtained by averaging the absolute squared magnitudes $|a^k(f)|^2$ over the all subsegments.

$$P(f) = \frac{C}{N_{\mathrm{seg}}} \sum_{k=1}^{N_{\mathrm{seg}}} |a^k(f)|^2, \tag{6.12}$$

where C is a normalisation factor. The spectra used in the analysis were made with a bin width equal to the expected linewidth of galactic DM ($\Delta\omega/\omega \approx 10^{-6}$, see Derevianko [319]). The amplitude spectrum $A(f) = \sqrt{P(f)}$ created in this way comprises $\approx 5.1 \cdot 10^6$ frequency bins between 50 Hz and 8 kHz.

The benefit of the LPSD algorithm when searching for frequency dependent linewidth signals can be seen in Figures 6.2 and 6.3. Figure 6.3 shows the difference between the optimal bin width and the returned bin width for a linear PSD calculation, a linear PSD calculation which has been calculated using four different time-series chunks spaced linearly throughout the frequency space, and the optimised LPSD method. The benefit of the Welch averaging can be seen in Figure 6.2 where the variance in the LPSD is poor at low frequencies, but better than that of the linear PSD at high frequency.

6.3.2.1 Adaptations from the LPSD method

The LPSD algorithm had previously been coded in the C language by the original authors of the algorithm [332]. However, several changes to this code were required for the purpose of this study.

Firstly, the original algorithm introduces a parameter, K_{des}, which sets the desired minimum number of segments for the Welch averaging. If the bin resolution requires segments too long for this averaging then the resolution is shifted to favour the averaging. This process is best explained by Equation 18 of [330]. Our modifications forced all bin width calculations into the first region such that all bin widths
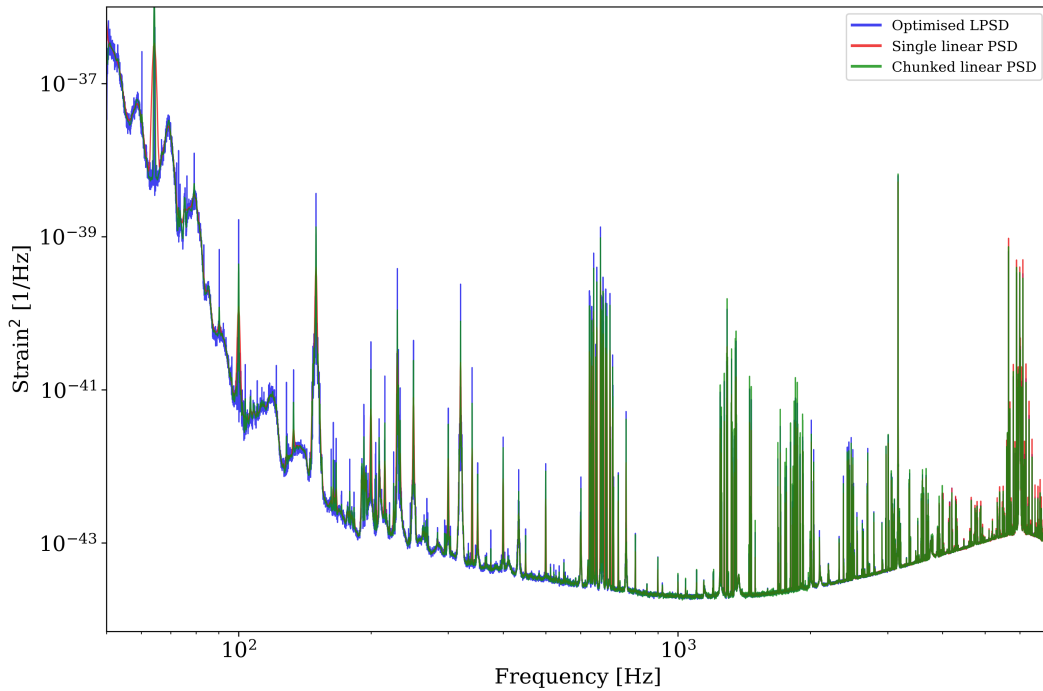
Figure 6.2: A comparison of three different PSD estimation methods for this search. The estimation here was made for a desired bin width of $\Delta\omega/\omega \approx 10^{-4}$ on 10,000 seconds of GEO 600 data. The optimised LPSD is the method used for our dark matter search. The single linear PSD is the typical method used in gravitational wave analyses, here the frequency bins are spaced linearly across the spectra. The chunked linear PSD is constructed of four linear PSD estimations, with narrower bins at higher frequencies set by manually changing the time segment lengths.

match our desired resolution, down-weighting the priority of the number of desired averages.

This is done in order to provide more equivalent PSD averaging across the spectra. However, the optimal search required a bypass of this adaptation in order to enforce the required bin width across the returned spectrum. The result of this adaptation is that the resulting high frequency bins have a much lower variance than those at low frequency.

The code itself was designed and tested to be run on shorter data sets, sampled at lower frequencies. The high sampling frequency of GEO 600, combined with the long segments necessary to estimate the bin width at lower frequencies, means that the code needed to be adapted considerably to run quickly and reliably. Checkpointing routines were added to provide returns in the case of failures and the code was parallelised in order to provide much faster calculation times.
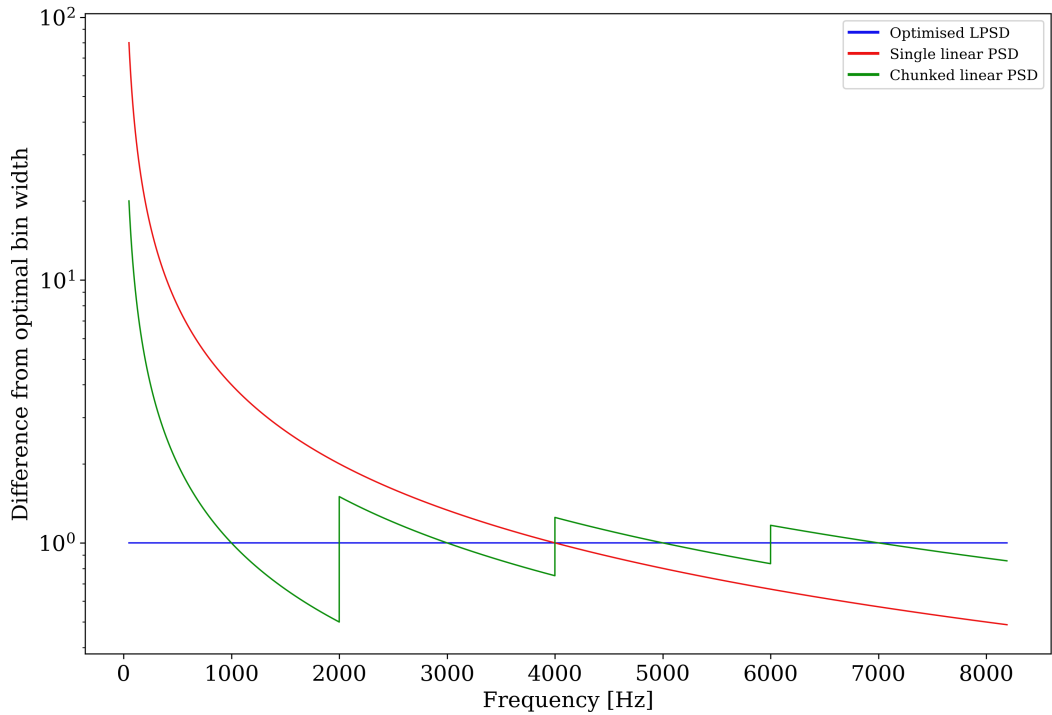
Figure 6.3: A comparison of the bin spacing in three different PSD estimation methods, with a value of one being the optimal bin width.

6.3.3 Data acquisition

The minimum frequency chosen for this investigation was 50 Hz[2], for the required bin width this meant a minimum segment length of 20,000 seconds of data at the sampling frequency of 16 kHz[3]. This, however, would only provide a single segment for several of the first frequency samples. The longer the segment the more averaging is possible. Therefore, eight data sets were analysed, four from 2016 and four from 2019. The shortest of these data sets was 69,000 seconds in length, giving four averages at 50 Hz, and the longest was 104,000 seconds, allowing a minimum of six averaged segments.

The chosen data sets were selected in order to provide coverage at approximately four month separations across the year to maximise potential Doppler shift in the signal. The Doppler shift is due to the Earth's orbit, about the sun, relative to the galactic halo. The limit of eight data sets was due to the number of available continuous data acquisitions and the computational cost of an LPSD estimation on them. One data set was later rejected due to data quality concerns.

Computation times for the spectra used in this work are ~ 10 s per frequency bin for each $\sim 10^5$ s data set, or $\sim 10^4$ CPU hours per spectrum. With the calculation time per frequency bin taking longer for smaller frequencies.

---

[2]The low frequency cut off for GEO 600

[3]16384 Hz, due to powers of two in the sampling.
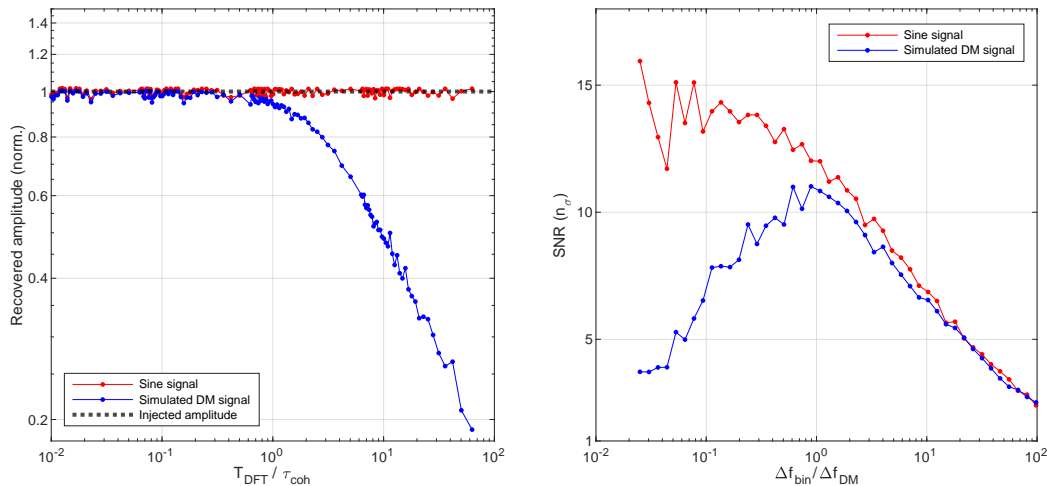
Figure 6.4: The spectral amplitude (left) and SNR (right) of a simulated DM signal (blue) and monochromatic sine wave (red) as recovered from spectra created using different frequency bin widths ($\Delta f_{\mathrm{bin}} = 1/T_{\mathrm{DFT}}$). The plotted recovered amplitude is normalised by the injected amplitude. The SNR (n_σ) is measured as the difference between the signal amplitude and the noise amplitude divided by the standard deviation of the noise. The appearance of a maximum for the SNR as shown on the right is a direct consequence of both the decrease of the recovered amplitude of signals with limited coherence (as shown on the left) and the scaling of white Gaussian noise with increasing integration time. The plot on the left was produced by injecting a simulated dark matter signal and a perfect sine into a segment of GEO 600 data and creating spectra using the modified LPSD technique described above. The plot on the right was made by injecting the same signals into white Gaussian noise and creating spectra using Welch's method. Note that for any single bin and for equal T_{DFT} the spectral estimate obtained with the LPSD method (Eq. 6.10) is mathematically equal to that obtained with Welch's method.

6.4   Dark matter search with LPSD

The SNR[4] for galactic DM signals in a logarithmically spaced spectrum is optimal given the minimum required data length, and can only be further improved by analysing more data. Additional data would allow for more averaging, which decreases the variance of the spectrum as the square root of the amount of data, such that the sensitivity approaches the noise floor. The noise floor can be lowered using longer DFT lengths at the cost of reduced SNR, but this is subject to severely diminishing returns; the sensitivity can only be improved by a factor proportional to the fourth root of the amount of data needed [319], and the computation time scales with the product of DFT length and the amount of data [330].

Figure 6.4 shows how the recovered signal to noise ratio of an injected scalar DM signal compares to that of a sinusoidal signal

---

[4]For the entirety of this chapter SNR refers to the ratio of signal to noise, not the matched filter SNR described in Section 1.5.1.

6.4.1 Estimation of noise statistics

The local noise parameters were estimated at every frequency bin by taking the median of the $w = 5 \cdot 10^4$ neighbouring bins. This method allows the underlying noise distribution to be estimated in a way that is independent of narrow, $\ll w$, spectral features, such as those due to mechanical excitation of the mirror suspensions. This is done under the assumption that the underlying noise spectrum is locally flat, and that is that the auto-correlation length of the noise spectrum is assumed to be $\gg w$. The choice of w represents a trade-off between incorrectly assuming that instrumental spectral artefacts or signals are features of the underlying noise spectrum, and erroneously assuming features of the underlying noise spectrum are instrumental spectral artefacts or signals. If a frequency bin differed from the median by more than 5.6σ then it was recorded to a catalogue of significant peaks. Figure 6.5 shows an example of these peaks in an LPSD amplitude spectrum.

Our analysis, using the LPSD method, found $\sim 10^4$ peaks above the 95% confidence level ($\gtrsim 5.6\sigma$), where the total error includes a frequency dependent amplitude calibration error of up to 30% inherent in GEO 600 data [333]. The frequency and amplitude stability of the peaks in time was then evaluated by cross-checking all candidates between spectra. Candidate peaks were rejected if their centre frequencies differed between spectra by more than the Doppler shift expected from the Earth's motion around the Sun through a galactic DM halo [334]. Peaks were also rejected if their amplitude changed significantly ($\gtrsim 5\sigma$) between spectra by more than an amount expected due to the underlying noise. Specifically, peaks that changed amplitude between spectra were only eliminated when there was a less than 1% ($\gtrsim 5\sigma$) probability that the amplitude change was due to noise, compensated for the look-elsewhere effect, so that on average only one peak would be falsely rejected if all cross-checks are performed 100 times.

Using this procedure, we eliminated all but 14 candidate peaks, where the vast majority ($> 99\%$) of peaks were rejected because they did not appear in all data sets within the centre frequency tolerance.

6.4.2 Follow-up analysis of candidates

After this process, fourteen candidate peaks remained. Thirteen of these peaks were found to have insufficient width to be DM signals. Further investigation of each of these candidates found that shifting the bin centre frequencies by an amount much smaller than the expected linewidth of DM signals of that frequency and amplitude and recomputing the spectra did not reproduce the peak. Additional work revealed these 13 candidate peaks were not present in spectra created using the same data and the same LPSD algorithm implemented in a different programming language[5], nor when slightly offset frequency bins were used, whereas the noise floor and other

---

[5]Basic algorithm implementations were written in `Python` and `MATLAB`.
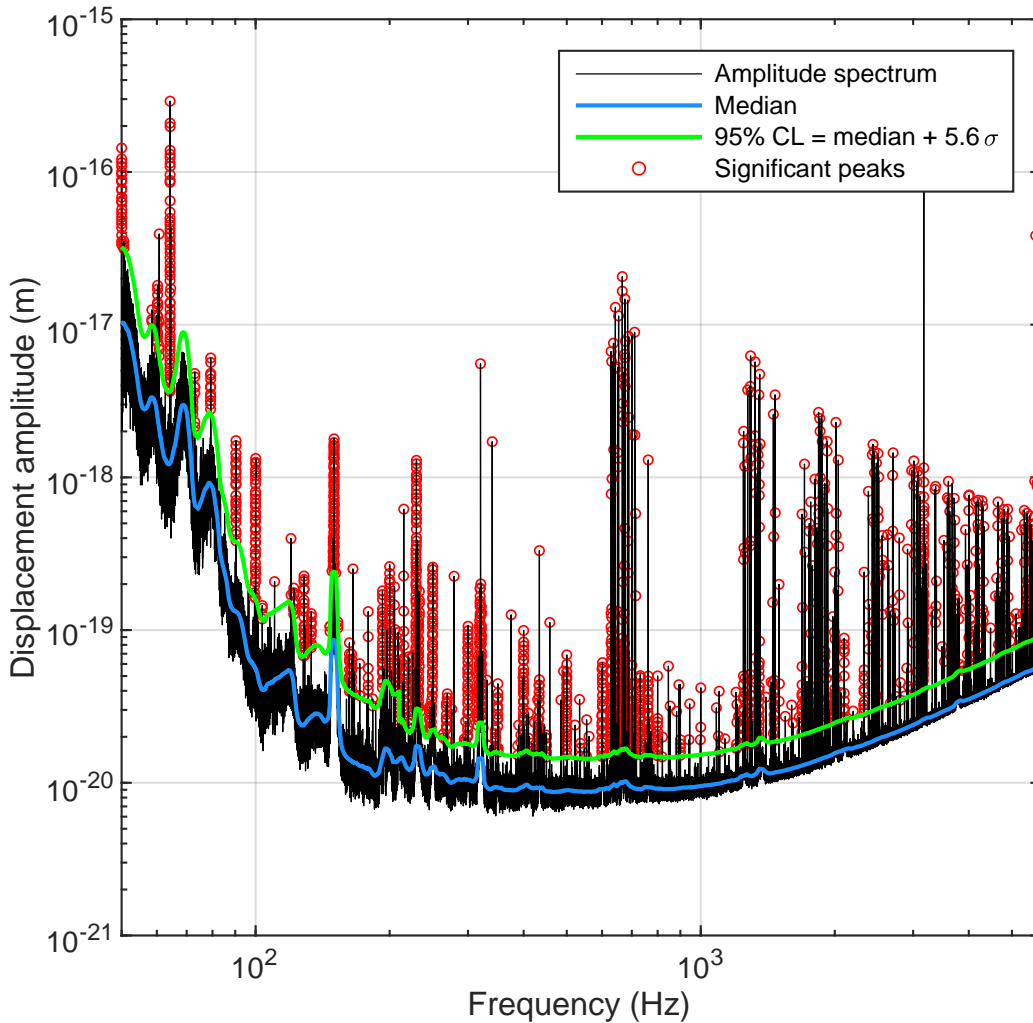
Figure 6.5: A typical amplitude spectrum (black) produced with frequency bins that are tuned to the expected dark matter linewidth using the modified LPSD technique. The noise spectrum was estimated at each frequency bin from neighbouring bins to yield the local noise median (blue) and 95% confidence level (green). Peaks (red) above this confidence level were considered candidates for DM signals and subjected to follow-up analysis.

spectral features were reproduced identically. These peaks were also not present when using the same LPSD algorithm, but with a different strain channel of GEO 600 data across the same time periods. These peaks are therefore likely artefacts of the numerical implementation of the LPSD technique. Figure 6.6 shows how these peaks are not present when the spectra is estimated using different resolution LPSDs, or with slightly offset frequency bins.

The coherence time of the single remaining candidate peak was probed by evaluating its height in the amplitude spectrum as a function of the DFT length. The height of the peak did not decrease for DFT lengths more than an order of mag-
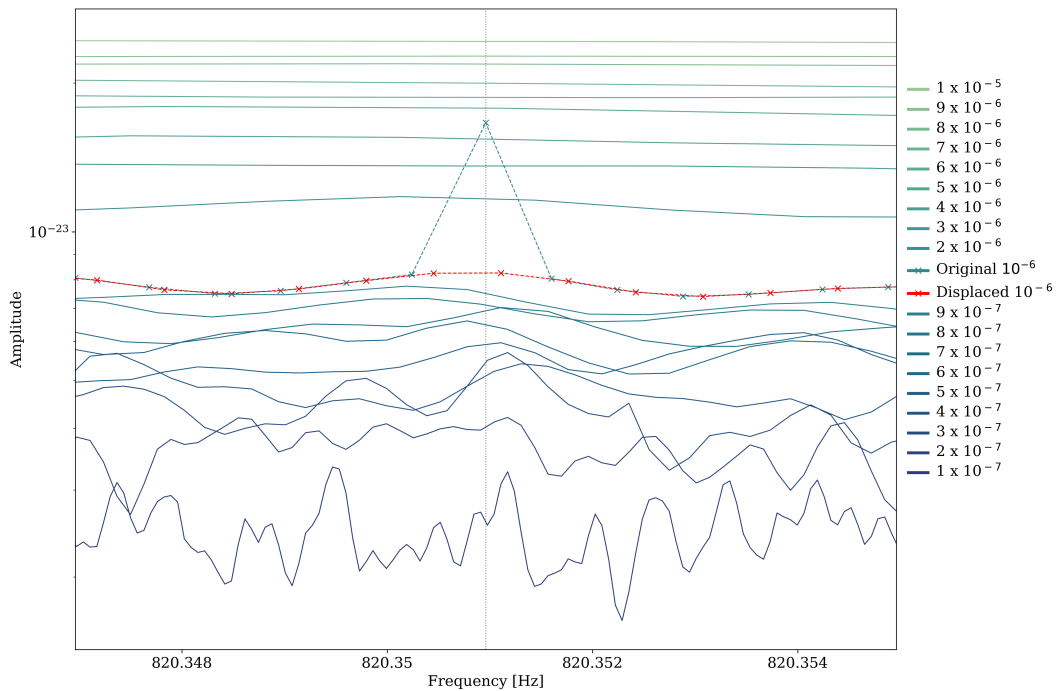
Figure 6.6: LPSD estimations of one of the thirteen single bin, persistent peaks. The dashed lines show estimations made with the $\Delta\omega/\omega \sim 10^{-6}$ resolution, with the red line estimated with a slightly different low frequency causing all subsequent bins to have displaced central frequencies. The other lines are estimations at different resolutions.

nitude greater than the expected DM coherence time, evidencing a coherence time much greater than that expected for a galactic DM signal of that frequency. To find the origin of the signal, and to check whether it could be due to the theoretically more coherent *Relaxion Halo* DM, we performed spectral analysis on data acquired on an auxiliary data acquisition system. The signal was not present in this data, whereas both noise and other signals from the interferometer were. This fact, in combination with higher-resolution, $\Delta\omega/\omega \sim 10^{-7}$, spectra revealing that the frequency at which the peak occurs is very close to and indistinguishable from an integer ($f_{\text{peak}} = 224 \pm (2 \cdot 10^{-5})$ Hz), implies the signal is most likely an artefact of a timing signal in the main data acquisition electronics. A representation of this process is shown in Figure 6.7, the reduction of amplitude can be seen in the peak at higher resolutions.

6.5 Results

Having determined that all significant peaks in the amplitude spectrum, above a confidence level of $> 99\%$, are not caused by scalar field DM, we can set constraints on the parameters of such dark matter at a 95% confidence level, corresponding to 5.6σ above the noise floor, using Eq. 6.8. We apply our results to three different
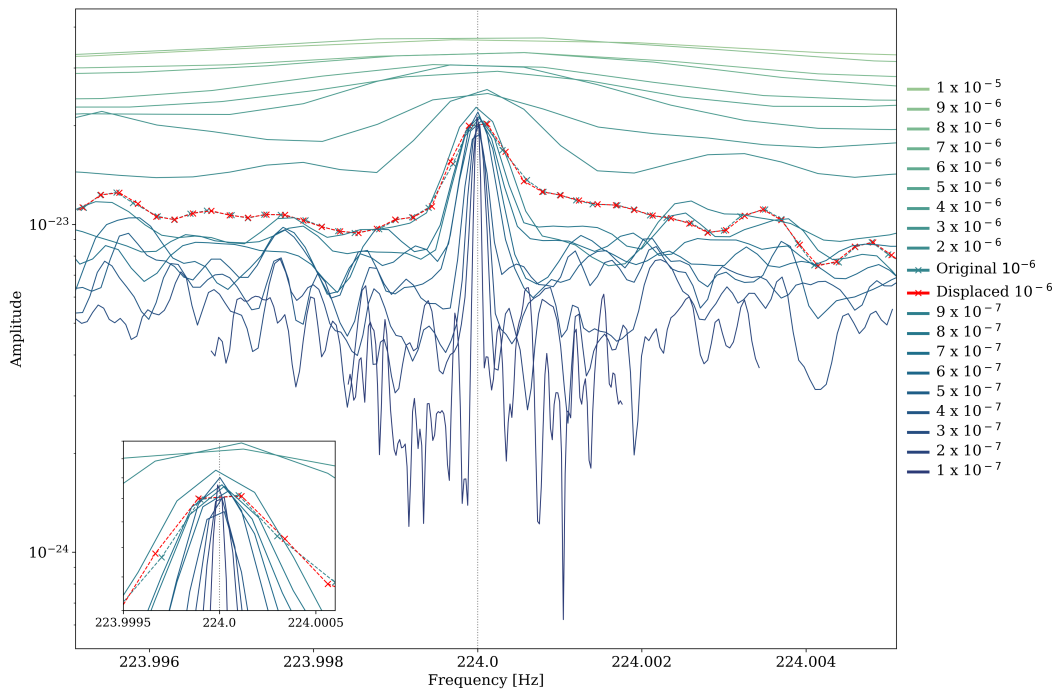
Figure 6.7: LPSD estimations of the 224 Hz, persistent peak. The dashed lines show estimations made with the $\Delta\omega/\omega \sim 10^{-6}$ resolution, with the red line estimated with a slightly different low frequency causing all subsequent bins to have displaced central frequencies. The other lines are estimations at different resolutions. The sub-plot in the lower left shows a close up of the region of interest.

scalar DM scenarios:

1. *Basic Scalar* (Figure 6.8): The scalar field DM is assumed to interact with the SM as given by the terms in 6.3, and is further assumed to be homogeneously distributed over the solar system with a density of $\rho_{\mathrm{GH}} = 0.4$ GeV/cm^3, as in the standard galactic DM halo model [318].

2. *Dilaton/Modulus* (Figure 6.9, left): In addition to the coupling to the electromagnetic sector as in Eq. 6.3, the field is assumed to have couplings to the QCD sector, and the coupling to the gluon field is assumed to be dominant [325–327, 335]. The local DM density is taken to be ρ_{GH}. Compared to the *Basic Scalar*, this scenario is subject to additional limits from tests of the equivalence principle, but is equally constrained by our result and those of other direct searches.

3. *Relaxion Halo* (Figure 6.9, right): In this scenario, the scalar field effectively couples to the SM as in the *Dilaton/Modulus* scenario, but these couplings arise through mixing with the Higgs boson [320, 321]. The local DM density in this scenario is taken to be dominated by a Relaxion halo gravitationally bound to earth, which leads to a local overdensity that depends on the field's mass and reaches values of up to $\rho_{\mathrm{local}}/\rho_{\mathrm{GH}} = 10^{11}$ for the mass range constrained

in this work [322].

For each scenario, we set constraints on the electron and photon coupling parameters Λ_e, Λ_γ, as a function of the field's mass m_ϕ (where for each coupling constant we assume the other to be zero); the constraints are plotted in Figures 6.8 and 6.9, together with previous upper limits. For the *Relaxion Halo* scenario, we assumed a mass-dependent halo density as described in [322].

Constraints from other direct experimental DM searches include those from various atomic spectroscopy experiments [306, 307, 337, 337, 339], a search using an optical cavity [309], and a resonant mass detector [338]. Tests of the equivalence principle using e.g. torsion balances [335, 341, 343] have also been used to set constraints on the parameters of undiscovered scalar fields; these bounds assume the scalar field manifests as a 'fifth force', and is sourced by a test mass (e.g. the Earth) [308, 324, 340]. The constraints on scalar fields inferred from these experiments depend in general on the composition and topography of the test masses and are independent of the local dark matter density.

6.6 Validations

To validate several aspects of our analysis methods, we simulated DM signals and injected them into sets of real and simulated data. The DM signals were created by superposing $\sim 10^2$ sinusoids at frequencies linearly spaced around a centre frequency, that of their simulated Doppler-shifted DM Compton frequency. The amplitude of each sinusoid was given by the quasi-Maxwellian DM line shape proposed in [319] and then scaled by a simulated DM coupling constant. The relative phases of the sinusoids were randomised to capture the thermalisation of the scalar field DM. A representation of the injected line shape is shown in Figure 6.10.

To test the spectral estimation, signal search, and candidate rejection, a blind injection of simulated DM signals into several GEO 600 data sets was performed. During this test the frequency, amplitude, and number of signals were randomly selected with their values hidden. All injected signals were recovered at their Compton frequency and at an amplitude corresponding to the hypothetical coupling constant, to within 3%, and were subsequently identified through cross-checks between spectra as persistent candidate DM signals.

We also tested the use of our modified LPSD algorithm as a method of obtaining optimal SNR [315, 319] using injected signals. Mock DM signals and monochromatic sine signals were injected into both real GEO 600 data and simulated Gaussian noise. We then produced spectra from this data for which the width of the frequency bins Δf_{bin}, and correspondingly the length of the DFTs T_{DFT}, was varied over four orders of magnitude. The recovered amplitude of signals injected into GEO 600 data in spectra created using the LPSD algorithm is plotted in Figure 6.4 (left). This shows
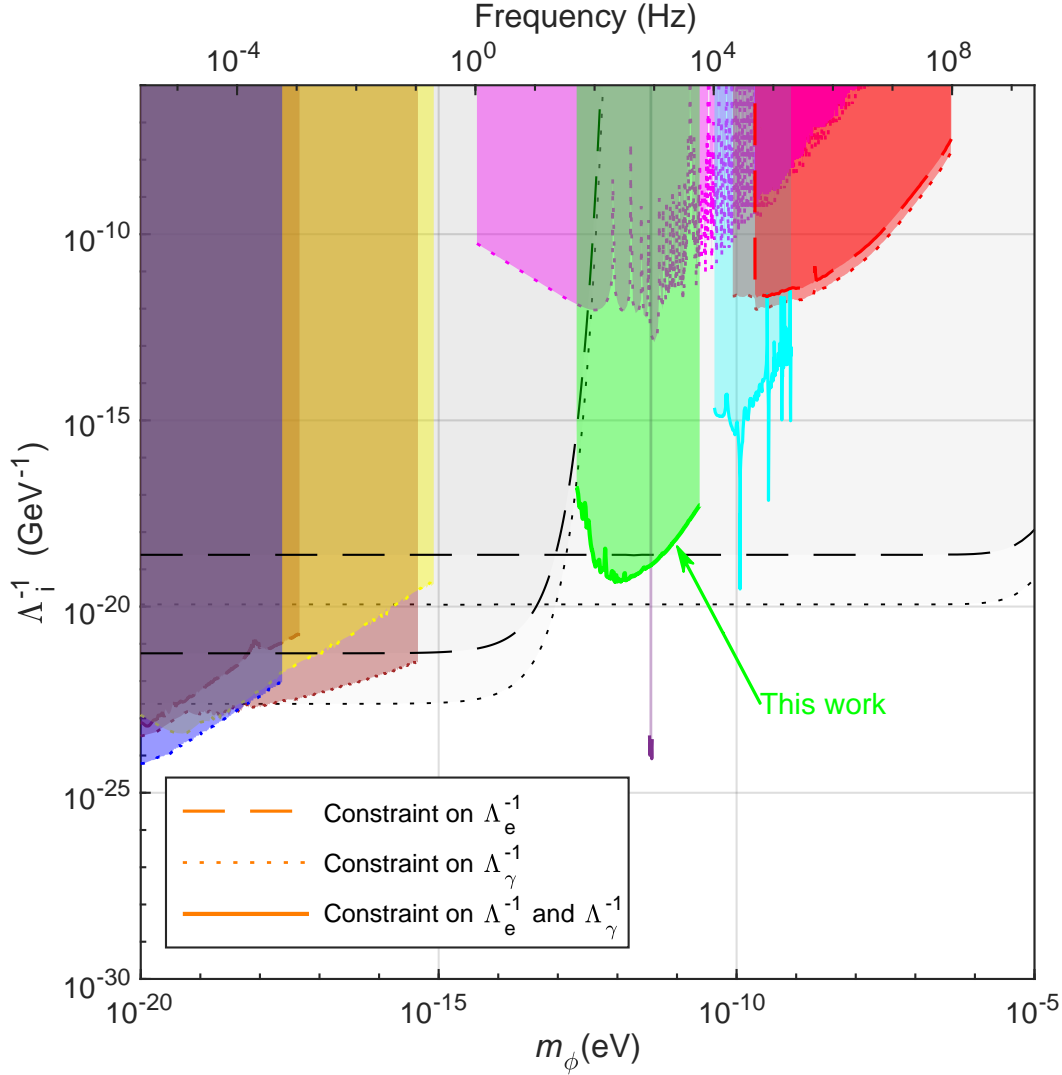
Figure 6.8: Constraints on the coupling parameters Λ_γ, Λ_e as a function of the field's mass m_ϕ, for scalar field DM as in the *Basic Scalar* scenario. The dashed lines represent constraints on the electron coupling Λ_e, while the dotted lines represent constraints on the photon coupling Λ_γ, at the 95% confidence level. The green region denotes the parameter space excluded in the current study through the spectral analysis of data from the GEO 600 GW detector. Other coloured regions indicate parameter space excluded through previous direct experimental searches; Hees et al [307] (blue), Van Tilburg et al [306] (yellow), Kennedy et al [336] (brown), Aharony et al [337] (magenta), Branca et al [338] (purple), Savalle et al [309] (cyan), and Antypas et al [339] (red). The black curves and grey regions correspond to previous constraints from "fifth-force" searches/tests of the equivalence principle; the most stringent such constraints for this DM scenario are from the MICRO-SCOPE experiment [308, 340] (limits shown in the range $m_\phi = [10^{-20}, 10^{-13}]$ eV), and the Cu/Pb torsion pendulum experiment performed by the Eöt-Wash group [324, 335, 341] (limits shown across the full mass range of this plot).
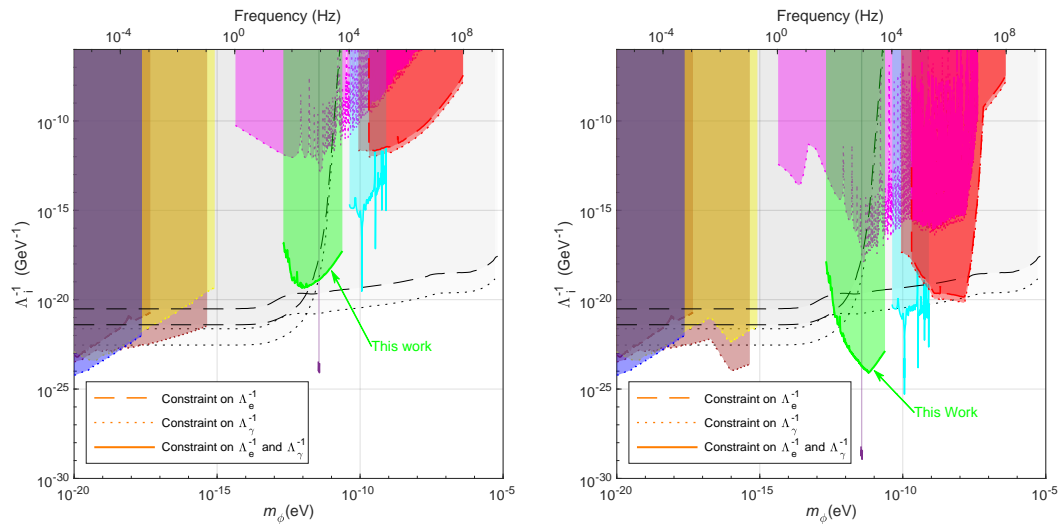
Figure 6.9: Constraints on the coupling parameters Λ_γ, Λ_e as a function of the field's mass m_ϕ, for scalar field DM as in the *Dilaton/Modulus* (left) *Relaxion Halo* (right) scenario. Dashed lines represent constraints on the electron coupling Λ_e and dotted lines represent constraints on the photon coupling Λ_γ, at the 95% confidence level. The green region denotes the parameter space excluded in the current study through the spectral analysis of data from the GEO 600 GW detector. Other coloured regions indicate the parameter space excluded through other direct experimental searches ([306, 307, 336–339, 342],). The black curves and grey regions correspond to previous constraints from "fifth-force" searches/tests of the equivalence principle; the most stringent such constraints for this DM scenario are from the MICROSCOPE experiment [308, 340] (limits shown in the range $m_\phi = [10^{-20}, 10^{-10}]$ eV), and the Cu/Pb torsion pendulum experiment performed by the Eöt-Wash group [324, 335, 341] (limits shown across the full mass range of this plot). The constraints for the *Relaxion Halo* scenario from direct experimental searches have been obtained by rescaling the originally reported constraints to account for the mass-dependent local over-densities as proposed in [322]. This produces novel constraints not reported before for *Relaxion Halo* DM from the results of [306, 307, 336–338]. The fifth force/equivalence principle constraints are independent of the local DM density so remain unchanged.
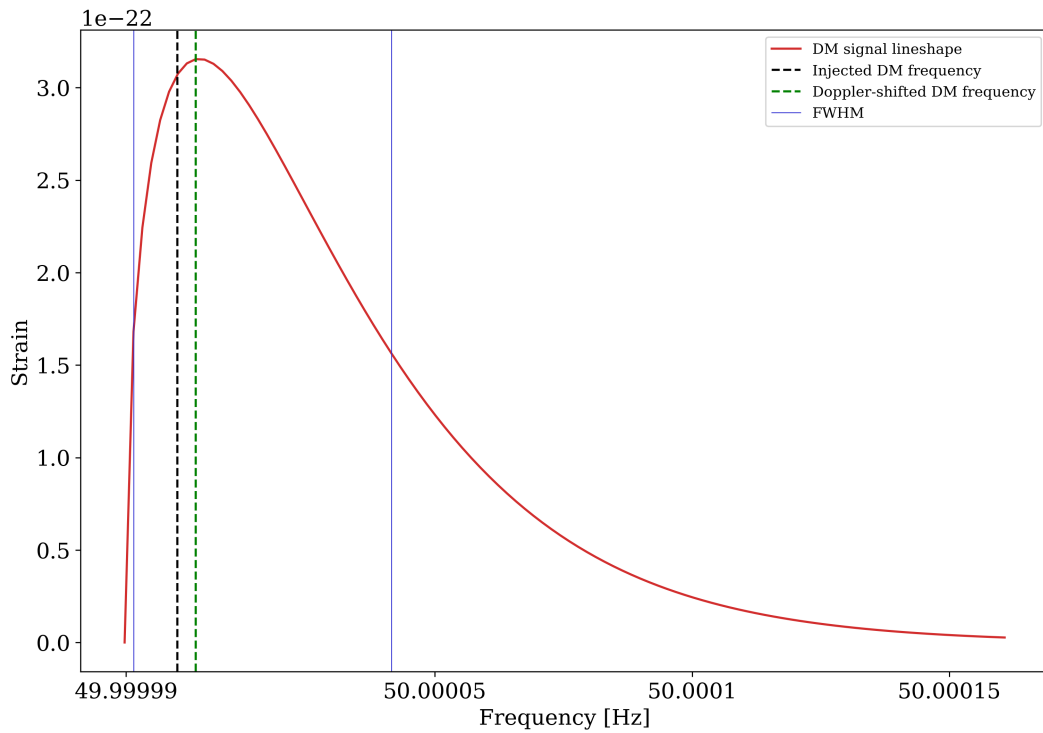
Figure 6.10: A representation of the line shape of a DM signal (red) injected at 50 Hz, black dashed line. The blue vertical lines show the positions of the signals Full Width Half Maxima (FWHM), and the green dashed line shows the peak frequency of the signal due to the doppler shift.

that the recovered amplitude of signals starts to decrease as the DFT length exceeds the coherence time (a monochromatic sine has infinite coherence time), and validates the rejection of the remaining candidate signal above as its amplitude was found to be roughly constant for $T_{\mathrm{DFT}}/\tau_c > 10$. The recovered SNR of signals injected into Gaussian noise in spectra created using Welch's method [117] is plotted in Figure 6.4 (right), which confirms that the SNR is maximal when the frequency bin width is roughly equal to the full-width at half-maximum Δf_{DM} of the spectral line shape of the signal. This is a consequence of the decrease in recovered amplitude for smaller bin widths and the scaling of white Gaussian noise.

6.7 Discussion

In this chapter, we presented the first search for signals of scalar field dark matter in the data of a GW detector. Scalar field dark matter would cause oscillations of the fine structure constant and electron mass, which in turn drive oscillations of the size and index of refraction of the beamsplitter in an interferometer, such as that of the GEO 600 detector. This would produce an oscillatory signal in a GW detector at a frequency set by the mass of the dark matter particle.

As exquisite classical noise mitigations are employed in GW detectors, quantum

technologies such as squeezed light can provide a major increase in sensitivity. Such technologies facilitate measurements beyond the shot-noise quantum limit, and yield unprecedented sensitivity to scalar field dark matter in a wide mass range. In addition, by tuning the frequency bin widths to the expected dark matter linewidth, our spectral analysis method improves on the analyses used in previous work that set constraints on dark photons using data from GW detectors, and other searches for scalar fields in frequency space. In contrast to these other efforts, the spectral analysis presented here yields the optimal signal-to-noise ratio for potential dark matter signals across the full frequency range.

We excluded the presence of such signals in the data of the GEO 600 GW detector, thereby setting new lower limits on dark matter couplings at up to $\Lambda_e, \Lambda_\gamma = 3 \cdot 10^{19}$ GeV for dark matter masses between 10^{-13} and 10^{-11} eV. The new constraints improve upon the current limits in this mass range obtained with atomic spectroscopy experiments by more than six orders of magnitude, and are up to four orders of magnitude more stringent than previous bounds from tests of the equivalence principle for some dark matter scenarios.

Tighter constraints on scalar field dark matter in various mass ranges can be set in the future using next generation GW detectors or other similar precision interferometers. Using the same methods as in this work these instruments would allow new limits to be set across their characteristic sensitive frequency range. Moreover, by slightly modifying the optics in such interferometers, e.g. by using mirrors of different thicknesses in each interferometer arm, their sensitivity to scalar field dark matter could be improved even further [314].

Through the reduction of losses, quantum technologies such as squeezed light are also expected to improve, allowing for ever-increasing noise mitigation [344]. These and other forthcoming technological advances make precision interferometers operating beyond quantum limits indispensable tools for dark matter detection and fundamental physics in general.

More stringent limits can theoretically be set by analysing more data. This allows for more averaging thus decreasing the variance of the spectrum proportional to the inverse of the square root of the amount of data, such that the constraint converges asymptotically to the mean noise level. Constraints can be set beyond this level using longer DFT lengths at the cost of reduced SNR, but this is subject to severely diminishing returns; the constraint can only be improved by a factor proportional to the fourth root of the amount of data needed [319], and the computation time scales with the product of DFT length and the amount of data [330, 331].

Chapter 7

Conclusions

The purpose of this thesis was to outline the difficulty of correctly identifying unusual signals in ground-based gravitational-wave interferometer data. These detectors are currently used to observe transient GW signals, so far constrained to the inspirals and mergers of compact binary systems. This has been done successfully with a number of astrophysical successes resulting from the analysis of the interferometer data. There is also a great deal of important research into physics and astrophysics, outside the field of CBC astrophysics, that is performed using this data. The complexity of this data can cause significant problems for such analysis if it is not correctly understood. In this chapter, I will give a summary of how this thesis presents some aspects of this problem.

7.1 Introduction to gravitational-wave interferometer data, signals and analysis methods

The aim of Chapter 1 was to give a summary of the data produced by GW interferometers, what the components of such data is, how it is collected and what analysis can be performed using it. I started with a brief summary of the purpose of ground-based GW interferometers, why they were built and what they were designed to observe. I outlined the basics of the design of these detectors and showed how the sensitivity of these detectors will increase with time. The step up in sensitivity from the first to second-generation of these observatories was significant, with the process of improving the current generation still providing considerable observing range improvements. The next generation of these detectors are expected to have orders of magnitude better sensitivity, and will revolutionise GW astrophysics.

I outlined the nature of the data extracted by these detectors. I explained how the data is typically converted from the time domain to the frequency domain, for analysis, via Fourier Transforms. I showed the dangers of incorrectly performing Fourier transforms and showed several techniques of how to get the best output from these processes. I also described some of the contributions to the noise floor

of the detector, and other sources of noise in the data, for example transient noise sources such as glitches.

As mentioned above, the only astrophysical signals confidently observed in these detectors have been CBCs. These signals are also the most prevalent subject of the studies presented in this thesis. I showed how these systems are modelled and outlined the subcategories of CBCs that we see, or expect to see, in these detectors. I then went on to describe the typical processes for detecting, interpreting and understanding these signals. I concluded this chapter with a brief introduction to other predicted sources of GWs that could theoretically be observed by current and future GW interferometers.

7.2 Estimation of the probability of observing two time-overlapping Compact Binary Coalescences

The aim of Chapter 2 was to examine and explain the potential failings of one of the key assumptions of current CBC analysis. This assumption is that any transient signal observed by these detectors is the only, non-noise, contribution to the strain in the detector. Our aim was to show that, while this assumption is reliable for current generation detectors, future detectors will likely be sensitive enough for this assumption to cause major problems for later analysis.

We outlined how transient signals in interferometers can be modelled using Poisson statistics. We then used the sensitivity curves of these detectors, coupled with current estimates for the rates of transient signals, to estimate the inter-arrival time. This time predicts the separation of transient signals. As these signals are visible in the detectors for a length of time we can then calculate the probability of a signal overlapping with another.

We used this calculation method to predict the probability of observing the time-overlap of binary black hole signals with other BBH signals, that of two binary neutron star, and the overlaps of BNS and BBH signals. We calculated this probability for several GW interferometer configurations in the current and future generations of detectors. We used this calculation to estimate the number of signals observed by each detector that will have a time-overlap with another signal.

We found that the proposed expansion of the current, second, generation of detectors LIGO-Voyager will likely observe such signals, particularly BNS+BBH overlaps, over its lifetime. We also found that no signal in the third generation observatory The Einstein Telescope will be observed in what would now be called "clean" data, data which only contains detector noise and a single signal. This is in large part due to the long observable duration of low mass signals, especially at lower frequencies. It was also found that most signals in ET will overlap with more than one other signal. These findings concur with similar studies by other

groups [266, 267]

We confirmed these findings with a purely numerical method of estimating the probability and number of these overlaps by drawing the parameters of possible signals at the rates expected in those detectors. We then used these predictions to estimate the number of signals that overlapped in time. The results of these two methods agreed.

This study showed that one of the key assumptions in transient GW astronomy will not hold for future interferometer configurations. If this assumption is not successfully mitigated in future analyses then the results of such signal analyses would potentially be biased away from the true astrophysical values. This would then lead to problems for other analyses of the results of these signals, or the population of signals as a whole.

It is important to note that this work did not account for several potentially important aspects of the parameter space of transient signals. We did not include analysis of burst-like signals such as supernovae. We also did not include the effect of redshift upon the population of binaries. Redshift would be an important correction to include for future predictions, particularly due for estimations of third generation detectors such as ET with larger viewing distances.

7.3 Parameter estimation bias from time-overlapping binary black hole signals in second-generation interferometers

As shown in Chapter 2 it is likely that, in the next decade, observed transient GW signals will overlap in time. The aim of the work in Chapter 3 was to understand what cases of these overlaps cause problems for the estimation of the parameters of observed binary black hole signals. By doing so it is possible to establish what cases of time-overlapping transient signals will significantly bias our results, should they go unnoticed. It is also possible to establish the cases that would not cause significantly different results from a standard, single signal, analysis and would therefore cause problem biases in the population of observed transient signals.

This test of the parameter space was performed across a selection of different second-generation detector networks and established the relative parameters of signals that would cause significant bias in the detector. Most notably we found that time-overlapping transient signals do not significantly bias the results of parameter estimation unless the two signals merge within $|\Delta t_c| \leq 0.1$ seconds of one another. We also found that, to produce significant bias in the resulting parameters, the two signals must have relatively similar signal-to-noise ratios. Further it was proved that, for quiet signals, otherwise undetectable sub-threshold signals can cause bias in parameter estimation.

It was also found that signals that overlap significantly in time result in observed waveforms similar to those of precessing signals. Such time-overlaps, if ignored, could lead to significant misunderstandings of the parameter space of CBC systems. However, a reanalysis of the probability calculation in Chapter 2 with the finding that significant bias only occurs when the signals are very close in merger time, shows that such events are exceedingly unlikely, even in third generation detectors.

The majority of this work agrees with the findings of similar studies, that were published at the same time [266, 267, 281, 282]. However, these studies differ in methodology. These studies focus mainly on third generation detectors, ignoring the early cases of advanced second-generation detectors where such events are likely to be first observed. They also use simpler waveform approximants, neglecting the presence of in-plane spin. As we showed, parameter estimation studies on data containing strongly overlapping signals are more likely to produce parameter distributions with high in-plane spin, in order to account for the beating of the two waveforms. Others of these studies do, however, include parameter estimation investigations into the overlaps of BNS signals both with other BNS signals, and those of BBH. It would be interesting to expand this investigation across a range of compact object masses in order to fully explore how the parameter estimation of signals containing different numbers of cycles and merging at different frequencies are affected by time-overlaps.

In this analysis, we also explored how the relative sky location of the two signals effects the resulting bias of the parameter estimation. It was found that signal pairings that arrive at similar merger times across the network cause less obvious bias. Utilising the change in merger time separation across the network could be a useful tool in distinguishing which detections are time-overlapping and then separating those signals.

7.4 Can modelled and unmodelled gravitational-wave searches detect time-overlapping transients?

Chapter 3 showed that biases in the parameter estimation of time-overlapping transient signals are not significant unless the signals merge very close together, and are similar in SNR. This category of time-overlapping transients are the least likely, but also the ones most likely to be spotted and separated due to the significance of their bias. Outside this region, analysed signal parameter will still be biased away from their true value, but are less likely to be acknowledged as non-single signal events. In Chapter 4, we examined how and where time-overlapping transient signals would be detected by current transient GW search algorithms.

We performed searches on simulated data containing both single signal events and time-overlapping transient signals. These searches were performed both with

modelled and unmodelled algorithms. We performed the search with differing techniques as the different methods can each catch signals that the other might miss. We found that both search methods could identify the majority of time-overlapping CBC signal. The algorithms did struggle when the signals were within their clustering windows. The algorithms naturally return a large number of possible signals around the time of significant noise or astrophysical signals. To avoid returning too many triggers, they employ clustering windows to return only the most significant of these. We found that if a secondary signal is within the clustering window of the search then only one trigger is returned. These algorithms would therefore require some modification to avoid such time-overlaps being ignored by search techniques.

The findings of our search, for the previously considered case of BNS+BNS time-overlaps in modelled searches, are similar to the findings of the first Einstein Telescope mock data challenge[284]. This study found that such time overlaps do not cause significant problems for matched filter searches. A later study[289] considered how these searches perform with noise curves estimated for data containing realistic numbers of time-overlapping transient signals. They too found that, for the majority of cases, the searches perform as expected.

7.5 Can we accurately identify which transient signal search triggers contain time-overlapping transient signals?

Chapters 3 and 4, showed that, for the vast majority of time-overlapping transient signals, the signals will still be detectable, and reasonably accurate analysis of the nature of these signals is still possible. Nonetheless, the main problem caused by time-overlapping transient signals will be those time-overlaps that go unnoticed. Unless the interferometer data is clean and stationary, then the results of astrophysical analysis of signals will not be reliable. We must therefore find a confident method of identifying such cases. In Chapter 5, we considered several possible methods of identifying which triggers from search pipelines contain multiple signals.

Three methods were proposed for time-overlap identification. The first two of these rely upon current search methods. For example, examining the SNR time-series of each template in the template bank of a modelled search. Multiple peaks in different time-series, or at separate times, would indicate that the trigger contains more than a single signal. The unmodelled search method would consider where and when there is excess power remaining in the null time-series, after the subtraction of the identified astrophysical signal. If there is this power, and in particular if that power is across different time-frequency bins, then such a time-overlap is possible.

We also proposed a new method, utilising convolutional neural networks, to identify which triggers contain time-overlapping BBH signals. By training a network

on large numbers of data sets containing either one or two signals, we were able to produce a network that can provide a binary output of the confidence of the network in signal pairings. The network was not successful at identifying the overlaps of signals with low SNR. However, it is likely that retraining the network with more examples of these missed cases would lead to a reliable method for identifying time-overlapping transient signals.

Unfortunately, none of these three methods have been fully tested for their accuracy in time-overlap identification. A detailed study into the merits and failings of each method could lead to a successful process for such identification and lead to more reliable measurements of the parameter space of merging binaries signals

7.6 Direct limits for scalar field dark matter from a gravitational-wave interferometer

In Chapter 1 we discussed the possibility of having signals, other than those of transient CBCs, detectable in the data. One possible source of such signals is that of scalar dark matter. A scalar dark matter signal would cause an oscillation in the interferometer's data at a specific frequency corresponding to the mass of the dark matter particle. For the purposes of transient signal analysis, such as that performed in Chapters 3 and 4, a dark matter signal of this nature would not cause problems. The signal itself, provided it remained constant over the visible duration of the signal, would merely contribute to the noise floor in any PSD estimation of that stretch of data.

However, such a signal, if it were found to exist, would be ground-breaking across many fields of physics and astronomy. Therefore, any search for such signals must take care in testing that any signals found truly are a dark matter source, and not just some specific noise source in the detector. For this purpose we designed a novel approach to searching for such signals. This involved taking a precisely tuned method of PSD estimation to produce multiple, high precision, amplitude spectra of the GEO 600 detector.

The result of this power spectra was a large number of peaks that could correspond to dark matter signals. We set a limit for confidence in a peak to those that differed from the median of the local noise floor by 5.6σ. Across the different spectra there were multiple candidate signals. These were removed with conditions on the stationarity of the peak across the spectra, both in frequency and amplitude. After this process was complete we had 14 candidate peaks. The majority of these peaks were clearly not dark matter due to their inconsistency across different methods of calculating the spectra and different channels of data collection. The final peak that passed all previous methods was found to be rejectable, as a dark matter signal, due to other inconsistencies with the candidate dark matter field. We tested this method

of dark matter searches by injecting dark matter signals into the real interferometer data and performing our search algorithm upon them. All blindly injected signals were found by this method. This search set new upper limits on the possible mass of scalar dark matter particles.

7.7 Final remarks

In recent years there have been many advances in various fields of physics and astrophysics gained through the use of gravitational-wave interferometer data. Each of these advances rest upon careful processes of manipulation of extremely complex data. In this thesis I aimed to show how and why any analyst considering this data must be careful to challenge the assumptions they make about the nature of the signals in their data. If this is not done correctly the results may be biased away from their true values. Analysts using any results from studies on GW interferometer data must also take care to understand what assumptions were made in the generation of these results.

Appendix A

Tables of parameters for circularised binary black hole signals

Name	Symbol	Typical range of values	Description
Chirp mass	$\mathcal{M}$	$[4, 70]\,\mathrm{M}_\odot$	See Equation 1.4 for definition
Mass ratio	q	$[0, 1]$	$q = m_2/m_1$ by convention
Component mass	m_1, m_2	$[5, 80]\,\mathrm{M}_\odot$	Alternative parameterisation to $\mathcal{M}$ & q
Effective spin	χ_{eff}	$[0, 1]$	The combined aligned spin parameter
Precessing spin	χ_{p}	$[0, 1]$	The combined in-plane spin parameter
Component spin magnitude	χ_1, χ_2	$[0, 1]$	$\chi_i = |\boldsymbol{\chi}_i|/m_i$ for spin vector $\boldsymbol{\chi}_i$
Spin azimuthal angle	θ_1, θ_2	$[0, \pi]$	Polar coordinate angles of each component
Spin polar angle	ϕ_1, ϕ_2	$[0, 2\pi]$	Polar coordinate angles of each component
Cartesian component spin	S_{1x}, S_{1y}, S_{1z}, S_{2x}, S_{2y}, S_{2z}	$[0, 1]$	Alternative parameterisation to χ_{eff}, χ_{p}, a_1, a_2, θ_1 and θ_2

Table A.1: A selection of parameterisations commonly used to describe the intrinsic properties of binary black hole signals, observable in second-generation ground-based interferometers. The values given for each parameter are typical values for observable, circularised, binary black hole signals.

Name	Symbol	Typical range of values	Description
Luminosity distance	d_L	$[0, 4000]$ Mpc	The line of sight distance to the binary
Right ascension	α	$[0, 2\pi]$	Describes the sky position
Declination	δ	$[0, \pi]$	Describes the sky position
Inclination	ι	$[-\pi, \pi]$	Angle between the binary's orbital angular momentum and the line of sight to the Earth
Coalescence time	t_c	-	Time of the merger when the signal reaches the Earth's centre. Typically given in GPS time [seconds]
Polarisation angle	ψ	$[0, 2\pi]$	The angle between the binary's orbital momentum to the sky
Phase angle	ϕ_c	$[0, 2\pi]$	Angle of the signals phase when at Earth's centre.

Table A.2: A selection of typical parameterisations used to describe the extrinsic properties of binary black hole signals, observable in second-generation ground-based interferometers, when observed from the Earth. The values given for each parameter are typical values for observable, circularised, binary black hole signals.

Appendix B

Additional plots
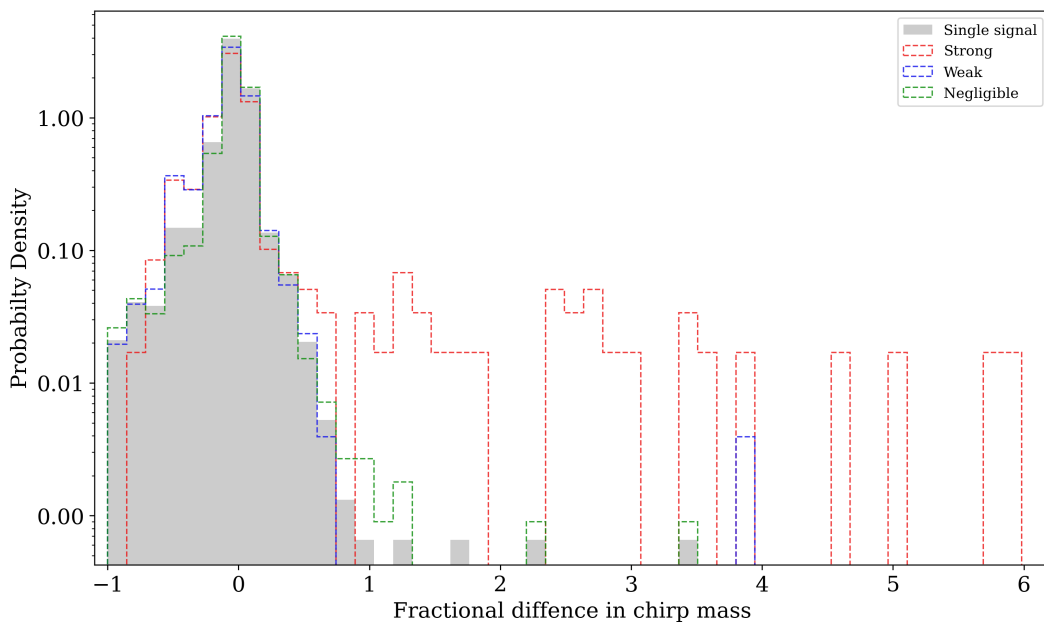
Figure B.1: Distribution, across the overlap regions, of the fractional difference between the recovered and injected chirp masses for `PyCBC` triggers in the PAIRS injection set. Also shown, in grey, is the same distribution for recovered and injected in the SINGLES injection set. A perfect pipeline, with an infinitely finely gridded template bank, would find injections with a delta spike on zero in this plot. This plot is included as an alternative to Figure 4.6 in Chapter 4 for direct comparison between the overlap regions.

Bibliography

[1] Relton, Philip and Raymond, Vivien. Parameter estimation bias from overlapping binary black hole events in second generation interferometers. *Physical Review D*, 104(8):084039, 2021.

[2] Relton, Philip and Virtuoso, Andrea and Bini, Sophie and Raymond, Vivien and Harry, Ian and Drago, Marco and Lazzaro, Claudia and Miani, Andrea and Tiwari, Shubhanshu. Addressing the challenges of detecting time-overlapping compact binary coalescences. *Physical Review D*, 106(10):104045, 2022.

[3] Vermeulen, Sander M and Relton, Philip and Grote, Hartmut and Raymond, Vivien and Affeldt, Christoph and Bergamin, Fabio and Bisht, Aparna and Brinkmann, Marc and Danzmann, Karsten and Doravari, Suresh and others. Direct limits for scalar field dark matter from a gravitational-wave detector. *Nature*, 600(7889):424–428, 2021.

[4] Price-Whelan, Adrian M and Lim, Pey Lian and Earl, Nicholas and Starkman, Nathaniel and Bradley, Larry and Shupe, David L and Patil, Aarya A and Corrales, Lia and Brasseur, CE and Nöthe, Maximilian and others. The Astropy Project: sustaining and growing a community-oriented open-source project and the latest major release (v5. 0) of the core package. *The Astrophysical Journal*, 935(2):167, 2022.

[5] Ashton, Gregory and Hübner, Moritz and Lasky, Paul D and Talbot, Colm and Ackley, Kendall and Biscoveanu, Sylvia and Chu, Qi and Divakarla, Atul and Easter, Paul J and Goncharov, Boris and others. BILBY: A user-friendly Bayesian inference library for gravitational-wave astronomy. *The Astrophysical Journal Supplement Series*, 241(2):27, 2019.

[6] Klimenko, S and Vedovato, G and Drago, M and Salemi, F and Tiwari, V and Prodi, GA and Lazzaro, C and Ackley, K and Tiwari, S and Da Silva, CF and others. Method for detection and reconstruction of gravitational wave transients with networks of advanced detectors. *Physical Review D*, 93(4):042004, 2016.

[7] Klimenko, Sergey and Vedovato, Gabriele and Necula, Valentin and Salemi, Francesco and Drago, Marco and Poulton, Rhys and Chassande-Mottin, Eric

and Tiwari, Vaibhav and Lazzaro, Claudia and O'Brian, Brendan and Szczepanczyk, Marek and Tiwari, Shubhanshu and V. Gayathri. cWB pipeline library: 6.4.1, December 2021.

[8] Speagle, Joshua S. dynesty: a dynamic nested sampling package for estimating Bayesian posteriors and evidences. *Monthly Notices of the Royal Astronomical Society*, 493(3):3132–3158, 2020.

[9] Frigo, Matteo and Johnson, Steven G. The design and implementation of FFTW3. *Proceedings of the IEEE*, 93(2):216–231, 2005.

[10] Jameson Rollins, Jolien Creighton. `pygwinc`, 2021.

[11] Chen, Hsin-Yu and Holz, Daniel E and Miller, John and Evans, Matthew and Vitale, Salvatore and Creighton, Jolien. Distance measures in gravitational-wave astrophysics and cosmology. *Classical and Quantum Gravity*, 38(5):055010, 2021.

[12] Macleod, D. M. and Areeda, J. S. and Coughlin, S. B. and Massinger, T. J. and Urban, A. L. GWpy: A Python package for gravitational-wave astrophysics. *SoftwareX*, 13:100657, 2021.

[13] Hunter, J. D. Matplotlib: A 2D graphics environment. *Computing in Science & Engineering*, 9(3):90–95, 2007.

[14] Harris, Charles R and Millman, K Jarrod and Van Der Walt, Stéfan J and Gommers, Ralf and Virtanen, Pauli and Cournapeau, David and Wieser, Eric and Taylor, Julian and Berg, Sebastian and Smith, Nathaniel J and others. Array programming with NumPy. *Nature*, 585(7825):357–362, 2020.

[15] Hoy, Charlie and Raymond, Vivien. PESummary: the code agnostic Parameter Estimation Summary page builder. *SoftwareX*, 15:100765, 2021.

[16] Allen, Bruce. $\chi 2$ time-frequency discriminator for gravitational wave detection. *Physical Review D*, 71(6):062001, 2005.

[17] Allen, Bruce and Anderson, Warren G and Brady, Patrick R and Brown, Duncan A and Creighton, Jolien DE. FINDCHIRP: An algorithm for detection of gravitational waves from inspiraling compact binaries. *Physical Review D*, 85(12):122006, 2012.

[18] Dal Canton, Tito and Nitz, Alexander H and Lundgren, Andrew P and Nielsen, Alex B and Brown, Duncan A and Dent, Thomas and Harry, Ian W and Krishnan, Badri and Miller, Andrew J and Wette, Karl and others. Implementing a search for aligned-spin neutron star-black hole systems with advanced ground based gravitational wave detectors. *Physical Review D*, 90(8):082004, 2014.

[19] Usman, Samantha A and Nitz, Alexander H and Harry, Ian W and Biwer, Christopher M and Brown, Duncan A and Cabero, Miriam and Capano, Collin D and Dal Canton, Tito and Dent, Thomas and Fairhurst, Stephen and others. The PyCBC search for gravitational waves from compact binary coalescence. *Classical and Quantum Gravity*, 33(21):215004, 2016.

[20] Nitz, Alexander H and Dent, Thomas and Dal Canton, Tito and Fairhurst, Stephen and Brown, Duncan A. Detecting binary compact-object mergers with gravitational waves: Understanding and Improving the sensitivity of the PyCBC search. *The Astrophysical Journal*, 849(2):118, 2017.

[21] Virtanen, Pauli and Gommers, Ralf and Oliphant, Travis E. and Haberland, Matt and Reddy, Tyler and Cournapeau, David and Burovski, Evgeni and Peterson, Pearu and Weckesser, Warren and Bright, Jonathan and van der Walt, Stéfan J. and Brett, Matthew and Wilson, Joshua and Millman, K. Jarrod and Mayorov, Nikolay and Nelson, Andrew R. J. and Jones, Eric and Kern, Robert and Larson, Eric and Carey, C J and Polat, İlhan and Feng, Yu and Moore, Eric W. and VanderPlas, Jake and Laxalde, Denis and Perktold, Josef and Cimrman, Robert and Henriksen, Ian and Quintero, E. A. and Harris, Charles R. and Archibald, Anne M. and Ribeiro, Antônio H. and Pedregosa, Fabian and van Mulbregt, Paul and SciPy 1.0 Contributors. SciPy 1.0: Fundamental Algorithms for Scientific Computing in Python. *Nature Methods*, 17:261–272, 2020.

[22] Michael L. Waskom. seaborn: statistical data visualization. *Journal of Open Source Software*, 6(60):3021, 2021.

[23] Martín Abadi and Ashish Agarwal and Paul Barham and Eugene Brevdo and Zhifeng Chen and Craig Citro and Greg S. Corrado and Andy Davis and Jeffrey Dean and Matthieu Devin and Sanjay Ghemawat and Ian Goodfellow and Andrew Harp and Geoffrey Irving and Michael Isard and Yangqing Jia and Rafal Jozefowicz and Lukasz Kaiser and Manjunath Kudlur and Josh Levenberg and Dandelion Mané and Rajat Monga and Sherry Moore and Derek Murray and Chris Olah and Mike Schuster and Jonathon Shlens and Benoit Steiner and Ilya Sutskever and Kunal Talwar and Paul Tucker and Vincent Vanhoucke and Vijay Vasudevan and Fernanda Viégas and Oriol Vinyals and Pete Warden and Martin Wattenberg and Martin Wicke and Yuan Yu and Xiaoqiang Zheng. TensorFlow: Large-Scale Machine Learning on Heterogeneous Systems, 2015. Software available from tensorflow.org.

[24] Newton, Isaac. *Philosophiae naturalis principia mathematica*. Royal Society, 1687.

[25] Hartle, James B. Gravity: an introduction to Einstein's general relativity, 2003.

[26] Einstein, Albert. Fundamental ideas of the general theory of relativity and the application of this theory in astronomy. *Preussische Akademie der Wissenschaften, Sitzungsberichte*, 315, 1915.

[27] Einstein, Albert. Näherungsweise Integration der Feldgleichungen der Gravitation. Sitzungsberichte der Königlich Preußischen Akademie der Wissenschaften (Berlin). *Translated as "Approximative Integration of the Field Equations of Gravitation," in Alfred Engel (translator) and Engelbert Schucking (consultant), The Collected Papers of Albert Einstein*, 6:1914–1917, 1916.

[28] Damour, Thibault and Vilenkin, Alexander. Gravitational wave bursts from cosmic strings. *Physical Review Letters*, 85(18):3761, 2000.

[29] Siemens, Xavier and Mandic, Vuk and Creighton, Jolien. Gravitational-wave stochastic background from cosmic strings. *Physical Review Letters*, 98(11):111101, 2007.

[30] Hulse, Russell A and Taylor, Joseph H. Discovery of a pulsar in a binary system. *The Astrophysical Journal*, 195:L51–L53, 1975.

[31] Weber, Joseph. *General Relativity and gravitational waves.* Courier Corporation, 2004.

[32] Weber, Joseph. Evidence for discovery of gravitational radiation. *Physical Review Letters*, 22(24):1320, 1969.

[33] Astone, Pia and Bassan, M and Bonifazi, P and Carelli, P and Castellano, MG and Cavallari, G and Coccia, E and Cosmelli, C and Fafone, V and Frasca, S and others. Long-term operation of the Rome" Explorer" cryogenic gravitational wave detector. *Physical Review D*, 47(2):362, 1993.

[34] Blair, David G and Ivanov, Eugene N and Tobar, Michael E and Turner, PJ and Van Kann, Frank and Heng, IS. High sensitivity gravitational wave antenna with parametric transducer readout. *Physical Review Letters*, 74(11):1908, 1995.

[35] Mauceli, Evan and Geng, ZK and Hamilton, WO and Johnson, WW and Merkowitz, S and Morse, A and Price, B and Solomonson, N. The Allegro gravitational wave detector: Data acquisition and analysis. *Physical Review D*, 54(2):1264, 1996.

[36] Cerdonio, Massimo and Bonaldi, Michele and Carlesso, D and Cavallini, E and Caruso, S and Colombo, A and Falferi, Paolo and Fontana, G and Fortini, PL

and Mezzena, R and others. The ultracryogenic gravitational-wave detector AURIGA. *Classical and Quantum Gravity*, 14(6):1491, 1997.

[37] Astone, Pia and Bassan, M and Bonifazi, P and Carelli, P and Coccia, E and Cosmelli, C and Fafone, V and Frasca, S and Marini, A and Mazzitelli, G and others. The gravitational wave detector NAUTILUS operating at T= 0.1 K. *Astroparticle Physics*, 7(3):231–243, 1997.

[38] Weiss, Rainer and Muehlner, Dirk. *Electronically coupled broadband gravitational antenna.* Citeseer, 1972.

[39] Aasi, Junaid and Abbott, BP and Abbott, Richard and Abbott, Thomas and Abernathy, MR and Ackley, Kendall and Adams, Carl and Adams, Thomas and Addesso, Paolo and Adhikari, RX and others. Advanced LIGO. *Classical and quantum gravity*, 32(7):074001, 2015.

[40] Acernese, Fet al and Agathos, M and Agatsuma, K and Aisa, D and Allemandou, N and Allocca, A and Amarni, J and Astone, P and Balestri, G and Ballardin, G and others. Advanced Virgo: a second-generation interferometric gravitational wave detector. *Classical and Quantum Gravity*, 32(2):024001, 2014.

[41] Kagra Collaboration. KAGRA: 2.5 generation interferometric gravitational wave detector. *Nature Astronomy*, 3(1):35–40, 2019.

[42] Abramovici, Alex and Althouse, William E and Drever, Ronald WP and Gürsel, Yekta and Kawamura, Seiji and Raab, Frederick J and Shoemaker, David and Sievers, Lisa and Spero, Robert E and Thorne, Kip S and others. LIGO: The laser interferometer gravitational-wave observatory. *science*, 256(5055):325–333, 1992.

[43] Adhikari, Rana and Fritschel, Peter and Waldman, Sam. Enhanced LIGO. *LIGO document, LIGO-T060156-01, http://www.ligo.caltech.edu/docs*, 2006.

[44] Abbott, B and Abbott, Robert and Adhikari, R and Ageev, A and Allen, Bruce and Amin, R and Anderson, SB and Anderson, WG and Araya, M and Armandula, H and others. Analysis of LIGO data for gravitational waves from binary neutron stars. *Physical Review D*, 69(12):122001, 2004.

[45] Fairhurst, Stephen. Triangulation of gravitational wave sources with a network of detectors. *New Journal of Physics*, 11(12):123006, 2009.

[46] Sidery, Trevor and Aylott, Ben and Christensen, Nelson and Farr, Ben and Farr, Will and Feroz, Farhan and Gair, Jonathan and Grover, Katherine and Graff, Philip and Hanna, Chad and others. Reconstructing the sky location of

gravitational-wave detected compact binary systems: methodology for testing and comparison. *Physical Review D*, 89(8):084060, 2014.

[47] Blas, Diego and Ivanov, Mikhail M and Sawicki, Ignacy and Sibiryakov, Sergey. On constraining the speed of gravitational waves following GW150914. *JETP letters*, 103:624–626, 2016.

[48] Baker, Tessa and Bellini, Emilio and Ferreira, Pedro G and Lagos, Macarena and Noller, Johannes and Sawicki, Ignacy. Strong constraints on cosmological gravity from GW170817 and GRB 170817A. *Physical review letters*, 119(25):251301, 2017.

[49] Cornish, Neil and Blas, Diego and Nardini, Germano. Bounding the speed of gravity with gravitational wave observations. *Physical review letters*, 119(16):161102, 2017.

[50] Acernese, Fausto and Amico, P and Arnaud, N and Arnault, C and Babusci, D and Ballardin, G and Barone, F and Barsuglia, M and Bellachia, F and Beney, JL and others. The present status of the VIRGO central interferometer. *Classical and Quantum Gravity*, 19(7):1421, 2002.

[51] Willke, Benno and Aufmuth, Peter and Aulbert, Carsten and Babak, Stanislav and Balasubramanian, Ramachandran and Barr, BW and Berukoff, S and Bose, Sukanta and Cagnoli, G and Casey, Morag M and others. The GEO 600 gravitational wave detector. *Classical and Quantum Gravity*, 19(7):1377, 2002.

[52] Tagoshi, Hideyuki and Kanda, Nobuyuki and Tanaka, Takahiro and Tatsumi, Daisuke and Telada, Souichi and Ando, Masaki and Arai, Koji and Araya, Akito and Asada, Hideki and Barton, Mark A and others. First search for gravitational waves from inspiraling compact binaries using TAMA300 data. *Physical Review D*, 63(6):062001, 2001.

[53] Abadie, J and Abbott, BP and Abbott, Richard and Abbott, TD and Abernathy, Matthew and Accadia, Timothee and Acernese, Fausto and Adams, Carl and Adhikari, Rana and Affeldt, Christoph and others. Search for gravitational waves from low mass compact binary coalescence in LIGO's sixth science run and Virgo's science runs 2 and 3. *Physical Review D*, 85(8):082002, 2012.

[54] Abbott, Rich and Adhikari, Rana and Ballmer, Stefan and Barsotti, Lisa and Evans, Matt and Fritschel, Peter and Frolov, Valera and Mueller, Guido and Slagmolen, Bram and Waldman, Sam. AdvLIGO interferometer sensing and control conceptual design. *LIGO Technical Document, T070247-01-I*, 2008.

[55] Abbott, R and Abbott, TD and Acernese, F and Ackley, K and Adams, C and Adhikari, N and Adhikari, RX and Adya, VB and Affeldt, C and Agarwal, D and others. GWTC-3: compact binary coalescences observed by LIGO and Virgo during the second part of the third observing run. *arXiv preprint arXiv:2111.03606*, 2021.

[56] Willke, Benno and Ajith, P and Allen, B and Aufmuth, P and Aulbert, C and Babak, S and Balasubramanian, Ramachandran and Barr, BW and Berukoff, S and Bunkowski, A and others. The geo-hf project. *Classical and Quantum Gravity*, 23(8):S207, 2006.

[57] Dooley, KL and Leong, JR and Adams, Thomas and Affeldt, C and Bisht, A and Bogan, C and Degallaix, J and Gräf, C and Hild, S and Hough, J and others. GEO 600 and the GEO-HF upgrade program: successes and challenges. *Classical and Quantum Gravity*, 33(7):075009, 2016.

[58] Grote, Hartmut and forthe LIGO Scientific Collaboration and others. The GEO 600 status. *Classical and Quantum Gravity*, 27(8):084003, 2010.

[59] Abbott, Benjamin P and Abbott, R and Abbott, TD and Abernathy, MR and Acernese, F and Ackley, K and Adams, C and Adams, T and Addesso, P and Adhikari, RX and others. GW150914: The Advanced LIGO detectors in the era of first discoveries. *Physical review letters*, 116(13):131103, 2016.

[60] Abbott, Benjamin P and Abbott, Richard and Abbott, TD and Abernathy, MR and Acernese, F and Ackley, K and Adams, C and Adams, T and Addesso, P and Adhikari, RX and others. Properties of the binary black hole merger GW150914. *Physical review letters*, 116(24):241102, 2016.

[61] Abbott, Benjamin P and Abbott, Richard and Abbott, TD and Acernese, F and Ackley, K and Adams, C and Adams, T and Addesso, P and Adhikari, Rana X and Adya, Vaishali B and others. GW170814: a three-detector observation of gravitational waves from a binary black hole coalescence. *Physical review letters*, 119(14):141101, 2017.

[62] Abbott, Benjamin P and Abbott, Rich and Abbott, TD and Acernese, Fausto and Ackley, Kendall and Adams, Carl and Adams, Thomas and Addesso, Paolo and Adhikari, RX and Adya, VB and others. GW170817: observation of gravitational waves from a binary neutron star inspiral. *Physical Review Letters*, 119(16):161101, 2017.

[63] LIGO Scientific Collaboration and Virgo Collaboration and KAGRA Collaboration and Abbott, R and Abe, H and Acernese, F and Ackley, K and Adhikari, N and Adhikari, RX and Adkins, VK and others. First joint observation by the

underground gravitational-wave detector KAGRA with GEO 600. *Progress of Theoretical and Experimental Physics*, 2022(6):063F01, 2022.

[64] Aso, Yoichi and Michimura, Yuta and Somiya, Kentaro and Ando, Masaki and Miyakawa, Osamu and Sekiguchi, Takanori and Tatsumi, Daisuke and Yamamoto, Hiroaki and Kagra Collaboration and others. Interferometer design of the KAGRA gravitational wave detector. *Physical Review D*, 88(4):043007, 2013.

[65] Abbott, BP and Abbott, Richard and Abbott, TDea and Abraham, S and Acernese, F and Ackley, K and Adams, C and Adhikari, RX and Adya, VB and Affeldt, Christoph and others. GWTC-1: a gravitational-wave transient catalog of compact binary mergers observed by LIGO and Virgo during the first and second observing runs. *Physical Review X*, 9(3):031040, 2019.

[66] Abbott, R and Abbott, TD and Abraham, S and Acernese, F and Ackley, K and Adams, A and Adams, C and Adhikari, RX and Adya, VB and Affeldt, Christoph and others. GWTC-2: compact binary coalescences observed by LIGO and Virgo during the first half of the third observing run. *Physical Review X*, 11(2):021053, 2021.

[67] Abbott, R and Abbott, TD and Acernese, F and Ackley, K and Adams, C and Adhikari, N and Adhikari, RX and Adya, VB and Affeldt, C and Agarwal, D and others. GWTC-2.1: Deep extended catalog of compact binary coalescences observed by LIGO and Virgo during the first half of the third observing run. *arXiv preprint arXiv:2108.01045*, 2021.

[68] Nitz, Alexander H and Capano, Collin and Nielsen, Alex B and Reyes, Steven and White, Rebecca and Brown, Duncan A and Krishnan, Badri. 1-OGC: The first open gravitational-wave catalog of binary mergers from analysis of public Advanced LIGO data. *The Astrophysical Journal*, 872(2):195, 2019.

[69] Nitz, Alexander H and Dent, Thomas and Davies, Gareth S and Kumar, Sumit and Capano, Collin D and Harry, Ian and Mozzon, Simone and Nuttall, Laura and Lundgren, Andrew and Tápai, Márton. 2-OGC: Open Gravitational-wave Catalog of binary mergers from analysis of public Advanced LIGO and Virgo data. *The Astrophysical Journal*, 891(2):123, 2020.

[70] Nitz, Alexander H and Capano, Collin D and Kumar, Sumit and Wang, Yi-Fan and Kastha, Shilpa and Schäfer, Marlin and Dhurkunde, Rahul and Cabero, Miriam. 3-OGC: Catalog of gravitational waves from compact-binary mergers. *The Astrophysical Journal*, 922(1):76, 2021.

[71] Nitz, AH and Kumar, S and Wang, YF and Kastha, S and Wu, S and Schäfer, M and Dhurkunde, R and Capano, CD. 4-OGC: Catalog of gravitational waves

from compact-binary mergers. arXiv eprints. *arXiv preprint arXiv:2112.06878*, 2021.

[72] LIGO Scientific Collaboration, Virgo Collaboration. GWTC-1. https://doi.org/10.7935/82H3-HH23, 2018.

[73] LIGO Scientific Collaboration and Virgo Collaboration. *GWTC-2 data release*, 2020.

[74] LIGO Scientific Collaboration and Virgo Collaboration. GWTC-2.1: Deep Extended Catalog of Compact Binary Coalescences Observed by LIGO and Virgo During the First Half of the Third Observing Run - Parameter Estimation Data Release, May 2022. LIGO Laboratory and Advanced LIGO are funded by the United States National Science Foundation (NSF) as well as the Science and Technology Facilities Council (STFC) of the United Kingdom, the Max-Planck-Society (MPS), and the State of Niedersachsen/Germany for support of the construction of Advanced LIGO and construction and operation of the GEO600 detector. Additional support for Advanced LIGO was provided by the Australian Research Council. Virgo is funded, through the European Gravitational Observatory (EGO), by the French Centre National de Recherche Scientifique (CNRS), the Italian Istituto Nazionale di Fisica Nucleare (INFN) and the Dutch Nikhef, with contributions by institutions from Belgium, Germany, Greece, Hungary, Ireland, Japan, Monaco, Poland, Portugal, Spain.

[75] LIGO Scientific Collaboration and Virgo Collaboration and KAGRA Collaboration. GWTC-3: Compact Binary Coalescences Observed by LIGO and Virgo During the Second Part of the Third Observing Run — Parameter estimation data release, November 2021. LIGO Laboratory and Advanced LIGO are funded by the United States National Science Foundation (NSF) as well as the Science and Technology Facilities Council (STFC) of the United Kingdom, the Max-Planck-Society (MPS), and the State of Niedersachsen/Germany for support of the construction of Advanced LIGO and construction and operation of the GEO600 detector. Additional support for Advanced LIGO was provided by the Australian Research Council. Virgo is funded, through the European Gravitational Observatory (EGO), by the French Centre National de Recherche Scientifique (CNRS), the Italian Istituto Nazionale di Fisica Nucleare (INFN) and the Dutch Nikhef, with contributions by institutions from Belgium, Germany, Greece, Hungary, Ireland, Japan, Monaco, Poland, Portugal, Spain. The construction and operation of KAGRA are funded by Ministry of Education, Culture, Sports, Science and Technology (MEXT), and Japan Society for the Promotion of Science (JSPS), National Research Foundation

(NRF) and Ministry of Science and ICT (MSIT) in Korea, Academia Sinica (AS) and the Ministry of Science and Technology (MoST) in Taiwan.

[76] Miller, John and Barsotti, Lisa and Vitale, Salvatore and Fritschel, Peter and Evans, Matthew and Sigg, Daniel. Prospects for doubling the range of Advanced LIGO. *Physical Review D*, 91(6):062005, 2015.

[77] Abbott, Benjamin P and Abbott, R and Abbott, TD and Abraham, S and Acernese, F and Ackley, K and Adams, C and Adya, VB and Affeldt, C and Agathos, M and others. Prospects for observing and localizing gravitational-wave transients with Advanced LIGO, Advanced Virgo and KAGRA. *Living reviews in relativity*, 23(3):1–69, 2020.

[78] Collaboration, LIGO Scientific. Instrument science white paper 2020. *Technical Report*, 2020.

[79] McCuller, L and Whittle, C and Ganapathy, D and Komori, K and Tse, M and Fernandez-Galiana, A and Barsotti, L and Fritschel, P and MacInnis, M and Matichard, F and others. Frequency-dependent squeezing for advanced LIGO. *Physical review letters*, 124(17):171102, 2020.

[80] Cahillane, Craig and Mansell, Georgia. Review of the Advanced LIGO gravitational wave observatories leading to observing run four. *Galaxies*, 10(1):36, 2022.

[81] Unnikrishnan, CS. IndIGO and LIGO-India: scope and plans for gravitational wave research and precision metrology in India. *International Journal of Modern Physics D*, 22(01):1341010, 2013.

[82] Saleem, M and Rana, Javed and Gayathri, V and Vijaykumar, Aditya and Goyal, Srashti and Sachdev, Surabhi and Suresh, Jishnu and Sudhagar, S and Mukherjee, Arunava and Gaur, Gurudatt and others. The science case for LIGO-India. *Classical and Quantum Gravity*, 39(2):025004, 2021.

[83] Fairhurst, Stephen. Improved source localization with LIGO-India. In *Journal of Physics: Conference Series*, volume 484, page 012007. IOP Publishing, 2014.

[84] Adhikari, Rana X and Arai, K and Brooks, AF and Wipf, C and Aguiar, O and Altin, P and Barr, B and Barsotti, L and Bassiri, R and Bell, A and others. A cryogenic silicon interferometer for gravitational-wave detection. *Classical and Quantum Gravity*, 37(16):165003, 2020.

[85] Bersanetti, Diego and Patricelli, Barbara and Piccinni, Ornella Juliana and Piergiovanni, Francesco and Salemi, Francesco and Sequino, Valeria. Advanced virgo: Status of the detector, latest results and future prospects. *Universe*, 7(9):322, 2021.

[86] Abbott, Benjamin P and Abbott, Richard and Abbott, Thomas D and Abernathy, MR and Ackley, K and Adams, C and Addesso, P and Adhikari, Rana X and Adya, VB and Affeldt, C and others. Exploring the sensitivity of next generation gravitational wave detectors. *Classical and Quantum Gravity*, 34(4):044001, 2017.

[87] Reitze, David and Adhikari, Rana X and Ballmer, Stefan and Barish, Barry and Barsotti, Lisa and Billingsley, GariLynn and Brown, Duncan A and Chen, Yanbei and Coyne, Dennis and Eisenstein, Robert and others. Cosmic explorer: the US contribution to gravitational-wave astronomy beyond LIGO. *arXiv preprint arXiv:1907.04833*, 2019.

[88] Evans, Matthew and Adhikari, Rana X and Afle, Chaitanya and Ballmer, Stefan W and Biscoveanu, Sylvia and Borhanian, Ssohrab and Brown, Duncan A and Chen, Yanbei and Eisenstein, Robert and Gruson, Alexandra and others. A horizon study for cosmic explorer: science, observatories, and community. *arXiv preprint arXiv:2109.09882*, 2021.

[89] Punturo, M and Abernathy, M and Acernese, F and Allen, B and Andersson, Nils and Arun, K and Barone, F and Barr, B and Barsuglia, M and Beker, M and others. The Einstein Telescope: a third-generation gravitational wave observatory. *Classical and Quantum Gravity*, 27(19):194002, 2009.

[90] Hild, Stefan and Chelkowski, Simon and Freise, Andreas and Franc, Janyce and Morgado, Nazario and Flaminio, Raffaele and DeSalvo, Riccardo. A xylophone configuration for a third-generation gravitational wave detector. *Classical and Quantum Gravity*, 27(1):015003, 2010.

[91] Punturo, Michele and Abernathy, M and Acernese, F and Allen, B and Andersson, N and Arun, K and Barone, F and Barr, B and Barsuglia, M and Beker, M and others. The third generation of gravitational wave observatories and their science reach. *Classical and Quantum Gravity*, 27(8):084007, 2010.

[92] Hild, S and Abernathy, M and Acernese, F and Amaro-Seoane, P and Andersson, N and Arun, K and Barone, F and Barr, B and Barsuglia, M and Beker, M and others. Sensitivity studies for third-generation gravitational wave observatories. *Classical and Quantum Gravity*, 28(9):094013, 2011.

[93] Maggiore, Michele and Van Den Broeck, Chris and Bartolo, Nicola and Belgacem, Enis and Bertacca, Daniele and Bizouard, Marie Anne and Branchesi, Marica and Clesse, Sebastien and Foffa, Stefano and García-Bellido, Juan and others. Science case for the Einstein telescope. *Journal of Cosmology and Astroparticle Physics*, 2020(03):050, 2020.

[94] Di Pace, Sibilla and Mangano, Valentina and Pierini, Lorenzo and Rezaei, Amirsajjad and Hennig, Jan-Simon and Hennig, Margot and Pascucci, Daniela and Allocca, Annalisa and Tosta e Melo, Iara and Nair, Vishnu G and others. Research Facilities for Europe's Next Generation Gravitational-Wave Detector Einstein Telescope. *Galaxies*, 10(3):65, 2022.

[95] Amaro-Seoane, Pau and Audley, Heather and Babak, Stanislav and Baker, John and Barausse, Enrico and Bender, Peter and Berti, Emanuele and Binetruy, Pierre and Born, Michael and Bortoluzzi, Daniele and others. Laser interferometer space antenna. *arXiv preprint arXiv:1702.00786*, 2017.

[96] Robson, Travis and Cornish, Neil J and Liu, Chang. The construction and use of LISA sensitivity curves. *Classical and Quantum Gravity*, 36(10):105011, 2019.

[97] Baker, John and Bellovary, Jillian and Bender, Peter L and Berti, Emanuele and Caldwell, Robert and Camp, Jordan and Conklin, John W and Cornish, Neil and Cutler, Curt and DeRosa, Ryan and others. The Laser Interferometer Space Antenna: unveiling the millihertz gravitational wave sky. *arXiv preprint arXiv:1907.06482*, 2019.

[98] Hu, Wen-Rui and Wu, Yue-Liang. The Taiji Program in Space for gravitational wave physics and the nature of gravity, 2017.

[99] Luo, Ziren and Wang, Yan and Wu, Yueliang and Hu, Wenrui and Jin, Gang. The Taiji program: A concise overview. *Progress of Theoretical and Experimental Physics*, 2021(5):05A108, 2021.

[100] The Taiji Scientific Collaboration. China's first step towards probing the expanding universe and the nature of gravity using a space borne gravitational wave antenna. *Communications Physics*, 4(1):34, 2021.

[101] Taiji Scientific Collaboration and Wu, Yue-Liang and Luo, Zi-Ren and Wang, Jian-Yu and Bai, Meng and Bian, Wei and Cai, Hai-Wen and Cai, Rong-Gen and Cai, Zhi-Ming and Cao, Jin and others. Taiji program in space for gravitational universe with the first run key technologies test in Taiji-1, 2021.

[102] Kawamura, Seiji and Ando, Masaki and Seto, Naoki and Sato, Shuichi and Nakamura, Takashi and Tsubono, Kimio and Kanda, Nobuyuki and Tanaka, Takahiro and Yokoyama, Jun'ichi and Funaki, Ikkoh and others. The Japanese space gravitational wave antenna: DECIGO. *Classical and Quantum Gravity*, 28(9):094011, 2011.

[103] Sato, Shuichi and Kawamura, Seiji and Ando, Masaki and Nakamura, Takashi and Tsubono, Kimio and Araya, Akito and Funaki, Ikkoh and Ioka, Kunihito

and Kanda, Nobuyuki and Moriwaki, Shigenori and others. The status of DECIGO. In *Journal of Physics: Conference Series*, volume 840, page 012010. IOP Publishing, 2017.

[104] Nelemans, Gijs and Yungelson, LR and Zwart, SF Portegies. The gravitational wave signal from the Galactic disk population of binaries containing two compact objects. *Astronomy & Astrophysics*, 375(3):890–898, 2001.

[105] Timpano, Seth E and Rubbo, Louis J and Cornish, Neil J. Characterizing the galactic gravitational wave background with LISA. *Physical Review D*, 73(12):122001, 2006.

[106] Crowder, Jeff and Cornish, Neil J. Solution to the galactic foreground problem for LISA. *Physical Review D*, 75(4):043008, 2007.

[107] Digman, Matthew C and Cornish, Neil J. LISA Gravitational Wave Sources in a Time-varying Galactic Stochastic Background. *The Astrophysical Journal*, 940(1):10, 2022.

[108] Hobbs, G. The Parkes pulsar timing array. *Classical and Quantum Gravity*, 30(22):224007, 2013.

[109] Manchester, RN and Hobbs, G and Bailes, M and Coles, WA and Van Straten, W and Keith, MJ and Shannon, RM and Bhat, NDR and Brown, A and Burke-Spolaor, SG and others. The parkes pulsar timing array project. *Publications of the Astronomical Society of Australia*, 30:e017, 2013.

[110] Kramer, Michael and Champion, David J. The European pulsar timing array and the large European array for pulsars. *Classical and Quantum Gravity*, 30(22):224009, 2013.

[111] McLaughlin, Maura A. The North American nanohertz observatory for gravitational waves. *Classical and Quantum Gravity*, 30(22):224008, 2013.

[112] Hobbs, George and Archibald, A and Arzoumanian, Zaven and Backer, D and Bailes, M and Bhat, NDR and Burgay, M and Burke-Spolaor, Sarah and Champion, D and Cognard, Ismaël and others. The international pulsar timing array project: using pulsars as a gravitational wave detector. *Classical and Quantum Gravity*, 27(8):084013, 2010.

[113] Davis, Derek and Areeda, Joseph S and Berger, Beverly K and Bruntz, R and Effler, Anamaria and Essick, RC and Fisher, RP and Godwin, Patrick and Goetz, Evan and Helmling-Cornell, AF and others. LIGO detector characterization in the second and third observing runs. *Classical and Quantum Gravity*, 38(13):135014, 2021.

[114] Cooley, James W and Tukey, John W. An algorithm for the machine calculation of complex Fourier series. *Mathematics of computation*, 19(90):297–301, 1965.

[115] Tukey, John W. An intoroduction to the calculation of numerical spectrum analysis. *Spectra Analysis of Time Series*, pages 25–46, 1967.

[116] Abbott, Benjamin P and Abbott, Rich and Abbott, Thomas D and Abraham, Sheelu and Acernese, Fausto and Ackley, Kendall and Adams, Carl and Adya, Vaishali B and Affeldt, Christoph and Agathos, Michalis and others. A guide to LIGO–Virgo detector noise and extraction of transient gravitational-wave signals. *Classical and Quantum Gravity*, 37(5):055002, 2020.

[117] P. Welch. The use of fast Fourier transform for the estimation of power spectra: A method based on time averaging over short, modified periodograms. *IEEE Transactions on Audio and Electroacoustics*, 15(2):70–73, 1967.

[118] Ossokine, Serguei and Buonanno, Alessandra and Marsat, Sylvain and Cotesta, Roberto and Babak, Stanislav and Dietrich, Tim and Haas, Roland and Hinder, Ian and Pfeiffer, Harald P and Pürrer, Michael and others. Multipolar effective-one-body waveforms for precessing binary black holes: Construction and validation. *Physical Review D*, 102(4):044055, 2020.

[119] Vahlbruch, Henning and Khalaidovski, Alexander and Lastzka, Nico and Gräf, Christian and Danzmann, Karsten and Schnabel, Roman. The GEO 600 squeezed light source. *Classical and Quantum Gravity*, 27(8):084027, 2010.

[120] Zevin, Michael and Coughlin, Scott and Bahaadini, Sara and Besler, Emre and Rohani, Neda and Allen, Sarah and Cabero, Miriam and Crowston, Kevin and Katsaggelos, Aggelos K and Larson, Shane L and others. Gravity Spy: integrating advanced LIGO detector characterization, machine learning, and citizen science. *Classical and quantum gravity*, 34(6):064003, 2017.

[121] Cabero, Miriam and Lundgren, Andrew and Nitz, Alex H and Dent, Thomas and Barker, David and Goetz, Evan and Kissel, Jeff S and Nuttall, Laura K and Schale, Paul and Schofield, Robert and others. Blip glitches in Advanced LIGO data. *Classical and Quantum Gravity*, 36(15):155010, 2019.

[122] Pankow, Chris and Chatziioannou, Katerina and Chase, Eve A and Littenberg, Tyson B and Evans, Matthew and McIver, Jessica and Cornish, Neil J and Haster, Carl-Johan and Kanner, Jonah and Raymond, Vivien and others. Mitigation of the instrumental noise transient in gravitational-wave data surrounding GW170817. *Physical Review D*, 98(8):084016, 2018.

[123] Abbott, BP and Abbott, R and Abbott, TD and Acernese, F and Ackley, K and Adams, C and Adams, T and Addesso, P and Adhikari, RX and Adya, VB

and others. Properties of the binary neutron star merger GW170817. *Physical Review X*, 9(1):011001, 2019.

[124] Payne, Ethan and Hourihane, Sophie and Golomb, Jacob and Udall, Rhiannon and Davis, Derek and Chatziioannou, Katerina. Curious case of GW200129: Interplay between spin-precession inference and data-quality issues. *Physical Review D*, 106(10):104017, 2022.

[125] Chatziioannou, Katerina and Cornish, Neil and Wijngaarden, Marcella and Littenberg, Tyson B. Modeling compact binary signals and instrumental glitches in gravitational wave data. *Physical Review D*, 103(4):044013, 2021.

[126] Edy, Oliver and Lundgren, Andrew and Nuttall, Laura K. Issues of mismodeling gravitational-wave data for parameter estimation. *Physical Review D*, 103(12):124061, 2021.

[127] Ashton, Gregory and Thiele, Sarah and Lecoeuche, Yannick and McIver, Jess and Nuttall, Laura K. Parameterised population models of transient non-Gaussian noise in the LIGO gravitational-wave detectors. *Classical and Quantum Gravity*, 39(17):175004, 2022.

[128] Macas, Ronaldas and Pooley, Joshua and Nuttall, Laura K and Davis, Derek and Dyer, Martin J and Lecoeuche, Yannick and Lyman, Joseph D and McIver, Jess and Rink, Katherine. Impact of noise transients on low latency gravitational-wave event localization. *Physical Review D*, 105(10):103021, 2022.

[129] Schutz, Bernard F. Determining the Hubble constant from gravitational wave observations. *Nature*, 323:310–311, 1986.

[130] Metzger, BD and Martínez-Pinedo, G and Darbha, S and Quataert, E and Arcones, Almudena and Kasen, D and Thomas, R and Nugent, P and Panov, IV and Zinner, NT. Electromagnetic counterparts of compact object mergers powered by the radioactive decay of r-process nuclei. *Monthly Notices of the Royal Astronomical Society*, 406(4):2650–2662, 2010.

[131] Peters, Philip Carl. Gravitational radiation and the motion of two point masses. *Physical Review*, 136(4B):B1224, 1964.

[132] Thrane, Eric and Talbot, Colm. An introduction to Bayesian inference in gravitational-wave astronomy: parameter estimation, model selection, and hierarchical models. *Publications of the Astronomical Society of Australia*, 36, 2019.

[133] Lower, Marcus E and Thrane, Eric and Lasky, Paul D and Smith, Rory. Measuring eccentricity in binary black hole inspirals with gravitational waves. *Physical Review D*, 98(8):083028, 2018.

[134] Schmidt, Patricia and Ohme, Frank and Hannam, Mark. Towards models of gravitational waveforms from generic binaries: II. Modelling precession effects with a single effective precession parameter. *Physical Review D*, 91(2):024043, 2015.

[135] LIGO Scientific Collaboration and Virgo Collaboration and KAGRA Scientific Collaboration and others. The population of merging compact binaries inferred using gravitational waves through GWTC-3. *arXiv preprint arXiv:2111.03634*, 2021.

[136] Apostolatos, Theocharis A and Cutler, Curt and Sussman, Gerald J and Thorne, Kip S. Spin-induced orbital precession and its modulation of the gravitational waveforms from merging binaries. *Physical Review D*, 49(12):6274, 1994.

[137] Kidder, Lawrence E. Coalescing binary systems of compact objects to (post) 5/2-Newtonian order. V. Spin effects. *Physical Review D*, 52(2):821, 1995.

[138] Baker, John G and Centrella, Joan and Choi, Dae-Il and Koppitz, Michael and van Meter, James. Gravitational-wave extraction from an inspiraling configuration of merging black holes. *Physical review letters*, 96(11):111102, 2006.

[139] Campanelli, Manuela and Lousto, Carlos O and Marronetti, Pedro and Zlochower, Yosef. Accurate evolutions of orbiting black-hole binaries without excision. *Physical Review Letters*, 96(11):111101, 2006.

[140] Blanchet, Luc. Gravitational radiation from post-Newtonian sources and inspiralling compact binaries. *Living reviews in relativity*, 17:1–187, 2014.

[141] Buonanno, Alessandra and Iyer, Bala R and Ochsner, Evan and Pan, Yi and Sathyaprakash, Bangalore Suryanarayana. Comparison of post-Newtonian templates for compact binary inspiral signals in gravitational-wave detectors. *Physical Review D*, 80(8):084043, 2009.

[142] Estellés, Héctor and Ramos-Buades, Antoni and Husa, Sascha and García-Quirós, Cecilio and Colleoni, Marta and Haegel, Leïla and Jaume, Rafel. Phenomenological time domain model for dominant quadrupole gravitational wave signal of coalescing binary black holes. *Physical Review D*, 103(12):124060, 2021.

[143] Estellés, Héctor and Husa, Sascha and Colleoni, Marta and Keitel, David and Mateu-Lucena, Maite and García-Quirós, Cecilio and Ramos-Buades, Antoni

and Borchers, Angela. Time-domain phenomenological model of gravitational-wave subdominant harmonics for quasicircular nonprecessing binary black hole coalescences. *Physical Review D*, 105(8):084039, 2022.

[144] Estellés, Héctor and Colleoni, Marta and García-Quirós, Cecilio and Husa, Sascha and Keitel, David and Mateu-Lucena, Maite and de Lluc Planas, Maria and Ramos-Buades, Antoni. New twists in compact binary waveform modeling: A fast time-domain model for precession. *Physical Review D*, 105(8):084040, 2022.

[145] Pratten, Geraint and Husa, Sascha and Garcia-Quiros, Cecilio and Colleoni, Marta and Ramos-Buades, Antoni and Estelles, Hector and Jaume, Rafel. Setting the cornerstone for a family of models for gravitational waves from compact binaries: The dominant harmonic for nonprecessing quasicircular black holes. *Physical Review D*, 102(6):064001, 2020.

[146] García-Quirós, Cecilio and Colleoni, Marta and Husa, Sascha and Estellés, Héctor and Pratten, Geraint and Ramos-Buades, Antoni and Mateu-Lucena, Maite and Jaume, Rafel. Multimode frequency-domain model for the gravitational wave signal from nonprecessing black-hole binaries. *Physical Review D*, 102(6):064002, 2020.

[147] Pratten, Geraint and García-Quirós, Cecilio and Colleoni, Marta and Ramos-Buades, Antoni and Estellés, Héctor and Mateu-Lucena, Maite and Jaume, Rafel and Haney, Maria and Keitel, David and Thompson, Jonathan E and others. Computationally efficient models for the dominant and subdominant harmonic modes of precessing binary black holes. *Physical Review D*, 103(10):104056, 2021.

[148] Bohé, Alejandro and Shao, Lijing and Taracchini, Andrea and Buonanno, Alessandra and Babak, Stanislav and Harry, Ian W and Hinder, Ian and Ossokine, Serguei and Pürrer, Michael and Raymond, Vivien and others. Improved effective-one-body model of spinning, nonprecessing binary black holes for the era of gravitational-wave astrophysics with advanced detectors. *Physical Review D*, 95(4):044028, 2017.

[149] Cotesta, Roberto and Buonanno, Alessandra and Bohé, Alejandro and Taracchini, Andrea and Hinder, Ian and Ossokine, Serguei. Enriching the symphony of gravitational waves from binary black holes by tuning higher harmonics. *Physical Review D*, 98(8):084028, 2018.

[150] Varma, Vijay and Field, Scott E and Scheel, Mark A and Blackman, Jonathan and Gerosa, Davide and Stein, Leo C and Kidder, Lawrence E and Pfeiffer, Harald P. Surrogate models for precessing binary black hole simulations with unequal masses. *Physical Review Research*, 1(3):033015, 2019.

[151] Ohme, Frank and Nielsen, Alex B and Keppel, Drew and Lundgren, Andrew. Statistical and systematic errors for gravitational-wave inspiral signals: A principal component analysis. *Physical Review D*, 88(4):042002, 2013.

[152] Hu, Qian and Veitch, John. Assessing the model waveform accuracy of gravitational waves. *Physical Review D*, 106(4):044042, 2022.

[153] Owen, Caroline B. and Haster, Carl-Johan and Perkins, Scott and Cornish, Neil J. and Yunes, Nicolás. Waveform accuracy and systematic uncertainties in current gravitational wave observations, 2023.

[154] Hannam, Mark and Hoy, Charlie and Thompson, Jonathan E and Fairhurst, Stephen and Raymond, Vivien and Colleoni, Marta and Davis, Derek and Estellés, Héctor and Haster, Carl-Johan and Helmling-Cornell, Adrian and others. General-relativistic precession in a black-hole binary. *Nature*, 610(7933):652–655, 2022.

[155] Abbott, R and Abbott, TD and Abraham, S and Acernese, F and Ackley, K and Adams, C and Adhikari, RX and Adya, VB and Affeldt, C and Agathos, M and others. GW190412: Observation of a binary-black-hole coalescence with asymmetric masses. *Physical Review D*, 102(4):043015, 2020.

[156] Clifford E. Rhoades, Jr. and Remo Ruffini. Maximum mass of a neutron star. *Phys. Rev. Lett.*, 32:324–327, 1974.

[157] Kiziltan, Bülent and Kottas, Athanasios and De Yoreo, Maria and Thorsett, Stephen E. The neutron star mass distribution. *The Astrophysical Journal*, 778(1):66, 2013.

[158] Rezzolla, Luciano and Most, Elias R and Weih, Lukas R. Using gravitational-wave observations and quasi-universal relations to constrain the maximum mass of neutron stars. *The Astrophysical Journal Letters*, 852(2):L25, 2018.

[159] Farrow, Nicholas and Zhu, Xing-Jiang and Thrane, Eric. The mass distribution of galactic double neutron stars. *The Astrophysical Journal*, 876(1):18, 2019.

[160] Landry, Philippe and Read, Jocelyn S. The Mass Distribution of Neutron Stars in Gravitational-wave Binaries. *The Astrophysical Journal Letters*, 921(2):L25, 2021.

[161] Özel, Feryal and Freire, Paulo. Masses, radii, and the equation of state of neutron stars. *Annual Review of Astronomy and Astrophysics*, 54:401–440, 2016.

[162] Dietrich, Tim and Coughlin, Michael W and Pang, Peter TH and Bulla, Mattia and Heinzel, Jack and Issa, Lina and Tews, Ingo and Antier, Sarah. Multi-messenger constraints on the neutron-star equation of state and the Hubble constant. *Science*, 370(6523):1450–1453, 2020.

[163] Jiang, Jin-Liang and Tang, Shao-Peng and Wang, Yuan-Zhu and Fan, Yi-Zhong and Wei, Da-Ming. PSR j0030+ 0451, GW170817, and the nuclear data: Joint constraints on equation of state and bulk properties of neutron stars. *The Astrophysical Journal*, 892(1):55, 2020.

[164] Lim, Y and Holt, JW. Bayesian modeling of the nuclear equation of state for neutron star tidal deformabilities and GW170817. *The European Physical Journal A*, 55(11):209, 2019.

[165] Lattimer, JM and Prakash, M. Neutron star structure and the equation of state. *The Astrophysical Journal*, 550(1):426, 2001.

[166] Lattimer, James M. The nuclear equation of state and neutron star masses. *Annual Review of Nuclear and Particle Science*, 62:485–515, 2012.

[167] Chaves, Andreas Guerra and Hinderer, Tanja. Probing the equation of state of neutron star matter with gravitational waves from binary inspirals in light of GW170817: a brief review. *Journal of Physics G: Nuclear and Particle Physics*, 46(12):123002, 2019.

[168] Tan, Hung and Noronha-Hostler, Jacquelyn and Yunes, Nico. Neutron Star Equation of State in light of GW190814. *Physical review letters*, 125(26):261104, 2020.

[169] Farr, Ben and Berry, Christopher PL and Farr, Will M and Haster, Carl-Johan and Middleton, Hannah and Cannon, Kipp and Graff, Philip B and Hanna, Chad and Mandel, Ilya and Pankow, Chris and others. Parameter estimation on gravitational waves from neutron-star binaries with spinning components. *The Astrophysical Journal*, 825(2):116, 2016.

[170] Davies, Gareth S. and Dent, Thomas and Tápai, Márton and Harry, Ian and McIsaac, Connor and Nitz, Alexander H. Extending the PyCBC search for gravitational waves from compact binary mergers to a global network. *Phys. Rev. D*, 102(2):022004, 2020.

[171] Zhu, Xingjiang and Thrane, Eric and Osłowski, Stefan and Levin, Yuri and Lasky, Paul D and others. Inferring the population properties of binary neutron stars with gravitational-wave measurements of spin. *Physical Review D*, 98(4):043002, 2018.

[172] Lo, Ka-Wai and Lin, Lap-Ming. The spin parameter of uniformly rotating compact stars. *The Astrophysical Journal*, 728(1):12, 2011.

[173] Abbott, BP and Abbott, R and Abbott, TD and Abraham, S and Acernese, F and Ackley, K and Adams, C and Adhikari, RX and Adya, VB and Affeldt, Christoph and others. GW190425: Observation of a compact binary coalescence with total mass ~3.4 $M_{\odot}$. *The Astrophysical journal letters*, 892(1):L3, 2020.

[174] Damour, Thibault. Gravitational radiation and the motion of compact bodies. *Lecture Notes in Physics, Berlin Springer Verlag*, 124:59–144, 1983.

[175] Damour, Thibault and Soffel, Michael and Xu, Chongming. General-relativistic celestial mechanics II. Translational equations of motion. *Physical Review D*, 45(4):1017, 1992.

[176] Yagi, Kent and Yunes, Nicolás. Love number can be hard to measure. *Physical Review D*, 89(2):021303, 2014.

[177] Favata, Marc. Systematic parameter errors in inspiraling neutron star binaries. *Physical review letters*, 112(10):101101, 2014.

[178] Wade, Leslie and Creighton, Jolien DE and Ochsner, Evan and Lackey, Benjamin D and Farr, Benjamin F and Littenberg, Tyson B and Raymond, Vivien. Systematic and statistical errors in a Bayesian approach to the estimation of the neutron-star equation of state using advanced gravitational wave detectors. *Physical Review D*, 89(10):103012, 2014.

[179] Hinderer, Tanja and Taracchini, Andrea and Foucart, Francois and Buonanno, Alessandra and Steinhoff, Jan and Duez, Matthew and Kidder, Lawrence E and Pfeiffer, Harald P and Scheel, Mark A and Szilagyi, Bela and others. Effects of neutron-star dynamic tides on gravitational waveforms within the effective-one-body approach. *Physical review letters*, 116(18):181101, 2016.

[180] Dietrich, Tim and Khan, Sebastian and Dudi, Reetika and Kapadia, Shasvath J and Kumar, Prayush and Nagar, Alessandro and Ohme, Frank and Pannarale, Francesco and Samajdar, Anuradha and Bernuzzi, Sebastiano and others. Matter imprints in waveform models for neutron star binaries: Tidal and self-spin effects. *Physical Review D*, 99(2):024029, 2019.

[181] Von Kienlin, A and Meegan, C and Goldstein, A. GRB 170817A: Fermi GBM detection. *GRB Coordinates Network*, 21520:1, 2017.

[182] Connaughton, V and Blackburn, L and Briggs, MS and Broida, J and Burns, E and Camp, J and Dal Canton, T and Christensen, N and Goldstein, A and Hamburg, R and others. LIGO/Virgo G298048: Fermi GBM trigger

170817.529 and LIGO single IFO trigger. *GRB Coordinates Network*, 21506:1, 2017.

[183] Goldstein, A ea and Veres, P and von Kienlin, A and Blackburn, L and Briggs, MS and Broida, J and Burns, E and Camp, J and Dal Canton, T and Christensen, N and others. LIGO/Virgo G298048-Update on Fermi/GBM GRB 170817A Analysis. *GRB Coordinates Network*, 21528:1, 2017.

[184] Abbott, Benjamin P and Abbott, R and Abbott, TD and Abraham, S and Acernese, F and Ackley, K and Adams, A and Adams, C and Adhikari, RX and Adya, VB and Affeldt, Christoph and others. Multi-messenger observations of a binary neutron star merger. *The Astrophysical Journal Letters*, 848(2), 2017.

[185] Moroianu, Alexandra and Wen, Linqing and James, Clancy W and Ai, Shunke and Kovalam, Manoj and Panther, Fiona and Zhang, Bing. An assessment of the Association Between a Fast Radio Burst and Binary Neutron Star Merger. *arXiv preprint arXiv:2212.00201*, 2022.

[186] Panther, Fiona H and Anderson, Gemma E and Bhandari, Shivani and Goodwin, Adelle J and Hurley-Walker, Natasha and James, Clancy W and Kawka, Adela and Ai, Shunke and Kovalam, Manoj and Moroianu, Alexandra and others. The most probable host of CHIME FRB 190425A, associated with binary neutron star merger GW190425, and a late-time transient search. *Monthly Notices of the Royal Astronomical Society*, 519(2):2235–2250, 2023.

[187] Abbott, R and Abbott, TD and Abraham, S and Acernese, F and Ackley, K and Adams, A and Adams, C and Adhikari, RX and Adya, VB and Affeldt, Christoph and others. Observation of gravitational waves from two neutron star–black hole coalescences. *The Astrophysical journal letters*, 915(1):L5, 2021.

[188] Foucart, Francois and Deaton, M Brett and Duez, Matthew D and Kidder, Lawrence E and MacDonald, Ilana and Ott, Christian D and Pfeiffer, Harald P and Scheel, Mark A and Szilagyi, Bela and Teukolsky, Saul A. Black-hole–neutron-star mergers at realistic mass ratios: Equation of state and spin orientation effects. *Physical Review D*, 87(8):084006, 2013.

[189] Zappa, Francesco and Bernuzzi, Sebastiano and Pannarale, Francesco and Mapelli, Michela and Giacobbo, Nicola. Black-hole remnants from black-hole–neutron-star mergers. *Physical review letters*, 123(4):041102, 2019.

[190] Abbott, Richard and Abbott, TD and Abraham, S and Acernese, Fausto and Ackley, K and Adams, C and Adhikari, Rana X and Adya, VB and Affeldt, Christoph and Agathos, Michail and others. GW190814: gravitational waves

from the coalescence of a 23 solar mass black hole with a 2.6 solar mass compact object. *The Astrophysical Journal Letters*, 896(2):L44, 2020.

[191] Bailyn, Charles D and Jain, Raj K and Coppi, Paolo and Orosz, Jerome A. The mass distribution of stellar black holes. *The Astrophysical Journal*, 499(1):367, 1998.

[192] Özel, Feryal and Psaltis, Dimitrios and Narayan, Ramesh and McClintock, Jeffrey E. The black hole mass distribution in the galaxy. *The Astrophysical Journal*, 725(2):1918, 2010.

[193] Farr, Will M and Sravan, Niharika and Cantrell, Andrew and Kreidberg, Laura and Bailyn, Charles D and Mandel, Ilya and Kalogera, Vicky. The mass distribution of stellar-mass black holes. *The Astrophysical Journal*, 741(2):103, 2011.

[194] Kreidberg, Laura and Bailyn, Charles D and Farr, Will M and Kalogera, Vicky. Mass measurements of black holes in X-ray transients: Is there a mass gap? *The Astrophysical Journal*, 757(1):36, 2012.

[195] Van Der Marel, Roeland P. Intermediate-mass black holes in the universe: a review of formation theories and observational constraints. *arXiv preprint astro-ph/0302101*, 2003.

[196] Coleman Miller, M and Colbert, Edward JM. Intermediate-mass black holes. *International Journal of Modern Physics D*, 13(01):1–64, 2004.

[197] Ebisuzaki, Toshikazu and Makino, Junichiro and Tsuru, Takeshi Go and Funato, Yoko and Zwart, Simon Portegies and Hut, Piet and McMillan, Steve and Matsushita, Satoki and Matsumoto, Hironori and Kawabe, Ryohei. Missing link found? The "runaway" path to supermassive black holes. *The Astrophysical Journal*, 562(1):L19, 2001.

[198] Inayoshi, Kohei and Visbal, Eli and Haiman, Zoltán. The assembly of the first massive black holes. *Annual Review of Astronomy and Astrophysics*, 58:27–97, 2020.

[199] Abbott, BP and Abbott, R and Abbott, TD and Abraham, S and Acernese, Fausto and Ackley, K and Adams, A and Adams, C and Adhikari, RX and Adya, VB and others. Search for intermediate mass black hole binaries in the first and second observing runs of the Advanced LIGO and Virgo network. *Physical Review D*, 100(6):064064, 2019.

[200] Abbott, Rich and Abbott, Thomas D and Acernese, Fausto and Ackley, Kendall and Adams, Carl and Adhikari, Naresh and Adhikari, Rana X and Adya, Vaishali B and Affeldt, Christoph and Agarwal, Deepali and others.

Search for intermediate-mass black hole binaries in the third observing run of Advanced LIGO and Advanced Virgo. *Astronomy & Astrophysics*, 659:A84, 2022.

[201] Abbott, Richard and Abbott, TD and Abraham, S and Acernese, F and Ackley, K and Adams, C and Adhikari, RX and Adya, VB and Affeldt, Christoph and Agathos, M and others. GW190521: a binary black hole merger with a total mass of 150 $M_\odot$. *Physical review letters*, 125(10):101102, 2020.

[202] Creighton, Jolien DE and Anderson, Warren G. *Gravitational-wave physics and astronomy: An introduction to theory, experiment and data analysis.* John Wiley & Sons, 2012.

[203] Canton, Tito Dal and Harry, Ian W. Designing a template bank to observe compact binary coalescences in Advanced LIGO's second observing run. *arXiv preprint arXiv:1705.01845*, 2017.

[204] Messenger, Christopher and Prix, Reinhard and Papa, Maria Alessandra. Random template banks and relaxed lattice coverings. *Physical Review D*, 79(10):104017, 2009.

[205] Harry, Ian W and Allen, Bruce and Sathyaprakash, BS. Stochastic template placement algorithm for gravitational wave data analysis. *Physical Review D*, 80(10):104014, 2009.

[206] Davies, Gareth S Cabourn and Harry, Ian W. Establishing significance of gravitational-wave signals from a single observatory in the PyCBC offline search. *Classical and Quantum Gravity*, 39(21):215012, 2022.

[207] Van Den Broeck, Chris and Brown, Duncan A and Cokelaer, Thomas and Harry, Ian and Jones, Gareth and Sathyaprakash, Bangalore Suryanarayana and Tagoshi, Hideyuki and Takahashi, Hirotaka. Template banks to search for compact binaries with spinning components in gravitational wave data. *Physical Review D*, 80(2):024009, 2009.

[208] Kapadia, Shasvath J and Caudill, Sarah and Creighton, Jolien DE and Farr, Will M and Mendell, Gregory and Weinstein, Alan and Cannon, Kipp and Fong, Heather and Godwin, Patrick and Lo, Rico KL and others. A self-consistent method to estimate the rate of compact binary coalescences with a Poisson mixture model. *Classical and Quantum Gravity*, 37(4):045007, 2020.

[209] Cannon, Kipp and Hanna, Chad and Peoples, Jacob. Likelihood-ratio ranking statistic for compact binary coalescence candidates with rate estimation. *arXiv preprint arXiv:1504.04632*, 2015.

[210] Messick, Cody and Blackburn, Kent and Brady, Patrick and Brockill, Patrick and Cannon, Kipp and Cariou, Romain and Caudill, Sarah and Chamberlin, Sydney J and Creighton, Jolien DE and Everett, Ryan and others. Analysis framework for the prompt discovery of compact binary mergers in gravitational-wave data. *Physical Review D*, 95(4):042001, 2017.

[211] Drago, Marco and Klimenko, Sergey and Lazzaro, Claudia and Milotti, Edoardo and Mitselmakher, Guenakh and Necula, Valentin and O'Brian, Brendan and Prodi, Giovanni Andrea and Salemi, Francesco and Szczepanczyk, Marek and others. Coherent WaveBurst, a pipeline for unmodeled gravitational-wave data analysis. *SoftwareX*, 14:100678, 2021.

[212] Christensen, Nelson and Meyer, Renate. Using Markov chain Monte Carlo methods for estimating parameters with gravitational radiation data. *Physical Review D*, 64(2):022001, 2001.

[213] Christensen, Nelson and Meyer, Renate and Libson, Adam. A Metropolis–Hastings routine for estimating parameters from compact binary inspiral events with laser interferometric gravitational radiation data. *Classical and Quantum Gravity*, 21(1):317, 2003.

[214] Van Der Sluys, Marc and Raymond, Vivien and Mandel, Ilya and Röver, Christian and Christensen, Nelson and Kalogera, Vicky and Meyer, Renate and Vecchio, Alberto. Parameter estimation of spinning binary inspirals using Markov chain Monte Carlo. *Classical and Quantum Gravity*, 25(18):184011, 2008.

[215] Veitch, John and Raymond, Vivien and Farr, Benjamin and Farr, Will and Graff, Philip and Vitale, Salvatore and Aylott, Ben and Blackburn, Kent and Christensen, Nelson and Coughlin, Michael and others. Parameter estimation for compact binaries with ground-based gravitational-wave observations using the LALInference software library. *Physical Review D*, 91(4):042003, 2015.

[216] Gramacy, Robert and Samworth, Richard and King, Ruth. Importance tempering. *Statistics and Computing*, 20:1–7, 2010.

[217] Skilling, John. Nested sampling. In *Aip conference proceedings*, volume 735, pages 395–405. American Institute of Physics, 2004.

[218] Skilling, John. Nested sampling for general Bayesian computation. *International Society for Bayesian Analysis*, 2006.

[219] Pankow, C and Brady, P and Ochsner, E and O'shaughnessy, R. Novel scheme for rapid parallel parameter estimation of gravitational waves from compact binary coalescences. *Physical Review D*, 92(2):023002, 2015.

[220] Lange, Jacob and O'Shaughnessy, Richard and Boyle, Michael and Bustillo, J Calderón and Campanelli, Manuela and Chu, Tony and Clark, James A and Demos, Nicholas and Fong, Heather and Healy, James and others. Parameter estimation method that directly compares gravitational wave observations to numerical relativity. *Physical Review D*, 96(10):104041, 2017.

[221] Wysocki, D and O'Shaughnessy, R and Lange, Jacob and Fang, Yao-Lung L. Accelerating parameter inference with graphics processing units. *Physical Review D*, 99(8):084026, 2019.

[222] Dax, Maximilian and Green, Stephen R and Gair, Jonathan and Macke, Jakob H and Buonanno, Alessandra and Schölkopf, Bernhard. Real-time gravitational wave science with neural posterior estimation. *Physical review letters*, 127(24):241103, 2021.

[223] Dax, Maximilian and Green, Stephen R and Gair, Jonathan and Pürrer, Michael and Wildberger, Jonas and Macke, Jakob H and Buonanno, Alessandra and Schölkopf, Bernhard. Neural Importance Sampling for Rapid and Reliable Gravitational-Wave Inference. *arXiv preprint arXiv:2210.05686*, 2022.

[224] Thrane, Eric and Talbot, Colm. An introduction to Bayesian inference in gravitational-wave astronomy: parameter estimation, model selection, and hierarchical models—Corrigendum. *Publications of the Astronomical Society of Australia*, 37:e036, 2020.

[225] Farr, WM. Marginalisation of the time parameter in gravitational wave parameter estimation. *URL: https://dcc.ligo.org/T1400460-v2/public*, 2014.

[226] Veitch, John and Del Pozzo, Walter. Analytic marginalisation of phase parameter. *LIGO Technical Document, LIGO-T1300326*, 2013.

[227] Singer, Leo P and Price, Larry R. Rapid Bayesian position reconstruction for gravitational-wave transients. *Physical Review D*, 93(2):024013, 2016.

[228] Zackay, Barak and Dai, Liang and Venumadhav, Tejaswi. Relative binning and fast likelihood evaluation for gravitational wave parameter estimation. *arXiv preprint arXiv:1806.08792*, 2018.

[229] Smith, Rory and Field, Scott E and Blackburn, Kent and Haster, Carl-Johan and Pürrer, Michael and Raymond, Vivien and Schmidt, Patricia. Fast and accurate inference on gravitational waves from precessing compact binaries. *Physical Review D*, 94(4):044031, 2016.

[230] GWOSC: Gravitation Wave Open Science Center. GW150914 Samples and PSD release.

[231] Wand, Matt P and Jones, M Chris. *Kernel smoothing.* CRC press, 1994.

[232] Rodriguez, Carl L and Zevin, Michael and Pankow, Chris and Kalogera, Vasilliki and Rasio, Frederic A. Illuminating black hole binary formation channels with spins in advanced LIGO. *The Astrophysical Journal Letters*, 832(1):L2, 2016.

[233] LIGO Scientific Collaboration and Virgo Collaboration and KAGRA Collaboration. The population of merging compact binaries inferred using gravitational waves through GWTC-3 - Data release, November 2021. LIGO Laboratory and Advanced LIGO are funded by the United States National Science Foundation (NSF) as well as the Science and Technology Facilities Council (STFC) of the United Kingdom, the Max-Planck-Society (MPS), and the State of Niedersachsen/Germany for support of the construction of Advanced LIGO and construction and operation of the GEO600 detector. Additional support for Advanced LIGO was provided by the Australian Research Council. Virgo is funded, through the European Gravitational Observatory (EGO), by the French Centre National de Recherche Scientifique (CNRS), the Italian Istituto Nazionale di Fisica Nucleare (INFN) and the Dutch Nikhef, with contributions by institutions from Belgium, Germany, Greece, Hungary, Ireland, Japan, Monaco, Poland, Portugal, Spain. The construction and operation of KAGRA are funded by Ministry of Education, Culture, Sports, Science and Technology (MEXT), and Japan Society for the Promotion of Science (JSPS), National Research Foundation (NRF) and Ministry of Science and ICT (MSIT) in Korea, Academia Sinica (AS) and the Ministry of Science and Technology (MoST) in Taiwan.

[234] Ott, Christian D. The gravitational-wave signature of core-collapse supernovae. *Classical and Quantum Gravity*, 26(6):063001, 2009.

[235] Abbott, BP and Abbott, R and Abbott, TD and Abraham, S and Acernese, Fausto and Ackley, K and Adams, C and Adya, VB and Affeldt, C and Agathos, M and others. Optically targeted search for gravitational waves emitted by core-collapse supernovae during the first and second observing runs of advanced LIGO and advanced Virgo. *Physical Review D*, 101(8):084002, 2020.

[236] Jaffe, Andrew H and Backer, Donald C. Gravitational waves probe the coalescence rate of massive black hole binaries. *The Astrophysical Journal*, 583(2):616, 2003.

[237] Amaro-Seoane, Pau and Santamaria, Lucia. Detection of IMBHs with ground-based gravitational wave observatories: a biography of a binary of black holes, from birth to death. *The Astrophysical Journal*, 722(2):1197, 2010.

[238] Yu, Shenghua and Jeffery, C Simon. The gravitational wave signal from diverse populations of double white dwarf binaries in the Galaxy. *Astronomy & Astrophysics*, 521:A85, 2010.

[239] Drasco, Steve and Hughes, Scott A. Gravitational wave snapshots of generic extreme mass ratio inspirals. *Physical Review D*, 73(2):024027, 2006.

[240] Lasky, Paul D. Gravitational waves from neutron stars: a review. *Publications of the Astronomical Society of Australia*, 32:e034, 2015.

[241] Glampedakis, Kostas and Gualtieri, Leonardo. Gravitational waves from single neutron stars: an advanced detector era survey. *The Physics and Astrophysics of Neutron Stars*, pages 673–736, 2018.

[242] Abbott, R and Abbott, TD and Abraham, S and Acernese, F and Ackley, K and Adams, A and Adams, C and Adhikari, RX and Adya, VB and Affeldt, C and others. All-sky search for continuous gravitational waves from isolated neutron stars in the early O3 LIGO data. *Physical Review D*, 104(8):082004, 2021.

[243] Abbott, R and Abbott, TD and Abraham, S and Acernese, F and Ackley, K and Adams, A and Adams, C and Adhikari, RX and Adya, VB and Affeldt, C and others. All-sky search in early O3 LIGO data for continuous gravitational-wave signals from unknown neutron stars in binary systems. *Physical Review D*, 103(6):064017, 2021.

[244] Abbott, R and Abbott, TD and Acernese, F and Ackley, K and Adams, C and Adhikari, N and Adhikari, RX and Adya, VB and Affeldt, C and Agarwal, D and others. Search of the early O3 LIGO data for continuous gravitational waves from the Cassiopeia A and Vela Jr. supernova remnants. *Physical Review D*, 105(8):082005, 2022.

[245] Abbott, R and Abe, H and Acernese, F and Ackley, K and Adhikari, N and Adhikari, RX and Adkins, VK and Adya, VB and Affeldt, C and Agarwal, D and others. Search for continuous gravitational wave emission from the Milky Way center in O3 LIGO-Virgo data. *Physical Review D*, 106(4):042003, 2022.

[246] Patruno, Alessandro and Watts, Anna L. Accreting millisecond X-ray pulsars. *Timing Neutron Stars: Pulsations, Oscillations and Explosions*, pages 143–208, 2021.

[247] Zhu, Sylvia J and Baryakhtar, Masha and Papa, Maria Alessandra and Tsuna, Daichi and Kawanaka, Norita and Eggenstein, Heinz-Bernd. Characterizing the continuous gravitational-wave signal from boson clouds around Galactic isolated black holes. *Physical Review D*, 102(6):063020, 2020.

[248] Lamberts, Astrid and Blunt, Sarah and Littenberg, Tyson B and Garrison-Kimmel, Shea and Kupfer, Thomas and Sanderson, Robyn E. Predicting the LISA white dwarf binary population in the Milky Way with cosmological simulations. *Monthly Notices of the Royal Astronomical Society*, 490(4):5888–5903, 2019.

[249] Maggiore, Michele. Gravitational wave experiments and early universe cosmology. *Physics Reports*, 331(6):283–367, 2000.

[250] The LIGO Scientific Collaboration & The Virgo Collaboration. An upper limit on the stochastic gravitational-wave background of cosmological origin. *Nature*, 460(7258):990–994, 2009.

[251] Abbott, Ryan and Abbott, TD and Abraham, S and Acernese, F and Ackley, K and Adams, A and Adams, C and Adhikari, RX and Adya, VB and Affeldt, C and others. Upper limits on the isotropic gravitational-wave background from Advanced LIGO and Advanced Virgo's third observing run. *Physical Review D*, 104(2):022004, 2021.

[252] Abbott, R and Abbott, TD and Abraham, S and Acernese, F and Ackley, K and Adams, A and Adams, C and Adhikari, RX and Adya, VB and Affeldt, C and others. Search for anisotropic gravitational-wave backgrounds using data from Advanced LIGO and Advanced Virgo's first three observing runs. *Physical Review D*, 104(2):022005, 2021.

[253] Walker, Marissa and Agnew, Alfonso F and Bidler, Jeffrey and Lundgren, Andrew and Macedo, Alexandra and Macleod, Duncan and Massinger, TJ and Patane, Oliver and Smith, Joshua R. Identifying correlations between LIGO's astronomical range and auxiliary sensors using lasso regression. *Classical and Quantum Gravity*, 35(22):225002, 2018.

[254] GWOSC: Gravitation Wave Open Science Center. GW170814 Samples and PSD release.

[255] GWOSC: Gravitation Wave Open Science Center. GW190828_063405 Samples and PSD release.

[256] GWOSC: Gravitation Wave Open Science Center. GW200306_093714 Samples and PSD release.

[257] Poisson, Siméon Denis. Probabilité des jugements en matière criminelle et en matière civile, précédées des règles générales du calcul des probabilitiés. *Paris, France: Bachelier*, 1:1837, 1837.

[258] Jameson Rollins, Jolien Creighton. GWINC: Inspiral-Range, 2021.

[259] LIGO Scientific collaboration. aLIGO O3 PSD, 2017.

[260] LIGO Scientific collaboration. aLIGO O4 PSD, 2017.

[261] LIGO Scientific collaboration. aLIGO Design PSD, 2017.

[262] ET collaboration. ET-D PSD, 2011.

[263] Aghanim, Nabila and Akrami, Yashar and Ashdown, Mark and Aumont, J and Baccigalupi, C and Ballardini, M and Banday, AJ and Barreiro, RB and Bartolo, N and Basak, S and others. Planck 2018 results-VI. Cosmological parameters. *Astronomy & Astrophysics*, 641:A6, 2020.

[264] Baibhav, Vishal and Berti, Emanuele and Gerosa, Davide and Mapelli, Michela and Giacobbo, Nicola and Bouffanais, Yann and Di Carlo, Ugo N. Gravitational-wave detection rates for compact binaries formed in isolation: LIGO/Virgo O3 and beyond. *Physical Review D*, 100(6):064060, 2019.

[265] Abbott, Rich and Abbott, TD and Abraham, S and Acernese, F and Ackley, K and Adams, A and Adams, C and Adhikari, RX and Adya, VB and Affeldt, C and others. Population properties of compact objects from the second LIGO–Virgo Gravitational-Wave Transient Catalog. *The Astrophysical Journal Letters*, 913(1):L7, 2021.

[266] Pizzati, Elia and Sachdev, Surabhi and Gupta, Anuradha and Sathyaprakash, BS. Toward inference of overlapping gravitational-wave signals. *Physical Review D*, 105(10):104016, 2022.

[267] Samajdar, Anuradha and Janquart, Justin and Van Den Broeck, Chris and Dietrich, Tim. Biases in parameter estimation from overlapping gravitational-wave signals in the third-generation detector era. *Physical Review D*, 104(4):044003, 2021.

[268] Abbott, R and Abe, H and Acernese, F and Ackley, K and Adhikari, N and Adhikari, RX and Adkins, VK and Adya, VB and Affeldt, C and Agarwal, D and others. All-sky search for gravitational wave emission from scalar boson clouds around spinning black holes in LIGO O3 data. *Physical Review D*, 105(10):102001, 2022.

[269] Abbott, R and Abe, H and Acernese, F and Ackley, K and Adhikari, N and Adhikari, RX and Adkins, VK and Adya, VB and Affeldt, C and Agarwal, D and others. All-sky search for continuous gravitational waves from isolated neutron stars using Advanced LIGO and Advanced Virgo O3 data. *arXiv preprint arXiv:2201.00697*, 2022.

[270] Romero-Shaw, IM and Talbot, C and Biscoveanu, S and D'Emilio, V and Ashton, G and Berry, CPL and Coughlin, S and Galaudage, S and Hoy, C and Hübner, M and others. Bayesian inference for compact binary coalescences with BILBY: Validation and application to the first LIGO–Virgo gravitational-wave transient catalogue. *Monthly Notices of the Royal Astronomical Society*, 499(3):3295–3319, 2020.

[271] Hannam, Mark and Schmidt, Patricia and Bohé, Alejandro and Haegel, Leïla and Husa, Sascha and Ohme, Frank and Pratten, Geraint and Pürrer, Michael. Simple model of complete precessing black-hole-binary gravitational waveforms. *Physical review letters*, 113(15):151101, 2014.

[272] Bohé, Alejandro and Hannam, Mark and Husa, Sascha and Ohme, Frank and Pürrer, Michael and Schmidt, Patricia. PhenomPv2–technical notes for the LAL implementation. *LIGO Technical Document, LIGO-T1500602-v4*, 2016.

[273] Husa, Sascha and Khan, Sebastian and Hannam, Mark and Pürrer, Michael and Ohme, Frank and Forteza, Xisco Jiménez and Bohé, Alejandro. Frequency-domain gravitational waves from nonprecessing black-hole binaries. I. New numerical waveforms and anatomy of the signal. *Physical Review D*, 93(4):044006, 2016.

[274] Khan, Sebastian and Husa, Sascha and Hannam, Mark and Ohme, Frank and Pürrer, Michael and Forteza, Xisco Jiménez and Bohé, Alejandro. Frequency-domain gravitational waves from nonprecessing black-hole binaries. II. A phenomenological model for the advanced detector era. *Physical Review D*, 93(4):044007, 2016.

[275] Fairhurst, Stephen and Green, Rhys and Hoy, Charlie and Hannam, Mark and Muir, Alistair. Two-harmonic approximation for gravitational waveforms from precessing binaries. *Physical Review D*, 102(2):024055, 2020.

[276] Scholz, Fritz W and Stephens, Michael A. K-sample Anderson–Darling tests. *Journal of the American Statistical Association*, 82(399):918–924, 1987.

[277] LIGO Scientific collaboration. adVirgo Design PSD, 2017.

[278] Schutz, Bernard. *A first course in general relativity*. Cambridge university press, 2022.

[279] Hu, Qian and Veitch, John. Accumulating errors in tests of general relativity with the Einstein Telescope: overlapping signals and inaccurate waveforms. *arXiv preprint arXiv:2210.04769*, 2022.

[280] Smith, Rory and Borhanian, Ssohrab and Sathyaprakash, Bangalore and Vivanco, Francisco Hernandez and Field, Scott and Lasky, Paul and Mandel, Ilya

and Morisaki, Soichiro and Ottaway, David and Slagmolen, Bram and others. Bayesian inference for gravitational waves from binary neutron star mergers in third-generation observatories. *arXiv preprint arXiv:2103.12274*, 2021.

[281] Antonelli, Andrea and Burke, Ollie and Gair, Jonathan R. Noisy neighbours: inference biases from overlapping gravitational-wave signals. *Monthly Notices of the Royal Astronomical Society*, 507(4):5069–5086, 2021.

[282] Himemoto, Yoshiaki and Nishizawa, Atsushi and Taruya, Atsushi. Impacts of overlapping gravitational-wave signals on the parameter estimation: Toward the search for cosmological backgrounds. *Physical Review D*, 104(4):044010, 2021.

[283] Davis, D and Littenberg, TB and Romero-Shaw, IM and Millhouse, M and McIver, J and Di Renzo, F and Ashton, G. Subtracting glitches from gravitational-wave detector data during the third LIGO-Virgo observing run. *Classical and Quantum Gravity*, 39(24):245013, 2022.

[284] Regimbau, Tania and Dent, Thomas and Del Pozzo, Walter and Giampanis, Stefanos and Li, Tjonnie GF and Robinson, Craig and Van Den Broeck, Chris and Meacher, Duncan and Rodriguez, Carl and Sathyaprakash, Bangalore S and others. Mock data challenge for the einstein gravitational-wave telescope. *Physical Review D*, 86(12):122001, 2012.

[285] Alex Nitz and Ian Harry and Duncan Brown and Christopher M. Biwer and Josh Willis and Tito Dal Canton and Collin Capano and Larne Pekowsky and Thomas Dent and Andrew R. Williamson and Gareth S Davies and Soumi De and Miriam Cabero and Bernd Machenschalk and Prayush Kumar and Steven Reyes and Duncan Macleod and dfinstad and Francesco Pannarale and Thomas Massinger and Sumit Kumar and Márton Tápai and Leo Singer and Sebastian Khan and Stephen Fairhurst and Alex Nielsen and Shashwat Singh and shasvath and Bhooshan Uday Varsha Gadre and Iain Dorrington. gwastro/pycbc: PyCBC Release v1.16.13, December 2020.

[286] The LIGO Collaboration. Advanced LIGO PSD, 2018. [Online; accessed 30-June-2022; last update 12-June-2018].

[287] Lynch, Ryan S and Freire, Paulo CC and Ransom, Scott M and Jacoby, Bryan A. The timing of nine globular cluster pulsars. *The Astrophysical Journal*, 745(2):109, 2012.

[288] Necula, V and Klimenko, S and Mitselmakher, G. Transient analysis with fast Wilson-Daubechies time-frequency transform. In *Journal of Physics: Conference Series*, volume 363, page 012032. IOP Publishing, 2012.

[289] Wu, Shichao and Nitz, Alexander H. A mock data study for 3G ground-based detectors: the performance loss of matched filtering due to correlated confusion noise. *arXiv preprint arXiv:2209.03135*, 2022.

[290] Salemi, F and Milotti, E and Prodi, GA and Vedovato, G and Lazzaro, C and Tiwari, S and Vinciguerra, S and Drago, M and Klimenko, S. Wider look at the gravitational-wave transients from GWTC-1 using an unmodeled reconstruction method. *Physical Review D*, 100(4):042003, 2019.

[291] Gu, Jiuxiang and Wang, Zhenhua and Kuen, Jason and Ma, Lianyang and Shahroudy, Amir and Shuai, Bing and Liu, Ting and Wang, Xingxing and Wang, Gang and Cai, Jianfei and others. Recent advances in convolutional neural networks. *Pattern recognition*, 77:354–377, 2018.

[292] Mukund, Nikhil and Abraham, Sheelu and Kandhasamy, Shivaraj and Mitra, Sanjit and Philip, Ninan Sajeeth. Transient classification in LIGO data using difference boosting neural network. *Physical Review D*, 95(10):104059, 2017.

[293] George, Daniel and Shen, Hongyu and Huerta, EA. Deep Transfer Learning: A new deep learning glitch classification method for advanced LIGO. *arXiv preprint arXiv:1706.07446*, 2017.

[294] George, Daniel and Huerta, EA. Deep neural networks to enable real-time multimessenger astrophysics. *Physical Review D*, 97(4):044039, 2018.

[295] Gabbard, Hunter and Williams, Michael and Hayes, Fergus and Messenger, Chris. Matching matched filtering with deep networks for gravitational-wave astronomy. *Physical review letters*, 120(14):141103, 2018.

[296] Massey Jr, Frank J. The Kolmogorov-Smirnov test for goodness of fit. *Journal of the American statistical Association*, 46(253):68–78, 1951.

[297] Robson, Travis and Cornish, Neil. Impact of galactic foreground characterization on a global analysis for the LISA gravitational wave observatory. *Classical and Quantum Gravity*, 34(24):244002, 2017.

[298] Littenberg, Tyson B and Cornish, Neil J and Lackeos, Kristen and Robson, Travis. Global analysis of the gravitational wave signal from galactic binaries. *Physical Review D*, 101(12):123021, 2020.

[299] Karnesis, Nikolaos and Babak, Stanislav and Pieroni, Mauro and Cornish, Neil and Littenberg, Tyson. Characterization of the stochastic signal originating from compact binary populations as measured by LISA. *Physical Review D*, 104(4):043019, 2021.

[300] Janquart, Justin and Baka, Tomasz and Samajdar, Anuradha and Dietrich, Tim and Broeck, Chris Van Den. Parameter estimation methods for analyzing overlapping gravitational wave signals in the third-generation detector era. *arXiv preprint arXiv:2211.01304*, 2022.

[301] Langendorff, Jurriaan and Kolmus, Alex and Janquart, Justin and Broeck, Chris Van Den. Normalizing flows as an avenue to study overlapping gravitational wave signals. *arXiv preprint arXiv:2211.15097*, 2022.

[302] Gianfranco Bertone and others. Gravitational wave probes of dark matter: challenges and opportunities. *SciPost Phys. Core*, 3:7, 2020.

[303] Arvanitaki, Asimina and Huang, Junwu and Van Tilburg, Ken. Searching for dilaton dark matter with atomic clocks. *Physical Review D*, 91(1):015015, 2015.

[304] Derevianko, A. and Pospelov, M. Hunting for topological dark matter with atomic clocks. *Nature Physics*, 10(12):933–936, 2014.

[305] Stadnik, Y. V. and Flambaum, V. V. Can dark matter induce cosmological evolution of the fundamental constants of Nature? *Physical Review Letters*, 115(20):201301, 2015.

[306] Van Tilburg, Ken and Leefer, Nathan and Bougas, Lykourgos and Budker, Dmitry. Search for Ultralight Scalar Dark Matter with Atomic Spectroscopy. *Physical Review Letters*, 115(1):011802, 2015.

[307] Hees, A. and Guéna, J. and Abgrall, M. and Bize, S. and Wolf, P. Searching for an oscillating massive scalar field as a dark matter candidate using atomic hyperfine frequency comparisons. *Physical Review Letters*, 117(6):061301, 2016.

[308] Leefer, N. and Gerhardus, A. and Budker, D. and Flambaum, V. V. and Stadnik, Y. V. Search for the Effect of Massive Bodies on Atomic Spectra and Constraints on Yukawa-Type Interactions of Scalar Particles. *Physical Review Letters*, 117(27):271601, 2016.

[309] Savalle, Etienne and others. Searching for dark matter with an unequal delay interferometer. *arXiv:2006.07055*, 2021.

[310] Grote, H. On the possibility of vacuum QED measurements with gravitational wave detectors. *Phys. Rev. D*, 91:022002, 2015.

[311] Chou, Aaron S. and others. First Measurements of High Frequency Cross-Spectra from a Pair of Large Michelson Interferometers. *Phys. Rev. Lett.*, 117:111102, 2016.

[312] Erik P. Verlinde and Kathryn M. Zurek. Observational Signatures of Quantum Gravity in Interferometers. *arxiv 1902.08207*, 2019.

[313] Vermeulen, Sander M. and others. An experiment for observing quantum gravity phenomena using twin table-top 3D interferometers. *Classical and Quantum Gravity*, 2021.

[314] Grote, H. and Stadnik, Y. V. Novel signatures of dark matter in laser-interferometric gravitational-wave detectors. *Phys. Rev. Research*, 1:033187, 2019.

[315] Pierce, Aaron and Riles, Keith and Zhao, Yue. Searching for Dark Photon Dark Matter with Gravitational Wave Detectors. *Physical Review Letters*, 121(6):061102, 2018.

[316] Hall, Evan D. and Adhikari, Rana X. and Frolov, Valery V. and Müller, Holger and Pospelov, Maxim. Laser interferometers as dark matter detectors. *Phys. Rev. D*, 98:083019, 2018.

[317] Guo, Huei-Ke and Riles, Keith and Yang, Feng-Wei and Zhao, Yeu. Searching for dark photon dark matter in LIGO O1 data. *Communications Physics*, 2:, 2019.

[318] Read, J. I. The Local Dark Matter Density. *arXiv:1404.1938*, 2014.

[319] Derevianko, Andrei. Detecting dark matter waves with precision measurement tools. *Physical Review A*, 97(4):042506, 2018.

[320] Flacke, Thomas and Frugiuele, Claudia and Fuchs, Elina and Gupta, Rick S. and Perez, Gilad. Phenomenology of relaxion-Higgs mixing. *Journal of High Energy Physics*, 2017(6):50, June 2017. arXiv: 1610.02025 version: 3.

[321] Banerjee, Abhishek and Kim, Hyungjin and Perez, Gilad. Coherent relaxion dark matter. *Physical Review D*, 100(11):115026, December 2019. arXiv: 1810.01889.

[322] Banerjee, Abhishek and Budker, Dmitry and Eby, Joshua and Kim, Hyungjin and Perez, Gilad. Relaxion stars and their detection via atomic physics. *Communications Physics*, 3(1):1, December 2020.

[323] Ringwald, Andreas. Exploring the Role of Axions and Other WISPs in the Dark Universe. *arXiv:1210.5081*, 2012.

[324] Hees, Aurélien and Minazzoli, Olivier and Savalle, Etienne and Stadnik, Yevgeny V. and Wolf, Peter. Violation of the equivalence principle from light scalar dark matter. *Physical Review D*, 98(6):064051, 2018.

[325] Damour, T. and Polyakov, A. M. The String Dilaton and a Least Coupling Principle. *Nuclear Physics B*, 423(2-3):532–558, July 1994. arXiv: hep-th/9401069.

[326] Arvanitaki, Asimina and Dimopoulos, Savas and Van Tilburg, Ken. Sound of Dark Matter: Searching for Light Scalars with Resonant-Mass Detectors. *Physical Review Letters*, 116(3):031102, January 2016. arXiv: 1508.01798.

[327] Damour, Thibault and Donoghue, John F. Equivalence Principle Violations and Couplings of a Light Dilaton. *Physical Review D*, 82(8):084033, October 2010. arXiv: 1007.2792.

[328] Geraci, Andrew A. and Bradley, Colin and Gao, Dongfeng and Weinstein, Jonathan and Derevianko, Andrei. Searching for ultra-light dark matter with optical cavities. *Physical Review Letters*, 123(3):031304, 2019.

[329] Lough, James and others. First Demonstration of 6 dB Quantum Noise Reduction in a Kilometer Scale Gravitational Wave Observatory. *Phys. Rev. Lett.*, 126:041102, 2021.

[330] Tröbs, Michael and Heinzel, Gerhard. Improved spectrum estimation from digitized time series on a logarithmic frequency axis. *Measurement*, 39(2):120–129, 2006.

[331] Tröbs, Michael and Heinzel, Gerhard. Corrigendum to "Improved spectrum estimation from digitized time series on a logarithmic frequency axis"" (vol 39, pg 120, 2006). *Measurement*, 42(1):170–170, 2009.

[332] Tröbs, Michael and Heinzel, Gerhard. LPSD Algorithm, 2019.

[333] Abbott, B. P. and others. Properties of the Binary Neutron Star Merger GW170817. *Phys. Rev. X*, 9:011001, 2019.

[334] Freese, Katherine and Lisanti, Mariangela and Savage, Christopher. Annual Modulation of Dark Matter: A Review. *Reviews of Modern Physics*, 85(4):1561–1581, 2013.

[335] Wagner, T. A. and Schlamminger, S. and Gundlach, J. H. and Adelberger, E. G. Torsion-balance tests of the weak equivalence principle. *Classical and Quantum Gravity*, 29(18):184002, August 2012. Publisher: IOP Publishing.

[336] Kennedy, Colin J. and Oelker, Eric and Robinson, John M. and Bothwell, Tobias and Kedar, Dhruv and Milner, William R. and Marti, G. Edward and Derevianko, Andrei and Ye, Jun. Precision Metrology Meets Cosmology: Improved Constraints on Ultralight Dark Matter from Atom-Cavity Frequency Comparisons. *Physical Review Letters*, 125(20):201302, November 2020. Publisher: American Physical Society.

[337] Aharony, Shahaf and others. Constraining Rapidly Oscillating Scalar Dark Matter Using Dynamic Decoupling. *arXiv:1902.02788*, 2019.

[338] Branca, Antonio and others. Search for an Ultralight Scalar Dark Matter Candidate with the AURIGA Detector. *Physical Review Letters*, 118(2):021302, 2017.

[339] Antypas, D. and Tretiak, O. and Garcon, A. and Ozeri, R. and Perez, G. and Budker, D. Scalar Dark Matter in the Radio-Frequency Band: Atomic-Spectroscopy Search Results. *Physical Review Letters*, 123(14):141102, October 2019. Publisher: American Physical Society.

[340] Bergé, Joel and others. MICROSCOPE Mission: First Constraints on the Violation of the Weak Equivalence Principle by a Light Scalar Dilaton. *Physical Review Letters*, 120(14):141101, 2018.

[341] Smith, G. L. and others. Short-range tests of the equivalence principle. *Physical Review D*, 61(2):022001, 1999.

[342] Savalle, Etienne and others. Novel approaches to dark-matter detection using space-time separated clocks. *arXiv:1902.07192*, 2019.

[343] Schlamminger, S. and Choi, K.-Y. and Wagner, T. A. and Gundlach, J. H. and Adelberger, E. G. Test of the Equivalence Principle Using a Rotating Torsion Balance. *Physical Review Letters*, 100(4):041101, January 2008. Publisher: American Physical Society.

[344] Pradyumna, S. T. and others. Twin beam quantum-enhanced correlated interferometry for testing fundamental physics. *Communications Physics*, 3(1):104, 2020.